



University of
Salford
MANCHESTER

**An Investigation into Methods for Dose Optimisation for
Paediatric AP Pelvis Projections When Considering Size
Variations**

Ali Hussein Mohammed Ali

School of Health Sciences,

University of Salford, Manchester, UK

Submitted in Partial Fulfilment of the Requirements for the

Degree of Doctor of Philosophy (PhD), July 2019

(Medical Physics)

Table of Contents

Table of Contents	I
List of Figures	V
List of Tables	IX
List of Publications, Conference Presentations and Seminars	X
List of Training Sessions	XII
Acknowledgements	XVII
List of Abbreviations	XVIII
Abstract	XX
Chapter One: Introduction	1
1.1 Introduction	1
1.2 Rationale.....	3
1.3 Research question.....	5
1.4 Aim.....	5
1.5 Objective	5
1.6 Statement of novelty.....	5
Chapter Two: Optimisation	7
2.1 Chapter overview	7
2.2 Background literature	8
2.2.1 Optimisation – a concept	8
2.2.2 Difficulties in paediatric dose optimisation	9
2.2.3 Paediatric radiography	10
2.2.4 Radiographic acquisition parameters	12
2.2.5 Imaging systems (film-screen, CR and DR)	16
2.2.6 Image quality evaluation.....	23
2.2.7 Estimating radiation dose.....	33
2.3 Current trends in paediatric dose optimisation – a review of the literature	36
2.3.1 Literature review methodology.....	36
2.3.2 Generic optimisation studies.....	37
2.3.3 Optimisation of pelvis X-ray examinations	41
2.4 Chapter summary	47
Chapter Three: X-ray Phantoms	48
3.1 Chapter overview	48

3.2	Introduction	48
3.2.1	Rationale for constructing bespoke pelvis phantoms.....	49
3.2.2	Objectives	50
3.3	Phantom Designs.....	51
3.3.1	Computational models	51
3.3.2	Physical phantoms	52
3.3.3	Commercially available phantom types for dose optimisation.....	56
3.4	Phantom criteria	57
3.4.1	Criteria for selecting tissue equivalence	57
3.4.2	X-ray interaction and attenuation.....	57
3.4.3	Selection requirements for phantoms.....	59
3.5	Availability of tissue substitutes	60
3.5.1	Background.....	60
3.5.2	Literature review	62
3.5.3	Manufacturing method for human tissue substitutes	63
3.6	Phantom application in the literature	65
3.6.1	Physical phantoms	65
3.7	Chapter summary	88
Chapter Four: Phantom Construction and Validation		89
4.1	Overview	89
4.2	Phantom construction: materials and methods.....	90
4.2.1	Constructional approaches	91
4.2.2	Method for the first manufactured phantom (Prototype 1).....	94
4.2.3	Modified method for manufacturing the phantoms (Prototype 2).....	96
4.3	Phantom validation methods	105
4.3.1	CT validation: Method.....	105
4.3.2	X-ray pixel value validity: method	112
4.3.3	Face Validity: method.....	117
4.3.4	Statistical analysis.....	119
4.4	Results: Phantom validation.....	120
4.4.1	CT validation	120
4.4.2	Pixel value validation.....	126
4.4.3	Face validity.....	129

4.5	Phantom validation: Discussion	132
4.5.1	CT validation	132
4.5.2	Pixel value validation.....	134
4.5.3	Face validity.....	135
4.6	Conclusion: phantom validity	136
4.7	Limitations	136
4.8	Future Consideration	137
4.9	Chapter summary	137
	Chapter Five: Optimisation Methods	138
5.1	Overview	138
5.2	Experimental set-up.....	138
5.2.1	X-ray equipment and quality assurance	138
5.2.2	Image detector.....	139
5.2.3	Display monitors.....	139
5.2.4	Phantoms.....	139
5.2.5	Dosimeter.....	140
5.3	Data acquisition.....	140
5.3.1	Factorial study design	140
5.3.2	Experimental study design and procedure	140
5.3.3	Acquisition factor selection	142
5.4	Optimisation method.....	145
5.5	Dose measurements.....	146
5.6	Image quality assessments	147
5.6.1	Methods used for calculating the net score of image quality.....	148
5.6.2	Physical image quality evaluation	149
5.6.3	Visual image quality evaluation.....	152
5.7	Optimisation and Figure of Merit (FOM)	158
5.8	Data analysis	159
5.9	Chapter summary	161
	Chapter Six: Optimisation Results.....	162
6.1	Chapter overview	162
6.2	Optimisation of AP paediatric pelvis radiography	163
6.2.1	Optimisation for a 1 year-old.....	163

6.2.2	Optimisation for a 5 year-old.....	165
6.2.3	Optimisation for a 10 year-old.....	167
6.3	Exposure factors effect on paediatric radiography.....	168
6.3.1	Main effect analysis.....	171
6.3.2	Correlations.....	196
6.3.3	Regression analysis.....	200
6.4	Chapter Summary.....	206
Chapter Seven: Discussion.....		207
7.1	Chapter overview.....	207
7.2	Optimisation of AP paediatric pelvis radiography.....	208
7.2.1	Optimisation for 1 year-old phantom.....	208
7.2.2	Optimisation for 5 year-old phantom.....	212
7.2.3	Optimisation for 10 year-old phantom.....	217
7.3	Effect of exposure factors on paediatric pelvis radiography.....	223
7.3.1	Main effect.....	223
7.3.2	Correlation.....	227
7.3.3	Regression analysis.....	230
7.4	Conclusion.....	234
7.5	Limitations.....	236
7.6	Recommendations.....	238
7.7	Future work.....	238
References.....		240
Appendices.....		266
	Appendix (I).....	266
	Appendix (II).....	283
	Appendix (III): Brochures of Commercial Phantoms.....	291
	Appendix (IV): Ethical Approvals.....	295
	Appendix (V): Quality Control Tests.....	297

List of Figures

Figure 2.1: The flowchart provides an overview of different types of digital detectors. CCD: charge coupled device and TFT: thin film transistor (Körner et al., 2007).	17
Figure 2.2: Indirect conversion - DR systems (Fauber, 2013).	21
Figure 2.3: Direct conversion - DR systems (Fauber, 2013).	22
Figure 2.4: represents a typical ROC curve (Thompson, 2014).	29
Figure 3.1: New-born, 1- & 5-year-old phantoms. All made with natural skeletons. TLD locations were optimised for each organ (Varchena, 2002).	52
Figure 3.2: Heterogeneous Anthropomorphic phantom for 5-year-old. Produced by ATOM Ltd. (Varchena et al., 1993).	53
Figure 3.3: CIRS (model 715) 5-year-old phantom. (a) Trunk (b) AP pelvis.	54
Figure 3.4: The Kyoto Paediatric Whole-Body Phantom, (a) 5-year-old and (b) 1 year-old.	55
Figure 3.5: X-ray interactions with water over the energy range 0.001 to 1 Mev (Aichinger et al., 2012).	59
Figure 3.6: linear attenuation coefficients for different human organs and substitutes.	61
Figure 3.7: (a) The Leeds Test Objects TOR CDR, (b) CT Prototype custom phantom representing normal anatomy and acute intracranial pathology.	66
Figure 3.8: The LucAl phantom: on the left, its components (Conway et al., 1984).	67
Figure 3.9: physical heterogeneous dosimetry phantom. (a) schematic diagram (b) body torso (Bower, 1997).	69
Figure 3.10: (a) Slices that were used the new-born phantom, (b) the new-born dosimetry phantom (A. Jones, 2006).	71
Figure 3.11: Adult anthropomorphic dosimetry phantom (Winslow et al., 2009).	72
Figure 3.12: the pelvic dosimetry phantom (a) assembled together (b) in slices (Harrison et al., 2011).	73
Figure 3.13: Schematic diagram of a semi-anthropomorphic chest phantom (Constantinou et al., 1986).	75
Figure 3.14: A schematic view of the realistic-analytic phantom (RAP) (Pina et al., 2004).	76
Figure 3.15: X-ray image of the anthropomorphic LucAl chest phantom (Vassileva, 2002).	78
Figure 3.16: Mega-voltage cone beam CT (MV-CBCT) images of coronal plain of the pelvis phantom (Schaly et al., 2009).	80
Figure 3.17: An image of a 3D abdomen phantom of 1 cm thickness, produced by (Jahnke et al., 2017).	82
Figure 3.18: Head and neck phantoms constructed using 3D printer assembled (a) with the paper-based 3D printer (b) the customized laminated object manufacturing procedure (Jahnke et al., 2019).	83
Figure 3.19: 3D printed thorax phantom presented by (Hazelaar et al., 2018). (a); represents bony structures printed in gypsum, (b); lung structures printed in nylon and (c); soft tissues outside the lungs are represented by silicone.	84
Figure 4.1: An illustration of the PMMA sections used to form the first prototype phantom. Within each slice, shapes have been removed (using a milling machine) from which PVC (bone) shapes would be inserted.	95
Figure 4.2: An X-ray image of the first prototype pelvis phantom (representing a 4-year-old). Black lines over the bony regions, part of the construction process, were considered technically unacceptable.	96
Figure 4.3: Coronal CT slices used to mimic the bony anatomies in pelvis.	97
Figure 4.4: (a) and (b), connected and smoothed edges of second prototype / final phantom design. .	99

Figure 4.5: PMMA slices are ready for PoP filling.	100
Figure 4.6: The scale used to weigh the plaster powder (on the left) and the water (on the right).	101
Figure 4.7: PMMA block filled with PoP and flatted to the PMMA surface.	102
Figure 4.8: All of the PMMA slices assembled together.	103
Figure 4.9: (a), (b) and (c) are X-ray images of the 1, 5 and 10 year old phantoms, respectively.	104
Figure 4.10: Samples of PoP during CT testing experiments.	108
Figure 4.11: Comparative measurements of bony anatomies (a) inside the patient, (b) inside the phantom (using CT windowing for bone).	109
Figure 4.12: for the 1 year old: (a) & (b) frontal view of the patient and the phantom, respectively.	110
Figure 4.13: for the 5-year-old: (a) & (b) frontal view of the patient and the phantom, respectively.	111
Figure 4.14: For the 10-year-old: (a) & (b) frontal view of the real patient and the phantom, respectively. (c) & (d) lateral view of the patient and the phantom, respectively.	112
Figure 4.15: X-ray acquisition set-up for (a), one of the phantoms (5-year-old) and (b) reference phantoms.	116
Figure 4.16: SNR measurements; ROIs placed (a) on each of the constructed phantom X-ray images and (b) on the adult valid phantom X-ray image.	117
Figure 4.17: CT density variations versus time for the different weight-mixing ratios.	120
Figure 5.1: Experimental setup of the 1-year-old phantom, DR detector and X-ray tube.	143
Figure 5.2: Experimental setup of the 5-year-old phantom, DR detector and X-ray tube.	144
Figure 5.3: Experimental setup of the 10-year-old phantom and X-ray tube. The table Bucky was used for all examinations involving this phantom.	145
Figure 5.4: Experimental setup for the radiation dose measurements.	147
Figure 5.5: This diagram illustrates the processes of assessing the IQ (physical and visual).	148
Figure 5.6: ROI measurements from the 1-year-old phantom using the ImageJ software.	150
Figure 5.7: ROI measurements from the 5-year-old phantom using the ImageJ software.	151
Figure 5.8: ROI measurements from the 10-year-old phantom using the ImageJ software.	151
Figure 5.9: The relative VGA monitor set-up for the phantom X-ray images; on the left-hand the reference image and on the left the random image viewed.	154
Figure 5.10: Distribution of IQ levels that chosen for the focus group (a), (b) and (c) are for the ages 1, 5 and 10 years, respectively.	157
Figure 5.11: Flow diagram for the focus group study design.	158
Figure 6.1: Histogram of SNR and CNR overlap between acceptable and non-acceptable image quality (1-year-old); (a) and (b) are measured from acceptable image quality, while (c) and (d) are measured from not acceptable image quality.	165
Figure 6.2: Histogram of SNR and CNR overlap between acceptable and non-acceptable image quality (5 year-old); (a) and (b) are measured from acceptable image quality, while (c) and (d) are measured from not acceptable image quality.	167
Figure 6.3: 1 year-old the main effect plot for dose (μGy) when increasing the kVp; (a) at 0 filtration, (b) at 2 mm Al, (c) at 0.1 mm Cu + 1 mm Al.	173
Figure 6.4: 5 year-old the main effect plot for dose (μGy) when increasing the SID; (a) at 0 filtration, (b) at 2 mm Al, (c) at 0.1 mm Cu + 1 mm Al.	173
Figure 6.5: 10 year-old the main effect plot for dose (μGy) when increasing the SID; (a) at 0 filtration, (b) at 2 mm Al, (c) at 0.1 mm Cu + 1 mm Al.	173
Figure 6.6: 1 year-old the main effect plot for physical image quality when increasing the kVp: (a-c) for SNR and (d-f) for CNR. (a)& (d) at 0 filtration, (b) &(c) at 2 mm Al and (c) & (f) at 0.1 mm Cu + 1 mm Al.	174

Figure 6.7: 5 year-old the main effect plot for physical image quality when increasing the kVp; (a-c) for SNR and (d-f) for CNR. (a)& (d) at 0 filtration, (b) &(c) at 2 mm Al and (c) & (f) at 0.1 mm Cu + 1 mm Al.	175
Figure 6.8: 10 year-old the main effect plot for physical image quality when increasing the kVp; (a-c) for SNR and (d-f) for CNR. (a)& (d) at 0 filtration, (b) &(c) at 2 mm Al and (c) &(f) at 0.1 mm Cu + 1 mm Al.	175
Figure 6.9: 1 year-old the main effect plot for visual image quality when increasing the kVp; (a-c) for IQ (sharpness) and (d-f) for IQ (clarity). (a)& (d) at 0 filtration, (b) &(c) at 2 mm Al and (c) &(f) at 0.1 mm Cu + 1 mm Al.	176
Figure 6.10: 5 year-old the main effect plot for visual image quality when increasing the kVp; (a-c) for IQ (sharpness) and (d-f) for IQ (clarity). (a)& (d) at 0 filtration, (b) &(c) at 2 mm Al and (c) & (f) at 0.1 mm Cu + 1 mm Al.	177
Figure 6.11: 10 year-old the main effect plot for visual image quality when increasing the kVp; (a-c) for IQ (sharpness) and (d-f) for IQ (clarity). (a)& (d) at 0 filtration, (b) &(c) at 2 mm Al and (c) & (f) at 0.1 mm Cu + 1 mm Al.	177
Figure 6.12: 1 year-old the main effect plot for IQ (sharpness and clarity) when increasing the kVp. (a) at 0 filtration, (b) at 2 mm Al and (c) at 0.1 mm Cu + 1 mm Al.	178
Figure 6.13: 5 year-old the main effect for IQ (sharpness and clarity) when increasing the kVp. (a) at 0 filtration, (b) at 2 mm Al and (c) at 0.1 mm Cu + 1 mm Al.	179
Figure 6.14: 10 year-old the main effect plot for IQ (sharpness and clarity) when increasing the kVp. (a) at 0 filtration, (b) at 2 mm Al and (c) at 0.1 mm Cu + 1 mm Al.	179
Figure 6.15: 1 year-old the main effect plot for FOM when increasing the kVp; (a-c) for FOM (SNR) and (d-f) for FOM (visual IQ). (a)& (d) at 0 filtration, (b) &(c) at 2 mm Al and (c) & (f) at 0.1 mm Cu + 1 mm Al.	180
Figure 6.16: 5 year-old the main effect plot for FOM when increasing the kVp; (a-c) for FOM (SNR) and (d-f) for FOM (visual IQ). (a)& (d) at 0 filtration, (b) &(c) at 2 mm Al and (c) & (f) at 0.1 mm Cu + 1 mm Al.	180
Figure 6.17: 10 year-old the main effect plot for FOM when increasing the kVp; (a-c) for FOM (SNR) and (d-f) for FOM (visual IQ). (a)& (d) at 0 filtration, (b) &(c) at 2 mm Al and (c) & (f) at 0.1 mm Cu + 1 mm Al.	181
Figure 6.18: 1 year-old the main effect plot for dose (μ Gy) when increasing the mAs; (a) at 0 filtration, (b) at 2 mm Al, (c) at 0.1 mm Cu + 1 mm Al.	182
Figure 6.19: 5 year-old the main effect plot for dose (μ Gy) when increasing the mAs; (a) at 0 filtration, (b) at 2 mm Al, (c) at 0.1 mm Cu + 1 mm Al.	182
Figure 6.20: 1 year-old the main effect plot for physical image quality when increasing the mAs: (a-c) for SNR and (d-f) for CNR. (a)& (d) at 0 filtration, (b) &(c) at 2 mm Al and (c) & (f) at 0.1 mm Cu + 1 mm Al.	183
Figure 6.21: 5 year-old the main effect plot for physical image quality when increasing the mAs: (a-c) for SNR and (d-f) for CNR. (a)& (d) at 0 filtration, (b) &(c) at 2 mm Al and (c) & (f) at 0.1 mm Cu + 1 mm Al.	183
Figure 6.22: 1 year-old the main effect plot for visual image quality when increasing the mAs; (a-c) for IQ (sharpness) and (d-f) for IQ (clarity). (a)& (d) at 0 filtration, (b) &(c) at 2 mm Al and (c) & (f) at 0.1 mm Cu + 1 mm Al.	184
Figure 6.23: 5 year-old the main effect plot for visual image quality when increasing the mAs; (a-c) for IQ (sharpness) and (d-f) for IQ (clarity). (a) & (d) at 0 filtration, (b) & (c) at 2 mm Al and (c) & (f) at 0.1 mm Cu + 1 mm Al.	185
Figure 6.24: 1 year-old the main effect plot for IQ (sharpness and clarity) when increasing the mAs. (a) at 0 filtration, (b) at 2 mm Al and (c) at 0.1 Cu + 1 mm Al.	185

Figure 6.25: 5 year-old the main effect plot for IQ (sharpness and clarity) when increasing the mAs. (a) at 0 filtration, (b) at 2 mm Al and (c) at 0.1 Cu + 1 mm Al.	186
Figure 6.26: 1 year-old the main effect plot for FOM when increasing the mAs; (a-c) for FOM (SNR) and (d-f) for FOM (visual IQ). (a)&(d) at 0 filtration, (b)&(c) at 2 mm Al and (c)&(f) at 0.1 mm Cu + 1 mm Al.	186
Figure 6.27: 5 year-old the main effect plot for FOM when increasing the mAs; (a-c) for FOM (SNR) and (d-f) for FOM (visual IQ). (a)&(d) at 0 filtration, (b) & (c) at 2 mm Al and (c) & (f) at 0.1 mm Cu + 1 mm Al.	187
Figure 6.28: 1 year-old the main effect plot for dose (μGy) when increasing the SID; (a) at 0 filtration, (b) at 2 mm Al, (c) at 0.1 mm Cu + 1 mm Al.	188
Figure 6.29: 5 year-old the main effect plot for dose (μGy) when increasing the SID; (a) at 0 filtration, (b) at 2 mm Al, (c) at 0.1 mm Cu + 1 mm Al.	188
Figure 6.30: 10 year-old the main effect plot for dose (μGy) when increasing the SID; (a) at 0 filtration, (b) at 2 mm Al, (c) at 0.1 mm Cu + 1 mm Al.	188
Figure 6.31: 1 year-old the main effect plot for physical image quality when increasing the SID: (a-c) for SNR and (d-f) for CNR. (a)&(d) at 0 filtration, (b)&(c) at 2 mm Al and (c)&(f) at 0.1 mm Cu + 1 mm Al.	189
Figure 6.32: 5 year-old main effect plot for physical image quality when increasing the SID: (a-c) for SNR and (d-f) for CNR. (a)&(d) at 0 filtration, (b)&(c) at 2 mm Al and (c)&(f) at 0.1 mm Cu + 1 mm Al.	190
Figure 6.33: 10 year-old main effect plot for physical image quality when increasing the SID: (a-c) for SNR and (d-f) for CNR. (a)&(d) at 0 filtration, (b)&(c) at 2 mm Al and (c)&(f) at 0.1 mm Cu + 1 mm Al.	190
Figure 6.34: 1 year-old main effect plot for visual image quality when increasing the SID; (a-c) for IQ (sharpness) and (d-f) for IQ (clarity). (a)&(d) at 0 filtration, (b)&(c) at 2 mm Al and (c)&(f) at 0.1 mm Cu + 1 mm Al.	191
Figure 6.35: 5 year-old main effect plot for visual image quality when increasing the SID; (a-c) for IQ (sharpness) and (d-f) for IQ (clarity). (a)&(d) at 0 filtration, (b)&(c) at 2 mm Al and (c)&(f) at 0.1 mm Cu + 1 mm Al.	192
Figure 6.36: 10 year-old main effect plot for visual image quality when increasing the SID; (a-c) for IQ (sharpness) and (d-f) for IQ (clarity). (a)&(d) at 0 filtration, (b)&(c) at 2 mm Al and (c)&(f) at 0.1 mm Cu + 1 mm Al.	192
Figure 6.37: 1 year-old the main effect plots for IQ (sharpness and clarity) when increasing the mAs. (a) at 0 filtration, (b) at 2 mm Al and (c) at 0.1 Cu + 1 mm Al.	193
Figure 6.38: 5 year-old the main effect plots for IQ (sharpness and clarity) when increasing the mAs. (a) at 0 filtration, (b) at 2 mm Al and (c) at 0.1 Cu + 1 mm Al.	193
Figure 6.39: 10 year-old the main effect plots for IQ (sharpness and clarity) when increasing the mAs. (a) at 0 filtration, (b) at 2 mm Al and (c) at 0.1 Cu + 1 mm Al.	194
Figure 6.40: 1 year-old the main effect plot for FOM when increasing the mAs; (a-c) for FOM (SNR) and (d-f) for FOM (visual IQ). (a)&(d) at 0 filtration, (b)&(c) at 2 mm Al and (c)&(f) at 0.1 mm Cu + 1 mm Al.	195
Figure 6.41: 5 year-old the main effect plot for FOM when increasing the mAs; (a-c) for FOM (SNR) and (d-f) for FOM (visual IQ). (a)&(d) at 0 filtration, (b)&(c) at 2 mm Al and (c)&(f) at 0.1 mm Cu + 1 mm Al.	195
Figure 6.42: 10 year-old the main effect plot for FOM when increasing the mAs; (a-c) for FOM (SNR) and (d-f) for FOM (visual IQ). (a)&(d) at 0 filtration, (b)&(c) at 2 mm Al and (c)&(f) at 0.1 mm Cu + 1 mm Al.	196

List of Tables

Table 3.1: X-ray phantoms described within the literature.....	84
Table 4.1: Mean (SD) CT densities for each of the mix ratios over time.	121
Table 4.2: Percentage difference and percentage change of PoP across the three phantoms.	123
Table 4.3: Comparison of CT density for the 1-year-old phantom materials versus human patient tissues.	125
Table 4.4: Comparison of CT density for the 5-year-old phantom materials versus human patient tissues.	125
Table 4.5: Comparison of CT density for the 10 year old phantom materials versus human patient tissues.....	126
Table 4.6: Mean correlation coefficient from comparing the adult anthropomorphic with each phantom of 21 cm thick.	128
Table 4.7: Questionnaire results from the 1, 5 and 10-year-old phantoms.	130
Table 4.8: Agreements of answers, number of answers for each question. The underlined questions are the one used for the 1 year old phantom IQ scale.	131
Table 4.9: Agreements of answers, number of answers for each question. The underlined answers are the one used for the 5 year old phantom image quality scale.	131
Table 4.10: Agreements of answers, number of answers for each question. The underlined answers are the one used for the 10 year old phantom image quality scale.	132
Table 5.1: The percentage of agreement by the observers on each level of image quality for the 1, 5 and 10 year-old phantoms.....	156
Table 6.1: Exposure factors that scored the five lowest doses with acceptable image quality (1-year- old).	164
Table 6.2: Exposure factors that scored the five lowest doses with acceptable IQ (5 year-old).....	166
Table 6.3: Exposure factors that scored the five lowest doses with acceptable IQ (10 year-old).....	168
Table 6.4: the 10-year-old radiation doses and image quality produced for each orientation.	169
Table 6.5: the 10-year-old phantom - radiation dose and image quality produced over each combination of ionisation chambers at HT orientation.....	170
Table 6.6: Exposure factors with a non-significant ($P>0.05$) impact on measured parameters for the 10- year-old phantom.	171
Table 6.7: Range of exposure factor correlation coefficients for each paediatric age.	199
Table 6.8: Absolute β values (descending order) for each exposure factor along with their ratios for the 1-year-old phantom.	202
Table 6.9: Absolute β values (descending order) for each exposure factor along with their ratios for the 5-year-old phantom.	204
Table 6.10: Absolute β values (descending order) for each exposure factor along with their ratios for the 10-year-old phantom.	205
Table 7.1: Dose optimised exposure factor combination for 1, 5- and 10-year-old pelvis radiography.	234

List of Publications, Conference Presentations and Seminars

No	Title	Status
1	Construction and validation of a low cost paediatric pelvis phantom. Ali Mohammed Ali, Peter Hogg, Safora Johansen, Andrew England. Eur. J. Radiol. 108 (2018) 84–91. doi:10.1016/j.ejrad.2018.09.015.	Journal article published in the European journal of radiology (EJR) 2018
2	Construction and implementation of a low cost paediatric pelvic imaging phantom for dose optimisation studies. Ali Mohammed Ali, Peter Hogg, Andrew England.	Conference paper presented in UKRC congress 2018
3	Image quality and radiation dose interrelationships during paediatric pelvis radiography - a factorial phantom study. Ali Mohammed Ali, Peter Hogg, Andrew England.	Conference poster presented in UKRC congress 2018
4	Relationships between image quality and radiation dose during paediatric pelvis radiography - a factorial phantom study. Ali Mohammed Ali, Peter Hogg, Andrew England.	Conference paper presented in ECR congress 2018
5	Development and validation of a low-cost paediatric pelvic phantom for digital radiography dose optimisation. Ali Mohammed Ali, Peter Hogg, Andrew England.	Conference paper presented in ECR congress 2018
6	Effect of tube current-time on image quality and radiation dose during paediatric pelvis radiography. Ali Mohammed Ali, Peter Hogg, Andrew England.	Conference poster presented in SPARK congress 2018
7	Development and Validation of a Paediatric Pelvic Phantom for Digital Radiography Dose Optimisation. Ali Mohammed Ali, Peter Hogg, Andrew England.	Conference poster presented in SPARK congress 2017
8	Impact of the anode heel effect on image quality and effective dose for AP pelvis: a pilot study. Carst Buissink, Matthew Bowdler, Ahmed khalid Abdullah, Sadeq Al-Murshedi, S. Custódio, Andrea Huhn, J. Pires-Jorge, Ali Mohammed Ali, A. Peters, Y. Rey, T. Urdahl and Peter Hogg	Book chapter OPTIMAX 2016

9	Construction and implementation of a low cost paediatric pelvic imaging phantom for dose optimisation studies.	“Three minute thesis”, a local ‘heat’ conducted within SPARC Conference at University of Salford, 2018 (part of the national scheme: <u>UK National 3MT Competition</u>)
---	--	--

List of Training Sessions

Course / training session	Date
Completing a Learning Agreement & the PhD Progression Points	15-10-2015
Intro to EndnotX7	4-11-2015
Introduction to Microsoft Office Specialist (MOS) Workshop	5-11-2015
Excel: Formulas and Functions	11-11-2015
TLD and dosimetry training	18-11-2015
Time Management and Procrastination	24-11-2015
Introduction to Literature Searching	25-11-2015
PowerPoint: Enhancing Your Presentation	26-11-2015
Analysing Data	27-11-2015
Organising and Synthesising your Work	30-11-2015
Excel: The Basics.	2-12-2015
Electronic Resources for Researchers	7-12-2015
Planning and Writing a Thesis	8-12-2015
Becoming a Researcher: Realizing your Potential and Raising your Profile	10-12-2015
PowerPoint - Creating Academic Posters	14-12-2015
Excel: Analysing Data	16-12-2015
Quantitative research method with SPSS - Day 1	13-01-2016
Quantitative research method with SPSS - Day 2	14-01-2016
Quantitative research method with SPSS - Day 3	15-01-2016
Myers Briggs Type Indicator	20-1-2016
Conversation analysis and online interaction	4-2-2016
The seven secrets of highly successful research student	5-2-2016
Advanced search and social care database	8-2-2016
Locating and Using Historical Archive for Research	10-2-2016
GTS students only: Introduction to learning and teaching in higher education	10-2-2016
Controversial issues in breast cancer diagnosis using full field digital mammography	10-2-2016
Google Scholar for research	16-2-2016
Research Ethics for PGRs	18-2-2016
GTS students only: Theories of learning and teaching	24-2-2016
PGR students meeting	26-2-16

Introduction to SPSS	29-2-2016
Introduction to NVivo using the literature review	29-2-2016
Quality Control.	3-3-2016
Diagnostic Imaging Research	7-03-16
Geographical Information Systems (GIS)	8-03-16
GTS students only: Inclusive teaching & classroom management.	9-3-2016
Geographical Information Systems (GIS)	15-03-16
Health Sciences Seminar: Direct x ray radiation dose measurements in human phantom.	1-4-2016
Research Data Management	6-04-2016
Higher leap session for academic Speaking	14-4-2016
Reflective Writing workshop	15-04-2016
Open research: open research publishing and research data managements	18-4-2016
Surviving your Internal Examination	19-4-2016
Higher leap session for academic Speaking	21-4-2016
PGR Presentation Practise Session. Taking part in the 3 Minute Thesis presentations	22-4-2016
Presenting at Academic Conferences	25-4-2016
GTS students only: Assessment and feedback (for GTS students engaged in assessment)	27-4-2016
CVs-Academic and non-academic	28-4-2016
Higher leap session for academic Speaking	28-4-2016
PGR monthly meeting	29-4-2014
Higher leap session for critical writing	03-5-2016
Higher leap session for critical writing	10-5-2016
Higher leap session for critical writing	16-5-2016
Critical thinking and critical writing at doctoral level	27-5-2016
Developing Critical Writing for PhD Science Students: Being Critical	10-11-2016
Developing Critical Writing for PhD Science Students: Building the Argument	17-11-2016
Developing Critical Writing for PhD Science Students: Methods	24-11-2016

Developing Critical Writing for PhD Science Students: Results	1-12-2016
Building resilience and bounceback ability: Improve your resilience to criticism	2-11-2017
Get more out of your reading: Practical exercises to help you read more in less time take more concise, relevant notes	2-11-2017
Your thesis: structure	3-11-2017
Your thesis: the thesis of your thesis	3-11-2017
Formatting and submitting your thesis	3-11-2017
Planning a cohesive story: writing workshops	11-1-2018
Writing argument: writing workshops	17-1-2018
Peer review and feedback: writing workshops	22-1-2018
Peer review and feedback: writing workshops	5-2-2018
Organising conferences, seminars and collaborative events	23-1-2018
Researcher Development Day - PGR Publishing Retreat	8-2-2018
Researcher Development Day - How to write an abstract	8-2-2018
Researcher Development Day - Proof reading, editing and letting go	8-2-2018
Researcher Development Day - Designing and presenting a poster: Communication Skills - Designing and presenting a poster	9-2-2018
Researcher Development Day - Giving confident presentations with impact	9-2-2018
Researcher Development Day - Promoting your work for high performing researchers	9-2-2018
Health science writing workshop: Advice and guidance on writing an abstract	26-2-2018
Get ready for the viva workshop practice	9-3-2018
Life after the PhD	18-04-2018
Research Seminar	14-05-2018
PGR Seminar: data analysis	16-05-2018
SPARC Chairing sessions - Training	25-06-2018
Session for confidence building for Public Speaking	26-06-2018
Presenting a talk at UKRC conference	02-07-2018
Presenting a talk at SPARK conference	04-07-2018

Participating in charring conference session	05-07-2018
Statistics workshop using SPSS	25-07-2018

Teaching Development sessions (October to December 2018)			
No.	Session title	Indicative content	Date
1	Introduction to Learning and Teaching in Higher Education.	Context of teaching in HE (national and local); teaching and its role in your career; the Quality Assurance Agency and Framework for Higher Education Qualifications; the Higher Education Academy and Fellowship Status; ongoing development as a teacher in HE; teaching in HE as a discipline in its own right; reflective practice as the cornerstone of good teaching.	03-10-2018
2	Theories of learning and teaching.	Approaches to Teaching Inventory; Ramsden's three theories of teaching; Surface and Deep approaches to learning; Student motivation; Taxonomies of knowledge (SOLO/Bloom's); Learning outcomes and constructive alignment.	17-10-2018
3	Large group and small group teaching.	Teaching in a lecture theatre; pushing the boundaries of teaching practice; student perspectives on large groups/lectures/small groups; pedagogic value of the lecture; good practice in the lecture theatre; viable lecture theatre activities; structuring a lecture; identifying the features of small group teaching in your own discipline; advantages of small group teaching; challenges and rewards of small group teaching	31-10-2018
4	Technology Enhanced Learning	Purpose and scope of TEL (what can we expect from it?); models for developing online collaboration; collaborative learning; asynchronous and synchronous; a brief history of technology in education; the impact of TEL.	14-10-2018
5	Inclusive teaching and classroom management.	What are inclusion and diversity? Benefits of inclusive teaching; general principles of inclusive teaching; andragogy as inclusive practice; classroom behaviour, dos and don'ts; respect for learners/teachers; expectations; designing interactive sessions to keep students on track; motivation, structure, assessment; encouraging student engagement.	28-11-2018
6	Assessment and feedback	Why do we assess? Formative and summative assessment; high-stakes/low-stakes assessment; backwash effect; variety	12-11-2018

	<p>of assessment; inclusive assessment; assessment criteria; assessment principles; what do we mean by feedback? Student views of feedback; double duty of assessment; assessing for learning.</p>	
--	---	--

Course / training session	Date
Team building activity	31-7- 2016
Team working	1-8-2016
Research methods	1-8-2016
Radiation Protection in the Laboratory	2-8-2016
Project Management	2-8-2016
Group work	2-8-2016
Statistics	3-8-2016
Conference presenting	10-8-2016
OPTIMAX 2016 Conference	19-8-2016

Acknowledgements

A period of more than three years has been dedicated to my acquiring a Doctorate of Philosophy. Throughout this period, I received a great amount of help and support from many people. To those who gave me guidance and inspiration to successfully finish my PhD study, I want to show my deepest appreciation and gratitude.

Among the first who I would like to thank is the supervisory team, namely, Dr. Andrew England and Professor Peter Hogg. They have never hesitated to offer me their knowledge and experience which has had a major contribution into my PhD journey. Also, I would like to mention Christopher Beaumont, Specialist Radiography Technician, who has provided me with a lot of technical knowledge, besides, helping me with the construction of my phantoms. Another person to thank is Dr. Katy Szczepura, who has continually provided very useful information and advice since the very beginning of my studies. In addition, I want to thank Professor Hussein Mraity, who has been instrumental in providing advice, particularly on the validation of the phantoms.

I would like to show special thanks to my parents, who have encouraged and supported me from the first moment at which I was awarded the scholarship. My mother always prayed for me to succeed in my studies and life, and has been my ultimate spiritual support.

Finally, I would like to show my greatest gratitude to my sponsor, the Higher Committee for Education Development in Iraq (HCED Iraq). Without their financial support I would not have been able to complete my studies in the United Kingdom.

List of Abbreviations

ADC: Analogue to Digital Converter

3D: Three Dimensional

AFC: Alternative Forced Choice

AM: Additive Manufacturing

BSF: Backscatter Factor

CCD: Charge Coupled Device

CEC: Commission of European Communities

CNR: Contrast to Noise Ratio

CR: Computed Radiography

DAP: Dose Area Product

DQE: Detective Quantum Efficiency

DR: Direct Digital Radiography

DRL: Dose Reference Level

ED: Effective Dose

ESAK: Entrance Surface Air Kerma

ESD: Entrance Surface Dose

FFD: Focus to Film Distance

FN: False Negatives

FOC: Fibre Optic Coupled

FP: False Positive

FP: False Positive

HVL: Half Value Layer

IAK: Incident Air Kerma

ICRP: International Commission on Radiological Protection

ICRU: International Commission on Radiation Units and Measurements

IQR: Inter-Quartile Range

IR(ME): Ionising Radiation (Medical Exposure)

KAP: Kerma Area Product

kVp: Kilo-Voltage peak

LLF: Lesion Localization Fraction

mAs: Tube current-time

NAI: Non-Accidental Injury

NLF: Non-lesion Localization Fraction
PSP: Photostimulable Phosphor Plate
PVC: Polyvinyl Chloride
r: correlation coefficient
ROC: Receiver Operative Characteristics
SD: Standard Deviation
SID: Source to Image Distance
SNR: Signal to Noise Ratio
SPS: Storage Phosphor Systems
TFT: Thin Film Transistor
TLD: Thermos-Luminescent *Dosimeter*
TN: True Negatives
TP: True Positive
VGA: Visual Grading Analysis

Abstract

Purpose

There is a lack of literature on paediatric x-ray dose optimisation; this is especially true for pelvis radiography using digital systems. Various reasons exist for this including the limited availability of paediatric phantoms on which to conduct optimisation studies and that the paediatric age/size range is broad, unlike the adult. This adds to the complexity of optimisation. The paediatric population presents a further complexity regarding the high potential for radiation damage. This is because they have a longer time left to live and are more radiosensitive.

To address the lack of phantoms available for optimisation studies, this thesis presents a novel, low-cost approach for the construction and validation of paediatric X-ray phantoms. Using this approach, three phantoms were produced to answer the research questions posed in this thesis. Using these phantoms, experiments were conducted to optimise dose and image quality. The outcomes of these experiments have value to AP pelvis X-ray imaging in children.

Method

Constructed of plaster of Paris and PMMA, the three phantoms were made to represent 1, 5 and 10-year-old paediatric pelvises. Using these phantoms, dose optimisation studies were undertaken combining assessments of image quality (IQ) and radiation dose for each paediatric age. Systematic variations (factorial design) of exposure factors (kVp, mAs, SID and additional filtration) were conducted to acquire AP pelvis X-ray images. Images for the 1 and 5-year-old phantom were acquired with manual exposure control. While the images for the 10-year-old were acquired with automatic exposure control (AEC), including assessing the effects of orientation and chamber configuration. IQ was assessed using SNR and CNR values measured by placing a region of interest (ROI) on the bony anatomies within the pelvic area. Visual IQ was assessed using relative and absolute VGA methods with an IQ scale, combining the sharpness and clarity of the visibility of bony anatomies. The radiation doses were measured by placing a dosimeter on the surface of each phantom. Analyses for optimisation included main effects, correlation and regression.

Results

Using physical and visual measures, phantom validation demonstrated close similarity to the human paediatric pelvis. Using the phantoms, 'dose optimised techniques' for diagnostically acceptable IQ for each paediatric age were as follows: 65 kVp, 2 mAs, 115 cm SID and 1 mm Al + 0.1 mm Cu additional filtration for 1 year-olds; 62 kVp, 8 mAs, 130 cm SID and 1 mm Al + 0.1 mm Cu additional filtration for 5 year-olds; 89 kVp, 130 cm SID and 1 mm Al + 0.1 mm Cu additional filtration (Head Away (HA) from the two other AEC chambers whilst using both of these chambers) for 10 year-olds. The main effect analysis showed a continuous increase/decrease for increasing exposure factors except for kVp. IQ at first increased with kVp until kVp reached a specific point, beyond which IQ decreased. The correlation test showed moderate and strong correlations between mAs and radiation dose, and physical and visual IQ for both imaging modes. kVp showed either a weak or no correlation with radiation dose and IQ for manual imaging. Physical and visual IQ measures showed moderate to strong correlations for manual and AEC. Regression analysis showed that mAs and filtration had the highest impact when undertaking manual imaging. The regression analysis for AEC imaging showed that filtration had the highest impact on radiation dose, while kVp had the highest impact on IQ.

Conclusion

Paediatric pelvis phantoms that are suitable for dose optimisation studies can be produced at low cost using readily available materials. Using the phantoms, optimal imaging techniques for AP pelvis were identified for 1, 5 and 10 year-olds. Further work is recommended, including developing electronic look-up tables for selecting exposure conditions which give acceptable image quality at low doses.

Chapter One: Introduction

1.1 Introduction

Since the discovery of X-rays by William Roentgen (1895), there has been considerable development in X-ray imaging systems for medical imaging applications. In conventional radiography, developments originally started with film-screen (FS) radiography, then moving to computed radiography (CR) and more recently to digital radiography (DR) (Neitzel, 2000). All of these approaches follow the same principle by applying an X-ray beam to a patient to form an image. Within all these approaches, image quality (IQ) and radiation dose are dependent on the characteristics of the incident X-ray photons for the particular examination (Dendy & Heaton, 2011). X-ray imaging involves ionising radiation which carries a potential risk, having the ability to cause somatic and genetic effects (Dendy & Heaton, 2011; Hendee & O'Connor, 2012; ICRP, 2007). As such X-ray imaging needs an appropriate balance between the applied radiation dose and the required IQ, this principle is called optimisation (Honey & Hogg, 2012; ICRP, 2007; Seibert, 2004). Film and digital approaches use different materials which convey different responses to ionising radiation. This results in each one needing its own optimisation process. As a result, any research on dose optimisation for FS and CR would not necessarily be valid for DR systems (Honey, MacKenzie, & Evans, 2005; Neitzel, 2000).

Radiographic IQ and radiation dose are governed by different factors, including tube current and potential, filtration, inclusion of an anti-scatter radiation grid and the source to image distance (SID). Each has its own impact on IQ and radiation dose, and consequently optimisation strategies need to consider all these factors in a systematic and combined fashion (Knight, 2014).

The radiation dose and IQ levels, for medical imaging purposes, are largely determined by patient size and the anatomy/abnormality to be imaged (Billinger, Nowotny, & Homolka, 2010; European Commission, 2018). This complicates the optimisation process for paediatric imaging due to the wide variations in patient size. Within the literature, children are often classified according to their age and grouped as 0, 1, 1 to 5, 5 to 10, and 10 to 15 years. However, children in any one of these groups can have considerable size differences (Hart & Wall, 2001). The issue with the paediatric age does not stop with size. It extends to the radiation risk of inducing cancer. This risk can be 2-3 times greater than that of adults, due to their longer life expectancy (ICRP, 2006). Also, because children's cells are in a state of continuous division, ionising

radiation can cause a greater detrimental effects when compared to adults (Perks et al., 2015). This increased lifetime risk for children necessitates effective radiation dose reduction which is in line with the ‘as low as reasonably practicable’ (ALARP) principle (ICRP, 2004b; IRMER, 2018; Vano, 2005).

Trauma can lead to fractures of the pelvis, this is a cause of death in children (Gänsslen, Heidari, & Weinberg, 2013). Sport or falls from various heights can also cause hip dislocations which can be classified as posterior, low-energy or high-energy (Waite & Krabak, 2008). The conventional anteroposterior (AP) pelvis projection is recommended when evaluating trauma (The Royal College of Radiologists, 2017). Fractures or dislocations of the pelvis can be associated with significant bleeding and are potentially life-threatening and mandate urgent imaging (Kwok et al., 2015). Different imaging modalities, specifically conventional radiography can also be used for imaging chronic paediatric hip problems such as transient synovitis, hip dysplasia, Perthes’ disease and slipped capital femoral epiphysis. The most common projection used is the AP projection (Hardy & Boynes, 2003). For some situations a frog-leg lateral alone may be sufficient for evaluating suspected irritable hip and slipped upper femoral epiphysis in children aged over nine (The Royal College of Radiologists, 2017). It is generally accepted the AP project plays a significant role in paediatric pelvic imaging but it is also acknowledged that the indications and projections will vary with age (The Royal College of Radiologists, 2017).

Previous optimisation studies have tended to focus on adult patients rather than paediatrics, this is probably due to adult patients being considered as a single unified size (ICRP, 1974), making it simpler to design experiments and generalise results. Optimisation research for paediatrics is lacking and more research is urgently needed. The general lack of paediatric optimisation studies can be related to the lack of equipment necessary for the study. There is a general lack of the availability of paediatric imaging phantoms used in visual IQ assessments. This problem stems from the size and age variations which exist amongst children (Hart, Hillier, & Wall, 2007).

Reflecting on the above, there is a need for paediatric dose optimisation studies using appropriate equipment, such as phantoms. Thus, this thesis comprises of two main parts. The first part focuses on the development and validation of a novel/systematic method for the construction of paediatric pelvis phantoms. This is necessary due to the lack of commercially available paediatric dose optimisation phantoms currently available. The second part focuses

on the issue of dose optimisation for paediatrics in DR examinations (anteroposterior pelvis projections).

1.2 Rationale

The widespread move to DR has brought additional challenges in balancing IQ with radiation dose. Energy responses of digital detectors are significantly different from FS, in addition, digital technology offers greater flexibility in utilising low radiation levels and processing algorithms for the X-ray image (Vaño et al., 2007). Optimisation for these parameters continues to be an ongoing topic of research. While the flexibility resulting from the post-processing of digital images provides the possibility of dose reduction, there is a potential of higher doses through ‘dose creep’. Unlike FS, if the radiation dose to the image detector is increased the IQ can stay acceptable or even improve (Al Khalifah & Brindhaban, 2004). On the other hand, if the radiation dose to a detector decreases then the images will start to appear noisy, and clinicians would observe that the IQ decreases (Al Khalifah & Brindhaban, 2004; Honey & Hogg, 2012). Thus, there is a need for standardised protocols and exposure parameters within education and training in order to retain a constant commitment toward the ALARP principle (Mc Fadden et al., 2017). Previously, various studies have highlighted a tendency for staff members to overexpose patients (Gibson & Davidson, 2012; T. Herrmann et al., 2012). As a result, several studies have demonstrated the need for dose optimisation in DR through determining the appropriate selection of technical parameters (Andria et al., 2016, 2014; C. J. Martin, 2007a; Mc Fadden et al., 2017; Schaefer-Prokop, Neitzel, Venema, Uffmann, & Prokop, 2008; Sun, Lin, Tyan, & Ng, 2012; Uffmann & Schaefer-Prokop, 2009).

Optimisation in paediatric radiography is more challenging than that of adults, wherein dose evaluations are commonly related to a patient population with a standard size and weight (approximately 70 kg). In paediatrics, the optimum exposure factors and therefore doses differ significantly with the age of the child. Exposure factors for infants are generally related to the weight of the new born, especially in the neonatal intensive care unit. Measurements of the thicknesses of the X-rayed body part can provide useful information for appropriate exposure factor selection, but this can be difficult to measure if the child is incapable, unwilling or too sick to co-operate (L. Martin et al., 2013).

Concerning paediatric radiography, children have longer remaining life expectancy and higher radio sensitivity than adults. As a result, they have a higher lifetime attributable risk from exposure to ionising radiation (Guo et al., 2013). More specifically, the pelvis region contains

highly radiosensitive organs. Some of these are reproductive organs such as the gonads. Therefore when imaging this region there are enhanced risks of inducing genetic/hereditary effects (ICRP, 2007; Mraity, 2015). Furthermore, the pelvis in general is a very frequent (third most common) area for radiographic examination and requires relatively high radiation dose compared with X-ray examinations of the other parts of the body. By way of example, one adult pelvic exposure equates to around 35 chest X-ray examinations (Bloomfield et al., 2014; Linet et al., 2012).

Wide variations in the radiation doses delivered to paediatric patients from similar examinations have been reported in the literature (Bijwaard et al., 2017; Hintenlang, Williams, & Hintenlang, 2002; T. Jones, Brennan, & Ryan, 2017; Kiljunen, Tietavainen, Parviainen, Viitala, & Kortetniemi, 2009; Graciano Paulo, Santos, Moreira, & Figueiredo, 2011). The analysis showed that the main reason for the variations in doses found in hospitals is the variations within the radiographic techniques. Such hospital variations emphasise the necessity for quality assurance and optimisation programs to highlight optimal techniques.

In addition, there is further opportunity for dose optimisation using DR, as this technology offers high potential for image quality improvement and/or radiation dose reduction (Valentin, 2004). This is related to post-processing techniques and detector design/material and the latest methods available for technical exposure parameter optimisation. However, such techniques are not understood well and clinical practitioners might be unaware of their benefits in clinical practice (H. Precht, Gerke, Rosendahl, Tingberg, & Waaler, 2012). Within DR, systems offer better performance due to more recent technological advances when compared to CR. These advances have generated a higher detective quantum efficiency (DQE) and wider dynamic range (Körner et al., 2007). In addition, DR is considered superior to CR by offering a higher contrast resolution (Bacher et al., 2003; K. Herrmann et al., 2002) and fast image readout times. DR imaging detectors have a built-in reader system which performs systematic image pre-processing. The precise effects of these pre-processing algorithms on detecting contrast detail remain unknown (Brosi, Stuessi, Verdun, Vock, & Wolf, 2011), therefore high quality clinical practice needs to take the full advantage of all features available within DR systems. In order to provide best practice in medical imaging, the selection of exposure factors needs to consider the patient's size and clinical condition. This selection must involve collaboration with clinicians, as it will determine the adequate image quality for diagnosis (T. Herrmann et al., 2012).

Finally, no organised attempt has been identified within the literature to optimise paediatric pelvis X-ray imaging examinations. Consequently, there is a lack of literature available on the methods needed to optimise radiation dose and IQ in paediatric pelvis radiography. Together with the added problem of the heightened radio-sensitivity in this patient population, this emphasises how urgently needed experimental work which seeks to minimise radiation risk without any reduction in IQ is.

1.3 Research question

What is the impact of acquisition parameters on IQ and radiation dose for 1, 5 and 10 year-old patients in DR pelvic radiography?

1.4 Aim

To develop and validate a method for dose optimisation in paediatric digital pelvic radiography when considering age variations in children.

1.5 Objective

- i. Design and construct paediatric pelvis phantoms for three ages 1, 5 and 10 years old to be used in a dose optimisation study.
- ii. Validate the three paediatric pelvis phantoms for DR dose optimisation research.
- iii. Use the newly constructed pelvis phantoms to study the changes in IQ when changing acquisition parameters such as the tube potential, mAs, SID and the additional filtration applied.
- iv. Evaluate the radiation dose and IQ resulting from applying different acquisition factor combinations.
- v. Undertake a systematic dose optimisation study for DR AP pelvis examination across the corresponding age range of the constructed phantoms.

1.6 Statement of novelty

The novel contributions intended to arise from this thesis are:

1. A method for the low-cost construction of a series of paediatric IQ/dose optimisation phantoms.
2. A suitable method for validating X-ray phantoms for use in dose optimisation research.
3. A method for the systematic optimisation of IQ and radiation dose for paediatric DR pelvis examinations using a factorial study design.

4. An optimised dose exposure technique for paediatric AP pelvis examinations of the ages 1, 5 and 10 years old.
5. Demonstrating the main effect of each exposure factor on radiation dose, physical image quality and clinical IQ within paediatric pelvis DR.
6. A method for exploring the effect size from each exposure factor on radiation dose and IQ measures.
7. Exploring the general exposure trends that maximise dose reduction and minimise the reduction on clinical IQ.

Chapter Two: Optimisation

2.1 Chapter overview

The purpose of this chapter is to highlight the two main themes used within this thesis and also to review the current paediatric optimisation trends reported in the literature.

The first part of this review contains seven subsections. The first is about the concept of optimisation in which the definition and the major influencing factors (dose and IQ) are discussed. The second subheading discusses the difficulties facing dose optimisation studies, such as a lack of cooperation from children, variations in size and potential methods to overcome these issues. The third section discusses paediatric radiography, including the key aspects and regulations, and follows with a subheading describing the common pathologies affecting in the pelvis. The later part of this subsection discusses the main differences between paediatric and adult patients, highlighting potential conditions affecting the pelvis and the imaging strategies used to diagnose conditions for each of them. The fourth subheading discusses radiographic exposure parameters alongside the effect of each of these on IQ and radiation dose. Additionally, the possible benefits are discussed in relation to their role in dose optimisation studies. The fifth subheading describes the imaging systems available, including image formation principles and the materials used in each type, e.g. film-screen (FS), computed radiography (CR) and digital radiography (DR). Within this subsection, the main differences between imaging systems are explained together with a discussion on the need for optimisation with the arrival of newer imaging systems, i.e. DR. Subheading six discusses the methods used for IQ evaluations, with explanations on the two main aspects of IQ (physical and visual). In each aspect, there are different types of measures, i.e. for physical there is SNR and CNR, and these are explained in detail together with their calculation methods. Visual evaluations, including visual grading analysis (VGA), relative VGA and receiver operative characteristics (ROC) methods, are described. The advantages and disadvantages of each method are also discussed. The last subheading in this subsection concerns the estimation of radiation doses, wherein different types of dose quantities are presented and discussed.

The second major theme of this chapter focuses on current trends in paediatric dose optimisation. It categorises paediatric dose optimisation into two areas. Firstly, generic dose optimisation studies undertaken with different dose optimisation approaches. These study methods were grouped into test objects, anthropomorphic phantoms and clinically based studies. Secondly, dose optimisation studies specifically focusing on the paediatric pelvis are

discussed. Here, relevant studies are reviewed and discussed critically alongside their limitations.

2.2 Background literature

2.2.1 Optimisation – a concept

In order to investigate the possibility of reducing the radiation dose received by the patient, two main factors must be considered: the desired IQ and the available acquisition parameters. After analysing each one, minimising the radiation dose whilst maintaining IQ is termed ‘optimisation’ (Willis, 2009). Optimisation can be further defined as producing an image with a radiation dose as low as reasonably practicable (ALARP principle) (ICRP, 2002; Khong et al., 2013), and is a fundamental principal of major international radiation legislature (ICRP, 2007; IRMER, 2017).

Within diagnostic radiography, IQ needs to be adequate for diagnostic purposes. Dose estimation processes involve varying levels of complexity (C. J. Martin, Sutton, & Sharp, 1999), however defining the quality of an image raises further challenges. Thus, within the work of optimisation there must be an emphasis on the requirement that reductions in radiation dose must not compromise IQ (Seeram & Brennan, 2006). Such theories are based on the relationship between radiation dose and the resultant IQ. Generally, the higher the radiation dose, the higher the quality of radiographic information provided in the examination (ICRP, 2004a).

The correlation between IQ and radiation dose might be more distinguishable for digital radiography systems than for film-screen. This comes from the material characteristics of the digital detector, which responds differently to different levels of radiation. This primary characteristic is called the linear response of the digital detector (Don, 2004; Mraity, 2015; Murphey et al., 1992) and is in contrast to the response of film-screen radiography screens. For example, in film-screen (analogue) radiography, high or low radiation levels can generate overly white or black images, respectively (Uffmann & Schaefer-Prokop, 2009). However, the linear response of the digital systems are compromised by computer-based image processing (Carroll, 2011). As such there is often a plateauing of image quality at a specific exposure level followed by no further IQ gain for any increases in dose.

Generally in CR and DR, dose optimisation techniques can be grouped into three categories, which are: changes in exam performance, imaging practice and imaging technology (Willis, 2009). The imaging techniques that contribute to IQ and radiation dose are: changes to receptor dose, receptor efficiency, radiation penetration and scattered radiation (C. J. Martin, 2007a;

Willis, 2009). Thus, the parameters that govern these imaging techniques, which can impact on dose and IQ, are: tube potential, tube current, SID, filtration and the inclusion of an anti-scatter radiation grid (Brindhavan & Al Khalifah, 2005; C. J. Martin, 2007a; C. J. Martin, Sutton, et al., 1999).

2.2.2 Difficulties in paediatric dose optimisation

The need for quality assurance programs (Schneider, 1995) specific for paediatrics was first recognised in the early 1980s. This need becomes more important when considering the higher sensitivity and the longer remaining life expectancy of children when compared to adults (Guo et al., 2013; ICRP, 2002). The standardisation of procedures, optimisation of protective measures and justification for radiographic requests are key principles in ionising radiation protection (ICRP, 2017). However, according to The National Imaging Board (2009) there are difficulties in the procedures for imaging children. These are described as follows: -

1. There are diseases and pathologies which are exclusive to children and also vary with age. The effectiveness of an examination is often dependent on the cooperation of the child; in some cases sedation or anaesthesia might be necessary.
2. The smallest sub-specialty in radiology is paediatrics.
3. There is no formal career structure for paediatric radiographers, thus, there is less motivation to join the paediatric sub-speciality. As a result, few radiographers are dedicated, outside of children's hospital, to the speciality of paediatric radiography.

There are some characteristics related to paediatric patients which may restrict optimisation studies. In order to optimise IQ and radiation dose there is a need for a suitable dose evaluation method, such as DAP measurements. However, due to variations in paediatric sizes, the field size would change and affect the DAP measurements accordingly. Since children vary in size considerably, it is challenging to have comparable data across large sample sizes (Sæther, Lagesen, Martinsen, Holsen, & Øvrebø, 2010). Measuring the thickness of the examined body part provides the most appropriate indication for optimum exposure factors, however it can be difficult to evaluate if the child is unwilling, unable, and/or too unwell to co-operate (L. Martin et al., 2013). Therefore, the easiest method for collecting data includes recording height, weight and age to check whether the child size is of standard size for their age (Hart, Hillier, & Wall, 2009; L. Martin et al., 2013). Optimisation, based on DRLs, is not considered for optimum exposures. This is because DRLs are usually derived from the third quartile level (75%) of dose distributions. The idea is that standard imaging procedures are not expected to exceed DRLs. If

so, departments need to investigate the reasons as to why (Billinger et al., 2010; European Commission, 2018). On the other hand, the increase of the IQ in DR systems with increasing the exposure is only true up to a specific threshold. This causes confusion to practitioners and has resulted in dose creep, which is compounded in paediatric patients due to their wide variation in sizes (Morrison et al., 2011).

2.2.3 Paediatric radiography

The principle of paediatric radiography research is to provide radiographers with evidence to be used during their clinical practice. It also aims to highlight aspects of paediatric healthcare that might have an influence on the practice of paediatric radiography (Hardy & Boynes, 2003). However, according to Hardy and Boynes (2003), it is not reflected strongly in radiography education, including in undergraduate or postgraduate programmes. This may have changed over recent years; however, the availability of published works on paediatric radiography is still limited.

The IR(ME)R regulations highlight the necessity for both ‘justification and optimisation’ as essential steps for radiographic exams in order to maintain radiation protection (IRMER, 2017). The justification of radiation exposures should be combined with understanding the balance between the risk and benefit of an examination (Hardy & Boynes, 2003).

Once the justification for a diagnostic examination has been issued, the process of imaging should be optimised by considering the relationship between the imaging process, as follows (Hardy & Boynes, 2003): -

1. The diagnostic information required from the radiographic image.
2. The radiation dose received by the patient.
3. The choice of radiographic technique.

Modalities, such as computed tomography (CT), magnetic resonance imaging (MRI) and ultrasound, are commonly utilised in paediatric imaging. However, projection radiography still remains an essential option for investigating a wide range of paediatric pathologies (Matthews, Brennan, & McEntee, 2014). For conventional (projectional) radiography, optimisation can be achieved by considering exposure factors such as tube potential, mAs and field size. Acquisition factors are controlled by radiographers. This highlights the role of radiographers in applying the principle of optimisation in practice (Matthews et al., 2014).

2.2.3.1 Common pathologies in paediatric pelvis

The pelvis in paediatrics differs from that of adults. The paediatric pelvis contains more cartilage which gives it more elasticity and the ability to absorb energy during an injury. For paediatrics the pelvis is commonly deformed rather than fractured, especially during loading (Gänsslen et al., 2013). The bony area of pelvis consists of the ilium, ischium, pubis, and sacrum. X-ray images of the pelvis are usually requested to identify early evidence of skeletal dysplasia. Knowledge about the development of normal pelvic embryology is, therefore, considered vital for recognising the early indications of various skeletal/pelvic dysplasias. A pelvic X-ray image often shows abnormalities in pelvis density, size, shape, the number of bones, ossification timing, amongst other things. Thus, it may identify vital clues for diagnosing paediatric pelvic disorders (Jana, Nair, Gupta, Kabra, & Gupta, 2017).

Non-accidental injury (NAI) is a global problem, with the incidence ranging from 0.47 to 2000 per 100,000 and varying with complex socio-economic reasons (Jha et al., 2013). Younger children remain at greater NAI risk than older ones, and care providers are often accused of abuse (Jha et al., 2013). Recommendations advise that each anatomical region should be imaged separately, with frontal views of the extremities and two views of the axial skeleton acquired as a minimum. In addition, lateral views of the spine and frontal views of the pelvis should be acquired (Don, 2004; Jha et al., 2013). Injuries to the skeleton, particularly rib fractures and classic metaphyseal lesions, are highly indicative of NAI in young children. However, recommendations can lead to a significant radiation exposure reduction in children, particularly to the gonads (Don, 2004; Jha et al., 2013).

Trauma is a leading cause of death in children (Gänsslen et al., 2013). Pelvis fractures can result from trauma such as those from high-energy forces, for example falls, motor vehicle collisions or crush injuries (Lagisetty, Slovis, Thomas, Knazik, & Stankovic, 2012). Hip dislocations are relatively rare but can be classified as posterior dislocations, low-energy dislocations and high-energy dislocations resulting from sport or falls from various heights (Waite & Krabak, 2008). The conventional anteroposterior (AP) pelvis projection is recommended when evaluating trauma. Fractures or dislocations of the pelvis can be associated with significant bleeding and are potentially life-threatening. They mandate urgent imaging (Kwok et al., 2015). This supports the statements by Hardy and Boynes (2003), who advocated that all X-ray images for pelvic trauma be technically of high standards in order to provide accurate clinical interpretations (Hardy & Boynes, 2003).

The diagnosis of Legg-Calve´ Perthes disease is carried out using pelvic radiography and is considered sufficient for diagnosing the degree of involvement in the lateral portion of the femoral head (Waite & Krabak, 2008). CT scans can be performed in negative cases wherein there is high medical suspicion, or suspected/persistent posterior joint instability (Quick & Eastwood, 2005; Waite & Krabak, 2008).

Radiography holds an important role in the assessment of children with pain, such as hip pain, and a suspected mass in the pelvic area (Welton, Jesse, Kraeutler, Garabekyan, & Mei-Dan, 2018). Within the literature, it has been identified that in pelvic radiography there are several features that need to be seen on the resultant X-ray image. These include bony anatomies, a range of structures and pathologies. In addition, the adjacent soft tissue structures need to be visualised. The priorities in which to visualise these structures depends on the clinical question. The value of visualising bony structures, such as the trabecular pattern, are of similar importance as the recognition of the margins of the cortical bone (Stieve, 1989; Welton et al., 2018). The key imaging priority is associated with the perception of subjective contrast from the bony structures and their margins. The second priority is the adjacent soft tissue, including the muscles, ligaments and intervertebral discs. Soft tissue and bone structures are equally necessary in clinical X-ray examinations (M. Singh, Riggs, Beabout, & Jowsey, 1972; Stieve, 1989).

2.2.4 Radiographic acquisition parameters

In conventional radiography, image formation involves a complicated relationship between many acquisition parameters. These parameters control the quality and the quantity of the X-ray photons striking the image detector. Such factors are controllable by the operator, or are purely technological and already contained within the equipment (C. J. Martin, Sutton, et al., 1999). Determining the effects from changing each of the acquisition factors is necessary in order to obtain an X-ray image with acceptable diagnostic quality, at the lowest possible radiation dose. These acquisition factors typically include: collimation and centring point, anode heel effect, anode target angle, tube potential (kVp), tube-current-time (mAs), X-ray beam filtration, focal spot size, use of an anti-scatter grid, source to image detector (SID), use of an air gap, image post-processing and using automatic exposure control (AEC) (Graham, Cloke, & Vosper, 2011; Mraity, 2015; Schueler, 1998). Beside their direct effect on image quality and radiation dose, they might have indirect impact on each other (Mraity, 2015). The acquisition factors that are under the control of the operator and within the scope of this study are explained in the following sections.

2.2.4.1 Tube potential (kVp)

Tube potential (kVp) refers to the applied potential difference between the anode and the cathode, which provides the electrons with enough kinetic energy to travel from the cathode toward the anode and produce the X-ray beam. Tube potential determines the penetrability of an X-ray beam through a material. Increasing the kVp increases the average energy and the intensity of the X-ray beam (Fauber, 2013; Graham et al., 2011). The most important function of tube potential is to provide at least partial penetration through all tissues that need to be recorded. A higher average X-ray energy level enables the X-ray beam to penetrate more tissue within the human body, therefore increasing the kVp is important to ensuring sufficient penetration to all tissue types. When using DR, there is significant flexibility in setting the tube potential as long as it is above a level for adequate penetration (Carroll, 2007, 2011).

It has been reported that the use of a high kVp in certain examinations could have advantages for reducing the radiation dose reaching the patient's surface (Jessen, 2004; C. Martin, Darragh, McKenzie, & Bayliss, 1993). Even if low contrast is obtained when using high kVp, the X-ray image quality may still be diagnostically acceptable (Jessen, 2004). Also, scattered radiation is mainly produced from larger body parts and field size, not simply from the tube potential (Carroll, 2011).

2.2.4.2 Tube current-time (mAs)

In radiographic imaging, mAs refers to the product of the tube current (mA) and the exposure time(s). The mAs is a direct way of controlling the quantity of X-ray photons. For example, doubling the mAs will double the number of X-ray photons (Carroll, 2007; Schueler, 1998). At low mAs values there will be few photons reaching the image detector. This results in images with quantum mottle, which are patterns of noise on the resultant image. A sufficient amount of X-ray photons are necessary for an acceptable image quality. As there is amplification of the signal (pixel value input) from the image processing algorithm in digital imaging, the density of the image will be less affected by radiation intensity. While the noise will have higher impact on image quality, since the image processing is not able to compensate for missing information from scattered radiation. Applying excessive mAs values for DR does not appear as high density, as it would for film-screen, hence the reported issue of dose creep exists (Carroll, 2011).

2.2.4.3 Tube filtration

In general, the primary beam contains different energy levels of X-ray photons. The lower part of the X-ray beam spectrum will be absorbed in the body tissues and will form a considerable portion of radiation dose, with no contribution to the X-ray image. This lower energy part should be removed or reduced within the incident beam (Fauber, 2013). Filtration techniques involve removing the low energy x-ray photons by placing a sheet of material, for example aluminium (Al), in the path of an x-ray beam (Carroll, 2007). Filtration can be inside the X-ray tube, called 'inherent filtration', or outside the tube, termed 'added filtration' (Fauber, 2013). Layers of different materials can be added together to become added filtration, for example copper (Cu) and aluminium (Al) due to their K-edge. This technique has been described in the literature as a dose reduction method, whilst still maintaining adequate image quality (Butler & Brennan, 2009; Ekpo, Hoban, & McEntee, 2014).

2.2.4.4 Beam collimation

Maintaining an X-ray field size including the area of interest is termed 'collimation' and is considered essential for two reasons. First, collimation has a direct effect on the radiation dose received by the patient. When increasing the field size, more patient tissue will be exposed to radiation and thus the dose is increased. Second, inadequate collimation may reduce the image quality by producing more scattered radiation and more noise from the extra tissue being exposed to ionising radiation (Fauber, 2013; Schaefer-Prokop, De Boo, Uffmann, & Prokop, 2009). Scattered radiation is produced from the patient's body tissue. It is generated in randomly and can hit the image receptor from any direction. By keeping the X-ray photoelectric and penetration interactions fixed when the scattered radiation is decreased, improvements in subject contrast or image quality will be seen (Carroll, 2011).

2.2.4.5 Source to image detector distance (SID)

SID is defined as the distance from the source of the X-rays to the image detector. This parameter can be used to control the quantity of radiation reaching the patient and the image receptor. The X-ray intensity changes according to the inverse square law- that the radiation intensity is inversely proportional to the squared distance to the source. A greater distance to the source will result in a larger divergence of the radiation. For example, doubling the SID will decrease the radiation intensity by four times (Fauber, 2013; Graham et al., 2011; Johnston & Fauber, 2011). In addition, a further advantage other than reducing the radiation dose to the patient is that increasing SID reduces the penumbra and increases the sharpness of the recorded details. A larger SID also results in less image magnification (Carroll, 2011). In the literature,

the effect of this parameter on the X-ray IQ and radiation dose was studied by many researchers, they found a decrease in effective dose (ED) and entrance surface dose (ESD) with no significant effect on IQ (Heath et al., 2011; Tugwell et al., 2014).

2.2.4.6 Anti-scatter radiation grid

Anti-scatter radiation grids consist of lead strips with surrounding carbon fibre as the interspaced material, thus allowing the X-ray beam to pass through to the image detector. There are different types of grids similar to their design. They vary in terms of strip ratio (strip height to the distance between them), strip frequency (number of strips per cm), strip pattern (linear and crossed) and strip focus (parallel and focused) (Fauber, 2013).

Grids are used to reduce the scattered radiation reaching the image receptor. This results in less noise and improved contrast in the image. An anti-scatter radiation grid is recommended for larger body parts under examination- for example, the thoracolumbar spine and abdomen. Some studies have suggested using grids for body thicknesses of more than 13 cm, which would generate enough scatter to require inclusion of an anti-scatter grid (Tucker, Souto, & Barnes, 1993). The usage of grids for radiographic examinations involving infants and young children is generally considered unnecessary (Hardy & Boynes, 2003).

On the other hand, the use of these grids requires an increase in the quantity of X-ray photons in order to compensate for the reduction when using the grid. This in turn will increase the radiation dose by 2 to 4 times (C. J. Martin, Sutton, et al., 1999). It is worth mentioning that digital systems are sensitive to the noise incident on the image receptor as the image processing algorithms are not able to interpret the information from the noise correctly (Carroll, 2011). Thus, DR systems still require enough signal in comparison to noise in order to produce X-ray images of acceptable quality.

2.2.4.7 Automatic exposure control (AEC)

Automatic exposure control (AEC) functions by controlling the X-ray tube in order to enable enough radiation to reach the image receptor by increasing the exposure time (Shah, Jones, & Willis, 2008). There are two types of AEC detectors that are routinely used for this technique: ionisation chambers and photo-timers. The photo-timers use photodiodes or photo-multiplier tubes and are uncommon, while ionisation chambers are used most of the time. The term 'ionisation chambers' refers to several chambers placed in front of the Bucky. Radiographers should, during optimisation, activate the best combination of the chambers for optimum imaging (Fauber, 2013).

An AEC technique has been used widely in radiography due to its ability to control the amount of radiation whilst producing an adequate and reproducible image quality. This technique facilitates the selection of a suitable tube-current time for different radiographic examinations (Johnston & Fauber, 2011). On the other hand, there are limitations and practitioners should be aware of the need for the correct selection of tube potential, mA, grid inclusion and image detector within the realms of AECs. However, AECs can generally be relied upon to directly control exposure time (Carroll, 2007; Mraity, 2015).

2.2.5 Imaging systems (film-screen, CR and DR)

Imaging systems in conventional radiography have developed significantly over the past two decades, from film-screen radiography to digital image quality systems (Oakley, 2003). Digital image receptors are generally categorised as either computed radiography (CR) or direct digital radiography (DR), and may be referred to as flat panel detectors which contain direct and indirect conversion detectors (Dendy & Heaton, 2011; Fauber, 2013). Figure (2.1) represents a flowchart providing an overview of the different types of digital detectors.

The image formation process is similar in both film-screen and digital systems. The image formation process first starts with generating the image then processing, archiving and finally presenting. Unlike film-screen, a DR imaging plate contains detectors that absorb X-ray radiation intensities, and transform them into electrical charges. It then records, digitises and translates them to different grey scales (Dendy & Heaton, 2011). However, the material response of each imaging system varies with different X-ray energies and K-edges (Aichinger, Dierker, Joite-Barfuß, & Säbel, 2012; Seeram, Davidson, Bushong, & Swan, 2013). Also, their capability to process the image differs (Honey et al., 2005).

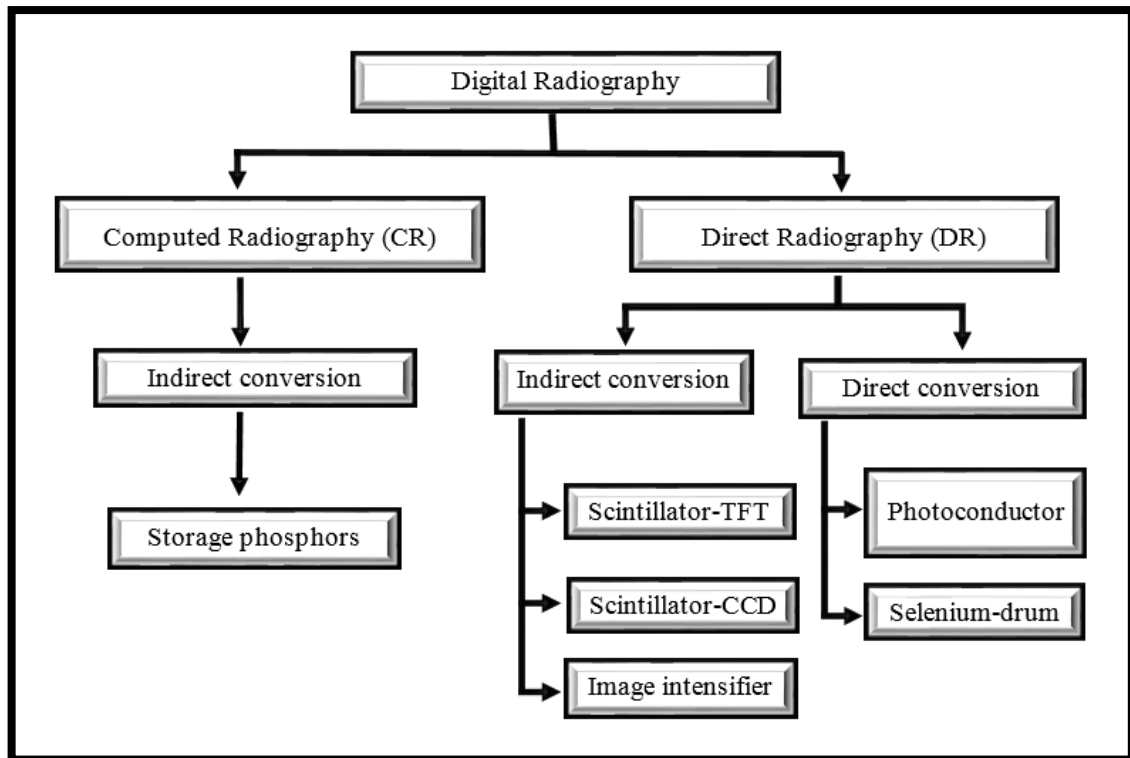


Figure 2.1: The flowchart provides an overview of different types of digital detectors. CCD: charge coupled device and TFT: thin film transistor (Körner et al., 2007).

2.2.5.1 Film-screen (FS)

In conventional film-screen radiography, the formation of the latent image is distinctly different to digital methods. A hard copy of the visible X-ray image is obtained by chemical processing of the latent image (Brindhavan & Al Khalifah, 2005; Fauber, 2013). Anatomical information on the film is formed from X-ray photons with different intensities that penetrate the human body. These photon intensities embed anatomical information about the regions of interest (Mraity, 2015). Calcium tungstate was first used as phosphor in intensifying screens (Bushberg, Seibert, Leidholdt, Boone, & Goldschmidt, 2003). More recently rare earth phosphors or screen-film combinations are used to reduce the dose administered to the patient because of their high sensitivity (Guerra, 2004). Also, they reduce exposure time, therefore reducing motion blur. However, they cause degradation to the spatial resolution (Nyathi, 2013). As a result of these processes, the methods for optimising film-screen examinations are different to that used in digital equipment.

2.2.5.2 Formation of digital X-ray image

A digital image is a matrix of numerical values called pixels. These pixels are the elemental components for each digital image. Each pixel is represented by a single level of brightness, when displayed on a monitor. The level of brightness varies from black to white with shades of

grey in-between, where each level of brightness depends on the pixel value. The position of each pixel within the matrix of the image corresponds to a specific area within the patient or the radiographed object. The determination of each pixel value is related to the attenuation of X-rays passing through the corresponding body part (Fauber, 2013). The amount of information contained in a digital image is determined by the number of pixels it contains, which represents the number of different intensities or shades from each pixel (Bourne, 2010).

2.2.5.2.1 Digital image processing

All digital systems in radiography are designed with preselected settings of dynamic range and average grey level to enhance the visibility of particular anatomical regions. Preselected image processing settings are customised by the manufacturer for specific radiographic procedures, based on the type of anatomy. Radiographers refer to these settings as procedural algorithms; such as a foot algorithm, chest algorithm, pelvis algorithm, abdomen algorithm and so on. By contrast, post-processing generally means any modification to the original parameters and protocol from which an X-ray image was initially acquired. These original image adjustments include at least three different methods: selecting a different procedural algorithm and reprocessing the image, windowing, and various special features- for example edge enhancement (Carroll, 2011). There are number of IQ factors that can be manipulated within post processing software, for example contrast enhancement, noise reduction, windowing and latitude (Carroll, 2007). However, the results from these algorithms may differ considerably (Körner et al., 2007).

Image processing is able to compensate overexposure by up to 500% and underexposure by 100%. This ability for digital systems can result in exposure or dose creep, and as such image processing can have potentially adverse effects to the patient (John et al., 2013). It is difficult to recognise whether a digital X-ray has been produced either from under- or overexposure due to the wide dynamic range and post-processing options available on digital detectors (Zhang, Liu, Niu, & Liu, 2013). Digital technology allows the use of a wide range of exposure factors when performing examinations. As a result, various levels of radiation dose can be administered to patients. The overexposure also means using too high a dose than necessary, which can occur whilst maintaining perceptually acceptable IQ (Ma et al., 2013). Another result of this could be overexposure to a patient, without producing a diagnostically acceptable image (Lança et al., 2014).

2.2.5.2.2 Dynamic range

The dynamic range can be described as the range of incident X-ray radiation intensities that an image detector can handle whilst still producing adequate diagnostic image quality. It enables the digital system to maximise the grey value number in the digital image, and therefore, improve post-processing. For example, the dynamic range is considerably wider for digital imaging systems in comparison to that of film-screen. (Lança & Silva, 2008). Thus, the use of digital imaging systems has improved the characteristics of IQ (Dendy & Heaton, 2011; Fauber, 2013). Another positive effect of a wide dynamic range is that it enables display differences between specific tissue absorptions (such as bone vs soft tissue) in one image without the need for additional images, for example fracture and foreign body detection (Körner et al., 2007).

2.2.5.3 Computed radiography (CR)

The first system to use digital radiography was developed by Fuji (Tokyo, Japan). This converted the X-ray energy into a digital signal using laser stimulated luminescence, these systems were brought to the market at the beginning of the 1980s (Lanca & Silva, 2013). Later, the photostimulable storage phosphor (PSP), or computed radiography (CR), was considered as a new imaging method for clinical practice. The CR process is similar to film-screen, except that the PSP stores the X-ray photons and emits light photons later, whilst the phosphor in film-screen systems emits light instantly (Bushberg, J.T., Seibert, J.A., Leidholdt Jr, E. and Boone, 2002). The CR receptor consists of a phosphor layer, a support layer and a protective layer. The phosphor layer consists of crystals of barium fluorohalide doped with europium. This layer stores intensities of X-ray photons in a crystal electron trap. Electrons are trapped in higher atomic energy states and emit light photons when they move to lower energy states after being stimulated by a laser beam of high intensity. The number and distribution of the captured electrons are related to the different X-ray absorptions of different human body tissues (Fauber, 2013). The X-ray absorption efficiency of a CR detector depends on three major points, namely: the composite thickness of the PSP, the X-ray energy and the upper limit (adjusted) of detective quantum efficiency for the CR system (Seggern, 1999).

Since the PSP does not emit light photons spontaneously like in film-screen, it requires photostimulation to emit light to form the X-ray image. The next step in acquiring an X-ray image for CR systems is to scan the CR image plate with a laser beam (Busch, 2004; Fauber, 2013). This stage involves using the reader to photostimulate the phosphor layer via a laser beam. After this process, blue light photons are emitted. The light emission is directed to a photomultiplier tube which collects, amplifies and records the light photons as an electric signal

proportional to the energy range that is stored in the image plate. The final digital X-ray image is produced by transforming the electric charges into a digital signal via an analogue to digital converter (ADC) (Fauber, 2013; Leblans, Vandenbroucke, & Willems, 2011). The CR phosphor crystals can store the X-ray energy for several hours, depending on their specific physical properties. The readout process should be undertaken directly after taking exposure because the quantity of trapped energy decreases with time (Körner et al., 2007).

2.2.5.4 Digital radiography (DR)

A digital radiography image receptor utilises an array of detectors that absorb the X-ray radiation and transform the varying intensities into a proportional electronic signal to produce a digital image. In contrast to CR, the imaging process combines the capture and the readout of the X-ray image; DR images are available almost immediately after exposure. However, DR imaging receptors are less rigid with a much higher cost when compared to CR receptors (Fauber, 2013). DR systems are categorised according to the way that the X-ray is converted to digital data. They fall into two categories: direct and indirect conversion (Körner et al., 2007).

Indirect conversion DR systems

Detectors used in indirect conversion use a scintillator layer of gadolinium oxysulfide (Gd_2O_2S) or caesium iodide (CsI) in order to convert the X-ray radiation into visible photons. The visible photons are then converted proportionally to electrical signals via photodetectors that are made from thin film transistor (TFT) array amorphous silicon. Capacitors in the TFT array temporarily store electronic signals which are to be digitalised and processed by a computer-see figure (2.2) (Fauber, 2013). The advantage of using CsI crystals in the scintillator is their ability to form small needles (width 2-10 μm). A needle can be placed perpendicular to the detector surface in order to reduce the light diffusion inside the scintillator layer. Therefore, a thicker scintillator layer is possible which leads to stronger light emission, better optical characteristics and higher quantum efficiency (Körner et al., 2007).

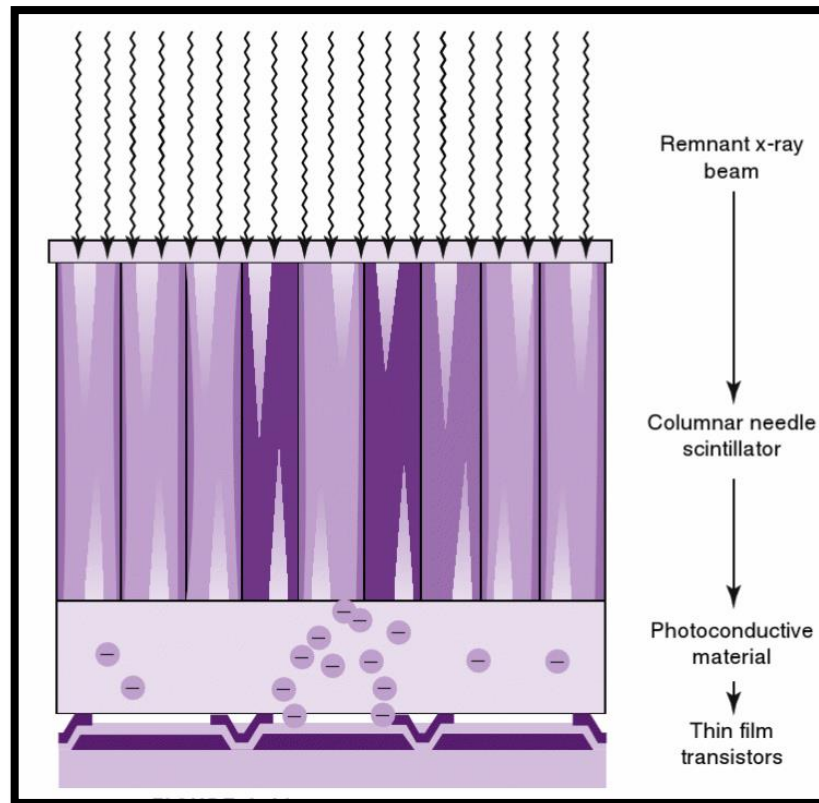


Figure 2.2: Indirect conversion - DR systems (Fauber, 2013).

Direct conversion DR systems

These systems require photoconductors to transform the energy of X-ray photons directly into electrical signals by releasing electrons. Some common photoconductor materials are amorphous selenium, lead oxide, thallium bromide, lead iodide and gadolinium compounds. The most common is selenium (Körner et al., 2007). To compensate for the average low atomic number (z) of selenium, its thickness is relatively high (about 1 mm) (Dendy & Heaton, 2011). When exposing it to X-ray photons, an electrical charge is generated which is proportional to the energy of the X-ray photons reaching the selenium drum surface. This is then recorded by the analogue to digital converter. An electric field is generated on the layer of selenium to prevent the electrons in selenium from diffusing laterally towards the TFT array. This results in excellent spatial resolution (Fauber, 2013). Also, the materials, such as selenium, have high inherent spatial resolution. Consequently, the matrix, pixel size and resolution related to direct conversion imaging detectors are limited by the devices reading and recording capabilities, and not their materials (Dendy & Heaton, 2011; Körner et al., 2007). Finally, like in indirect conversion detectors, capacitors in the TFT array temporarily store the electrical signals which are to be amplified, digitalised and processed in a computer- see figure (2.3) (Fauber, 2013).

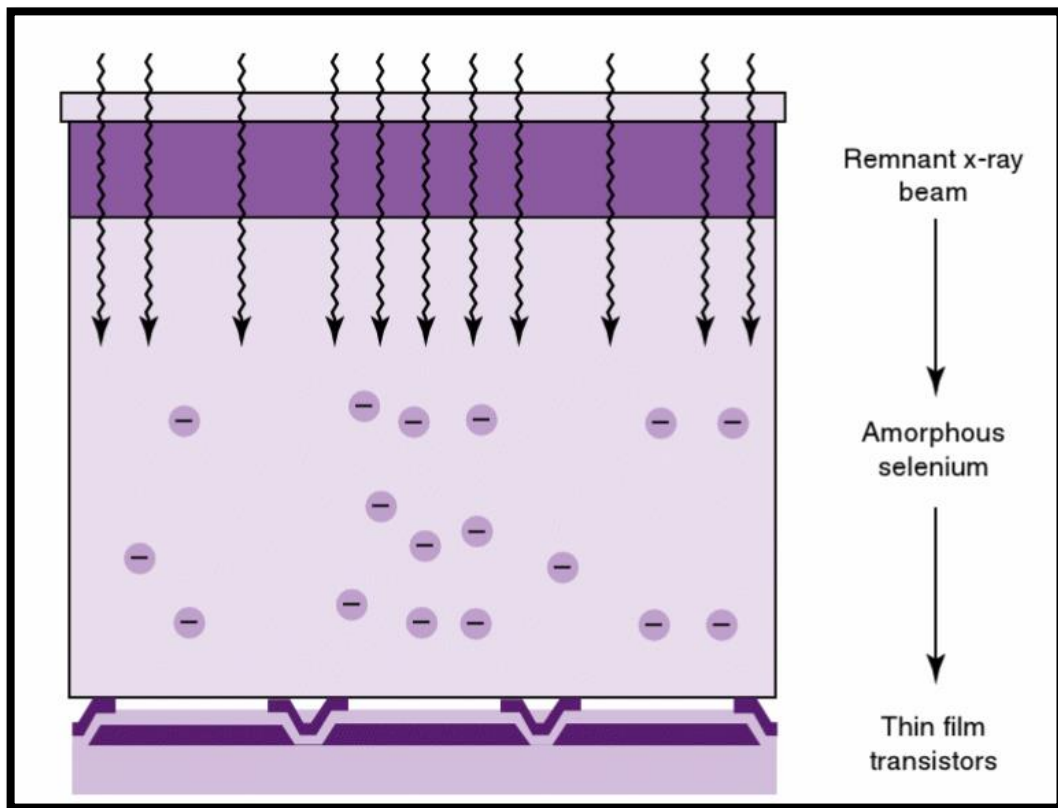


Figure 2.3: Direct conversion - DR systems (Fauber, 2013).

In all DR systems, the conversion of electric signals into digital data is via the ADC. The intensities of digitalised pixels are patterned in the form of an image matrix in the computer. The image matrix consists of a digitalised composite of various X-ray intensities that penetrate the patient. Each pixel in the image is presented with a brightness level related to the attenuation characteristics of the unit volume of the human body (Fauber, 2013).

Som comparison between digital and film-screen imaging systems are as follows: -

1. Unlike film-screen, CR and DR introduce enhancements to the resultant X-ray image from image processing, storage and archiving, and provide a low necessity for repeat examination due to incorrect exposure factor selection. This is due to the manipulation possible through image processing and the wide dynamic range (John et al., 2013; Körner et al., 2007).
2. In terms of beam energy response, the CR material (BaFBr/I) has a k-edge of approximately 37 keV, while for film-screen (Gd₂O₂S) the k-edge is higher at about 50 keV (Seeram et al., 2013).

3. Spatial resolution of CR imaging plates is usually lower than that of screen-film combinations. However, several studies have stated that the diagnostic value of storage-phosphor imaging is equivalent to that of screen-film (Körner et al., 2007). A study by Aufrichtig (1999) reported significantly better contrast detectability from the digital detector than for film-screen when assessed using disc-shaped objects.
4. In view of the wide dynamic range and signal normalisation, image quality becomes less dependent on dose for DR systems when compared to film-screen. Consequently, image quality has been produced with better consistency in term of density and contrast for DR systems (Schaefer-Prokop et al., 2009).

Some comparisons between CR and DR radiography are as follows: -

1. In terms of cost-effectiveness, CR is less expensive than DR, but it requires readout units which add extra cost. Nevertheless, the number of images that CR can read in the same amount of time is much less than that of DR systems (Dendy & Heaton, 2011).
2. Many clinical studies have reported that images from DR (selenium drum) detectors have superior IQ when compared to both film-screen and CR images (Körner et al., 2007). This also includes their spatial resolution, which is limited by the size of the detector element (Fauber, 2013).
3. DR systems are of a higher dose efficiency when compared to CR. However, the differences in radiation dose required are still relatively small (Schaefer-Prokop et al., 2009).
4. The flat panel detectors have a higher DQE than CR PSP image detectors (Aufrichtig & Xue, 2000).

2.2.6 Image quality evaluation

Image quality assessments can be divided into two methods: visual assessment (e.g. Visual Grading analysis (VGA), and Receiver Operator characteristics (ROC) methodologies) and physical assessments, such as signal to noise ratio (SNR) and contrast to noise ratio (CNR). Relationships between visual and physical methods vary, with some researchers finding good agreement (De Crop et al., 2012; Ullman et al., 2004) and others finding low levels of agreement (Alves et al., 2016; Lanca & Hogg, 2016). However, work by Mraity in 2015 found a significant correlation between visual grading and physical measures (SNR) for X-ray examinations of the pelvis using an adult phantom (Mraity, 2015). However, this work reported

that the physical measurements needed to be combined with perceptual assessments to give extra support to the results.

A recent study (Lanca & Hogg, 2016) using low dose levels (≤ 2 mGy) showed that there is poor correlation between visual and physical assessment (SNR and CNR), which suggests that physical measurements might not be adequately representative of clinical IQ. This might be due to the lack of validity of physical measures or their inability to measure attributes which reflect the clinical demands of the image. However, combining different types of measurements might support the overall visual analysis (Mraity & Alrowilly, 2016). This approach could be of further use for dose reduction if there are no consequences to visual IQ (Lanca & Hogg, 2016).

2.2.6.1 Physical measurements

Physical measurements describe how well an imaging system performs. Such measurements are capable of describing the performance of the whole radiographic system by evaluating the IQ and include SNR, CNR, noise power spectrum (NPS), modulation transfer function (MTF) and detective quantum efficiency (DQE) (Desai, Singh, & Valentino, 2010; Månsson, 2000). Work within this thesis will focus on the most commonly used measures, namely CNR and SNR. CNR and SNR are useful measures since they have been identified by several researchers as having a good correlation with visual IQ (Brindhaban, Al Khalifah, Al Wathiqi, & Al Ostath, 2005; Moore, Wood, Beavis, & Saunderson, 2013; Mraity, 2015). As such, it is worth evaluating the relation between visual and physical IQ metrics. Also, SNR and CNR can be used in Figure of Merit calculations in order to provide a single quantity representing the dose/IQ relationship and would be useful in optimisation studies, as well as in predicting the clinical image quality (Båth, 2010; Sund, Båth, Kheddache, & Månsson, 2004). The SNR value, for example, has been found to have a threshold minimum value (5 or greater) for humans to recognise the signal. This was proven experimentally by Albert Rose (Bushberg, Seibert, Leidholdt, & Boone, 2012; Rose, 1973). Thus, it is possible to investigate its relationship with visual IQ when increasing it more than the threshold. Further advantages are that it can be measured directly from the image of the phantom/patient by measuring pixel values (Bloomfield et al., 2014 ; Mraity, 2015). When using an anthropomorphic phantom with anatomical features, these physical measurements would include effects of anatomical visibility and noise. Such measures can provide a useful correlation with visual IQ.

SNR can be defined simply as the ratio between the signals received by the detector to the attached noise within the image, which are fluctuations generated randomly that appear as standard deviations in the image pixel values. While the definition of CNR is the difference

between the two signals strengths against the noise that appears on the image, contrast is a consequence of various attenuations to the x-ray beam (Desai et al., 2010; C. J. Martin, 2007a).

$$CNR = \frac{S_1 - S_2}{N_{bgr}} \dots\dots\dots (2.1)$$

(Desai, Singh, & Valentino, 2010)

The SNR is the same as equation (2.1), except that it is calculated for one region only (S_1). As follows (Desai, Singh, & Valentino, 2010):

$$SNR = \frac{S_1}{N_{bgr}} \dots\dots\dots (2.2)$$

S_1 represents the signal intensity of area 1; S_2 represents the signal intensity of area 2. The N_{bgr} can either represent the noise from background (Desai, Singh, & Valentino, 2010) or the noise from both the background and the signal (Alves et al., 2016; Alzimami, Sassi, Alkhorayef, Britten, & Spyrou, 2009).

From their definitions and the above equations, it can be seen that SNR and CNR vary due to attenuations in the X-ray beam that weaken the signal strength. The only difference is that CNR is calculated relative to the attenuations produced from the background. SNR and CNR can be measured using computer software (e.g. ImageJ). Regions of interest relating to the important radiographic regions of the anatomy in question are selected to aid analysis (Bloomfield et al., 2014 ; Mraity, 2015).

2.2.6.1.1 Signal to Noise Ratio (SNR)

One of the most commonly used approaches as a surrogate measure for information visible on an image is SNR. The *signal* represents the desirable information from subject contrast within the X-ray image. The signal represented in the radiographic image includes: (penetrated) dark shades, the (attenuated) medium shades, and the (absorbed) light shades. The presence of those three elements creates useful diagnostic information. Noise is created by the random scattering of X-rays photons hitting the patient’s body, random electrical static and other disinformation in the image. SNR is a useful mean when comparing images between exposure settings (Carroll, 2011).

For digital radiography, a well-established description of IQ is the signal-to-noise ratio (SNR). This is because, when using image processing, the appearance of large low contrast detail is limited only by noise (Neitzel, 1992; E. Samei et al., 2009). The SNR is a physical measure of

IQ used extensively in optimisation studies (Bloomfield et al., 2015b; Doyle, Martin, & Gentle, 2005; Mraity, 2015; Tugwell et al., 2014). Several authors have commented that SNR values can influence and limit image processing (Aichinger et al., 2012; J. Hansson et al., 2005). In radiography the signal of an image, which is related to diagnosis, is formed by the ‘important image details’. This is how they are defined in numerous important publications, such as the European Guidelines on Quality Criteria for Diagnostic Radiographic Images (European Commission, 1996). It is necessary to perceive these details against the background of the surrounding tissue for diagnostic purposes. The perceptibility inside the image is limited by noise (Hasegawa, 1991) that is produced by statistical fluctuations of the X-ray photons (the quantum mottle), which take part in image formation. Therefore, the difference between the signal and the noise must be as high as possible. In theory, assumptions have been made that the SNR value of a signal shall be at least 3 to 5, so that the detail of an image can be recognised by the human eye with sufficient reliability (Aichinger et al., 2012; Rose, 1948, 1973).

There are some weaknesses to using SNR as an IQ metric which might affect its validity and reliability for IQ evaluations (Alsleem & Davidson, 2012). Firstly, the size of the object is not considered, thus it might have weak agreement with observer performance. Secondly, the noise value (the measured standard deviation of pixel values) is too simplistic for comparing the observer’s sensitivity to the noise texture. To explain this, the SNR is partially related to quantum noise, which is dependant on the photon density at the image receptor. However, the observer is influenced by other background noise textures such as detector noise, anatomical noise and system noise (Bochud, Valley, Verdun, Hessler, & Schnyder, 1999). Thus, the SNR measurements might not be able to provide IQ features relevant to the evaluation process used in clinical practice, i.e. lesion detection. Consequently, measurements of SNR should be considered together with a human observation study (McCollough, Bruesewitz, & Kofler, 2006; Mraity, 2015).

2.2.6.1.2 Contrast-to-noise ratio (CNR)

The most significant factor that varies with the quality/energy of radiation is image contrast and its influence on the image can be defined by the contrast to noise ratio (CNR). It is related to the difference in signal between objects and their background, but it does not include information related to the resolution of the image. CNR provides an evaluation of imaging performance aspects, which are related to the choice of X-ray exposure parameters (C. J. Martin, 2007a). In addition, the CNR is a metric used to calculate the degradation in contrast and noise in the image (Desai et al., 2010). It is used to identify the target (area) of interest from

its surroundings. Therefore, CNR is considered to be a good indicator of a radiographic system's ability to visualise an abnormality/lesion as well as anatomical structures inside an X-ray image (Dhawan, 2011).

In the calculation process of CNR, the difference between the signal of the object and the signal of its background is divided by the noise (SD) from the background (Desai et al., 2010; C. J. Martin, 2007a), or divided by the combined SD of the background and the signal (Alves et al., 2016; Alzimami et al., 2009). This signal difference can produce image quality with high SNR and low CNR (or the opposite), unless the image has high contrast to make the recognition of the lesion from the normal tissue easier. This results in no such agreement on whether CNR can indicate the level of noise (Smith & Webb, 2010).

2.2.6.1.3 DQE

DQE is a measure for how efficient an imaging system is in receiving and refining contrast, noise and resolution of the incoming X ray photons to signal output (Månsson, 2000). For modern medical applications, including direct and indirect X-ray imaging detectors, accurate clinical diagnosis requires high SNR transfer characteristics, which is described by the DQE (Liaparinos & Kandarakis, 2011). There are many factors affecting DQE such as spatial frequency, radiation exposure, MTF, and detector material. The energy of the X-ray radiation is also an important factor which influences DQE (Illers, Buhr, & Hoeschen, 2005).

Measuring DQE is calculated by comparing the SNR ratio: detector output vs detector input signal as a function of spatial frequency (Körner et al., 2007; Spahn, 2005). The ideal detector has a DQE value equal to 1, which means there is full conversion of the incident radiation energy into image information. However, In practice, the value for DQE, within digital detectors, is limited to a range 0.45 at 0.5 cycles/mm (Körner et al., 2007). A standard was introduced by International Electrotechnical Commission (IEC62220-1) in 2003 to normalise DQE measurements, thus, comparison can be made. The performance of DQE was improved by including additional elements such as MTF and NPS, and thus, DQE can be an indicator for detector sensitivity and resolution (Båth, 2010).

One point to mention is that identifying DQE is measure for only one component of imaging chain, which does consider the effect from image processing and anatomical variation on image quality (Alsleem & Davidson, 2012). Therefore, DQE cannot be a valid indicator for clinical observation (Båth, Sund, & Månsson, 2002; Mraity, 2015).

2.2.6.2 Psychometric approaches to image quality evaluation

2.2.6.2.1 Receiver operative characteristics (ROC)

In medical imaging, the fundamental task for an observer is to explain whether an image refers to a patient with a disease or not. This initiated the need for determining the performance of the observer (Báth, 2010). ROC analysis is described as a method for measuring an observer's performance in a binary classification task. It is a standardised measure for estimating the accuracy of combined observer and modality performance (Chakraborty, 2002; Thompson, 2014). The ROC analysis method requires observers in the field of medical imaging to recognise whether there is a lesion/pathology or not (Chakraborty, 2011).

When the observer recognises disease on an image for a patient with true disease, this is termed as a true positive (TP). When the observer responds with a non-diseased interpretation for a patient with true disease, this is termed as a false positive (FP). False negatives (FN) and true negatives (TN) are the complements of TP and FP actions, respectively. TNs and TPs are correct decisions, and FNs and FPs are incorrect decisions (Bewick, Cheek, & Ball, 2004; Chakraborty, 2011).

X-ray images are displayed individually with a potentially identifiable pathology. The observer is requested to score a described scale of her/his level of certainty for the given pathology. The data collected from this method enables evaluation of the trade-off between the False Positive Fraction (FPF) and the True Positive Fraction (TPF) forming the ROC curve (ICRU, 1996). The TPF is also known as the sensitivity and the TNF as specificity (Chakraborty, 2011).

The ROC curve is a simple graphical approach used to show the diagnostic accuracy of an examination. It offers a valuable visual comparison of the performance of different examinations or observers. An ROC curve is created for each diagnostic test or imaging modality, including each observer being evaluated (Thompson, 2014). Figure (2.4) represents a typical ROC curve. The maximum area under the curve (AUC) can be equal to 1. A test with AUC around 0.9 is considered to have high diagnostic accuracy, while 0.75 is considered to be moderate (Obuchowski, 1994). Thus, this method identifies the observer performance for a diagnostic procedure (Báth, 2010).

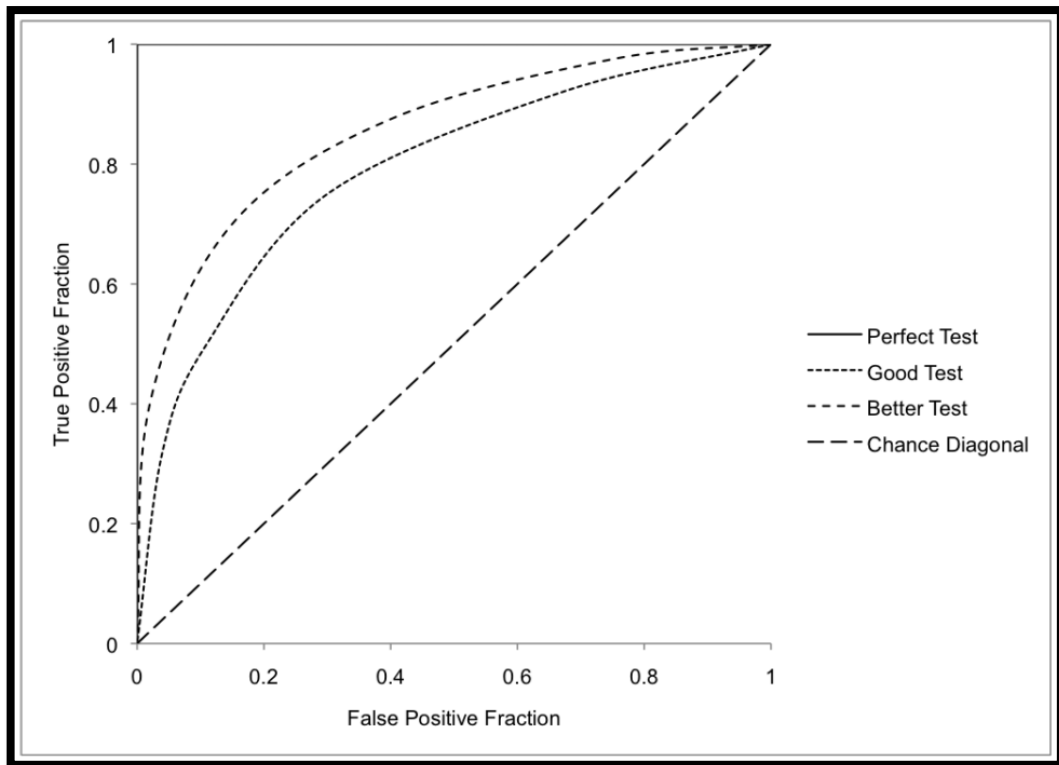


Figure 2.4: represents a typical ROC curve (Thompson, 2014).

ROC analysis is broadly implemented in radiology to visually evaluate the X-ray image and observer performance. This type of study was created from the Signal Detection Theory, wherein an observer attempts to identify a signal with low contrast in a noisy surrounding. The clinical application for this method is when observers distinguish abnormalities out of a set of images with normal background (Månsson, 2000). For this, a participant is requested to rate a set of X-ray images wherein there is a suspected disease. Consequently, the number of correct answers will evaluate observer diagnostic performance. However, ROC figures have a major drawback as they are highly dependent on disease prevalence. Furthermore, the images must be categorised into normal and abnormal, indicating to a need for a large number of images. The ROC methodology is not efficient for images with multiple lesions and the lesion localisation is not considered. Therefore a case could be diagnosed as abnormal while the true lesion is still missing (Båth, 2010; Zarb, Rainford, & McEntee, 2010).

In order to overcome the above-mentioned limitations, attempts have been made to enhance the performance of ROC. These trials included the enhancement of ROC's statistical power when using a low number of images (Månsson, 2000). For example, in Localisation Receiver Operating Characteristic (LROC), the lesion must be identified and localised by an observer (Zarb, Rainford, & McEntee, 2010). In the localisation ROC model (LROC) the observer scores

one rating per case and refers to the location of the most suspected region (Chakraborty & Berbaum, 2004). The analysis suggests independence between the location of the most suspicious noise and the disease/signal on the image, wherein each contains a maximum of 1 lesion/pathology per image (Chakraborty & Berbaum, 2004).

A later improvement to the ROC method was the Free Receiver Operating Characteristic (FROC). Since not only is the existence of diseases important but also their locations, this paradigm is considered to be more relevant to clinically practice (Chakraborty, Yoon, & Mello-Thoms, 2007). In this model, the participant is required to observe and localise many lesions together with her/his level of confidence towards, for example, whether the lesion is malignant or non-malignant. This method provides good statistical power and uses an appropriate number of cases and readers which are derived from standard tables (Zarb, Rainford, & McEntee, 2010). The curve for this model is drawn by plotting the x-axis with a non-lesion localization fraction (NLF) and the y-axis is done with the lesion localization fraction (LLF) (Chakraborty, 2011).

Alternative Free-response ROC (AFROC) is defined as a plot of a hybrid curve between the false-positive fraction (FFP) on the x-axis and the lesion localization fraction (LLF) on the y-axis (Chakraborty, 2010, 2011). It combines the x-axis of the ROC curve with the y-axis of the FROC curve (Thompson, 2014). The area under the curve of this plot is used as figure of merit in Jack-knife FROC (JAFROC) analysis (Chakraborty, 2010).

The Jack-knife Alternative FROC (JAFROC) method can be defined as an approach used for analysing the data from FROC paradigm. It implements additional information (such as location) and therefore has greater statistical power. This means it has a higher ability for detecting smaller variations between imaging modalities comparing to the ROC method. (Chakraborty, 2010). It also has the advantage of using a reduced sample size in diagnostic performance studies (Chakraborty & Berbaum, 2004). Its figure of merit is described as the probability that a true lesion rating scores higher than a false-positive (FP) rating (Chakraborty, 2010).

Additional improvement related to the ROC method is the Free-response Forced Error (FFE). Here, the objective for the observer is to identify abnormalities which exist in the image, then rank them according to the level of confidence. The observer must rank 1 for the most apparent, 2 for the second most apparent, etc. (Chakraborty & Winter, 1990). The marking procedure continues until false positive error occurs, as a result the fraction of correctly identified answers before the false positive occurring indicates a better performance of the imaging modality

(Tingberg, 2000). Finally, Differential Receiver Operating Characteristic (DROC) was developed in order to compare between different imaging systems. DROC statistical power is considered to be higher than that of ROC. All the above-mentioned approaches can be used in clinical imaging situations (Båth, 2010).

Overall, rigorous statistical analysis and a good relationship with the clinical task are the advantages of ROC and ROC-related methods (for example; JAFROC analysis). These methods are suitable for IQ studies with large-scale comparisons between imaging modalities, due to their detection performance for specific pathologies (Båth, 2010). These studies are considered to be the gold standard when evaluating IQ. However, many concerns have been raised in terms of the clinical relevance of ROC data. For example, radiologists might behave in different way from in a clinical environment when compared to the task within the ROC study (Båth, 2010; Gur et al., 2007). Additionally, these types of experiments can be cumbersome as they rely on establishing truth for all cases and require a large amount of cases to provide meaningful results with statistical significance (this means that there is low reliability associated with them). For the reasons mentioned, the ROC-related methods are unlikely to be a suitable choice for the majority of optimisation studies (Båth, 2010).

2.2.6.2.2 Visual Grading Analysis (VGA)

This method involves the visual quantification of IQ within medical imaging applications. This approach invites the observer to state how clearly the visibility of different anatomical structures is. Such a human response based method provides clinical relevancy in assessing image quality (Mraity & Alrowilly, 2016; Seeram, Davidson, Bushong, & Swan, 2014). This approach deals with visual grading related to the visibility of key anatomical or pathological components. The simplicity and powerful discriminatory ability are advantages of this technique (Månsson, 2000). It has moderate time consumption, at least in terms of observation time, and is easier to conduct compared to ROC methods (Båth, 2010). There is, however, an assumption of a strong correlation between the visibility of normal anatomy and the detectability of pathological structures (Sund et al., 2004). In that context, it is worth mentioning that the significance of VGA as a replacement for pathology detection methods (i.e. ROC) has been examined and approved within the literature (Sund et al., 2000; Tingberg et al., 2000). In addition, a strong correlation has been found between VGA and the measurements of physical image quality (Båth, 2010; Sandborg, McVey, Dance, & Carlsson, 2000; Sandborg et al., 2001; Sandborg, Tingberg, Ullman, Dance, & Carlsson, 2006a). It is, also, an easy way to evaluate

visual image appreciation and is more representative of evaluation methods used within clinical practice (Månsson, 2000; Sund et al., 2000).

2.2.6.2.3 Justification for a VGA approach

In an article by Båth in 2010 a number of justifications are provided for using a visual grading methodology for image evaluation studies (Båth, 2010), including: 1) VGA validity is considered high, as the anatomical components selected are relevant to clinical practice; 2) VGA requires fewer images and observers when compared to ROC; 3) a relatively shorter time is required for VGA when compared to other methods. In addition, unlike VGA, there are certain preparatory steps which are needed for other methods, such as that ROC requires that half of the images need to include lesions (Båth, 2010). VGA has also shown agreement with detection studies when using human observers study (such as; ROC) (Sund et al., 2000; Tingberg et al., 2000) and physical measurements in specific situations (Sandborg, Tingberg, Ullman, Dance, & Carlsson, 2006b).

On the other hand, despite VGA and ROC approaches providing results which are relevant to the visibility of anatomical structures, they have two main drawbacks (Ludewig, Richter, & Frame, 2010; Månsson, 2000). First, they reflect the opinion of the participant and therefore variations with other observers are highly possible (Sund et al., 2004). Second, there is a need for pre-specified questions about the anatomical components under evaluation (Mraity, 2015; Shet, Chen, & Siegel, 2011). The VGA method can be subdivided into two:

1. Absolute VGA

This scale uses absolute grading with no references. It relies on the observer rating how much certain anatomical or pathological structures are visible. The scoring scale is based on ordinal data (Båth & Månsson, 2007). The absolute VGA score ($VGAS_{abs}$) can be calculated from equation (2.3) (Sund et al., 2004), as follows:

$$VGAS_{abs} = \frac{\sum_{i=1}^I \sum_{s=1}^S \sum_{O=1}^O G_{(abs)i,s,o}}{I.S.O} \dots\dots (2.3)$$

Where $G_{(abs) i, s, o}$ refers to the absolute rating for structure (s), a particular image (i) and observer (O). The letters S, I and O refer to the number of structures, images and observers, respectively.

2. Relative VGA

The relative grading scale includes the use of one or more images as references. This is performed by comparing well-defined pathological structures, anatomical landmarks, and/or

physical parameters from images with the corresponding structures in a reference image (Månsson, 2000). The observer scores the visibility of every component using a scale (e.g. -2, -1, 0, 1, 2), wherein ‘0’ refers to a visibility equal to the reference image (Båth & Månsson, 2007; Månsson, 2000). The relative VGA score ($VGAS_{rel}$) can be calculated from equation (2.4) (Sund et al., 2004), as follows:

$$VGAS_{rel} = \frac{\sum_{i=1}^I \sum_{s=1}^S \sum_{O=1}^O [-1] \cdot G_{(rel)i,s,o}}{I.S.O} \dots\dots (2.4)$$

Where $G_{(rel) i,s,o}$ refers to the relative rating for structure (s), a particular image (i) and observer (O). The letters S, I and O refer to the number of structures, images and observers, respectively.

The rating/scoring in a relative VGA study is, naturally, related to the quality of the reference image. In this case, the rating scale will have a fixation point represented by a reference image and thus no bias can occur. Not all experiments can be performed with using one reference image, however a randomisation of reference images may be necessary, such as comparing different imaging modalities. Therefore, biased results are likely to exist, due to a comparison with many reference images (Månsson, 2000).

2.2.6.2.4 Alternative forced choice

This model contains the 2-alternative forced-choice (2AFC) method which offers two images to observers and asks that they choose one (i.e. the best image quality). Then there is the multiple-alternative forced- choice (MAFC), wherein the viewed images are more than 2 ($m>2$), instantaneously (ICRU, 1996).

The 2AFC method includes using two display areas. With each trial, a specific reference or target is placed in one display area and the other one is empty. The observer is asked to detect the one that contains the target. This method is extended to multi-alternative forced choice wherein there are multiple display fields with one reference (Green & Swets, 1966; ICRU, 1996). The advantage of this forced choice model is that more reproducible results are obtained, however, it has the disadvantage of being different to the clinical task (ICRU, 1996).

2.2.7 Estimating radiation dose

There are several types of radiation dosimeters used in diagnostic radiology and they are divided into two groups: ionisation chambers and solid-state detectors. Solid-state detectors include optically stimulated luminance dosimeters (OSL), thermo-luminescence dosimeters (TLD) and semiconductor detectors (Bushong, 2013; IAEA, 2013). Their measured quantities are

numerous, and they are used for determining the radiation dose received by patients. These radiation doses are measured after applying different radiographic exposure factors leading to measuring quantities, such as dose area product (DAP) (or air Kerma Area product - KAP) and entrance surface dose on a patient's skin (ESD) (or Entrance Surface Air Kerma - ESAK) (European Commission, 2014; C. J. Martin, 2007b).

DAP, is the dose product in the air (or air kerma) inside the area of an X-ray beam. It is measured in mGy cm^2 or $\mu\text{Gy cm}^2$. It is considered, therefore, to represent the amount of X-ray radiation incident on the patient. DAP can be determined using an ionisation chamber placed close to the X-ray tube (C. J. Martin, 2007a). Entrance Surface Dose (ESD) is defined as the dose reaching the patient's skin at the point wherein the X-ray beam hits the body. It includes both the dose to the patient's skin and back-scattered radiation. Both air kerma and ESD are commonly measured in either mGy or μGy . ESD can be measured either by placing a small dosimeter on the skin, or estimated from the radiographic exposure factors when combined with output measurements from the X-ray tube (George et al., 2004; C. J. Martin, 2007a). Air kerma measurements are an indicator of the radiation exposure levels from radiographic examinations. ESD and DAP can be used to explain and compare radiation doses from different radiological exposures (Brindhaban & Al Khalifah, 2005; C. J. Martin, 2007a). Additionally, they can be used to compare doses for normalised patient ages/sizes against reference dose levels (Hart & Wall, 2001).

DAP and ESD are estimations of doses received by patients during routine X-ray examinations. They are useful for comparing between doses (Hufton, Doyle, & Carty, 1998). None of these quantities provide an assessment of the risk to patients, however they still provide an indication of organ doses using an appropriate conversion factor (Lanca & Silva, 2013). Absorbed doses of each organ multiplied by its tissue weighting factor are summed to produce the effective dose, and therefore an estimation of risk (ICRP, 2007).

Air kerma can be measured using an ionisation chamber placed on the surface of an object. The resultant air kerma can be converted to ESD by including a backscatter factor (BSF) (Chapple, Faulkner, & Hunter, 1994; R. Harrison, 1982). The backscatter factor is usually small for paediatrics when compared to adult patients. This is due to the smaller field sizes, and in some cases it requires a more sensitive detection equipment (IAEA, 2013). BSF depends on four factors- the X-ray energy, the phantom/patient field size, the geometry of the beam and the

incident material. It can vary in magnitude from 1.01 to 1.7 (R. Harrison, 1982; Petoussi-Henss, Zankl, Drexler, Panzer, & Regulla, 1998).

Effective Dose (ED) provides a quantity that represents the risk of health damage for a standard human from the stochastic effect of radiation (ICRP, 2007). It takes into account the radio-sensitivity of organs in different parts of the human body. It is measured either by simulations from computational phantoms or physical dosimetry phantoms (A. Jones, 2006; Choonik Lee, 2006; Varchena, 2002). A computerised method such as the Monte-Carlo modelling, despite the advantages in terms of time and cost, generates large uncertainty as data comes from organ dose estimations and is limited to a standard size patient simulation only with no simulation for differences in equipment (C. J. Martin, 2007a). Also, simulation methods in general have uncertainty and this is due to the stochastic uncertainties. Within the model there needs to be a balance between choosing the number of scattered photon trajectories whilst still balancing the computer processing time and required precision (computer processing time vs stochastic precision). Systematic uncertainties must also be considered (uncertainties from the estimation of various input parameters, such as the Half Value Layer (HVL) of the X-ray spectrum) (Menser, Manke, Mentrup, & Neitzel, 2016; Ullman, 2008). By contrast, physical phantom measurements are also limited by the availability of different sized phantoms (CIRS Tissue Simulation and Phantom Technology, 2011). Direct measurements of organ dose and effective dose in humans are not possible. Also, it is considered both difficult and time-consuming to measure organ and effective dose experimentally using physical phantoms (Lanca & Silva, 2013). Monte-Carlo based simulation methods have the advantage in terms of cost and time but again they have uncertainties within their calculations (Menser et al., 2016).

In DR there is a term called exposure index (EI), which is an indication of the quantity of radiation exposure on the image receptor and is calculated automatically by the system (Willis, 2009). EI in DR is used to monitor the exposure levels in imaging systems and provide feedback to practitioners. This is to avoid over exposure to patients by DR systems that compensates the image quality of the X-ray image (Mothiram, Brennan, Lewis, Moran, & Robinson, 2014). EI is perceived to be an objective exposure measure of the radiation dose administered to a patient during the radiographic examination (Lanca & Silva, 2013). However, EI has limitations in that there are wide variations in its application between different imaging equipment vendors, in terms of EI magnitude and scale. Philips, Fuji and Siemens utilise a linear scale, whereas Kodak and Agfa use a logarithmic one. This means that the same dose received by two detectors from different manufacturers will produce different EI values. This inconsistency between

different manufacturers can confuse practitioners and might cause exposure errors when imaging patients (Lanca & Silva, 2013). This also may limit the comparability of doses from clinical examinations with DRLs (Schaefer-Prokop & Neitzel, 2006).

There have been attempts to unify the EI of different equipment vendors. An international standardised EI has been developed by the American Association of Physicists in Medicine (AAPM) and the International Electrotechnical Commission (IEC) (Mothiram et al., 2014). However, there are certain factors that would limit the application of EI for technique comparison or optimisation studies. EI is determined by several technical factors such as kVp, filtration, mAs, SID, grid and beam collimation. It is also related to the *remnant radiation* that passes through a patient's body. The radiation reaching the digital detector is converted into an electronic signal and then to digital image with DQE that related to SNR squared. When there is a larger patient, the SNR will be less, and DQE is less. Thus, IE is not applicable in optimisation and comparison studies. This will be of a larger impact in paediatrics due to their higher size variation and radiation sensitivity (Seibert & Morin, 2011).

2.3 Current trends in paediatric dose optimisation – a review of the literature

The initial part of this literature review focuses on dose optimisation studies for general paediatric X-ray imaging. Studies have been divided into three main categories: 1) test objects, 2) anthropomorphic phantoms and 3) clinical studies. The aim of reviewing these studies was to highlight the various research strategies used for dose optimisation in paediatric radiography. Following the initial (general) review of the literature, a more focused review was conducted. This specifically investigated optimisation for paediatric pelvis radiography examinations. Studies investigating the factors affecting the radiation dose and IQ, including but not limited to tube potential and additional filtration, were included as part of the review.

2.3.1 Literature review methodology

The search strategy for this literature review was based on searches using SCOPUS, ScienceDirect, PubMed, Web of Science and Medline. Search terms included the following keywords: 'diagnostic X-ray *imaging', 'paediatric or paediatric or child or children', '*pelvis and dose', '*optimisation or *optimization'. These helped to refine the search. Also used were keyword combinations, such as: paediatric/pediatric/child/children and dose *optimisation/*optimization. Searches considered both UK and US spelling alternatives, i.e. paediatric and paediatric. Searches also used the Google Scholar search engine and any

identified publications were also reviewed for relevant references. Appraised studies were limited to those published in the English language. It was deemed likely that there would be limited information available on dose optimisation in paediatrics and, as such, no time limits were imposed on search results. The search was mainly focused on studies which utilised digital imaging systems. Literature identified as relevant was evaluated using the Critical Appraisal Skills Programme (CASP) methodology¹.

2.3.2 Generic optimisation studies

In this section, a number of different optimisation techniques are presented. These were focused on anatomical areas other than the pelvis. As stated, these studies are subdivided into three types: 1) test objects, 2) anthropomorphic phantoms and 3) clinically based studies.

2.3.2.1 Test objects

A number of optimisation studies have been carried out for adults using phantoms without any anthropomorphic features (Honey et al., 2005; Helle Precht, Tingberg, Waaler, & Outzen, 2014; Veldkamp, Kroft, Boot, Mertens, & Geleijns, 2006). Others have used physical measures of IQ and have not relied on any visual assessments (Sj et al., 2015). A number of investigations have been carried out for dose optimisation experiments in paediatric radiography. For example, Gislason et al. used a detailed phantom placed on a slab of PMMA, representing the thickness of a paediatric chest, and also simulating the iodine-based contrast medium used in clinical examinations (Gislason, Davies, & Cowen, 2010).

Another study by Shannon and co-workers used lead disks with 5 mm thickness and diameters of 2.5 mm, 5 mm, 7.5 mm, 10 mm, 15 mm, 17.5 mm and 20 mm, embedded within PMMA (Fritz & Jones, 2014). They added a Solid Water phantom with a thickness ranging from 7 to 16 cm (3 cm increments) to simulate the abdomen of children of corresponding age. The aim of the study was to determine the threshold thickness for using an anti-scatter radiation grid during paediatric abdominal radiography.

A study by Park et al. used a standard paediatric chest phantom equivalent to a 15-month-old child, constructed from acrylic and aluminium with an air gap simulating the lung cavity (Park et al., 2014). The aim of this study was to investigate dose optimisation possibilities in chest radiography examinations by changing technical parameters (such as scattered radiation from the object, the blur caused by the focal spot, geometric magnification and detector

¹ <https://casp-uk.net/wp-content/uploads/2018/01/CASP-Diagnostic-Checklist.pdf>

characteristics). This study's outcome measure was the effective DQE (eDQE), which was the primary measure of IQ.

The above studies were restricted in that they could not observe the effect of exposure parameter variations on the anatomic areas they examined. Within the literature it has been identified that the radiographic visibility of anatomy depends on the size, shape and radiographic attenuation properties (International Commission on Radiation Units and Measurements (ICRU), 1992; White et al., 1992a). Therefore, since the above studies have no representation of human body characteristics, there are issues in generalising when interpreting the results (Uffmann et al., 2005).

An optimisation study by Menser et al. used the Monte-Carlo simulation for assessing dose and IQ in new-born chest radiography (Menser et al., 2016). It evaluated radiation dose and IQ for the same simulated radiographic exam when changing tube voltage and pre-filtration. Simulation methods, such as the Monte-Carlo, in general have uncertainties (Menser et al., 2016; Ullman, 2008). Also, generating images in the shape of a test object, without any anthropomorphic features, would limit its applicability to general practice.

2.3.2.2 Anthropomorphic phantoms

As for adult based studies, some researchers have used anthropomorphic phantoms in their optimisation studies (Lança et al., 2014; Mraity, 2015). For paediatrics, there is a general lack of anthropomorphic phantoms available (Hart, Hillier, & Shrimpton, 2012). As a direct consequence, researchers usually design and construct their own phantoms for experimental use. Such examples include a study by Precht et al., who examined using multi-frequency processing (MFP) software to reduce dose for DR systems (H. Precht et al., 2012). Within this work an animal phantom (a 6 month-old lamb femur equivalent to a 5 year-old femur) was used and a relative visual grading analysis (5-point Likert scale) was used to generate phantom images. A CDRAD phantom was also used for an objective assessment of contrast and spatial resolution. Direct dose measurements of the skin dose were performed using a solid-state dosimeter (Unfors Xi dosimeter). Tube current-time ranged from 0.5 to 16 mAs and the other exposure factors were kept constant (60 kV, filtration of 5.2mm Al, an SID of 100 cm and field sizes set up for the size of the anthropomorphic femur or the CDRAD phantom). The authors reported a dose reduction of up to 88% compared to their reference image (16 mAs). This work was later applied to paediatric femur radiography (H. Precht, Gerke, Rosendahl, Tingberg, &

Waalder, 2014) wherein the optimal IQ was reported at 6.3 mAs. However, their results showed that an mAs of 0.5 still produced acceptable (diagnostic) IQ.

Another study by Hansson et al. used a living rabbit to simulate the chest of a neonate (J. Hansson et al., 2005). They recruited ten radiologists to evaluate the effect tube potential (40 to 90 kVp) on the visibility of peripheral vessels, central vessels, carina and thoracic vertebrae. They validated their study results by comparing them with neonatal chest X-ray examinations from hospitals using the same tube voltage (70 kVp). They found that 90 kVp provides superior IQ in terms of the reproduction of important structures. The limitation of these studies was that the anthropomorphic animal phantom was based on the femur of a lamb or living rabbit. Subsequently, the processing parameters were based on the characteristics of the animal, which are close to but not the same as a paediatric human femur or neonatal chest. Differences are likely to exist in terms of geometry, size and/or anteroposterior thickness, and thus these results should be used cautiously.

A study by Lança et al. used a Kyoto Kagaku 5 year-old paediatric anthropomorphic phantom to study the effect of mAs and filtration on visual IQ during the imaging of the ribs (projections; AP and oblique) and wrist (projections; AP and lateral) (Lança et al., 2018a). Their visual IQ parameters were contrast, sharpness and noise. This VGA score (using the observers' score) was calculated then correlated with the fracture visibility for each projection. Physical IQ measurements (CNR) were also added to the study. Dose measurements included, DAP which was used in calculations of ESD. Correlations between physical and visual IQ were found to be between moderate and strong. A decrease in VGA, fracture visibility and ESD was observed when the filtration level was increased. An increase in VGA and ESD was observed when mAs was increased. This study used a valid anthropomorphic phantom to carry out such observations, however the phantom has limitations in performing dose optimisation for pelvis as it contains plastic joins of the femurs. It is meant for positioning training not for pelvis imaging.

A study by Jones et al., investigated the effect of beam quality by changing tube potential and filtration for a specific age range (A. Jones, Ansell, Jerrom, & Honey, 2015). The resultant IQ and radiation dose for infant lateral ankle projections were observed. Image quality was evaluated visually and physically (CNR) using a DR detector and an anthropomorphic infant foot phantom. Effective dose was estimated from the exposure parameters and the Monte-Carlo

PCXMC software. The authors reported an improvement in the scores of clinical IQ at lower beam energy.

2.3.2.3 Clinical data studies

Several studies have used clinical data to estimate the radiation dose and/or examine the probability of dose reduction whilst maintaining clinical IQ. Data collected from hospitals is based on patients, however in general wide variations can exist in the reliability of hospital records. Such reliability issues can be seen in the recording of exposure factors, radiographic techniques and age specific sizes which can have a major impact on IQ and radiation dose (Agarwal & Newbery, 2016; Brennan & Johnston, 2002).

Several studies have undertaken a combined assessment of IQ and radiation dose of clinical exposures for optimisation purposes. For example, A study by Frayre et al. evaluated the ESD, using TLDs, for neonatal CXR examinations and the associated visual IQ when using CR (Frayre et al., 2012). Optimisation was done through determining the ESD up to the level of quantum noise thought to be acceptable for diagnosis. Using this technique, they were able to reach an ESD 50 μ Gy lower than the DRL. A further paediatric chest optimisation study by Jacob and his colleagues used patient X-ray images to investigate IQ in terms of acceptable noise levels (Jacob et al., 2009). The corresponding dose measurements (ESD) were extracted from the dose exposure level provided by the Agfa CR detector. The aim of this study was to recommend an optimal exposure, in terms of dose and acceptable IQ, for children aged from 0 to 15 years, in four age groups (1, 1-5, 5-10 and 10-16 years old). Dose reduction from this study reached a factor of 2.5. A similar method was used by Korir, Wambani and Ochieng wherein hospital data was collected for paediatric CXRs (Korir, Wambani, & Ochieng, 2010). Again, the ESD was measured using TLDs and a dose reduction of up to 77% was reported.

A study by Guo et al. assessed visual IQ and radiation dose (DAP) from paediatric CXR examinations in children aged 0 to 14 years old (Guo et al., 2013). They grouped exposures according to tube potential into low (50 to 81 kVp), intermediate (60 to 90 kVp), and high (70 to 102 kVp) in addition to adult (102 kVp). Patient ages were divided into 0 to 1, 1 to 3, 4 to 7, 7 to 11 and 11 to 14 years old. The authors reported a significant difference in DAP with the higher tube potentials in comparison to the low and intermediate kVp values. An algorithm for paediatric CXR optimisation was introduced by Kostova et al. who measured kerma–area product (KAP) and visual IQ for each child (the age ranges were: 0 to 1, 1 to 4, 5 to 9 and 10 to 15 years old) (Kostova-Lefterova, Taseva, Hristova-Popova, & Vassileva, 2015). The

measured parameters were divided according to the values of tube potential, exposure time (s) and mAs which were adapted to patient size. They found a dose reduction of between 1.5 to 5 times compared with DRLs values reported by Hart, Wall and Shrimpton (1999). A study by Karami et al. used clinical data to investigate source to image distance (SID) when optimising CR imaging systems (paediatric CXR) (Karami, Zabihzadeh, Danyaei, & Shams, 2016). The image quality of the resultant images were assessed visually using the European Guidelines, while the corresponding radiation dose was measured using TLDs. The study found that the increased SID, from 100 to 130 cm, reduced the dose by 32.2%, with no significant effect on IQ ($P>0.05$).

Another study Billinger, Nowotny and Homolka aimed to report the doses received by paediatric patients in Austria (Billinger et al., 2010). Within this work they measured IAK, ESAK and KAP and compared them to DRLs from Europe, Germany and Great Britain. Again, they reported variations between different hospitals for children of the same age and for similar examinations by a factor up to eight. Such data provides further evidence of dose variations between institutions and highlights the need for more formalised dose optimisation.

2.3.3 Optimisation of pelvis X-ray examinations

This section focuses on critical reviewing studies specifically aimed at paediatric pelvis dose optimisation:

A group of researchers (Bloomfield et al., 2015b) examined the benefit of changing kVp, mAs and filtration in order to reduce the radiation dose whilst maintaining adequate IQ. The study made use of a paediatric ATOM dosimetry phantom (representing a 5 year-old) in order to simulate a paediatric patient. Results suggest that approximately half of the 27 images acquired were of acceptable IQ, but were acquired with a lower dose than those from standard acquisition parameters. Image quality was assessed using a 5-point Likert scale. A relative VGA technique and additional physical measurements (SNR and CNR) were also used to assess the IQ and optimise the effective dose. It should be noted that effective dose estimates were based on Monte Carlo calculations using DAP and this could have introduced some errors when compared to direct ESD measurements. An evident strength of the above study is that the authors used combined methods of objective (SNR and CNR) and visual methods for evaluating IQ. This study did have several additional limitations, including the sample size (27 images used to investigate three parameters). The phantom used in the study was designed for dosimetry purposes and did not contain subtle anatomical detail. As illustrated in CIRS data

sheet, bone was represented by an homogenous density that was averaged for both the cortical and trabecular bone (CIRS Tissue Simulation and Phantom Technology, 2011). These cover a wide range of electron densities and therefore also cover a wide range of linear attenuation coefficients (ICRP, 2002). From the diagnostic X-ray perspective, according to C. Martin et al. (1999) the contrast of different structures appearing on X-ray images comes from interactions which depend on the X-ray energy and object density. As a result, the contrast of the bone in the ATOM phantom might not be a true representative for human bone. This may have an effect on the optimisation process. Furthermore, the slices of the ATOM phantom appear as a shadow of black lines on the resultant X-ray image, as mentioned by Mraity (2015). These lines could affect image quality assessments and the physical measures of image quality.

In another study, a group of researchers (Brosi et al., 2011) used different thicknesses of PMMA (7, 10 and 14 cm) to mimic children (0 to 1, 2 to 7 and 8 to 18 years) in order to assess the effect of copper filtration on image quality. Within this study IQ was assessed using a CDRAD test phantom and the effective dose was measured using the PCXMC computer software after measuring the ESD using an ionisation chamber. The authors found that there is no reduction in effective dose for anterior-posterior projections for pelvis, abdomen and posterior-anterior chest. The exception was for AP chest examinations in which dose reductions were found to be due to the location of the radiosensitive organs in the AP projection. While a reduction was recorded for ESD, there was a clear decrease in image quality when adding more filtration. The study was suitably designed using the CDRAD phantom which provided a consistent approach to image quality grading. The PCXMC software was used for effective dose calculations. Despite this, the CDRAD as discussed by Veldkamp et al. (2006) does not consider anatomical noise and as such provides a limited representation of clinical images. Within this study there was only one type of material (PMMA) used to represent the thicknesses of different sized paediatric patients wherein bone contrast has significant role in determining the IQ of pelvis radiograph (M. Singh et al., 1972; Stieve, 1989).

A study by McEntee & Doherty (2011) evaluated the effect of copper filtration on IQ and radiation dose using different tube potentials typically used in paediatric examinations (McEntee & Doherty, 2011). Filtration levels of 0, 0.1, 0.2 and 0.3 mm Cu were tested on different tube potentials ranging from 45 to 55 kVp for a one year-old, 50 to 60 kVp for 5 year-old and 65 to 85 kVp for a 10 year-old. The study used a dosimetry phantom in combination with the CDRAD to test the IQ for both CR and DR imaging systems. The imaging criteria were based on those from the European Commission. For dose estimation, PCXMC was used

for estimating the effective dose from DAP measurements. Considerable dose reductions were achieved by adding additional filtration with no loss of IQ. Nevertheless, this study showed considerable discrepancies in tube potential between DR and CR which are capable of giving acceptable IQ. For example, for a 5 year-old the suggested tube potential for CR was 45 kVp, while for DR this was 90 kVp. However, dosimetry phantoms have average bone density (cortical and trabecular bone) (CIRS Tissue Simulation and Phantom Technology, 2011) which is advantageous for dose measurements but not for IQ studies.

A further study which considered the issue of optimisation for paediatric patients was carried out by Butler & Brennan (2009). In this study different ATOM phantom sizes representing paediatric patients of 0, 5 and 15 year-olds were used (Butler & Brennan, 2009). They investigated the impact of adding different thicknesses of aluminium and copper on the radiation dose and IQ for AP pelvis projections. Radiation dose measurements were carried out using a Multi-Purpose Detector (RTI Electronics Inc, Molndal, Sweden) placed on the phantom surface and allowed the measurement of ESD. Using ESD, the effective dose was calculated from the conversion factors published by the National Radiological Protection Board (NRPB) (Hart, Jones, & Wall, 1996). Images from the Agfa CR reader were evaluated by radiographers with four scores available for each image. The results showed a reduction in radiation dose with no remarkable decrease in the IQ. The methodology applied in this study was successful as it considered two radiation dose quantities (ESD and ED) and a clinical approach for the assessment of IQ. However, using ATOM phantoms (with the bone density averaged for cortical and trabecular bone) may challenge the reliability of the findings.

A study by Hufton, Doyle and Carty compared the doses from paediatric CR examinations with the doses from 600 speed FS acquisitions (Hufton et al., 1998). Data from 900 paediatric patients who had pelvis, abdomen, chest and skull radiographs were collected. The tube potential used with CR was higher on average by 0.5 kV when compared with FS. Paediatric patients were grouped according to age (0 to 1 months, 1 to 12 months, 1 to 5 years, 5 to 10 years and 10 to 15 years). ESD was evaluated from the measured outputs of the X-ray tube, records of the exposure factors as well as DAP. Image quality assessment was done through clinical criteria that were taken from the Commission of the European Communities (CEC). The study results showed a possible reduction in radiation dose of around 40% with CR, except for the chest wherein the dose differences were not significant. This work presented the advantage of using digital imaging systems that can decrease the dose received by the paediatric patient.

A study by Ludwig et al. investigated the dose reduction possibility in paediatric pelvis radiography in patients with congenital hip dysplasia using digital flat panel systems (Digital Diagnostics, Philips Medical System, Hamburg), with half the radiation dose that was formerly used with phosphor-storage CR systems (ADC compact, Agfa, Leverkusen) (Ludwig, Ahlers, Sandmann, et al., 2003). The images were acquired in hospitals and were assessed visually (5-point scale) on an absolute VGA scale for their visibility of anatomical details and suitability for orthopaedic radiography. Study results found no significant difference ($P > 0.05$) in the IQ between the two systems. The authors concluded that radiation dose could be reduced to half when digital flat panel detectors are used instead of the phosphor-storage CR system. As there are differences in radiographic techniques and sizes between patients, which affected the precision and limited the study, a reduced dose can be achieved. This study indicates a potential dose reduction and suggests a need for optimisation between digital systems when DR is replaced with CR. A study by Thorsen et al. (2015) was similar, 25 pelvis images were acquired for children aged 3 to 7 years-old. This study aimed to achieve optimisation through the use of software post-processing (multi-frequency processing software). No dose measurements were introduced in the study, which is a major limitation. The SID, focal spot, air-gap, tube potential and filtration were fixed, and only the mAs varied ranging from 2 to 4. The software showed significant noise reduction for the acetabulum only.

A study by Martin et al. aimed to identify initial exposure factors for paediatric chest (AP and PA) and AP pelvis examinations at an acute hospital in the UK (L. Martin et al., 2013). The age range included 1, 5, 10 and 15 years, and they compared these exposure factors with the European and UK guidelines. The impact of the changes was estimated by evaluating IQ and radiation dose differences. The dose measured for each exposure was the ESD calculated using output data from quality assurance tests of each X-ray room. The IQ assessment was performed using visual grading analysis and sought to establish whether the IQ was useful for diagnosis when different exposure factors (kVp and mAs) were used for CR. This comparison led to new exposure factors being implemented and were in agreement with the European guidelines (CEC, 1996). The optimised exposures achieved an ESD reduction of up to 50% for the AP pelvis and 55% for the PA chest. This study considered patients of a standard size, however the age range still had variations in body size within each age group. Estimations of patient size were based on measurements of weight and height (Hart, Wall, Shrimpton, & Dance, 2000). Measuring the thickness of a body part provides the most useful indicator for exposure factor selection (Hart et al., 2009; L. Martin et al., 2013). Images were produced with different

exposure factors applied onto different patient sizes (within each age), and subsequently generated a range of image qualities and radiation doses (C. J. Martin, 2007a). In addition, their exposure factors were limited, such as that there was no consideration to the effect from added filtration and changes to SID. Such acquisition factors have demonstrated a significant effect on IQ and radiation dose, as reported by Brosi et al. (2011), and would affect the determination of the dose-optimised exposure technique (Brosi et al., 2011).

A study by Karami et al. used X-ray images from a hospital acquired using a CR system (Karami, Zabihzadeh, Shams, & Gilavand, 2017). The purpose of the study was to examine the effect of increasing SID from 100 to 130 cm on visual IQ and radiation dose (ESD). The paediatric age range covered in the study was 0 to 14 years old for radiographic examinations of the pelvis (AP), abdomen (AP), skull (AP and lateral view), and spine (AP and lateral view). The radiation dose was measured by placing TLDs in the central field for each projection. Visual IQ was assessed using visual grading analysis (VGA) and the European image criteria (CEC, 1996). The authors reported a statistically significant reduction in radiation dose (skull lateral: 21.9%; skull AP: 23.4%; abdomen AP: 25.2%; spine AP: 26.6; pelvis AP: 30.6%; and spine lateral: 35.2%) and a non-significant reduction in IQ. Despite the data being collected from hospitals and from patients, there were wide variations in exposure factors and radiographic techniques reported which could potentially impact the IQ and radiation dose (Agarwal & Newbery, 2016; Brennan & Johnston, 2002). In addition, results from this study were generalised over a wide paediatric age range (0 to 14 years old for pelvis), which also had significant size variations (Varchena, 2002). The number of appraised images could be considered as a small sample size (24 to 32 images) for all of the paediatric ages included.

A study by Paulo, Santos, Moreira, and Figueiredo (2011) aimed to perform dose optimisation in hospitals by comparing two kinds of exposure factors: routine kVp (60 for pelvis and 70 for chest) and a new proposed tube voltage (by radiographers) (Paulo, Santos, Moreira, & Figueiredo, 2011). Dose and IQ was assessed. Data collection done was from 429 clinically justified paediatric examinations aged between 0 to 18 years, containing 272 and 157 for the chest and pelvis, respectively. For the pelvis, the proposed exposure values by radiographers were: 70, 81 and 90 kV for patients weighing <20 kg, between 20 and 40 kg and >40 kg, respectively. The imaging system was CR and the AEC and anti-scatter radiation grid were used. The DAP and ESD were recorded for the radiation dose. Image quality was assessed by inviting three radiographers to evaluate the image using a visual absolute grading analysis. The authors found no statistically significant difference in IQ between the two kinds of kVp

exposures. Twenty percent dose reductions in the ESD values were recorded. Exposure and size/age variation from the hospital examination data could have had a significant effect on this study (Brosi et al., 2011). The authors do, however, recommend using the new technology for dose reduction.

Other studies (Borisova, Ingilizova, & Vassileva, 2008; G. Paulo, Vaño, & Rodrigues, 2016; Sæther et al., 2010; Hintenlang et al., 2002; and Kiljunen, Tietavainen, Parviainen, Viitala, & Kortetniemi, 2009) were carried out to estimate either or all of the following: ESD, Kerma-Area Product (KAP) and/or Dose Area product DAP from hospital based examinations in different countries. The aims of these studies were to establish dose reference levels and/or provide guidance on reducing doses in paediatric radiography. In general, the authors found large variations between hospitals of the same country which suggest a need for dose optimisation in paediatric radiography examinations. Another study by Zhang et al. (2013) measured the ED using a Fluke phantom (PMMA) (Zhang et al., 2013). Brindhavan and Eze (2006) carried out an estimation of radiation dose from Kuwaiti hospitals examinations (Brindhavan & Eze, 2006). They used an ionisation chamber, backscatter factor and conversion factor to measure ESD then ED and their corresponding risk. The target ages were 0 and 1 year-olds for a range of different anatomical areas include the AP pelvis. The radiation risk they estimated ranged from 0.6 to 23.4 per million. The above investigations estimated the radiation doses and ignored the issue of IQ. As such, no data was provided in these studies to explain the IQ trend which may have resulted from changes in the radiation dose. Although these studies are important, evaluating IQ is extremely important for dose optimisation work.

The limitations of the above studies, together with a lack of information within published literature, provides a strong rationale for the focus of this thesis. From the existing studies, no phantom has been described which addresses the demands of the proposed research and, as a consequence, phantoms for this thesis will need to be specifically developed and validated. From the above studies, it is also worth noting that there were no discriminations of the visibility or contrast for each age group. This is important, as each body size has different thicknesses of soft tissue together with different bony dimensions and components. This may generate different levels of tissue visibility or contrast and as a result different optimisation strategies might be needed across a range of paediatric ages.

2.4 Chapter summary

This chapter has highlighted several different points regarding the factors and limitations which affect the optimisation studies reported within literature. It has identified that optimisation studies for previous imaging systems are not valid for modern DR systems. Also, this chapter referred to the difficulties which specifically exist in paediatric imaging and the connection with the wider difficulties in paediatric dose optimisation studies. There was a section in this chapter which showed the essential role of projection radiography in paediatric imaging and how dose optimisation can be achieved using different exposure factors. The chapter then presented the utility of conventional radiography in paediatric pelvis imaging, referring to the key imaging priority which is the perception of subjective contrast from the bony structures and their margins. The chapter presented the key principles for each exposure factor, imaging system, image quality evaluation, and radiation dose. The last part within this chapter was a review of the optimisation studies currently reported in the literature. It indicated three methods of dose optimisation studies, namely test objects, anthropomorphic phantoms and clinical data studies. The review of the three dose optimisation methods led to a conclusion that there was a lack of systematic dose optimisation studies within paediatric pelvic radiography.

Chapter Three: X-ray Phantoms

3.1 Chapter overview

This chapter focuses on the background and research studies which have previously described the use of X-ray imaging phantoms. The chapter starts by introducing phantoms (their forms and uses) and the rationale for developing and constructing X-ray phantoms. Current options for phantom design which can be divided into mathematical and physical phantoms, together with their advantages and disadvantages, are also described. This chapter also presents phantoms which are commercially available for dose optimisation studies. A critical analysis of phantom designs is also included within the chapter with the intention of identifying the most appropriate phantom for use within this thesis. Following this, the chapter discusses a series of phantom suitability criteria, including the physical principles of radiation interactions and specific criteria for using phantoms in X-ray imaging (radiography). Methods for choosing tissue substitutes for use within the phantoms are outlined, for example, linear attenuation coefficient and CT density (referred to as Hounsfield units, HU) from computed tomography (CT) scans. Within a phantom the tissue, substitutes can be specified for each radiation type. Matching them according to the operating energy range of the X-ray modality will be discussed. Within this topic, the X-ray radiation characteristics of possible human tissue substitutes will be presented. A review of various types of tissue equivalent materials within the literature, starting from water through to resins, will be provided. Also, the manufacturing processes for modern tissue substitutes will be presented and classified into four types according to their base material, with the advantages and disadvantages of each outlined. Each of the manufacturing methods have been categorised according to the purpose the phantom was constructed for, such as for dose measurements, quality control or diagnostic imaging. Each manufacturing approach is presented and critically discussed in terms of its applicability for dose optimisation studies. The last topic discussed within this chapter is the application of phantoms within medical imaging.

3.2 Introduction

Phantoms can be simply described as a volume of tissue equivalent materials that are used to mimic the radiation interaction processes in humans. Phantoms are used in radiation protection, medicine, and radiology to standardise radiation detection systems and estimate the radiation dose administered to humans (Schettini, Maia, & Campos, 2007; Varchena, 2002). To simulate the absorption and scattering that occurs when X-rays interact with the human body, both the

geometry and composition of the phantom need to be accurate. The requirements of such phantoms will depend on the type of application. Phantoms exist in a number of forms, from a single sheet of plastic to a full size anthropomorphic human body (International Commission on Radiation Units and Measurements (ICRU), 1989; Varchena, 2002). Phantoms are usually categorised according to their function, either for calibration, dosimetry or IQ purposes (Yohannes, Kolditz, Langner, & Kalender, 2012). Calibration phantoms are used to test the performance of radiation detectors, whereas dosimetry phantoms are implemented for in-depth dose measurements. Imaging phantoms are generally more complex and are designed for IQ assessments. There are three types, namely reference, standard and body phantoms. Reference computational models are used for measurements of dose quantities. Standard phantoms are used to compare measurements under standard conditions. Body phantoms have the components and the shape of the human body and are composed from a range of tissue equivalent materials corresponding to parts or all of the human body. Geometric variations are available, ranging from simple shapes to complex ones, such as anthropomorphic phantoms (International Commission on Radiation Units and Measurements (ICRU), 1992; White et al., 1992b).

3.2.1 Rationale for constructing bespoke pelvis phantoms

The investigation of IQ can be undertaken using several methods, including physical measurements of IQ and those based on psychophysical evaluations (ICRU, 1996). Many authors have demonstrated that physical measurements are not enough on their own to investigate the clinical benefit of one imaging technique over another (Alves et al., 2016; BIR, 1989; ICRU, 1996; Stieve, 1989). The evaluation of clinical X-ray images, although a powerful technique, needs considerable resources and is usually unjustifiable from an ethical/radiation protection point of view, if it were to involve humans. Such studies would require repeat exposure for individuals and as such cannot be justified under current radiation protection legislation. Alternatives are therefore needed (Vassileva, 2002).

Anthropomorphic phantoms which mimic human tissue composition, size and shape are not always accessible because of manufacturing complexity, lack of availability and their high overall cost. More simpler geometrical phantoms have therefore been designed for dosimetry and imaging purposes (Conway et al., 1984; Vassileva, 2002), but again are limited in design, function and availability.

X-ray equipment used for diagnostic radiology is usually adjusted during installation by the manufacturer to provide acceptable IQ with acceptably low doses. However, the principle of as low as reasonably practicable (ALARP) is not necessarily aligned with the clinical aim of the diagnostic examination (Tung et al., 2007). Currently, to commission X-ray imaging systems, there is a lack of equipment which can be used in clinical practice to provide rapid assessment of the systems before implementation (Schaly, Varchena, Au, & Pang, 2009). Contrast-detail (CD) phantoms (Rajapakshe, Luchka, & Shalev, 1996) have frequently provided quality assurance data for X-ray imaging systems, but do not provide a clear indication of the capability of these systems to visualise key anatomical areas in patients. A potential solution could be for humans to volunteer to directly evaluate the imaging system for detailed anatomical tissue imaging. However, this method is associated with unnecessary radiation exposure, is time consuming, inconvenient and has ethical considerations. Nevertheless, human imaging for these purposes does occur, but on a limited basis and after extensive investigations using phantoms in order to minimise the risk to human participants. A more direct and convenient solution is to assess image quality by using an anthropomorphic phantom (Schaly et al., 2009).

It has been reported that the simulation of the human body from the new-born to adult for radiographic examinations is likely to be challenging (L. Martin et al., 2013; Varchena, 2002). It is known that there are huge variations in the dimensions of the body and tissue densities across this age range. As a result, there are many approaches which can be used to tackle this problem. Such options include designing computational/mathematical and physical phantoms, wherein the later could include dosimetry and imaging phantoms.

There is a general lack of imaging phantoms that can be used in visual IQ assessments. This problem is further confounded in paediatrics wherein size and age variations exist (Hart et al., 2007). If physical IQ is to be measured then a phantom must be constructed with the proper characteristics. In view of the lack of availability of paediatric pelvic anthropomorphic phantoms which are suitable for dose optimisation experiments, a series of phantoms were needed to be created for this thesis.

3.2.2 Objectives

- vi. To design and construct paediatric pelvis phantoms for 1, 5 and 10 year-olds to be used in dose optimisation studies.
- vii. To validate the three paediatric pelvis phantoms for use in DR dose optimisation research.

3.3 Phantom Designs

There are different kinds of phantoms available commercially. These are computational/mathematical models or physical phantoms (International Commission on Radiation Units and Measurements (ICRU), 1992). The later can be categorised according to their application: test objects (for quality control), dose measurements or diagnostic imaging evaluations (Watanabe & Constantinou, 2006). The following section introduces the available phantoms designs together with a discussion of their advantages and disadvantages.

3.3.1 Computational models

There are different mathematical model types of phantoms. Initially, there were elliptical shape paediatric models which were developed by Cristy (1980). Later, there were significant developments by Yamaguchi (1994), and the current status is that there are five age groups available: new-born, 1, 5, 10 and 15 years old. Each computational phantom is adjustable by the weight and size (Yamaguchi, 1994). For example, a commercial version of a Monte Carlo mathematical calculation is the PCXMC 2.0 software, which estimates organ and effective dose from conventional X-ray imaging (STUK, Helsinki, Finland). A series of tomography phantoms were developed by Zankle et al. in 1988. These phantoms were for the ages of 2 months and 7 years. Data for these phantoms came from CT scans of cadavers in which they acquired a 3D representation of the whole body with a variety of different tissues (Zankl et al., 1988). These phantoms are very precise as the pixel sizes are 1.5 by 1.5 mm. However, the drawback with these phantoms is their availability. Their availability depends on the CT data needed for the models and there are discrepancies in sizes when comparing across age groups (Varchena, 2002).

There are two types of human computational phantoms used for dosimetry calculations: voxel and stylized phantoms that simulate human anatomy via 3D voxel matrices and mathematical equations of surfaces, respectively. A series of hybrid phantoms following the ICRP 89 report have been presented by the University of Florida for the ages new-born, 15 years old, and adult male and female. Later, these series attached extra age phantoms of 1, 5 and 10 years old (Choonsik Lee et al., 2010). A disadvantage of computer-based phantoms is that they cannot evaluate new imaging systems, e.g. new DR detectors or image recording systems, because they are written using a computer program and therefore without a physical presence can only consider generic issues.

3.3.2 Physical phantoms

Many researchers have used physical objects of various shapes and sizes to represent the body of children across different age groups. Materials such as paraffin and epoxy resin have been used as tissue equivalents. A key publication came from Alderson in 1987 wherein a phantom simulating a 6 year-old child embedded with a natural skeleton was introduced. A year later (1988), another anthropomorphic phantom simulating a new-born, again including a natural skeleton, became available. The name of these phantoms is “ATOM”. A prototype of a new-born child phantom was introduced by Varchena in 1988, without a skeleton, however contained lungs and soft tissue- see figure (3.1). The second generation of these ATOM phantoms included a natural skeleton and artificial lungs and, soon after, in 1988, two paediatric ages were added- 1 and 5 years old, both with natural skeletons (Varchena, 2002). Further developments were made by Varchena in 1993 with the introduction of five sizes of paediatric phantoms with artificial skeletons. Skeletons were homogeneous since making them realistic (cortical and trabecular pattern) was difficult (Varchenya, Gubatova, Sidorin, & Kalnitsky, 1993). In these phantoms the bone substitutes for each age group allowed greater simulation of the shape and density relevant to a specific age group. In each model, a total of six tissues were simulated and the density of the lung varied from exhalation to full inhalation (Varchena, 2002).

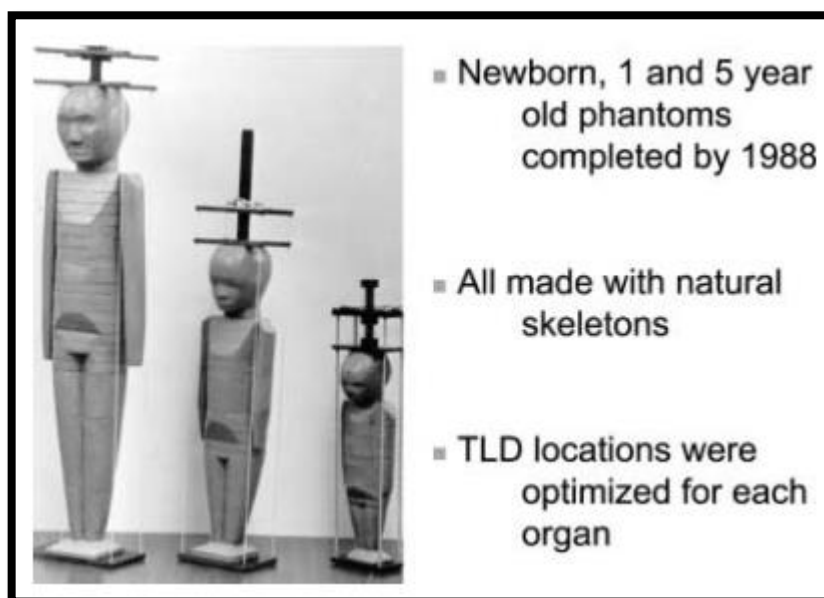


Figure 3.1: New-born, 1- & 5-year-old phantoms. All made with natural skeletons. TLD locations were optimised for each organ (Varchena, 2002).

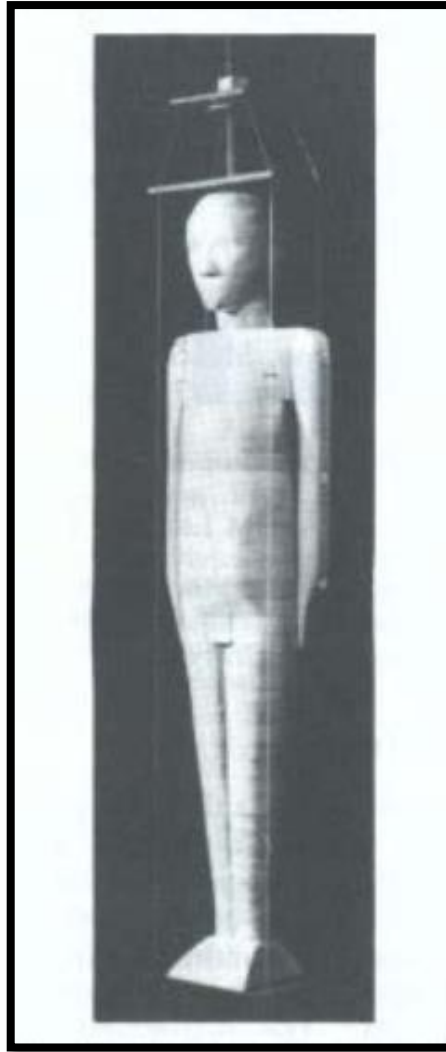


Figure 3.2: Heterogeneous Anthropomorphic phantom for 5-year-old. Produced by ATOM Ltd. (Varchenya et al., 1993).

In addition, there are a series of natural skeleton adult phantoms known as PIXY (male and female) anthropomorphic phantoms (Radiology Support Devices, Long Beach, CA). Early versions of these phantoms tended to utilise natural human skeletal bone within their design, however due to ethical and logistical issues most radiology phantoms now make use of synthetic bone within their design. They are suitable for teaching, positioning and training. In addition, they have been used in image quality and dose optimisation studies (Davey & England, 2015). Another type of adult natural (or tissue substitutes) skeletal phantom is the Alderson phantom; more details are mentioned in the following subsection (page 56). This phantom is mainly used in radiotherapy and imaging optimisation studies. In addition, there is a new paediatric phantom simulating a 5 year-old child from CIRS (model 715). The bone in this phantom has both cortical and trabecular patterns, growth plates and ossification centres similar to a 5 year-old (Figure 3.3). Also, for one and five year-old paediatric ages there are the Kyoto Paediatric

Whole-Body Phantoms (KYPH2C and KYPH50N, respectively). They provide valuable opportunities for hands-on training and experience- see figure (3.2). Figure (3.4) shows that the two phantoms have hip joints which exist for positioning training, however the joints would make using the phantoms in dose/image quality optimisations problematic as they are not constructed out of tissue equivalent material.



(a)



(b)

Figure 3.3: CIRS (model 715) 5-year-old phantom. (a) Trunk (b) AP pelvis.



(a)



(b)

Figure 3.4: The Kyoto Paediatric Whole-Body Phantom, (a) 5-year-old and (b) 1 year-old.

3.3.3 Commercially available phantom types for dose optimisation

Before making the decision on constructing paediatric pelvis phantoms for imaging purposes, a comprehensive search was undertaken in order to identify commercially available phantoms suitable for this research purpose. Few phantoms were found that were commercially available, (e.g. ATOM and ALDERSON dosimetry phantoms) and they have limitations in their design such as that the bone density does not match with cortical or trabecular bone tissue equivalent materials (CIRS Tissue Simulation and Phantom Technology, 2011). The Alderson dosimetry phantom has air voids that misrepresent human body. The availability of this phantom is restricted for paediatrics and this is a key disadvantage (Watanabe & Constantinou, 2006). For paediatric ages, the CIRS 5 year-old phantom (model 715 series) was found to be suitable for imaging purposes. However, this phantom is available only for a 5 year-old (see the brochures listed in Appendix (III)).

From the literature search, words/phrases that were used for the phantom mentioned above included: phantoms in X-ray imaging, pelvis phantom for X-ray imaging, paediatric or paediatric phantom in X-ray imaging and pelvis/pelvic pediatric/paediatric phantom X-ray imaging.

In order to consider the research question, a phantom for various ages would be needed to allow the assessment of IQ and radiation dose for paediatric pelvis radiography. At the time of conducting the research in this thesis, no paediatric pelvic phantoms existed which would be suitable to conduct this research, except for a five year-old (CIRIS Model 715)- see subsection 3.3.2. Consequently, to conduct the research in this thesis, a set of phantoms for different paediatric ages needed developing and validating. However, construction of a phantom is not considered to be simplistic. Manufacturing a phantom for X-ray imaging research requires that the materials used are human tissue equivalent and that the phantom geometry matches the actual anatomy of a human (International Commission on Radiation Units and Measurements (ICRU), 1992).

Designing and constructing a phantom for X-ray imaging research purposes requires careful consideration of different criteria. Firstly, the selection of materials that give a similar response to radiation for specific energies needs to be similar to human tissue. These materials are subsequently termed tissue substitutes. The second criterion is the ability of those tissue substitutes to physically form the internal and external components of the paediatric human

body (Orton, 1982 ; Varchena, 2002). The criteria, listed below, will be now be discussed in detail:

3.4 Phantom criteria

3.4.1 Criteria for selecting tissue equivalence

When selecting a tissue equivalent material the following quantities need to be similar to that of human tissue (Orton, 1982; Watanabe & Constantinou, 2006; White & Constantinou, 1982):-

1. Photon mass attenuation and mass absorption coefficients.
2. Electron mass stopping powers and mass angular scattering powers.
3. Mass stopping powers for heavy charged particles and heavy ions.
4. Neutron interaction cross-sections and kerma factors.
5. The mass densities of the two materials, which must be the same.

Considering the above criteria, it is clear that only the material with the same elemental compositions and same proportion by mass of the equivalent human tissue can be considered a tissue substitute across all radiation modalities. The agreement between the substitute and the tissue is dependent on the requirements of the phantom. Imaging techniques such as CT can now readily discriminate differences of less than 1% in photon linear attenuation coefficients (White & Constantinou, 1982). It is clear that for tissue substitutes for X-ray imaging there is no need to match all of the above criteria. Moreover, in X-ray diagnostic applications (energy > 150 KeV) it is only necessary to have a linear attenuation coefficient agreement within the clinical energy range (i.e. those generated by diagnostic X-ray equipment). Once agreement in the linear attenuation coefficient has been established, the radiation characteristics of the substitute should give a similar response to the human target tissue (Schaly et al., 2009; Watanabe & Constantinou, 2006).

3.4.2 X-ray interaction and attenuation

When an X-ray beam enters a target there are three possibilities (Aichinger et al., 2012):-

1. The X-ray photon can pass through the target without interaction.
2. The X-ray photon interacts with the material and be completely absorbed by depositing its energy.
3. The X-ray photon interacts and is scattered from its original direction, possibly depositing some of its energy.

X-ray interactions with matter can be divided into five types (Aichinger et al., 2012):-

1. Compton effect.
2. Photoelectric effect.
3. Rayleigh scattering.
4. Pair production.
5. Nuclear photo effect.

In the diagnostic range, the energy of the X-ray photon is not enough for pair production or nuclear photo effect. Rayleigh scattering is elastic, that is, the photon merely changes its direction with a small angle and no loss of energy. Only the first two types of interactions are considered important for diagnostic imaging (Compton and Photoelectric effects) (Aichinger et al., 2012).

If the energy range is ≤ 100 keV, the photoelectric effect (μ_{pe}) depends on both the atomic number and the photon energy, as shown in equation (3.1):

$$\mu_{pe} \sim \rho \cdot \frac{Z^3}{(hv)^3} \dots\dots\dots (3.1)$$

Where: ρ : the density, Z : Atomic number, A : mass number and $h\nu$: photon energy.

Compton scattering (μ_{incoh}), or incoherent scatter, changes only with the atomic number, as shown in equation (3.2). However, the Z/A ratio varies (0.4-0.5), except for the hydrogen atom, which is equal to 1, where A decreases gradually with the increase of Z . Therefore, Compton attenuation coefficient is almost independent from Z (Aichinger et al., 2012).

$$\mu_{incoh} = \rho \cdot N_A \cdot \sigma_e \cdot \frac{Z}{A} \dots\dots\dots (3.2)$$

Where; σ_e : total K-N cross section per electron and A : Avogadro's number.

The total mass attenuation coefficient can be written (equation 3.3) as the summation for the mass attenuation coefficients of the photo-electric effect, Compton (incoherent) scattering and Rayleigh (coherent) scattering (Aichinger et al., 2012).

$$\frac{\mu}{\rho} = \frac{\mu_{ep}}{\rho} + \frac{\mu_{incoh}}{\rho} + \frac{\mu_{coh}}{\rho} \dots\dots\dots (3.3)$$

Where: μ_{coh} : Rayleigh scattering.

From equations 3.1, 3.2 and 3.3, it can be seen that increasing the energy decreases the photoelectric effect significantly. At a specific point there is a crossover wherein their curves show response with increasing photon energy to incoherent scatter and lose domination over the total linear attenuation coefficient, as shown in Figure (3.5) (Aichinger et al., 2012).

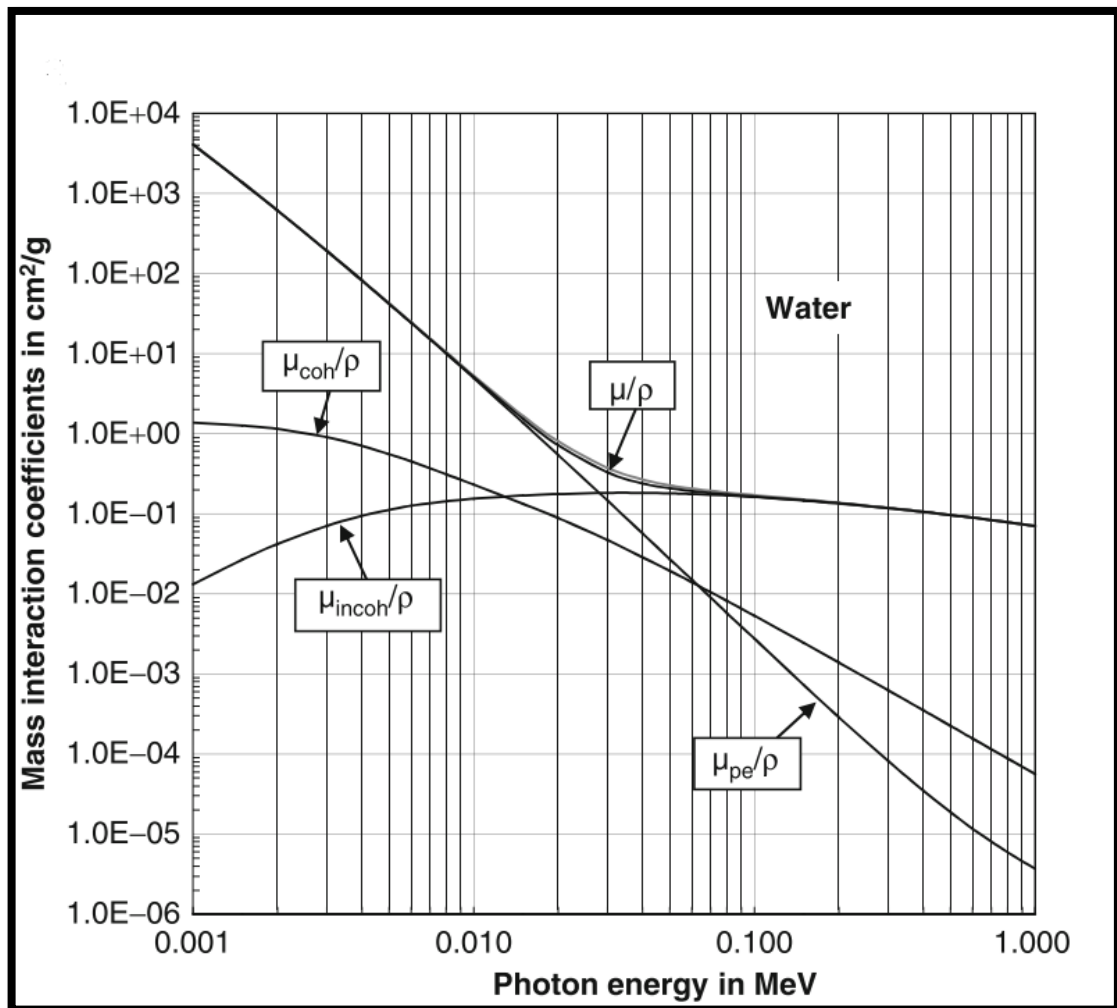


Figure 3.5: X-ray interactions with water over the energy range 0.001 to 1 Mev (Aichinger et al., 2012).

3.4.3 Selection requirements for phantoms

For a phantom to be used in medical imaging, the requirements are for it to assess the capability of an imaging system in terms of providing an opportunity to visualise abnormal and normal anatomical structures inside the area of interest. The threshold visibility of details within an X-ray image depends on the physical dimensions, shape and radiation characteristics (absorbing and scattering properties) of the anatomical structures. This threshold also depends on the attenuation properties of the body tissue volume in which the anatomical structures are

embedded (International Commission on Radiation Units and Measurements (ICRU), 1992; White et al., 1992a). In general, tissue equivalent materials need to have acceptable linear attenuation coefficients which are within 5%, however this uncertainty is recommended to be reduced to 1% in CT and general X-ray examinations (International Commission on Radiation Units and Measurements (ICRU), 1989, 1992).

3.5 Availability of tissue substitutes

3.5.1 Background

The human body contains a large variety of components, including soft tissue, adipose tissue, and bones of different compositions. Each one of these structures will have a different response when exposed to X-rays. This response is determined by the attenuation coefficient, or more precisely the photoelectric effect and Compton scattering of the substitute. When selecting a substitute material, these attributes need to be matched with the human body part of interest, together with the density (Orton, 1982 ; White, 1974). The matching ability between the tissue of interest and the substitute depends on the implementation of the substitute itself. In the diagnostic X-ray range, photoelectric effect and Compton scattering are considered dominant for X-ray interaction with matter. The photoelectric effect varies with the X-ray energy and the density of the atomic number, whereas Compton scattering changes with atomic number only. As a result, the similarity in attenuation coefficients should be considered over the energy range of diagnostic X-rays (Aichinger et al., 2012).

A survey was conducted to find human tissue substitutes, wherein different tissue equivalent materials were presented as possible substitute materials for all kinds of radiation (International Commission on Radiation Units and Measurements (ICRU), 1989). Different substitutes were recommended for photon interactions with a wide range of X-ray energies, including the diagnostic X-ray range. One available substitute for cortical bone was Polyvinyl Chloride (PVC). Poly methyl methacrylate (PMMA) and water were then selected as a substitute for the soft tissue and bone, respectively.

On the other hand, theoretical matching between the human tissue parts and different tissue substitutes can be made by calculating attenuation coefficients (Hubbell, 1995). Using this approach, mass attenuation coefficients can be calculated after entering the compound proportions of any material using web-based software. In this study, the elemental proportions of each body tissue were taken from literature (ICRP, 2002; International Commission on

Radiation Units and Measurements (ICRU), 1989). By way of an example, the results for different tissues have been calculated by the author and are presented in Figure (3.6) below:

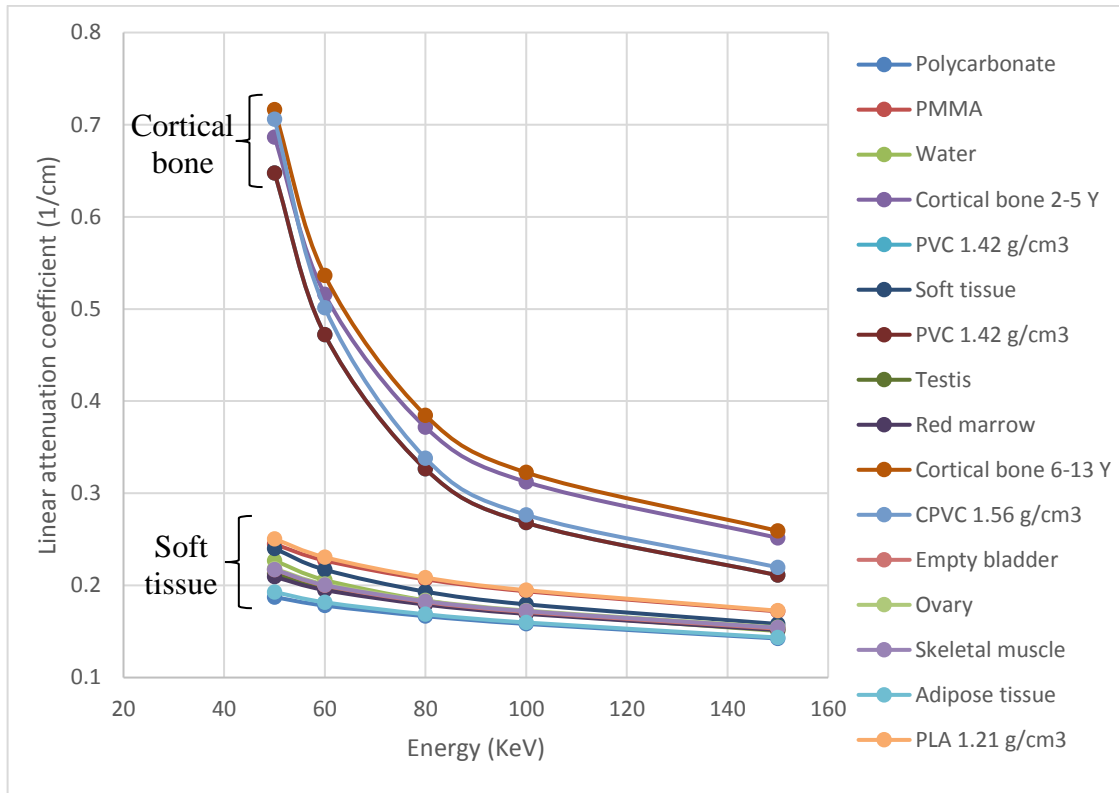


Figure 3.6: linear attenuation coefficients for different human organs and substitutes.

Figure (3.6) shows that all of the organs within the pelvis are of a comparable linear attenuation coefficient when compared to soft tissue. Furthermore, PVC was reported as a substitute for cortical bone, as mentioned in ICRU 44 (International Commission on Radiation Units and Measurements (ICRU), 1989). The percentage error from the soft tissue range for the PVC starts at 5.7 at 50 kV, and then increases to 14.2 at 100 kV. For PMMA the percentage error ranges from 1.97% to 7.90%, at 50 kV and 100 kV, respectively, with an average of 5.3%. Red marrow showed similar X-ray attenuation to soft tissue and water.

Despite the difficulties when matching for elemental equivalent tissue substitutes, it is not necessary to match for all radiation types. This is an advantageous point. A tissue substitute may not be representative of some radiation types and highly representative of others, even without elemental equivalency (Watanabe & Constantinou, 2006). This could ease the choice for equivalent tissue if only one type of radiation is used, as would be the case for the experiments within this thesis.

A common classification in the literature for tissue substitutes is according to their linear attenuation discrepancies from the corresponding human tissue. A discrepancy within 5% from the human tissue is considered to be a Class A substitute. Class B is between 5 and 20%, and a Class C substitute is more than 20% error. If the discrepancy is within 1%, the substitute classified with A* (Watanabe & Constantinou, 2006).

3.5.2 Literature review

There are various attempts in literature to find human tissue substitutes for X-ray imaging. This was first started with water as the first tissue substitute chosen in radiation measurements (Kienbock, 1906). Wax was then introduced (Baumeister & Rocky, 1923) as a tissue substitute. Siemen's wax was then produced by Zur (1937), which composed of paraffin wax and magnesium oxide (Zur, 1937). Subsequently, other wax-based substitutes were introduced such as Hariss wax (J. Harris, Tuddenham, Stanton, Glauser, & Pendergrass, 1956), Mix D (Zur, 1937) and M3 (Markus, 1956). These have been used, later, for forming simple and complex phantoms (Watanabe & Constantinou, 2006). An increasing tendency to include rubbers and plastics in phantom design has been found in the manufacturing of anthropomorphic phantoms. These materials include polyethylene-based Markite (HH & G, 1956), plastics (Shonka, F.R. ; Rose, J.E. ; Failla, 1958) and polyurethane (RV, AL, & PN, 1976). A liquid mixture of water, sucrose, glycerol and urea was presented by Rossi and Failla (HH & G, 1956) as elementally equivalent to soft tissue. Goodman simplified the mixture. Out of many tissue substitutes before 1970, only the above were within 5% of human tissue radiation characteristics and water was the most important one (Goodman, 1969).

In 1970, a program aimed at finding human tissue equivalent materials commenced at Bartholomew's Hospital in London. Over 160 materials were identified as tissue substitutes for different body components (Constantinou, 1978; White, 1974). Also, various other groups started to develop tissue substitutes. Herman and colleagues in the 1980s (Hermann, Geworski, Hatzky, Lietz, & Harder, 1986; Hermann, Geworski, Muth, & Harder, 1985; Kalender & Suess, 1987) produced an equivalent material to water, fat and muscle. Homolka and co-workers mixed polymer powders with additives to adjust for photon characteristics (Homolka, Gahleitner, Prokop, & Nowotny, 2002; Homolka & Nowotny, 2002). They found water, bone, adipose and muscle tissue substitutes for diagnostic x-ray examinations (energy < 100 KeV). Suess and colleagues (1999) made a phantom derived from polyurethane resin for low contrast measurements in computer tomography (Suess, Kalender, & Coman, 1999). Researchers Jones, Hintenlang and Bolch developed tissue substitutes to study dosimetry in paediatric radiology

(A. Jones, Hintenlang, & Bolch, 2003). Iwashita mixed resin of polyurethane with CaCO_3 to simulate cortical and cancellous bones (Iwashita, 2000).

3.5.3 Manufacturing method for human tissue substitutes

Modern human tissue substitutes can be divided according to their base material into four types (Watanabe & Constantinou, 2006):-

1. Epoxy resin based materials are produced by White, Constantinou and Martin (White, Constantinou, & Martin, 1986). These contain viscous resin and other less viscous diluents (liquid hardener). The mixing process is based on mass proportions determined by chemical reactions. These resin systems consist of adequate concentrations of hydrogen and nitrogen, but they are low in oxygen percentage compared to humans. The process requires a vacuumed vessel during the mixing in order to exclude air bubbles from the substitute (Watanabe & Constantinou, 2006).
2. Polyurethane, which contains a series of organic units coupled by urethane. This can be manufactured in a variety of textures and solidities by changing monomers and adding other materials. It is often used for producing foam rubber (Watanabe & Constantinou, 2006). Some researchers used resin of low density polyurethane to manufacture human tissue substitutes for low contrast phantoms (Suess et al., 1999). Their mixture contains high density polytetrafluorethylene (PTFE) with small proportions of low density phenolic micro-spheres; thus the density can be adapted. The process needs humidity control, as different levels of humidity affect the polymerisation and this results in variations in the density. Also, the temperature needs to be fixed before mixing (20°C) and during curing (40°C) to assure homogeneous and reproducible density. The whole process needs to be kept under vacuum conditions to eliminate air bubbles and reduce humidity. The whole procedure demands a sophisticated mixing and curing methodology to be carried out (Suess et al., 1999; Watanabe & Constantinou, 2006). Also, polymer processing requires mixing large amount of substances, which limits its application in laboratory (Homolka & Nowotny, 2002).
3. A polyethylene-based method was reported (Hermann et al., 1985). This method mixes polyethylene powder with inorganic admixtures (CaCO_3 and MgO) in a powder form. The melting point of the polyethylene powder is 105°C and its density is 0.917 g/cm^3 . Its processing temperature is in the range of 200 to 240°C . The polyethylene powder and inorganic powder is dry mixed in a long Plexiglas drum rotated on a lathe, and the mixing process is facilitated by internal Plexiglas shelves within the drum. The mixture

is then poured on iron plates. Plastic plates are then formed at a melting point of 180 °C. Smooth and homogeneous plastic materials are obtained with adding inorganic admixtures of up to 10 % of the total mass. Machining was easy in order to make different thickness of plates. In order to make thinner foils, a milling machine was provided with a vacuum fixing device.

4. A polymer powder-based method was described by Homolka and Nowotny (2002), which explains the manufacturing techniques of phantoms made from polymer powder bases (Homolka & Nowotny, 2002). The base materials for this procedure are polymer powders made of polypropylene, polystyrene, polyethylene, and polyurethane. Powder particles were <100 μm. Typical admixtures were MgO, TiO₂, CaCO₃, calcium hydroxyapatite (bone mineral), and graphite of high purity. These admixtures are available in an appropriate grain size of <100μm. The material is then sintered (transforming into solid) in an air evacuated vessel at a temperature above the melting point of the polymers. During the sintering process, the sample volume is reduced to approximately half of its initial volume. A vacuum pressure of about 1 Pa is applied during the sintering process, in order to remove any air or other gases.

Reflecting on the above mentioned tissue substitutes, despite the fact that these materials have high precision mimicking soft tissues over a wide range of radiation types and energies, there are many difficulties from implementing these materials in phantoms during the manufacturing process. These challenges include the shrinking size of materials during solidification (Homolka & Nowotny, 2002) which offsets the forming of anatomical geometry. This is more difficult when the anatomy has more than one layer within a specific density, as each density would have a different shrinking rate. Also, the procedure could require repeating in order to estimate the shrinking rate which adds extra cost to the already sophisticated procedure.

The mixing procedure requires maintaining a high level of quality control for temperature, vacuum pressure and mixing apparatus. There is also a difficult issue when dealing with the vacuumed vessel. The sealing of the vessel would prevent any direct access into the vessel, so during the curing process pouring the materials in geometry equivalent moulds would be limited. To overcome this, remote control devices need to be placed inside. This requires extra space inside the container, and they would be added to the mixing tools and the large amount of substances mixed to form the tissue substitute. Also, it has been reported that the material has a variety of toxicity levels during the manufacturing procedures. However, the exact composition of some materials is subjected to industry confidentiality (K. Harrison et al., 2011).

3.6 Phantom application in the literature

X-ray phantoms can be used for imaging or dosimetry purposes. Imaging phantoms are mainly divided into two groups - physics and anthropomorphic phantoms. Dosimetry phantoms are used for estimating the radiation dose received by the patient when undergoing imaging or radiotherapy treatments (Watanabe & Constantinou, 2006). The following provides a review of phantoms illustrated within the literature.

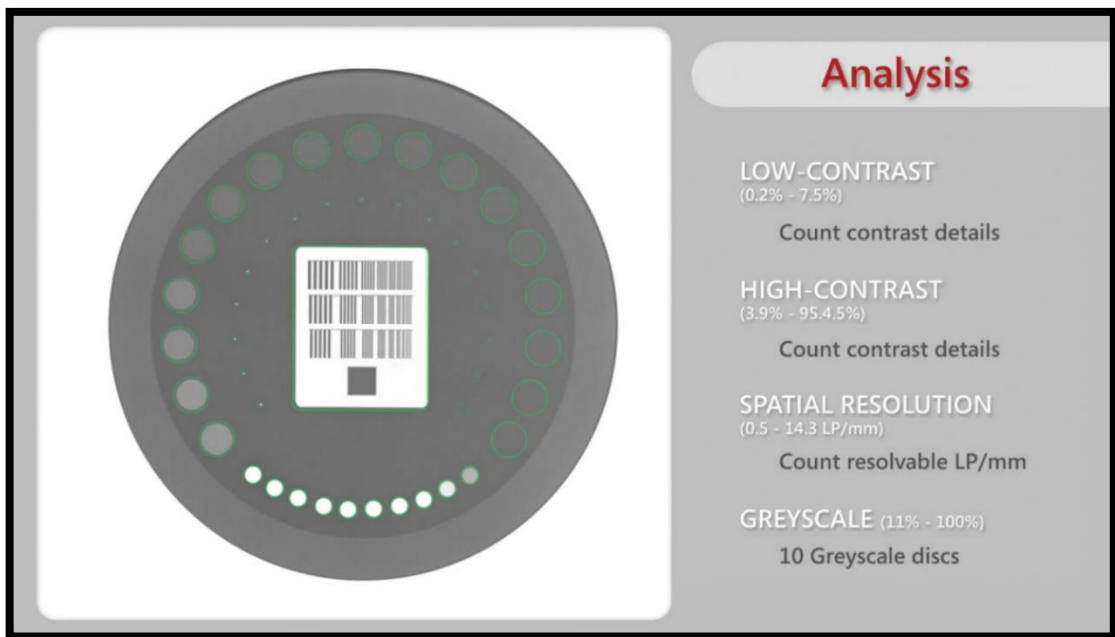
3.6.1 Physical phantoms

3.6.1.1 Test object

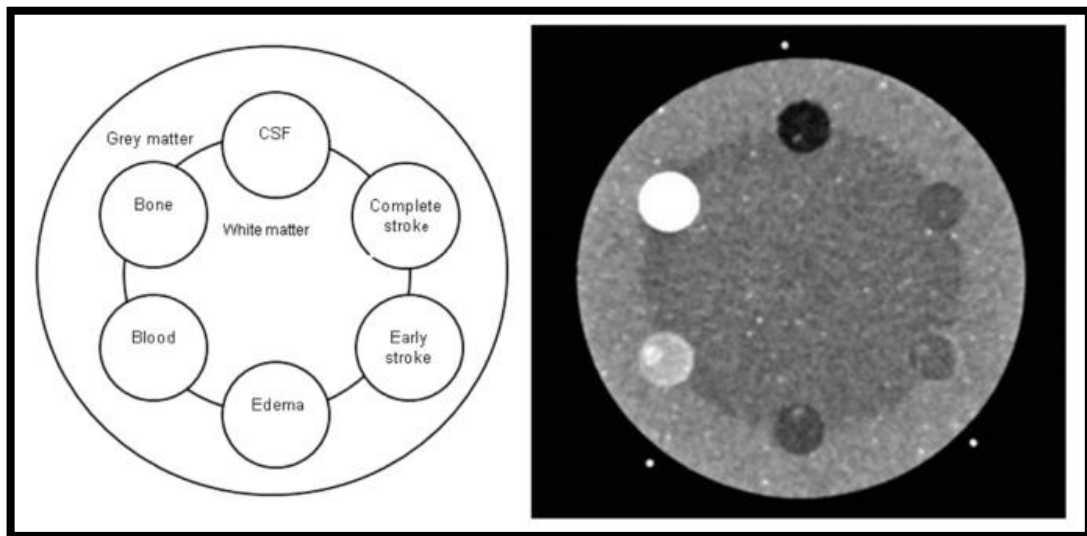
Physics phantoms and test tools are used to evaluate physical aspects of IQ such as spatial resolution, sharpness, subject contrast, and quantum noise. Examples of commercially available phantoms for these measures are line-pair test templates used to measure sharpness and spatial resolution (Carroll, 2011; Chan & Fung, 2015). Contrast detail detectability tests (CDRAD phantom) often use a quality control phantom (Roberts, Evans, & Rees, 2006). The phantom contains test objects, within drilled holes which have different depths and diameters, on an acrylic sheet. The observer is asked to indicate the borderline visibility of the holes in the X-ray image from the phantom (Thijssen & Bijkerk, 1998). Data from this phantom are used to determine the variations between different digital imaging systems used in clinical practice (Veldkamp et al., 2006). Important information about IQ can be obtained from contrast-detail studies, however the CDRAD phantom delivers a limited simulation of clinical applications because of the lack of anatomical noise in the images. Quantum noise and thus radiation dose levels may play a more dominant role in contrast-detail investigations than in clinical studies using anthropomorphic phantoms or with patients (Burgess, Jacobson, & Judy, 2001). Also, the Leeds Test Objects, including the TOR CDR which incorporates both line pair phantoms and low-contrast discs, is a similar but different option. This phantom is designed for the routine checking of imaging performance, including sensitometric measurements (10 test point details, 5.6mm diameter), Resolution limit (0.5 to 14.3 LP/mm), Low-contrast large-detail detectability (17 details, 11mm diameter) and High-contrast small-detail detectability (17 details, 0.5mm diameter) (Leeds Test Object\medical imaging phantom)². Also, there is a CT prototype custom phantom (Leeds Test Objects Ltd., Boroughbridge, UK) used with various concentrations of urethane rubber to mimic the attenuation characteristics of common acute intracranial

² <http://www.leedstestobjects.com/index.php/phantom/tor-cdr>

pathologies alongside normal anatomies (M. Harris, Huckle, Anthony, & Charnock, 2017). See Figure (3.7) below:



(a) (<http://www.leedstestobjects.com/index.php/phantom/tor-cdr/>)



(b) (M. Harris et al., 2017)

Figure 3.7: (a) The Leeds Test Objects TOR CDR, (b) CT Prototype custom phantom representing normal anatomy and acute intracranial pathology.

Another common procedure for evaluating IQ is to measure the modulation transfer function (MTF) of an imaging system. The MTF is a descriptive graph of how well an imaging system maintains contrast when increasing spatial resolution. Using edges or wires, the derivation of MTFs can be achieved by measuring the line spread function (LSF) of an imaging system,

before taking the Fourier transformation of the LSF, which represents the optical transfer function (OTF) of the system. The MTF is a convenient descriptive measure of the performance of an imaging system (A. Jones, 2006; Moore et al., 2013).

The LucAl phantom is a geometrical phantom which was originally designed by Conway et al. (1984) to facilitate surveys of the average patient exposure from AEC during postero-anterior chest radiography. It is made from Lucite and Aluminium which gives it preferable properties such as its sturdiness, its light weight and its transportability. The LucAl phantom consists of 25 cm x 25 cm of PMMA plates and 1100 pieces of Al alloy with specific thicknesses (Figure 3.8). The total thickness of the phantom is 26.7 cm, with 0.41 cm Al, 7.3 cm PMMA and a 19 cm air cavity. The different phantom components, including the thicknesses and relative positions, have been formed to precisely mimic primary and scatter transmission through the lung-field regions of a standard anthropomorphic chest phantom for diagnostic X-ray chest (Conway et al., 1984; Vassileva, 2002). See the Figure (3.8) below:

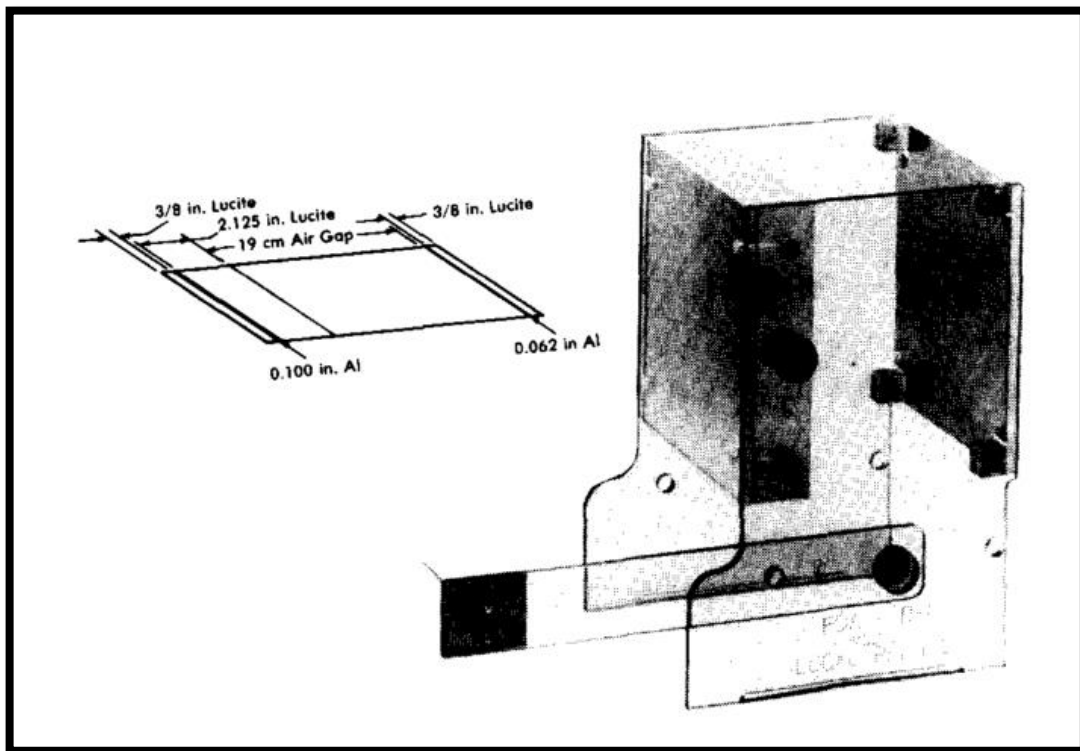


Figure 3.8: The LucAl phantom: on the left, its components (Conway et al., 1984).

3.6.1.2 Dosimetry phantoms - literature review

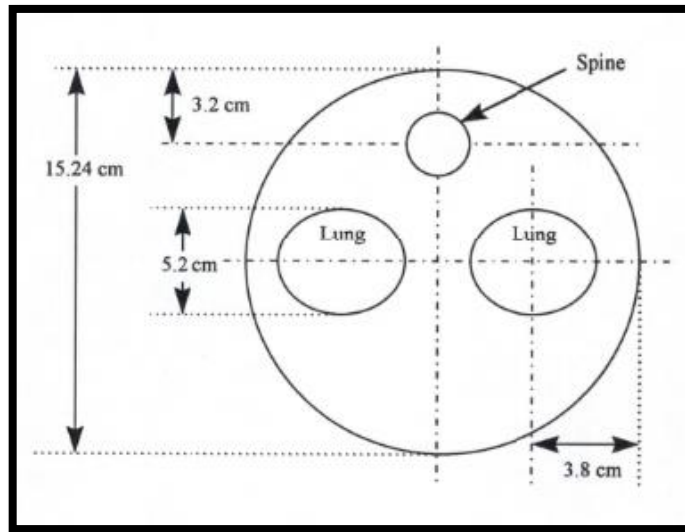
Dosimetry phantoms can be developed from water, solid water and gel which serve as uniform and large dose measurement mediums. Geometric phantoms have been used as a quality assurance tool to measure the geometrical accuracy of radiotherapy treatment planning software

(Fraass et al., 1998). Later, many phantoms simulating a single human body part were built, for example the Gammex-RMI at the Phantom Laboratory, CIRS. Many of these phantoms were used in dose measurements to verify radiation therapy treatment plans (Watanabe & Constantinou, 2006). The humanoid or anthropomorphic phantoms provide high precision of the radiation dose delivered to the patient by geometric replication of the human body, such as the anthropomorphic Rando and Alderson phantoms and CIRS anthropomorphic dosimetry family phantoms of all ages. The latter include the adult male, adult female, 10 year old, 5 year old, 1 year old and new-born (CIRS Tissue Simulation and Phantom Technology, 2011). These phantoms can be used to measure the radiation dose delivered to the patient during diagnostic imaging and radiation therapy procedures (Watanabe & Constantinou, 2006). Alderson male and female phantoms contain a series of horizontally sliced slabs, 5 cm thick, with the ability to insert radiographic film between slabs for radiation dose measurements. This phantom contains slices of natural human skeleton. While the lung and breast are very close substitutes to the original tissue, they are coated with soft tissue equivalent material. Each slice contains holes for TLD chips to be inserted with bone equivalent, soft tissue equivalent or lung tissue equivalent pins (Watanabe & Constantinou, 2006). The CIRS family phantoms contain only tissue equivalent substitute for all kinds of tissues, including soft tissue and lung tissue. However, bone tissue is a homogenous substitute for the averaged densities of cortical and trabecular bone. The manufacturer claims that this has advantages over natural skeletal bone by having a more consistent size and density, which eliminates air voids in natural trabecular bone and simplifies dose measurements by eliminating the uncertainty of the cortical to trabecular bone ratio (CIRS Tissue Simulation and Phantom Technology, 2011).

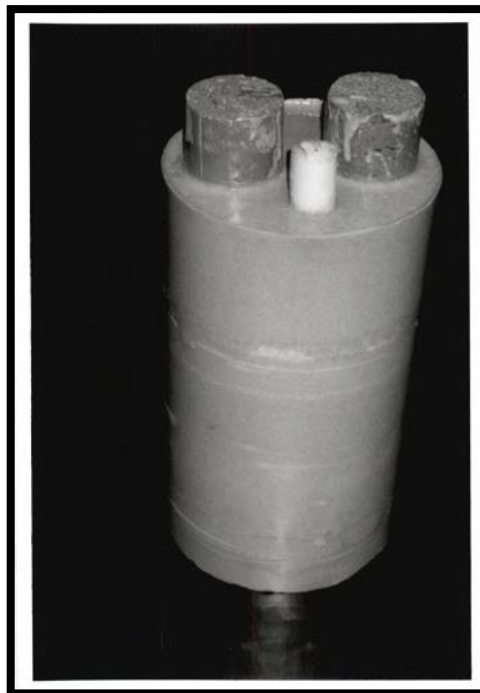
Beside the commercial dosimetry phantoms (mentioned in subsection 3.3.3, page 56), there are a few academic attempts which have aimed to manufacture phantoms for dose measurement purposes. A study aimed to identify suitable tissue equivalent substitutes in the diagnostic energy range for a phantom simulating an 8-year-old child (Akhlaghi, Miri-Hakimabad, & Rafat-Motavalli, 2015). They cited a voxel phantom which was modelled on tissue substitutes. Their study found that the physical properties (physical density, electron density, effective atomic number, linear attenuation coefficient and HU) of water and polyurethane (as soft tissue), B-100 and polyvinyl chloride (PVC) (as bone) and polyurethane foam (as lung) were suitable substitutes for human tissues.

A doctoral thesis by Bower (1997) reported that epoxy resin based tissue substitutes can be useful for making a physical heterogeneous phantom for dosimetry (see Figure 3.9) (Bower,

1997). Bower's reference for tissue substitutes were the X-ray characteristics that were used in the Cristy and Eckerman mathematical phantom. He used these as a human tissue reference for a one-year old child, which typically contain three types of tissue including soft tissue, lung tissue and bone. All of the bone contents- cortical bone, inactive marrow, trabecular bone and active marrow- are represented by a homogenous mixture, as well as soft tissue organs. This homogeneity is likely to be suitable for dosimetry purposes but not for image quality evaluations.



(a)



(b)

Figure 3.9: physical heterogeneous dosimetry phantom. (a) schematic diagram (b) body torso (Bower, 1997).

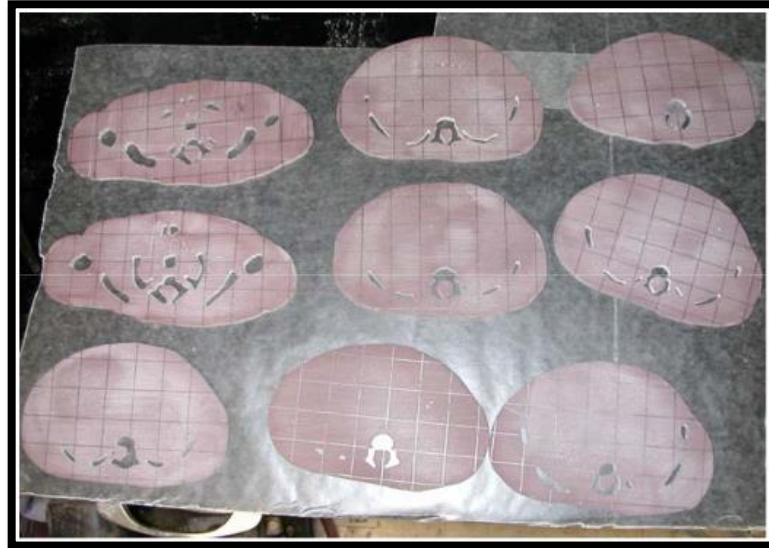
A study by Jones et al. (2003) presented a series of tissue substitutes designed to radiographically simulate human tissue at diagnostic photon energies (10–150 keV) (A. Jones et al., 2003). The work included the tissue substitutes for soft tissue, bone tissue and lung tissue for three ages: new-born, child (1, 5, 10 and 15 years) and adult. In all cases, targeted reference elemental human tissue compositions were taken from Cristy and Eckerman's Oak Ridge National Laboratory stylized computational model series. For each substance, reference values of mass density, mass attenuation coefficients, and mass energy absorption coefficients were matched to acceptable levels over the diagnostic photon energy range.

A series of simple acrylic cylindrical dosimetry phantoms were built (Nickoloff, 2002). Different diameters were chosen to represent different ages (6, 10, 16 and 32 year olds) and then they evaluated the effect of different (patient) sizes using CT dose index, the effect of different scanning types, scanning modes, kVp and mAs selection.

Anthropomorphic phantoms are considered to be the gold standard in radiography. These kind of phantoms closely represent the external and internal components of the human body (A. Jones, Simon, Bolch, Holman, & Hintenlang, 2006). The phantoms can represent 0, 2, 6, and 12 year old children (Giacco, Cannata, Furetta, Santopietro, & Fariello, 2001). Each one is made from nine sections of acrylic that mimic the head, thorax, neck, lungs, legs and arms. The acrylic shells are filled with deionised water, except the section representing the lungs which is filled with air. The size of all parts are based on data from a handbook in clinical auxology (Hall, Froster-Iskenius, & Allanson, 1989).

Past doctoral work has illustrated a tomographic new-born phantom which was constructed from human tissue-equivalent materials for use in evaluating the radiation doses delivered to paediatric patients as a result of diagnostic imaging (A. Jones, 2006). The tissues simulated include soft tissue, heterogeneous bone and lung tissue. Fibre optic coupled (FOC) dosimeters were used along with the phantom to measure average organ doses during projection radiography. The new-born phantom was constructed from 5 cm thick axial slices (Figure 3.10). Later, another study presented an adult anthropomorphic phantom for use in dosimetry studies (Winslow, Hyer, Fisher, Tien, & Hintenlang, 2009), this study was based on the previous work of Jones (2006). This included using a urethane base instead of a resin base in the formulation of soft tissue and lung tissue substitutes, as this is a more pliable material (see Figure (3.11)). The best example of anthropomorphic dosimetry phantoms were those introduced by Varchenya et al. (1993) and were presented earlier (subsection 3.3.2, page 52). These phantoms

contain a set of tissue equivalent materials representing various ages, including 0, 1, 5, 10 and 15 year-olds (Varchenya et al., 1993). These phantoms offer a high quality of patient modelling for lung, exterior and skeletal anatomy, but their limitation is that they are not based on anatomical derived CT data (A. Jones, 2006).



(a)



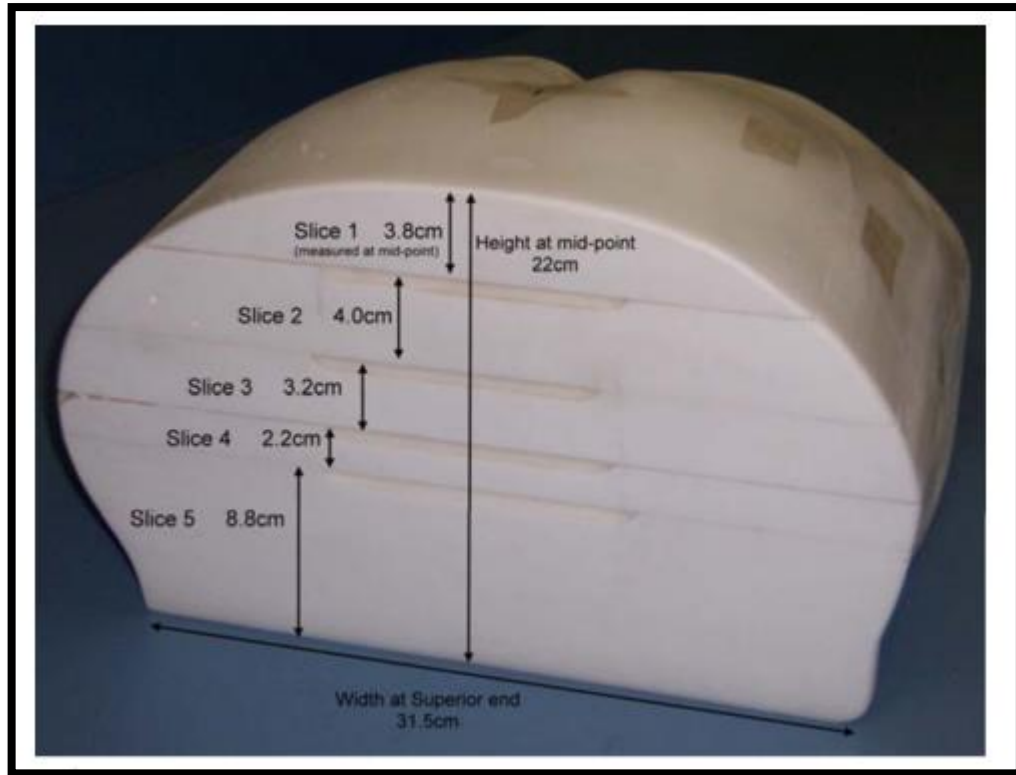
(b)

Figure 3.10: (a) Slices that were used the new-born phantom, (b) the new-born dosimetry phantom (A. Jones, 2006).



Figure 3.11: Adult anthropomorphic dosimetry phantom (Winslow et al., 2009).

An anthropomorphic pelvic phantom was designed and constructed by Harrison et al. (2011) to satisfy particular criteria for dosimetry measurements of a multi-centre radiotherapy study (K. Harrison et al., 2011). The basic 3D design of the realistic external and internal anatomical shapes were made from CT data of a male pelvis. The phantom comprised of three tissue equivalent materials for bone, organs and ‘backfill’ (representing fat and surrounding muscle). Several suitable material samples that were used as tissue analogues, were provided by the phantom manufacturer for radiological testing. All chosen materials were polyurethane based, and the physical parameters were provided by the phantom manufacturer. The production procedure was epoxy resin based and this has been described by White (1978). The material testing was checked via the calculation of linear attenuation coefficients using the CT density from the CT data. The total number of slices was five and their thickness varies from 2.2 to 8.8 cm. See the Figure (3.12) below.



(a)



(b)

Figure 3.12: the pelvic dosimetry phantom (a) assembled together (b) in slices (Harrison et al., 2011).

3.6.1.3 Imaging phantoms – a literature review

A modular chest phantom was developed by Christensen, Dietz, Murry and Moore (1980) and was made from many layers of Lucite with the dimensions 30 cm x 35 cm and 1 cm in thickness. Each layer represented a specific component, such as the heart that was mimicked by wax, the fixed and inflated lung of a canine, and human ribs cut to size (Christensen, Dietz, Murry, & Moore, 1980). This phantom was designed for investigating the relationship between the detection of pulmonary disease and quantum mottle. A more realistic human shape was

produced by Pearce, Gillan and Rock (1980). This phantom included structures of the lung vasculature and mimicked pathological conditions (Pearce, Gillan, & Rock, 1980). It also consisted of a thoracic skeleton inserted into a Plexiglas material together with lungs from a canine fixed in formalin. The lungs and mediastinum (rubber-based) were embedded inside the thoracic cage, while the rest was filled by urethane foam.

Two kind of phantoms were built by Constantinou, Cameron, DeWerd and Liss (1986), Semi anthropomorphic and geometric phantoms (Constantinou, Cameron, DeWerd, & Liss, 1986). The first one consisted of four layers: 1) various test pieces to investigate high contrast resolution, low contrast detectability and film latitude. 2) a solid water layer to simulate the mediastinum and the thorax, meant to test the detectability of the pathological structure normally found within these regions 3) a layer of Lucite and aluminium representing the two dimensions of the rib cage, and 4) a scatter layer. The third and fourth layers, extra scatter layers, aimed to investigate the impact of extra scatter on the resolution and detectability of low contrast nodules. The total dimensions of the phantom were 35 x 35 x 20 cm, which demonstrated the equivalent optical density of an X-ray image taken on an average adult human chest (Figure 3.13). The second phantom, a geometric phantom, consisted of three slices: one with a 6 cm thick test object, for the same functionality as in the first phantom, and two dimensions of 30 x 30 x 2 cm. This latter phantom was developed for routine quality tests. Both phantoms lacked anatomical representation in terms of geometry and tissue substitutes.

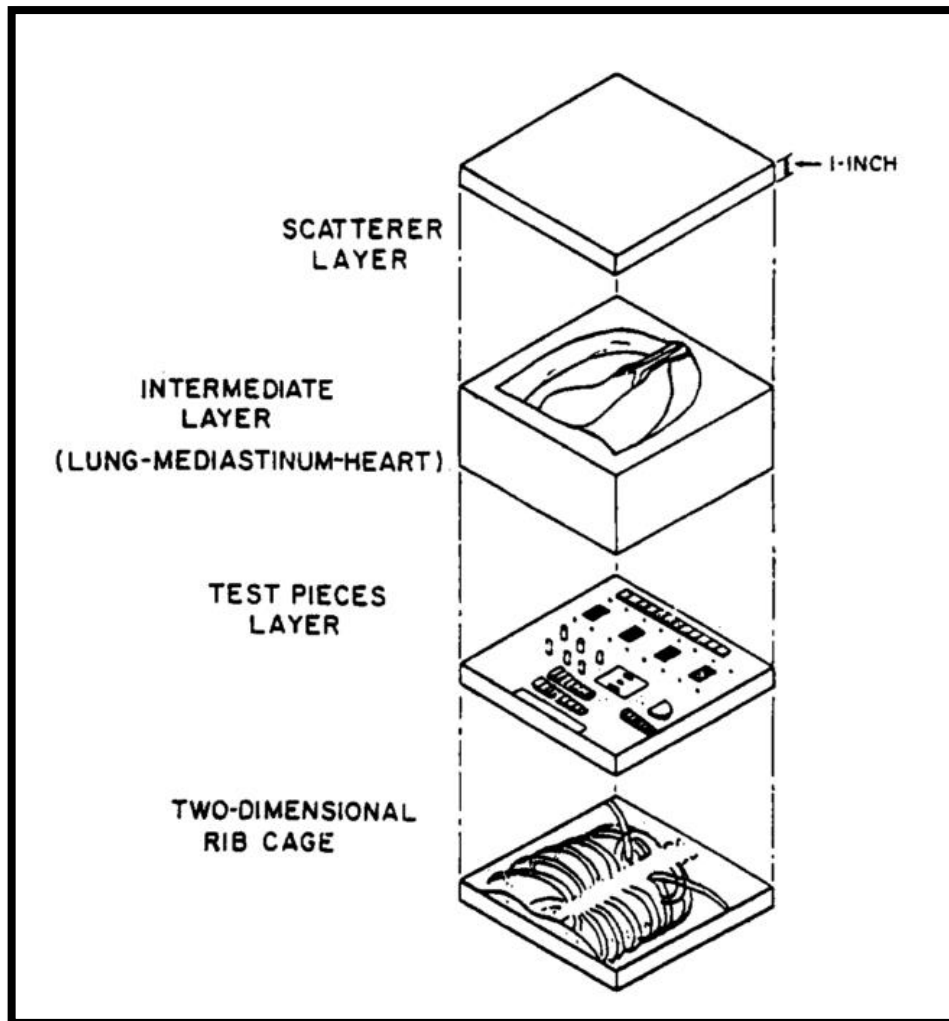


Figure 3.13: Schematic diagram of a semi-anthropomorphic chest phantom (Constantinou et al., 1986).

A realistic analytic phantom (RAP) was constructed by Pina et al. (2004). This phantom was developed from the acrylic-based Patient Equivalent Phantom (PEP) by Pina, constructed in 2002 (Pina, 2002; Pina et al., 2004). The RAP components were based on the recommendations of the International Commission on Radiation Units and Measurements (ICRU) (1989) and the International Commission on Radiation Units and Measurements (ICRU) (1992). They contained several test tools which enabled the quantification of contrast and optical density for different radiographic techniques. It consisted of an acrylic slab which was 5 cm thick and had an area of 30.48 cm². The RAP contains the following (Pina et al., 2004) (Figure 3.14), however anatomical representation not was considered in the making of these phantoms.

- (A) Five acrylic steps plus air gaps simulating cavities.
- (B) Five acrylic steps plus PVC simulating bone structures.
- (C) Four nylon spherical segments simulating tumours.

- (D) Three nylon cylinders simulating fat tissue.
- (E) Six aluminium spheres to determine the degree of visualization of the bone tissue boundaries.
- (F) Four groups of human organic micro-calcification, simulating cortical bone based on different sizes.
- (G) One spatial resolution grid.
- (H) ½ a human thoracic vertebra.
- (I) Two steel spheres, separated by 0.80 cm for magnification analysis.
- (J) One tin wire to determine the coincidence of light and radiation fields.

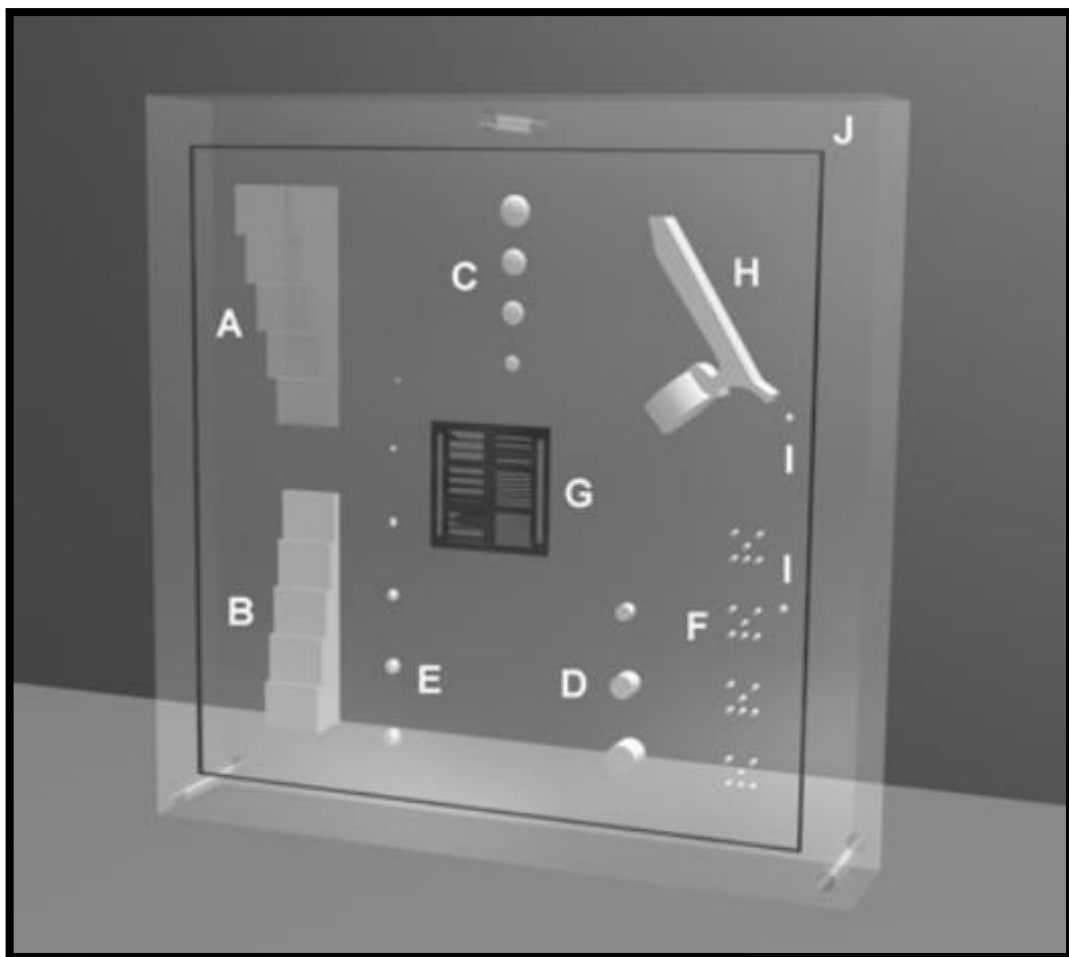


Figure 3.14: A schematic view of the realistic-analytic phantom (RAP) (Pina et al., 2004).

A series of homogeneous phantoms were designed and developed by different researchers. First to be considered is a phantom that was extensively used in X-ray image quality control (American National Standard Institute (ANSI), 1982; Gray et al., 1983). Next, one of the most

frequently used geometric phantoms is the patient equivalent phantom (PEP). This homogenous phantom consisted of aluminium and Lucite mimicking bone and soft tissue, respectively. This phantom was used in optimising radiographic techniques for the chest, pelvis and skull (Pina et al., 2004). Later, the same phantom construction method was used to build homogeneous phantoms simulating the chest, pelvis and skull, but for non-standard patient sizes (Pina, Duarte, Ghilardi Netto, & Morceli, 2009). The development of the homogeneous phantoms to simulate a non-standard patient was based on the homogeneous phantoms currently accepted and used extensively in radiographic IQ control. In previous works the PEP phantom was used to determine the optimised radiographic technique for the chest, skull and pelvis for the standard patient (Pina et al., 2000, 2004). A patient equivalent phantom (PEP) was constructed by Alves, Miranda, Neto, Duarte, & Pina, (2015), and Alves, Pina, Neto, Ribeiro and Miranda (2014). These authors produced separate skull and chest equivalent phantoms for paediatric patients of 1 and 5 years old (Alves, Miranda, Neto, Duarte, & Pina, 2015; Alves, Pina, Neto, Ribeiro, & Miranda, 2014). Again, no anatomical representation was considered within these phantoms.

A study by Vassileva in 2002 used a LucAl phantom to mimic the optical density of chest anatomical parts such as the mediastinum, heart and soft tissue organs in the subdiaphragmal area as they appear in an anthropomorphic phantom (Vassileva, 2002). He added PMMA for muscles (subdiaphragm and heart) and Al as phantom material for bones (including; spine and ribs) to the original LucAl phantom, mimicking the X-ray transmission through the regions of the chest. The spine was simulated by a strip of Al which was 3.5 cm width and 0.5 cm thick. A 1 cm PMMA slab was placed in the centre of the phantom to represent the X-ray beam attenuation of the upper mediastinum. Cylindrical slabs of PMMA were selected for the subdiaphragmal organs and the heart, with thicknesses of 7.5 cm and 6.4 cm, respectively. Two Al strips of 0.3 cm thickness were placed to the right lung region in order to acquire information about changing optical density from the ribs. The anatomical shape and level of tissue simulation is restricted by the absorption and scattering of the material substitutes used in the phantom (Figure 3.15). This can be seen below.

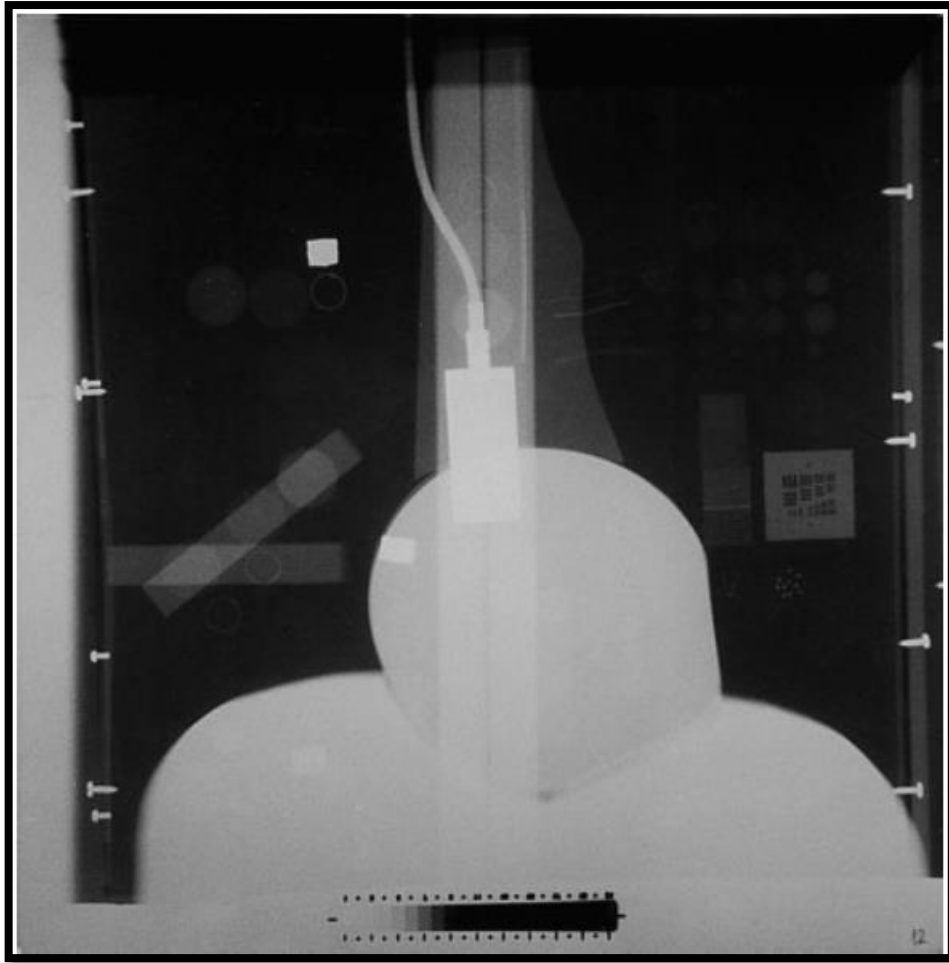


Figure 3.15: X-ray image of the anthropomorphic LucAl chest phantom (Vassileva, 2002).

In phantom development procedures there have been many reports in the literature which aimed to develop neonate chest phantoms. Brindhaban (2004) used a one litre bottle filled with water to mimic a 1 kg neonate, which was a crude approximation and no anatomical representation of a real neonate was included in the design. A better simulation by Vergara et al. used a PMMA (Imperial Chemical Industries, London, UK) phantom with air gaps to represent the lungs (Vergara et al., 1999). More precision was implied in the work by Akahane et al. who constructed a neonatal phantom from rectangular solids. In this solid water and lung phantom, substitutes were used and the lungs shapes were not symmetrical due to the volume of the heart (Akahane et al., 2000). All the above phantoms were still limited in their presentation of human anatomy.

A neonatal chest phantom was constructed from eight Perspex sheets 1 cm thick, 13 cm wide and 21.8 cm in length (N. Jones, Palarm, & Negus, 2001). In a procedure to mimic the neonatal lungs, two rectangular sections were removed from the Perspex sheets. This left air cavities (88 ml in capacity) in order to represent a lung capacity of neonate with 2.5 kg at his/her peak

inspiration. The anatomical representation of the shape and the tissue substitutes in this phantom is limited by the rectangular shape and lack of vessels within the lung, respectively. There was also an absence of ribs.

A two-block style phantom was constructed to mimic the neonate. The two phantoms were built from white water tissue substitute (Duggan et al, 2003). The inside of each phantom was designed to house a soft tissue substitute or lung substitutes to modify the torso tissue density. Lung substitutes were inserted inside the large phantom and one was placed inside the small phantom. The phantoms were designed to represent neonates weighing 700 g and 2000g and were represented by dimensions of 10 cm wide, 25 cm long and 7 cm thick and 6 cm wide, 8 cm long and 2 cm thick, respectively. A line pair resolution gauge and a contrast resolution tool were inserted into the phantom for the investigation of IQ. These phantom anatomies represented the scatter and the absorption of real patients and this phantom was used for investigating factors affecting radiation dose. However, this phantom has limited visual properties as it insufficiently mimics human anatomy.

Anatomically, the most superior phantom simulation developed was the Gammex RMI 610 model (Gammex Inc. Middleton WI, 2013). However, the radiological equivalence of the phantom could not be obtained (Groenewald & Groenewald, 2014). Later, an anatomical improvement to the Gammex RMI 610 phantom was attempted by Groenewald and Groenewald (2014), who constructed a neonatal chest phantom with particular anatomical structures such as muscle, cortical bone and foetal deflated/inflated lung simulated by agar gelatine, Gammex SB3 and Gammex Solid Water/Gammex LN300, respectively (Groenewald & Groenewald, 2014). This phantom has been used to investigate the relationship between radiation dose and image quality. A CT scan from a neonatal cadaver was used to mimic the average shape and dimensions of the respective anatomies. Also, the shapes of the included structures were simplified to be less rounded and flatter and as such did not represent the geometry of the neonatal chest. The phantom was validated by comparing the mean intensities from different regions in an image of the phantom to those of a real neonatal chest. Thus, an indication of the radiological similarity was observed between real neonatal chest and the phantom with an overall deviation of 32.5%.

A relatively recent study described a more sophisticated phantom which was the adult anthropomorphic male pelvic phantom from CIRS Inc., Norfolk, VA, USA (Schaly et al., 2009). It simulates the pelvic region with a complete human adult male cross-sectional

anatomy. It includes mimicking of such properties as an actual prostate anatomy for radiotherapy treatment planning and image-quality assessment. The bone density in this phantom is averaged for cortical and trabecular bone for dose measurements purposes, which is not suitable for evaluating image quality for pelvis X-ray examinations (Figure 3.16).

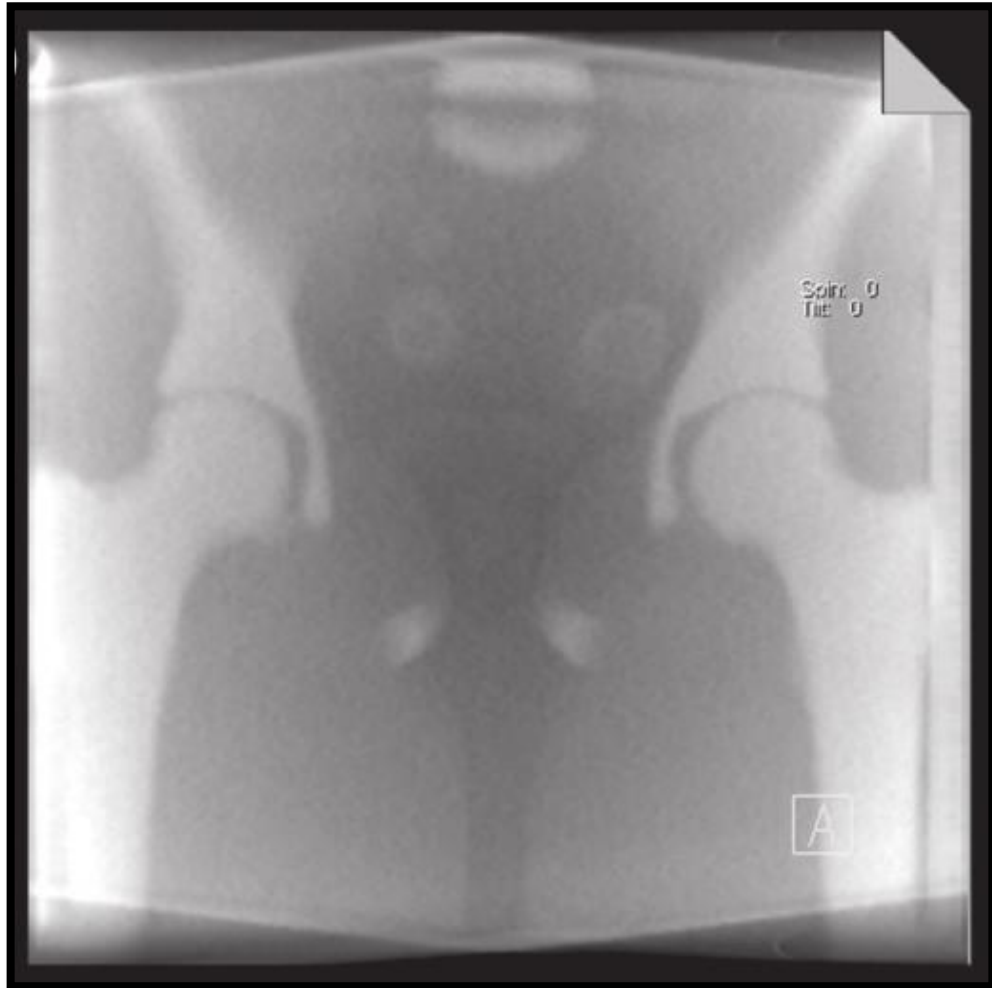


Figure 3.16: Mega-voltage cone beam CT (MV-CBCT) images of coronal plain of the pelvis phantom (Schaly et al., 2009).

The recent developments of, multi-material additive machines have expanded the potential use of anatomic 3D printed, accurate phantoms as teaching tools. Current studies have attempted to use 3D printing technology in the manufacturing of phantoms for medical X-ray imaging. For example, Waran et al. (2014) used CT data of a patient with a brain tumour in 3D printing an anthropomorphic model to be used in training neurosurgeons when performing craniotomies (Waran, Narayanan, Karupiah, Owen, & Aziz, 2014). Leng et al. (2016) used 3D printing technology (a commercial 3D printer) to build brain and liver phantoms with heterogeneous backgrounds and pathologies (Leng et al., 2016). For the brain phantom, the images were

divided into three objects, according to their HU values (at 120 kVp of CT scan), simulating white matter (125 HU), grey matter (134 HU), and cerebrospinal fluid (108 HU). The liver phantom contained materials simulating lesions (77.8 HU), lung tissue (96.6 HU), and vessels (137.5 to 428.4). Solomon et al. (2016) constructed 165 mm diameter cylindrical shaped phantom containing simulation of subtle soft-tissue lesions (with spherical shape) in homogeneous background usually exist in low-contrast detectability phantoms. They used a commercial multi-material 3D printer with native print resolution ($42 \times 84 \times 30 \mu\text{m}$). They used two materials: TangoPlus and VeroWhite, both are photopolymer resins with approximate radiological attenuations (at 120 kVp CT scan) 75 HU and 115 HU, respectively (Solomon, Ba, Bochud, & Samei, 2016). The aforementioned studies describe the applicability of 3D printing technology in manufacturing imaging phantoms, however, they did not include simulation for anatomy in term of geometry and/or attenuation characteristics. This can be related to the AM filaments, which currently lacks higher attenuation materials which in turn match the radiological characteristics of bone (Ceh et al., 2017).

In order to include anatomic representation in 3D printed phantoms, Jahnke et al. (2017) created anthropomorphic phantoms using layer-by-layer (paper based) 3D printing approach (Jahnke et al., 2017). They used a standard inkjet 3D printer to stack 100 layers each with 1 mm thickness to create abdomen phantom (included abdominal aorta, muscle, intraabdominal fat, spleen, left cortical kidney, pancreas, vertebral spongiosa, portal vein, and liver) of 1 cm thickness, see Figure (3.17). Iodine-enhanced ink was used in combination with standard inkjet technology to produce high resolution radiopaque phantoms, therefore, increased the radiological attenuations reaching a mean value of 1174 HU (SD 30) from CT scanning at 120 kVp. A further step was made by Jahnke et al. (2019), where two methods for assembling 3D printing papers were presented and each produced a full head and neck phantom (Jahnke et al., 2019). They used radiopaque 3D printing papers and aqueous potassium iodide solution (0.6 g/ml), assembling-method-1: a paper-based 3D printer and assembling-method-2: customized laminated object manufacturing procedure, see Figure (3.18). The above studies, by Jahnke et al., presented 3D printing technology with some advantages including anatomical precision and cost effective, however, the radiological attenuation characterises of real anatomies were not matched. Also, the paper-by-paper 3D printing approach used in their studies has reported many limitations such as resolution errors, mechanical properties (air entrapped materials) and automation (reduce need for technicians (Leary et al., 2015). Hazelaar et al. (2018) used a clinical thorax CT scan of patient with lung cancer to 3D print thorax phantom (Hazelaar et al.,

2018). The phantom contained three different materials: 1- bony structures which was printed in gypsum. 2- lung structures (including airways, blood vessels, outer lung surface and three lung tumours) all were printed in nylon. While 3- soft tissues (including mediastinum, muscles, fat, skin); were all presented by silicone made from silicone which was poured into a mold in order to form the thorax body, see Figure (3.19). The work by Hazelaar et al. (2018) showed high precision for anatomical representation in thorax. However, their study was relatively low cost (total cost \$3,500) but the phantom was not fully 3D printed as the soft tissue parts were constructed using mold.

Overall, the 3D printing materials have been used in previous studies were matched in density equivalent to the radiological attenuation of mimicked tissues at specific kVp (for CT scan). However, there was no tissue substitute used in 3D printing technology that follow ICRU report (1989) which reported tissue substitutes and stated that tissue substitute needs to match radiological properties over the energy rang used in the clinical application (International Commission on Radiation Units and Measurements (ICRU), 1989).

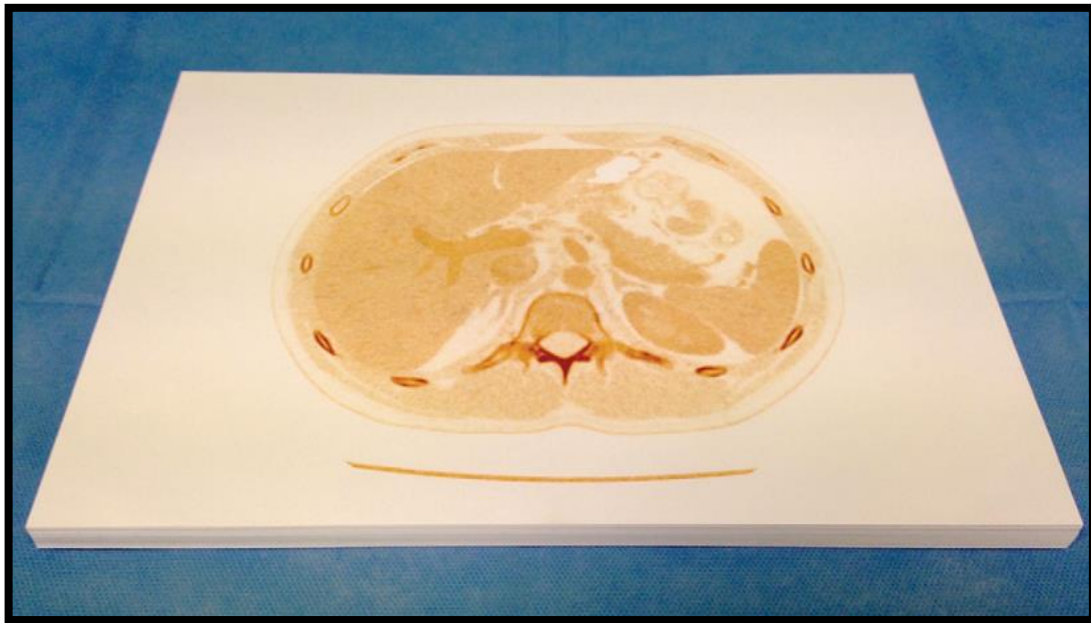
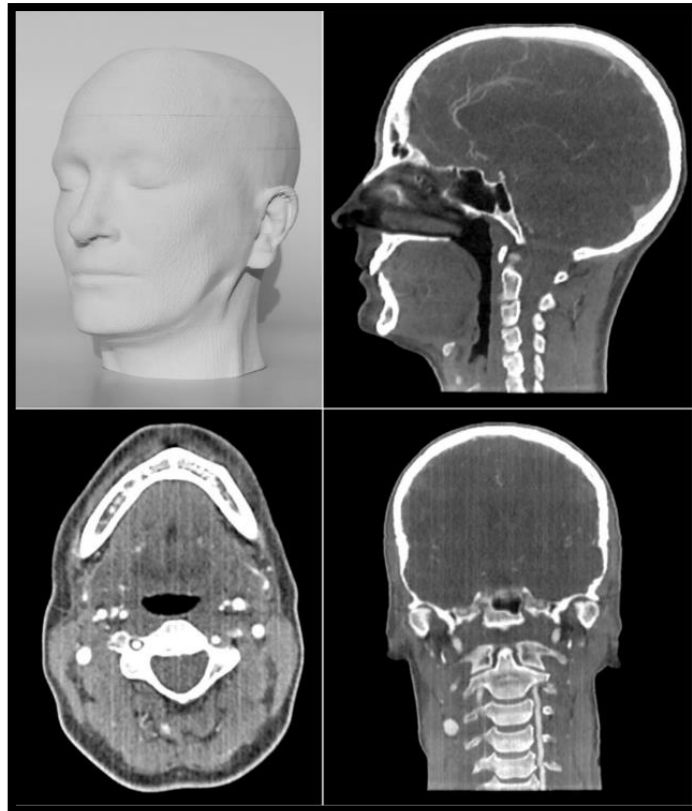
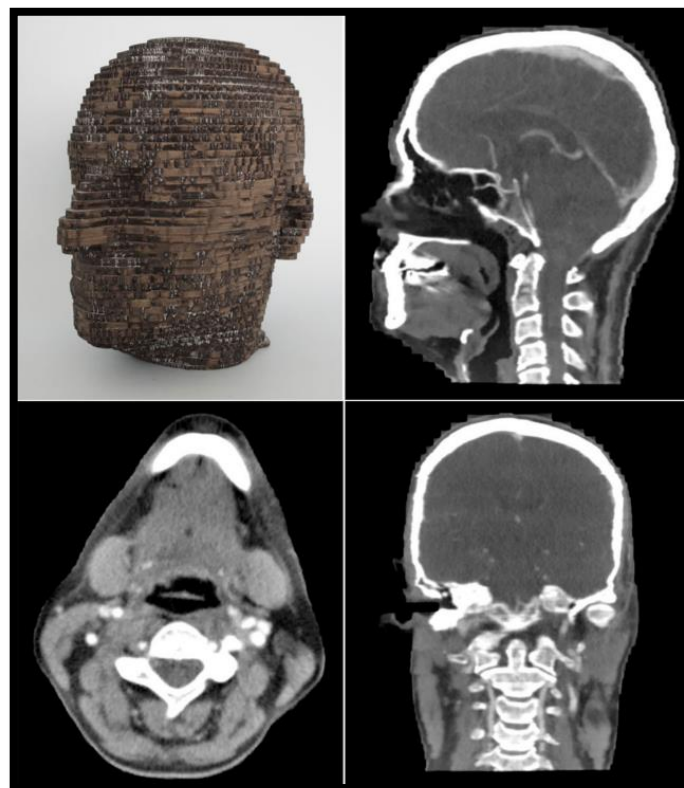


Figure 3.17: An image of a 3D abdomen phantom of 1 cm thickness, produced by (Jahnke et al., 2017).

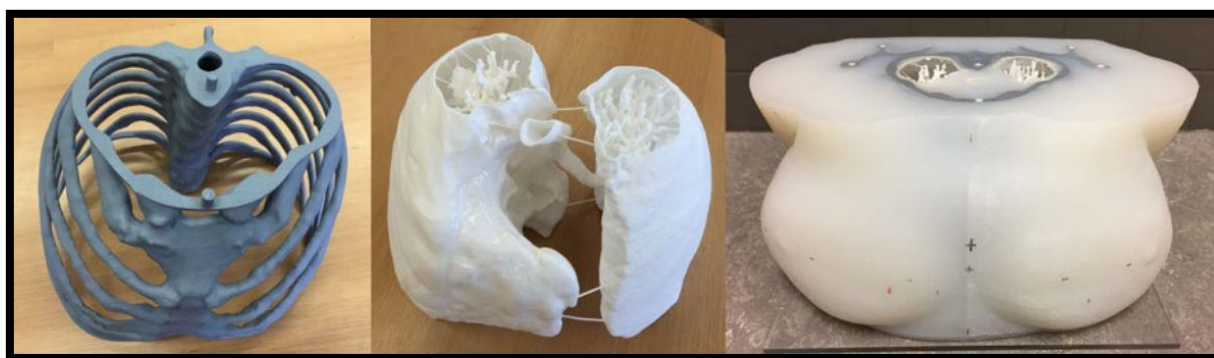


(a)



(b)

Figure 3.18: Head and neck phantoms constructed using 3D printer assembled (a) with the paper-based 3D printer (b) the customized laminated object manufacturing procedure (Jahnke et al., 2019).



(a)

(b)

(c)

Figure 3.19: 3D printed thorax phantom presented by (Hazelaar et al., 2018). (a); represents bony structures printed in gypsum, (b); lung structures printed in nylon and (c); soft tissues outside the lungs are represented by silicone.

As seen within this chapter, a variety of phantoms currently exist, each with their own specific purpose and advantages and disadvantages. A more comprehensive summary of the currently available X-ray phantoms is described in Table (3.1).

Table 3.1: X-ray phantoms described within the literature.

<u>Authors/ Year</u>	<u>Phantom purpose</u>	<u>Simulated tissues</u>	<u>Anatomy/ age/s</u>	<u>Constructional method</u>	<u>Advantage/ Disadvantage</u>
(Conway et al., 1984)	Test object: Quality Control (QC)	Soft tissues: Lucite, bone: aluminium and lung: air gap.	Chest/ Adult	PMMA plates and 1100 pieces of Al alloy.	No anatomical representation.
(Bower, 1997)	Dosimetry	Soft tissue, heterogeneous bone and lung tissue.	Chest/ one-year-old	Cylindrical rod of soft tissue substitute includes rods of bone and lung substitutes	No anatomical representation.
(Nickoloff, 2002)	Dosimetry	Soft tissue: Acrylic	Whole body / 6, 10, 16 and 32 year-old	simple acrylic cylinders	No anatomical representation.
(Giacco et al., 2001)	Dosimetry	Soft tissue: Acrylic	Whole body / 0, 2, 6, and 12 year-old	Each phantom is made from nine sections of acrylic.	No anatomical representation.
(A. Jones, 2006)	Dosimetry	Soft tissue, heterogeneous bone and lung tissue. All are base	Whole body / new-born	Tomographic Templates of CT data.	Anthropomorphic, but crude anatomical representation.

		of Araldite GY-6010 with a Jeffamine T-403 hardener.			
(Winslow et al., 2009)	Dosimetry	Soft tissue, heterogeneous bone and lung tissue. All are base of Araldite GY-6010 with a Jeffamine T-403 hardener.	Whole body / Adult	Tomographic Templates of CT data.	Anthropomorphic, but crude anatomical representation.
(K. Harrison et al., 2011)	Dosimetry	Bone, organs and 'backfill' (fat and representing surrounding muscle). All are polyurethane based.	Pelvis / Adult	Coronal slices from male CT data.	Anthropomorphic, but crude anatomical representation.
(Christensen et al., 1980)	Imaging	Lucite: soft tissue, heart: wax, inflated lung of a dug and human ribs.	Chest / Adult	Many layers of Lucite contain the simulated tissues.	Crude anatomical representation.
(Pearce et al., 1980)	imaging	Lung vascular and mimicked pathological conditions.	Chest / Adult	Thoracic skeleton inserted into a Plexiglas material together with lungs from a canine.	Intermediate anatomical representation.
(Constantino et al., 1986)	QC	Test objects: contrast resolution, mediastinum and thorax includes two dimensions of the rib cage.	Chest / Adult	Axial layers of the simulated tissue and test objects.	Semi anthropomorphic.
(Pina, 2002)	QC	Soft tissues: Acrylic	Chest / Adult	Acrylic slices of the simulated tissue.	No anatomical representation.

(Pina et al., 2004)	QC : optimising radiographic technique	Bone: aluminium and soft tissue: Lucite.	chest, pelvis and skull / Adult	Layers of the simulated tissues for standard patient	No anatomical representation.
(Pina et al., 2009)	QC: optimising radiographic technique.	Bone: aluminium and soft tissue: Lucite.	chest, pelvis and skull / Adult	Layers of the simulated tissues for non-standard patient.	No anatomical representation.
(Alves et al., 2015)	QC: optimising radiographic technique.	Bone: aluminium and soft tissue: Lucite.	chest, pelvis and skull / Ages: 1-5 year	Layers of the simulated tissues.	No anatomical representation.
(Vassileva, 2002)	Imaging: optimising radiographic technique.	Mediastinum, heart and soft tissue: different thickness of PMMA. Ribs and Supine: Aluminium.	Chest / Adult	Anthropomorphic insert represented by Cylindrical slabs of different thickness of PMMA to simulate different soft tissues types. Two strips of Aluminium.	Weak anatomical representation.
(Brindhavan, 2004)	Imaging	Soft tissue: water	Chest / Neonate	One litre bottle filled with water.	No anatomical representation.
(Vergara et al., 1999)	Imaging	Soft tissue: PMMA. Lung: Air gap	Chest / Neonate	PMMA layers	No anatomical representation.
(Akahane et al., 2000)	Imaging	Soft tissues: Solid water. Lung: Kyoto kagaku material.	Whole body / Neonate	Rectangular shapes for each part of human body, with lung substitute embedded.	No anatomical representation.
(N. Jones et al., 2001)	Imaging	Soft tissue: Perspex sheets. Lung: air cavity	Chest / Neonate	Perspex sheets and air cavities.	No anatomical representation.
(Duggan et al., 2003)	Imaging and Dosimetry	Soft tissue: white water.	Chest and Abdomen / Neonate	Box made from while water. It contains contrast tool and spaces for dose measurements.	No anatomical representation.
(Groenewald &	Imaging	Cortical bone: Gammex SB3, soft tissues: agar gel	Chest / Neonate	A pair of 3-D triangles represent the lungs. 2-D slabs	Limited geometrical representation for chest anatomies.

Groenewald, 2014)		mix, deflated (sick) lung: Gammex Solid Water and inflated (healthy) lung: Gammex LN300.		represent the ribs. Both inside a box of soft tissue substitutes.	
(Paliwal et al., 1998)	Imaging, volume rendering, treatment planning, and dosimetry applications for performing quality assurance.	Soft tissue: Solid water, organs (prostate, bladder, And rectum): alterations to solid water and bone (the left and right femurs.): a material with calcium.	Pelvis / Adult	Based on axial CT slices taken from a patient study.	Poor representation of the bony anatomies and Significant discrepancy between real bone and its substitute.
(Waran et al., 2014)	Imaging and training neurosurgeons.	brain	Adult	3D printing	No anatomical representation.
(Leng et al., 2016)	Imaging	1-brain: white matter, grey matter and grey matter 2-liver: lesion, lung tissue and vessels.	Adult	3D printing	Poor anatomical representation.
(Solomon et al., 2016)	Imaging	Subtle soft-tissue lesions.	Adult	3D printing	No anatomical representation.
(Jahnke et al., 2017)	Imaging	Abdomen: abdominal aorta, muscle, intraabdominal fat, spleen, left cortical kidney, pancreas, vertebral spongiosa, portal vein, and liver.	Adult	layer-by-layer 3D printing	Anthropomorphic, but limited attenuation characteristics.
(Jahnke et al., 2019)	Imaging	Head and neck.	Adult	layer-by-layer 3D printing	Anthropomorphic, but limited attenuation characteristics.

(Hazelaar et al., 2018)	Imaging	Thorax: bony structures, lung structures and soft tissues.	Adult	Partly 3D printing	Anthropomorphic
-------------------------	---------	--	-------	--------------------	-----------------

3.7 Chapter summary

This chapter presented phantom types and the rationale for the construction of phantoms in dose optimisation studies. The chapter showed that phantoms can be developed in many different forms, either as computer algorithms or a physical phantoms. Physical phantoms can vary in design from very simplistic, i.e. water phantoms to sophisticated phantoms, i.e. anthropomorphic phantoms. It was shown in the presented literature that criteria for selecting tissue substitutes vary with the beam energy and that soft tissues/organs in the pelvis are of similar X-ray characteristics. Simulating the pelvis for conventional radiography examinations can be done using cortical bone and soft tissue equivalent materials. The availability of tissue equivalent materials has shown a range of preparation difficulties. They can be low cost and available, such as water, or more complicated in their preparation technique, such as resin based materials. Reviewing the literature has shown multiple functions of X-ray phantoms, and they can be used as test objects, or for dosimetry and imaging purposes. Each phantom type has shown its reliability for the purpose it was constructed for, but implementing them into another kind of study (like dose optimisation) is not always possible, especially when considering anatomical visibility.

Chapter Four: Phantom Construction and Validation

4.1 Overview

In this chapter, the methods used in the construction of the phantoms and the materials used for this are described. The chapter begins by reviewing possible phantom construction methods, along with their associated advantages and disadvantages. Following this the details of the actual phantom construction method is then reported. This includes a detailed explanation as to the approach used to mimic the precise geometry of the bony pelvis. Within this chapter, a description and evaluation of two phantom prototypes are discussed; the first one is described together with its materials and the design approach used, and the subsequent limitations. The second prototype is described with enhancements borne out of the first prototype; these include new materials and a modified design. Prototype 2 is the phantom used in the experimental part of this thesis and as such a detailed evaluation of it will be presented in this chapter.

Following this, the method for the validation of the tissue substitutes is explained. Next, the three methods used to validate the phantoms are presented. The methods included measuring the density obtained from CT scans, X-ray pixel value measurements (SNR) and an assessment of face validity utilising Cronbach's alpha coefficient to estimate whether the phantom produced X-ray images which were representative of a paediatric pelvis. In this chapter, each evaluation method is introduced together with the relevant literature in order to provide sufficient background for this work. The approach to statistical testing is also outlined within this chapter.

Following an explanation of the phantom evaluation methods, the results from each of the three [validation] methods are presented. This included the results of determining the plaster / water mixing ratios used in the simulation of bone for each paediatric age. Within the validation results, the results from the CT density calculation experiments are presented first. A comparison of the CT density (HU) for each phantom against its respective reference patient data is presented. The second element of the results is from the pixel value validation experiment. In this method, each phantom was compared with a commercially available adult anthropomorphic pelvis phantom by measuring SNR over a range of exposure factors (kVp and mAs). The final [validation] results that are presented are from the face validity experiment. The results from this approach evaluated human perception of the pelvis X-ray images resulting from the phantoms and how valid they are for the visual evaluation of image quality.

After this the results from the phantom validation work are presented. Within this section there is a discussion which explains the literature basis for each validation approach. The results were critically analysed in terms of the limitations and possible implications for phantom use in optimisation studies. The over-arching possibility of undertaking optimisation studies using these phantoms is discussed. Firstly, in terms of X-ray interactions and how each phantom can simulate imaging of the human body. Secondly, in terms of SNR results regarding the degree of correlation between the phantoms used in this thesis and a commercially available phantom. This would reflect their applicability for use in dose optimisation studies using physical IQ measurements over various exposure factors. Lastly, the results from the face validity experiments are discussed, including a discussion on whether the resultant X-rays are deemed a suitable replication of clinical paediatric pelvis X-ray images.

Conclusions are then made based on the results, especially those of the CT scans which showed that the phantoms are capable of mimicking the radiological properties of the human body. The results from the pixel value validation led to a conclusion that the phantoms have a valid response to various exposure parameters in terms of SNR when undertaking conventional DR. One further conclusion is made from the face validity data, wherein experimental data showed a valid performance of each phantom for replicating paediatric pelvis X-ray imaging and for allowing the assessment of visual IQ.

The last two sections within this chapter discuss the limitations of the phantoms and future work. In the limitations section, an explanation is offered on how the phantoms can be used in IQ / dose optimisation studies. Furthermore, phantom limitations are discussed in relation to potential future studies. The last section, 'Further Considerations', was included in this chapter to explain possible future directions for '*in-house*', locally produced phantoms for medical imaging research.

4.2 Phantom construction: materials and methods

The construction process for creating a pelvis phantom is neither straightforward nor clear when first considered. Many ideas and options need to be investigated before the construction process commences. Many mistakes can be made during the manufacturing process of the first prototype, and accordingly, many lessons have been learned which were of benefit for the second manufactured phantom. Within this thesis the construction process, along with many of the difficulties which arose along the way, will now be discussed.

4.2.1 Constructional approaches

3D Printing

The design of a human anthropomorphic phantom is a sophisticated process; this is due to the difficulties in moulding the tissue substitutes into anatomically representative components. Several methods were considered within this doctoral thesis, for example, the formation of bone tissue substitutes to replicate the bones of the pelvis using a three-dimensional (3D) printer. This approach generated a number of advantages and disadvantages which include the ability to precisely replicate complex anatomical components. A lack of access to 3D printing filaments which were density matched for tissue equivalence meant that this was not a realistic possibility. As a result, materials that mimic the human bone were not, at the time, available with this technology although it is accepted that this is likely to change in the future. Further difficulties exist with 3D printing technology. There are issues with the maximum size of the printed models and the resolution/level of detail is not necessarily adequately accurate for areas in which high definition is required. Due to these limitations, there is a very limited number of anthropomorphic phantoms either available or currently under development for studies using X-ray imaging. (Anderson et al., 2014; Bliznakova, 2016; Palareti et al., 2016).

Three dimensional (3D) printing, known as additive manufacturing (AM), is defined as a method of constructing objects by increments or layer-by-layer. In modern life, this technology has been presented as effective method for manufacturing complex parts. Machines using such technology are presently able to create objects made from polymers, metals and ceramics (Ceh et al., 2017; Wimpenny, Pandey, & Kumar, 2017). Developing 3D printed models offers a relatively cheap and convenient substitute to relying on cadavers for educational and training purposes (Ceh et al., 2017).

Practically, all medical applications of 3D printing processes fall into five sequential stages regardless to the class of application (Tuomi et al., 2014):

1- Medical Imaging and Three-Dimensional Digitising

Different imaging modalities have been used for constructing medical models, including CT imaging, however, ultrasound and magnetic resonance is also used (Bibb & Winder, 2010).

2- 3D Modelling

This stage transforms (a series of 2D images, such as DICOM) anatomical slices data into 3D file in STL format, necessary adjustments need to be considered such as removing imaging artefacts or unnecessary tissue (Cabibihan, 2011).

3- Additive Manufacturing

It is about the production of the precise physical model of the patient or the mimicked anatomy. Each medical application requires specific criteria in the materials, such as the radiation characteristics for medical imaging applications, used in the AM technology (Tuomi et al., 2014).

The design, material, and production requirements for the manufactured part need to be fully compatible before starting the AM stage. More important, this stage can be restricted for material or dimensional requirements, which the 3D printers must be able to meet (Tuomi et al., 2014).

Despite the fact that AM machines operate automatically, a degree of specialist expertise is required for running them such as to set the parameters for the 3D printers process and post process (Salmi, 2013).

4-Finishing

After AM stage, the manufactured part may require finishing phase, which can be washing, polishing, coating or sterilisation (Tuomi et al., 2014).

5-Clinical Application

The ultimate goal of medical 3D printing is the use in clinical application. A framework of full medical procedures describing the use of 3D printed parts is required.

Notably, errors can exist in the anatomical models if process issues occur between collecting the imaging data and transforming it into a printable form. Thus, careful tests must be considered regarding quality control standards, communication, and measurements of the constructed model in order to ensure the anatomical accuracy (Ceh et al., 2017; Salmi, 2013).

Despite the significant clinical opportunities, technical challenges exist in 3D printing technology and must be overcome in order to enable using the method in manufacturing radiation dosimetry phantoms (Leary et al., 2015). Such technical limitations are:

1. Resolution errors: 3D printing models are typically constructed using a sequential, layer-by-layer, approach. Such discrete manufacturing strategy inherently leads to resolution errors (Leary, Babae, Brandt, & Subic, 2013; Leary et al., 2015).
2. Mechanical properties: the mechanical properties of AM components might be compromised when using the layer-by-layer approach (Ahn, Montero, Odell, Roundy, & Wright, 2002). In addition, AM approach might cause porosity, such air entrapped

materials can influence the imaging characteristics of the 3D printed phantom (Leary et al., 2015).

3. Availability: There are limited availability of materials, design methods, and processing data within the 3D printing field that are related to the relative modernity and complexity of AM approaches particularly in the radiological applications (Doubrovski, Verlinden, & Geraedts, 2011; Leary et al., 2015).
4. Economical low-batch production: The AM approach requires significant automation in order to reduce the specially the need for specialists in AM technology (Leary et al., 2015).

Laser cutting

Laser cutting technology can provide smooth and accurate cutting for a variety of materials including PMMA, when using a CO₂ laser (Atiyah, Powell, Petring, Stoyanov, & Voisey, 2018; Choudhury & Shirley, 2010). Such a technology could be also an option for cutting the PMMA sheets used in the construction of pelvis phantoms, however, there were concerns about the total cost of acquiring such a system. In addition, there was uncertainty about the ability and utility of such technology in making a cut on an incline as can be undertaken when using a hand held cutting machine. Cutting with an inclination is required in the PMMA sheets in order to avoid deformation in the shape of the bone structures, see figure (the figure that shows the incline cut within the phantoms). The cost of laser cutting typically depends on the cutting time, labour (unloading and verifying the pieces) and the risks involved (emission of toxic gases: larger sizes are more risky). The type of materials and their thicknesses determine the cutting time and the risk associated with cutting them using laser beam (Chen, Shen, & Zhou, 2016; Wits, Carmignato, Zanini, & Vaneker, 2016). For Perspex sheet, cutting a 3 mm thick slab starts from \$0.15 per inch³ with \$25 minimum order per material type. While other manufacturers are asking for a minimum £150 (+VAT) payment⁴ (this dedicated for relatively large sizes). The calculations of the cost for cutting each PMMA slice within each phantom vary due to the variations in the geometry of bone structures in pelvis.

3D milling

A further option for consideration was a 3D milling technique. In this process, blocks of PMMA can be manufactured into individual [bony] shapes/components and then assembled. Some practical issues could have a negative effect on the process, such as the thickness in which the drill can work and the flexibility or the angle of the drill when forming complex shapes. The

³ <https://www.pololu.com/docs/0J24/2>

⁴ <https://www.cut-tec.co.uk/quote/>

availability of a 3D milling machine and the technical expertise needed to operate such as system were also reasons for opting for an alternative approach.

4.2.2 Method for the first manufactured phantom (Prototype 1)

The pelvic area of the human body has a complicated geometry of bony components, such as the iliac crest, pubis, sacrum and the femur. Each component is shaped in a way where its thickness varies along with its dimensions. To simulate each bony component accurately the clinical (anatomical) characteristics of the image must be considered, as a result, the inherent geometry of a phantom should be shaped similarly to those components or anatomies within human body.

The manufacturing method for the Prototype 1 phantom is outlined as follows. A simplistic method to construct a radiographic imaging phantom was used to build it from axial slices, based on CT data. This method has been used successfully for dosimetry phantoms (A. Jones, 2006), but for imaging phantoms it would produce axial black lines which would result from the air-gap between sections (Chan & Fung, 2015; Mraity, 2015). In order to overcome this problem, the phantom was constructed from coronal slices, as used by Harrison et al. (2011). These, theoretically, would not show these shadows (K. Harrison et al., 2011). In the first model (Prototype 1), CT data from a 4-year-old child was taken from an anonymous imaging archive. As mentioned in the literature, CT data from a patient provides a realistic reproduction of patient anatomy and its measurements provide accurate dimensions for typical anatomy (K. Harrison et al., 2011). Also, the body trunk dimensions, including length, width and height, were taken from CT measurements.

The design was carried out by taking templates from the CT data from coronal (reformatted) images and cutting them from PMMA slabs using a handheld milling tool. The CT slices were 2 mm thick in order to maintain anatomical detail as thicker slices would produce a less representative shape of the human pelvis bone. The slices were chosen to be manufactured out of PMMA, as it is reported in literature to be a suitable soft tissue substitute (Aichinger et al., 2012; Hubbell, 1995; International Commission on Radiation Units and Measurements (ICRU), 1989). The slices were marked, aligned, and then drilled so that they had a reproducible shape within the pelvis phantom. Figure (4.1) shows how the slices were lined up to make the pelvic shape of the phantom. The same shapes from the CT coronal images were drawn on PVC to represent cortical bone equivalent material, as was reported in ICRU report 44 (International Commission on Radiation Units and Measurements (ICRU), 1989). The PVC sheets of 2 mm

thickness were cut out to be filled inside their corresponding slices of PMMA. This method included some drawbacks as there are some ‘air gaps’ between the two tissue substitutes and also there were sharp edges between all the slices that limited the accuracy of the anatomical geometry. This resulted in some black lines appearing in the X-ray image of Prototype 1 phantom, due to the sharp interface between the PVC and the PMMA as well as the air gaps between the two tissue substitutes (Figure 4.2). Thus, the construction method for phantom was not sufficient to achieve the objectives of this thesis. Therefore, a modified method (Prototype 2) was considered to improve the resultant X-ray image, as described in the next section.



Figure 4.1: An illustration of the PMMA sections used to form the first prototype phantom. Within each slice, shapes have been removed (using a milling machine) from which PVC (bone) shapes would be inserted.

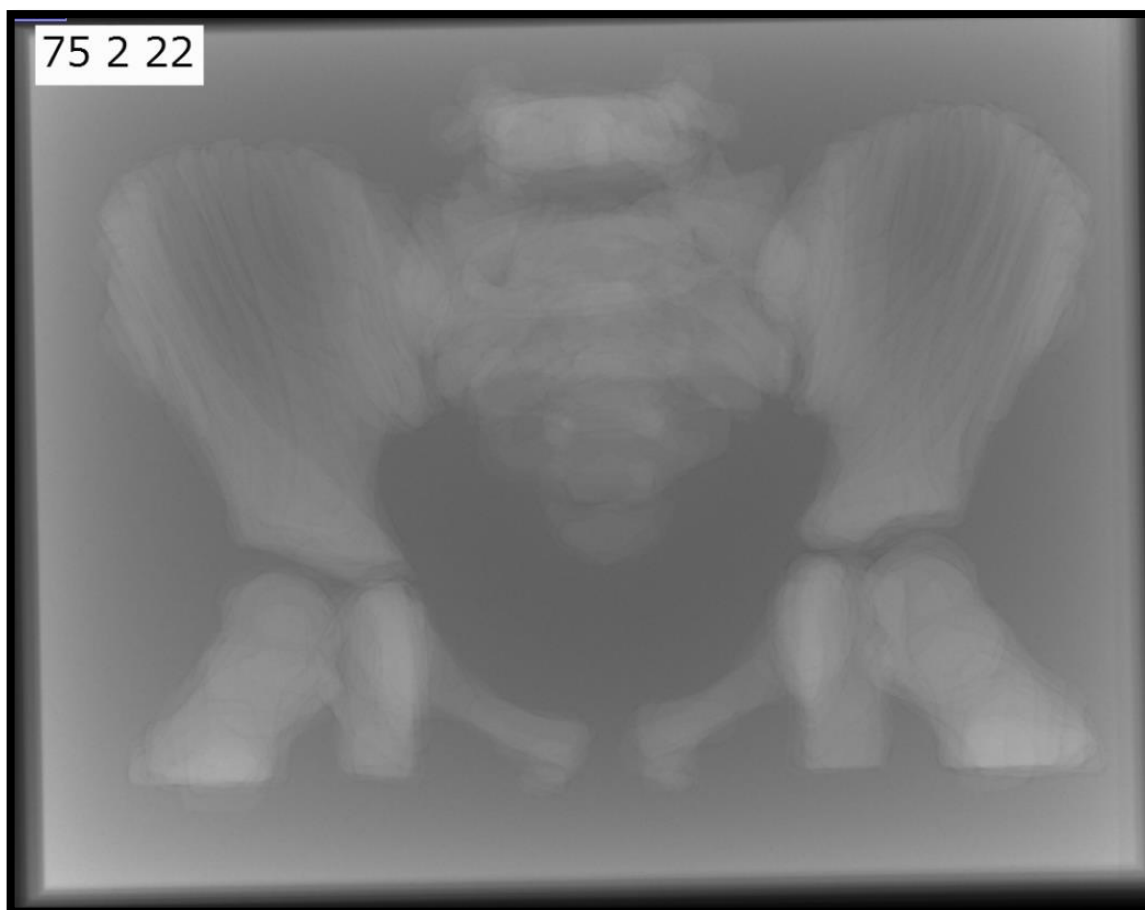


Figure 4.2: An X-ray image of the first prototype pelvis phantom (representing a 4-year-old). Black lines over the bony regions, part of the construction process, were considered technically unacceptable.

4.2.3 Modified method for manufacturing the phantoms (Prototype 2)

The second generation was the Prototype 2 phantom, which was the final attempt and considered as an acceptable/final modified phantom form to be used for the manufacturing purpose. The aim in this thesis was to undertake dose optimisation for pelvis radiography across a range of paediatric ages. Accordingly, there is a need to consider the variation in paediatric size as follows:

Patient size has high impact on calculations of radiation dose delivered to patients during diagnostic examinations. In addition, it has a confounding impact on the evaluation of radiation doses and image quality (Morrison et al., 2011; Seibert & Morin, 2011). Paediatric size has large variations across the new-born to 15 years age range. Thus, it is impractical to choose one size as a single reference size. As a result, age ranges have been grouped as 0, 1, 5, 10, 15 years, so that the comparison of doses between these age groups is practicable (Hart & Wall, 2001). Also, it was found that within each age group there are variations in the dimension of internal organs by up to 15% (Varchena, 2002). The age group differences, beside the limitation of the

available study time within a doctoral thesis, led to the choice of the three manufactured phantoms of corresponding ages of 1, 5 and 10 years, which covers a significant paediatric age size range. 15 year-olds are close to adult size and were not studied since there are already commercially available adult phantoms (Butler & Brennan, 2009).

Prototype 1 phantom was developed from a CT scan from a 4-year-old child, however the intended construction of phantoms were to represent children of ages 1, 5 and 10 years old. Accordingly, CT data were taken from a CT manufacturer's educational archive of ages corresponding to the proposed ages of the three phantoms for this thesis. The body trunk dimensions including length, width and height were taken from CT measurements of a 5 year-old.

Using the computer software, RadiAnt DICOM viewer (Medixant, Poznan, Poland), coronal CT images were reconstructed with a slice thickness of 0.5 mm. As the thickness of the PMMA⁵ (International Commission on Radiation Units and Measurements (ICRU), 1989) slabs is 2 mm, 1 image was taken from each group of 4 coronal images in order to match the coronal anatomical distance inside the patient with the phantom, see Figure (4.3). The construction of the phantoms started with converting the DICOM CT images into a printable format image and calibrating their dimensions to realistic measurements in millimetre length units. These images were aligned and then anatomical outlines were drawn onto PMMA slabs.

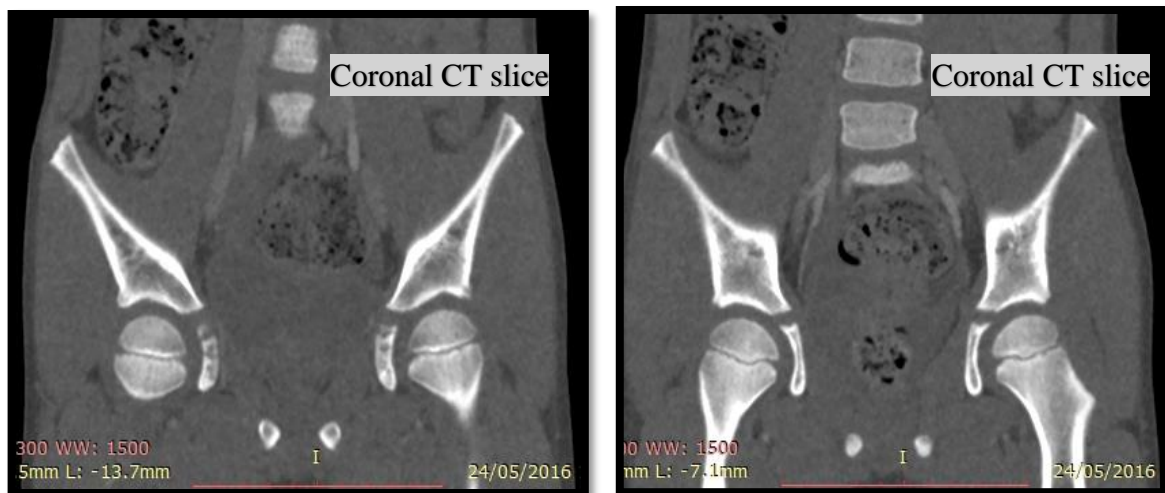


Figure 4.3: Coronal CT slices used to mimic the bony anatomies in pelvis.

Following the line artefacts which appeared on the Prototype 1 phantom X-ray image, some modifications were needed to eliminate these black lines and improve the anatomical shape. A

⁵ <http://www.performance-plastics.co.uk/product/classification/acrylic-pmma>

realistic option for the phantom design modification would have been to find mouldable cortical bone tissue substitutes since the PVC was a solid material. However, heating PVC would give off toxic gases, and can also risk changing its chemical formula. A mouldable bone equivalent material can fill all complicated cavities that form the bony pelvic shape, hence better anatomical shape and smooth edges can be provided for the new phantom. After examining the literature to find alternatives for PVC as a cortical bone substitute, Plaster of Paris (PoP) was reported in ICRU 44 (International Commission on Radiation Units and Measurements (ICRU), 1989; V. P. Singh, Badiger, & Kucuk, 2014). It has been used in the literature for the imaging of paediatric distal extremities (Knight, 2014) and the construction of body contours (Goitein, 1982). The problem with this substitute is that its density is not exactly the same as paediatric cortical bone (White, 1974). This is a potential source of error and could disqualify the selection requirements for phantom materials mentioned previously. However, it was found on a casting website ⁶ (MARAGON- ARTS & CRAEFTS) that different mixing ratios of the plaster with water resulted in different densities of the plaster. This was tested using CT scans and was then used to match the density of the plaster to the attenuation characteristics similar to that of the cortical bone from the CT data. This process has been explained in the following validation subsection, 4.3.1.2.

Cutting of the 2 mm thick PMMA slices was undertaken using a number of different steps: 1) removing the shape of the bone with a hand milling machine from each slice in turn, 2) smoothing the edges by combining different contiguous slices with a smoothing tip on the milling machine and 3) sanding the edges with glass paper. Cutting the PMMA slabs connects each slab edge with its adjacent slabs. From previous experience, this is important for providing an accurate anatomical shape with smoothed edges, as the PMMA slices will now play the role of a plaster mould and form the anatomical bone shapes (Figure 4.4). The aim of these modifications was to produce a deformation free (no black lines as appeared in Prototype 1) X-ray image. Thus, the X-ray images would then be appropriate for visual evaluations (Figure 4.9). Also, all of the PMMA slices were marked from a common central point so that they could be lined up to form a full pelvic bony shape. They were then drilled and supported with compression plastic screws (at four corners).

⁶ <http://www.maragon.co.uk/plaster-guide.html>



(b)



(b)

Figure 4.4: (a) and (b), connected and smoothed edges of second prototype / final phantom design.

The next steps describe the preparation for the Plaster of Paris (PoP) prefilling process, firstly, by selecting an appropriate group of slices (as many as possible) in one block. The perfect solution is to fill liquid PoP in all the slices together, however, the complicated geometry of the pelvic bony anatomies would not allow this because some of the voids were small and had complex joining angles preventing the easy flow of PoP and the elimination of air. Therefore, the number of slices included in each block was dependant on the geometry and the ability to fill all the cavities with liquid PoP. As many different shaped cavities existed in the coronal plane, this resulted in different block thicknesses, each with a different number of slices. For the final phantom, each contained 5-9 blocks forming the shape of the full phantom and were ready for the liquid PoP (Figure 4.5). All of the blocks were tightened to make sure that the filler (plaster) did not spread laterally between contiguous slices. The second step was carried out using a weighing scale with an accuracy of ± 0.0001 grams, then weighting the proportions of water and the PoP powder ratios 32, 30 and 29 g of water and 50 g of PoP for each phantom of the corresponding ages- 1, 5 and 10, respectively, see Figure (4.6). This mixing ratios method is explained in the CT validation method (subsection 4.3.1.2). Following this, the mixing of water with PoP powder was ready to be carried out.



Figure 4.5: PMMA slices are ready for PoP filling.



Figure 4.6: The scale used to weigh the plaster powder (on the left) and the water (on the right).

The filling procedure for the PMMA slices included mixing the PoP powder with water and stirring the mixture for a few minutes to make sure that the mixture had no air bubbles and was at a proper moulding viscosity. The viscosity will change with time until the plaster becomes solid. Next, the cavities were filled with the liquid plaster mix and which was squeezed into each cavity ensuring a thorough fill. After filling the cavities of each block, the plaster surfaces were flattened for each PMMA block by wiping the plaster surface right after it had solidified (Figure 4.7). This was to make sure that the assembly of all the blocks were flat and fitted together adequately, see Figure (4.8). The X-ray images of each of the three phantoms are presented in Figure (4.9).

In addition to the insertion of a cortical bone substitute, a trabecular pattern was included in the phantoms via the inclusion of animal bones- Figure (4.9). A chicken bone was inserted in the phantoms for the ages 1 and 5 years to represent the trabecular and cortex bone; it was placed next to the L4 vertebral body as it would not be affected by scatter radiation produced by the iliac crest. The chicken bone has been previously used in literature to simulate parts of the human body such as a foot (Sheridan & McNulty, 2016). A lamb bone was inserted in the 10 year-old phantom to correspond with the higher bone density of 10 year-old (ICRP, 2002).

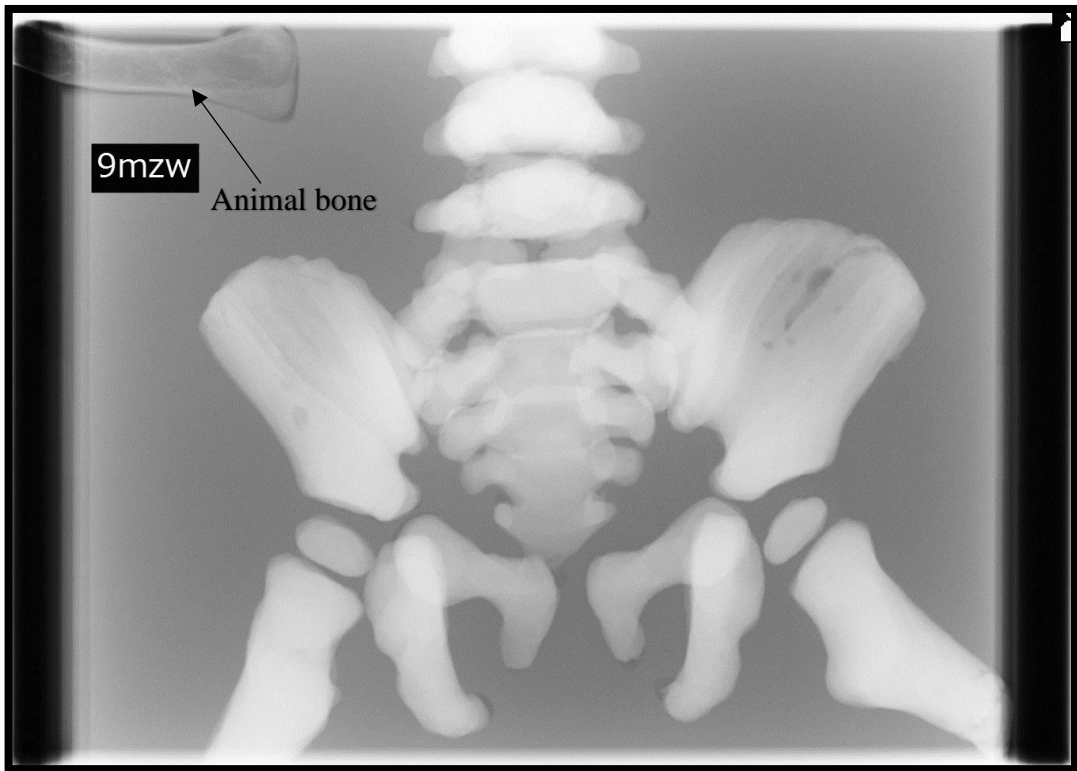
Animal bones, including those from animals like lambs, rabbits, and monkeys, have been mentioned and used in the literature to simulate X-ray imaging for paediatrics (J. Hansson et al., 2005; Hart, Wall, & Shrimpton, 2000; Ludwig, Ahlers, Wormanns, et al., 2003; H. Precht et al., 2012).



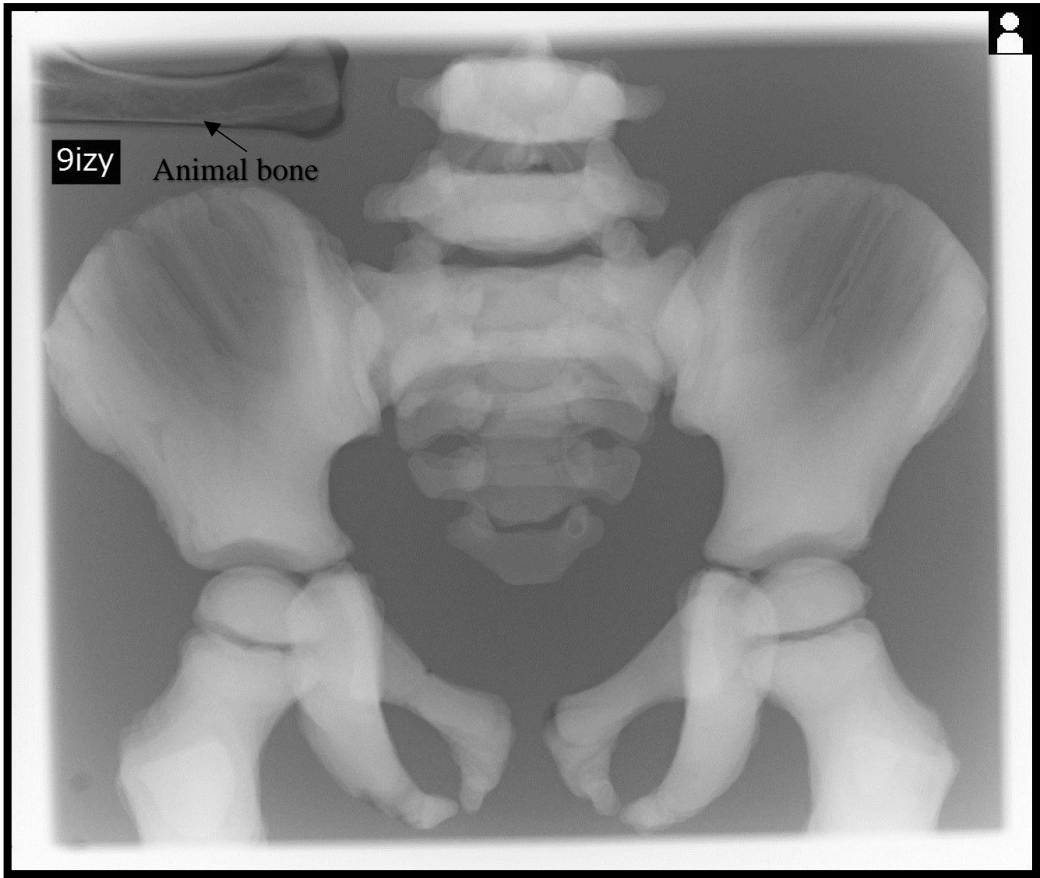
Figure 4.7: PMMA block filled with PoP and flattened to the PMMA surface.



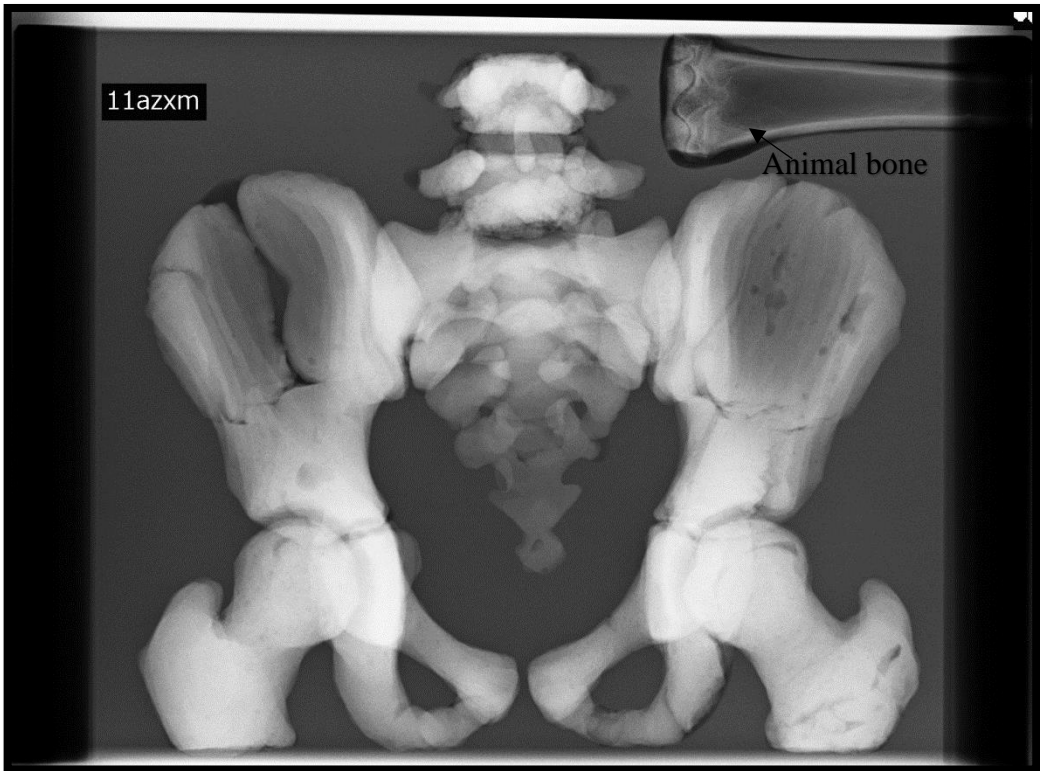
Figure 4.8: All of the PMMA slices assembled together.



(a)



(b)



(c)

Figure 4.9: (a), (b) and (c) are X-ray images of the 1, 5 and 10 year old phantoms, respectively.

4.3 Phantom validation methods

The phantoms should fulfil the purpose they were designed for and the testing of such is a process called *validation*. Within this thesis the research aim that the phantoms must be capable of facilitating is to allow the investigation of the impact of different acquisition parameters on image quality for different paediatric patient sizes, for pelvic radiography using DR. Ultimately, the phantoms should provide a method for dose optimisation for the corresponding paediatric ages. As these phantoms are designed for diagnostic X-ray imaging, they need to be tested to see whether the phantom is able to provide a valid and reliable object ('pelvis phantom') for use within a method for assessing image quality responses and dose optimisation based on X-ray interactions within the diagnostic energy range (i.e. 50-100 KeV). The validation procedure was performed in three stages, namely, CT density assessment, X-ray DR pixel value assessment and face validation.

4.3.1 CT validation: Method

4.3.1.1 Background

Computed tomography (CT) employs multiple X-ray projections to build a cross-sectional image of the body that shows a 2D map of the X-ray attenuation coefficients of the body tissue. The attenuation coefficients are saved as CT numbers (as pixel/voxel values) which represent the X-ray attenuation relative to water. See equation (4.1) below;

$$CT = \frac{\mu - \mu_{water}}{\mu_{water}} K \dots\dots\dots (4.1)$$

Where μ is the linear attenuation coefficient and K is a scaling constant.

When $K = 1000$ the CT numbers are Hounsfield Units (HU) (Bourne, 2010).

Some researchers have developed a method for the optimisation of the composition of phantom materials for diagnostic radiology using CT Hounsfield units (Homolka et al., 2002). Their work shows how robust this modality is for measuring the radiological characteristics of materials. Also, these methods have been used in the literature for tissue substitute validation by calculating the linear attenuation coefficient of X-ray photons from the CT density (HU) of CT scans (K. Harrison et al., 2011; Homolka & Nowotny, 2002).

The CT density for water = 0 HU; air = -1000 HU; adipose tissue is between -190 and -30 HU; and skeletal muscle is 30-100 HU. The tissue area (cm²) for the different tissues on each

cross-sectional CT image can be calculated by either manual or computerized segmentation (Mattsson & Thomas, 2006).

CT X-ray attenuation depends on the elemental tissue density, tissue composition, and photon energy. The photon spectrum presented in the voxel depends predominantly on the X-ray spectrum, which depends on tube voltage, voltage anode angle and ripple, however other parameters might also affect the spectrum such as patient size, additional filtration, bone in the cross-section and the distribution of organs. There are substantial differences in CT scanner design and beam filtration across the different manufacturers and models (Homolka et al., 2002). However, it is widely reported that CT machines are calibrated to one uniform material (water) (Zarb et al., 2010). This can cause all the above mentioned parameters to be of limited effect on CT HU value variation when comparing between two or more machines.

4.3.1.2 CT Density: Method

The validation method of the three phantoms using CT density included comparing the HU measurements from each phantom with its correspondingly aged patient CT data, which were previously used as templates in the phantom construction process. The CT scan parameters were chosen to be as close as possible to the parameters of the real patient CT data. Phantoms image acquisition was undertaken on a Toshiba Acquillion 16 CT scanner. The scan parameters were 80 kVp, 100 mAs, a detector configuration of 1 X 16 mm, a rotation time of 0.5 seconds, an image thickness of 1 mm and a reconstruction interval of 1 mm.

The clinical CT data from the 1, 5 and 10 year-old patients included 303, 525 and 549 images, respectively, for the abdominal-pelvic region, each with a thickness 0.625 mm. CT data acquisitions were undertaken using a GE Medical Systems scanner, the Revolution CT, in a helical scan mode with image dimensions of 521 by 512 with pixel spacing of 0.578828\0.578828. The exposure factors were 80 kVp with automatic mA modulation ((125: 122-138), (100: 86-105) and (130: 124-137) over the pelvic area of 1, 5 and 10 year-old datasets, respectively).

The PoP was used to simulate the cortical bone within the phantoms. Before making the choice for the PoP, a series of tests were carried out to make sure that the PoP had similar attenuation characteristics to the cortical bone using the CT data from the 1, 5 and 10 year-old children. This was achieved by finding the correct weight-mixing ratio between the PoP powder and water. In order to identify the correct mix, five different weight-mixing ratios were prepared: 30/50, 34/50, 38/50 and 42/50 (water/PoP). The same exposure parameters, with the PoP casted

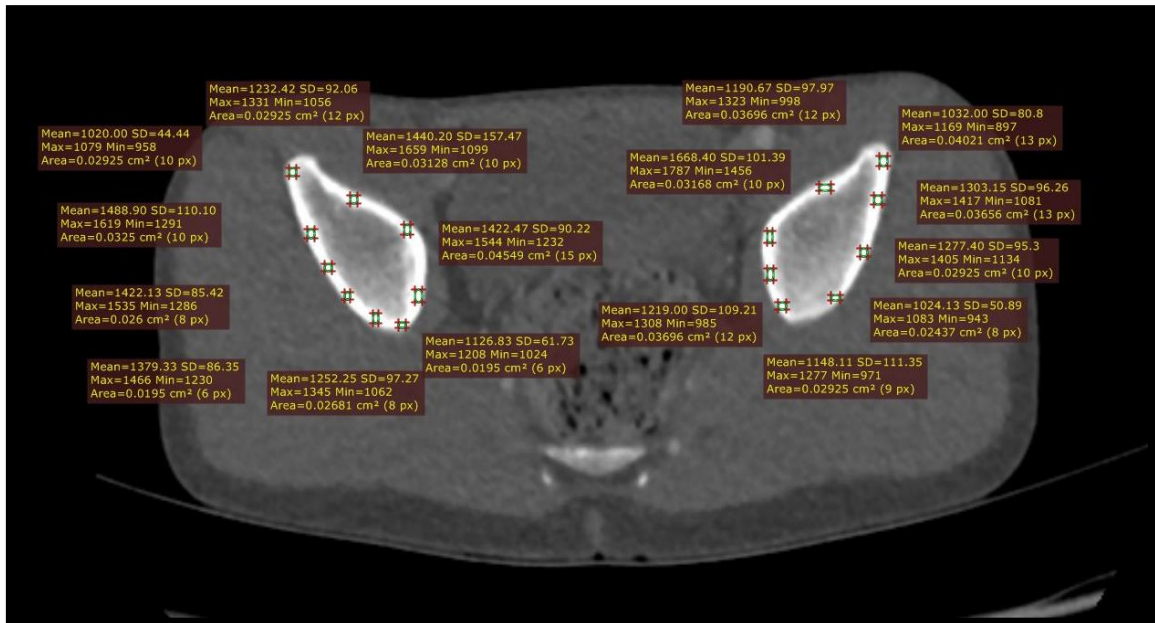
in disposable plastic cups (see Figure (4.10)), were used in scanning the completed phantom as they all were the closest possible to the real patient exposure parameters. In both tests the paediatric pelvis protocol was chosen for the CT scans.

For each mixing ratio, three samples were made (per mix) to examine the repeatability of the production method, as seen in Figure (4.10). The region of interest measurements were taken over four locations along the Z-axis of each sample volume to insure uniform measurements for the samples. Each mix was prepared by placing the PoP powder and water into disposable cups and weighting them, separately, using a scale with a 0.001g error. Following this they were then mixed together and allowed to dry. After 3 days, scheduled CT scans were carried out to identify the time at which the PoP mix had a constant and stable density. The goal was to find the correct mixing-ratio for a cortical bone substitute and the time it takes to dry/stabilise.

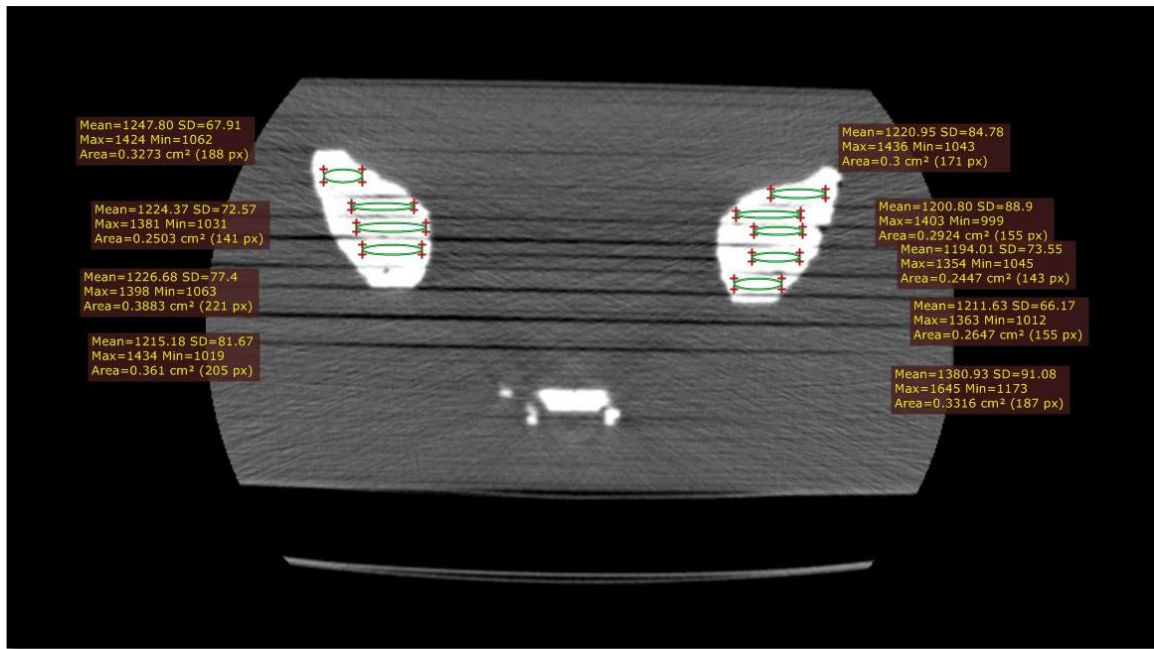
The second step was scanning the completed 1, 5 and 10 year-old phantoms, similarly to the PoP samples. Scanning was repeated over time to make sure the PoP had fully dried and reached constant density. From each of the CT scans, the density using CT HU values was measured over different bony landmarks (Figure 4.11). Following this, the data from the X-ray acquisitions for the optimisation study were started and all of the X-ray images were taken for the optimisation study. This was the primary reason for constructing the phantoms. These measurements were undertaken with the same computer software (RadiAnt DICOM viewer). Figure (4.11) provides examples of these measurements. All the data acquired with this software represents the average of the mean HU (SD) from each of the points measured. In addition, measurements from the animal bones were included in order to examine their tissue X-ray simulation in the phantoms.



Figure 4.10: Samples of PoP during CT testing experiments.



(a)



(b)

Figure 4.11: Comparative measurements of bony anatomies (a) inside the patient, (b) inside the phantom (using CT windowing for bone).

4.3.1.3 CT Density: homogeneity test

It is well known that CT numbers represent X-ray attenuation characteristics of respective materials, and are related to the density of the tissue or its substitute (Homolka & Nowotny, 2002). The lower the density of the material, the lower the measured HU will be from a CT scan. Hence, this is an accepted method used in literature to identify the density and compositions of tissues (Homolka & Nowotny, 2002; Mattsson & Thomas, 2006).

The standard deviation (SD) from the CT based region of interests can be used as an indication of the homogeneity of materials when compared to a valid tissue substitute (Homolka & Nowotny, 2002). This can be performed by looking into the SD (min-max), the PoP/animal bone, and the PMMA and comparing them to cortical bone and soft tissue, respectively. Mean (HU) values were calculated for the PoP using the RadiAnt DICOM viewer software. The minimum and maximum SD values were found to be 50.24 to 135.5 HU. For the cortical bone (from the clinical CT scans) the minimum and maximum SDs were 24.81 and 278.65 HU, respectively. Thus, from the SD (min-max) values, it appears that there is no substantial heterogeneity of the bone substitutes used. The literature already reports a wide range of HU values for the soft tissues, including the fat and muscle (Mattsson & Thomas, 2006), and as such demonstrates natural heterogeneities which occur in the human body.

4.3.1.4 CT: Geometry simulation

CT scanning can be used to compare the dimensions of the phantom against the patient-based CT dataset. In the literature, CT data can be used to generate templates for phantoms with high precision as well as generating templates for the three dimensional (3D) construction of human inherent parts (K. Harrison et al., 2011). Similarly, from each phantom CT dataset, a 3D bony shape, using RadiAnt DICOM viewer, was constructed. Each has noticeable geometry matched with the 3D reconstruction of a corresponding real patient, as seen Figure (4.12) below:

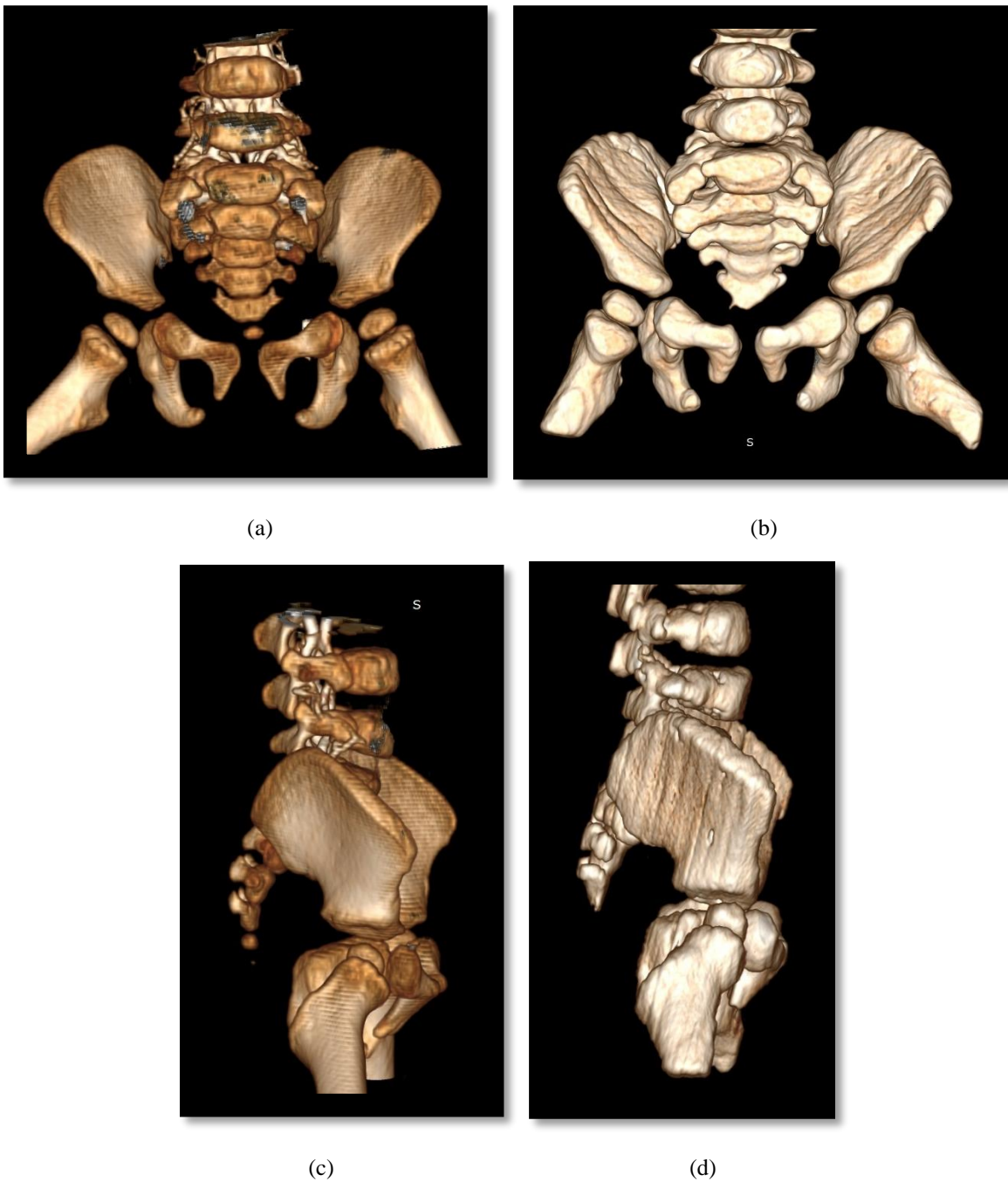
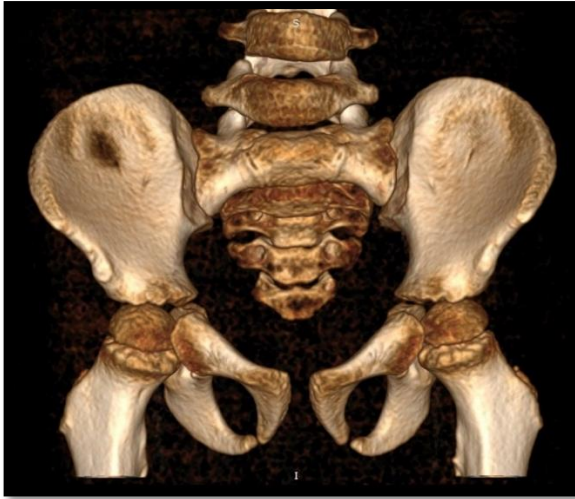


Figure 4.12: for the 1 year old: (a) & (b) frontal view of the patient and the phantom, respectively.



(a)



(b)



(c)



(d)

Figure 4.13: for the 5-year-old: (a) & (b) frontal view of the patient and the phantom, respectively.

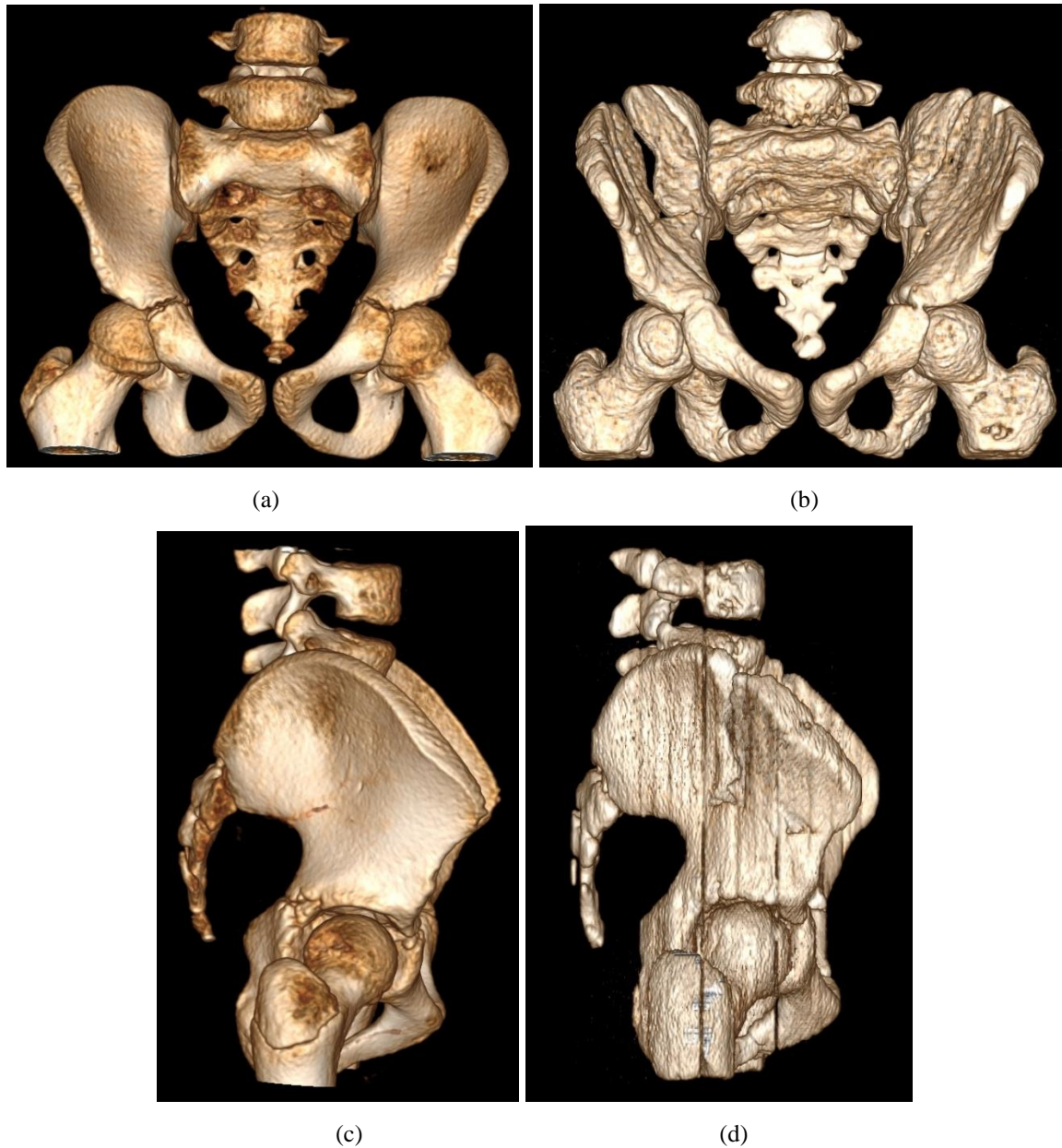


Figure 4.14: For the 10-year-old: (a) & (b) frontal view of the real patient and the phantom, respectively. (c) & (d) lateral view of the patient and the phantom, respectively.

4.3.2 X-ray pixel value validity: method

This method consists of comparing the pixel values of the images from each phantom with commercially available and *valid* phantoms. Pixel values were represented by the SNR measurements. As discussed previously (in chapter two / subsection 2.2.5.2), the pixel value is the elemental component of a digital image. In DR, each pixel value represents a level of brightness related to the attenuation of X-rays that pass through the corresponding body part and form the X-ray image (Fauber, 2013). The SNR includes the signal representing the desirable information of subject contrast within an X-ray image. Noise is generated from the random scattering of X-rays, random electrical static and other disinformation within the image

(Carroll, 2011). Thus, SNR is an X-ray attenuation metric which can be used when comparing between images generated from different exposure settings.

Comparisons between each of the phantoms used in this thesis and the commercially available phantom were carried out by exposing them to a similar range of X-ray acquisitions (with variation in kVp and mAs, whilst keeping the other exposure factors constant). Next, the total SNR value from each exposure for each phantom was compared with the commercial phantom. The comparison was made using SNR as it represents a key aspect of image quality (Neitzel, 1992). In comparison to CNR, it can be seen from equation (2.1) that CNR scales signal difference (between the anatomy and background) with noise, unlike SNR which represents signal and noise equally. This is useful for comparing the amount of signal and noise between the two phantoms.

All image acquisitions were carried out in the Medical Imaging Laboratory within the Radiography Directorate at the University of Salford. The X-ray tube used in this study was a Wolverson Arcoma Arco Ceil general radiography system (Arcoma, Annavägen, Sweden), with a high frequency generator and a VARIAN 130 HS X-ray tube. The imaging system used for image acquisition was an Aero DR System (model CS-7; Aero DR System, Konica Minolta Medical Imaging, USA INC, Wayne, NJ). An adult anthropomorphic pelvis phantom (N1 “LUNGMAN”, Kyoto Kagaku Co., Ltd., Kyoto, Japan) was used as a reference phantom for the comparison against the new manufactured 1, 5 and 10 year-old pelvis phantoms (Figure 4.15).

The parameters set for comparing the SNR of the 1, 5 and 10 year-old phantoms with the adult phantom were as follows: the tube potential range used was 50 to 101 kVp with 3 kVp increments; the mAs range varied from 1 to 20, except for the 1 year-old phantom which was 1 to 16 mAs; the SID was fixed at 110 cm and no grid was used; the collimation was adjusted to the phantom area for the reference phantom (29 by 34 cm) and for the 1, 5 and 10 year old phantoms ((20 by 16 cm), (24 by 20 cm) and (30 by 26 cm)); and the image processing was set to a quality control test in order to avoid any manipulation in pixel values during the pre-processing algorithm of image quality.

The thicknesses of the phantoms were defined by measurements from the CT data and the equivalent thicknesses of the different childhood ages (Vano et al., 2008). However, in this comparison, the thickness for the phantoms used in this thesis was set at 21 cm, which was matched to the equivalent dose measured through the commercially available anthropomorphic

phantom. This was to reduce the difference from the thickness of the reference phantom and thus reduce the detector saturation or creep at high doses. The initial comparison was made for the 5 year-old phantom with the adult anthropomorphic phantom, using the thickness from CT measurements (12 cm). This comparison showed lower correlation compared to the correlation using dose equivalent thickness (21 cm). Thus, dose equivalent thickness was used (21 cm) for the three phantoms to reduce dose creep to the DR detector and to provide a fair comparison.

The estimation of the 21 cm thickness was undertaken by placing a solid-state dosimeter under the clear acrylic of the adult anthropomorphic phantom then measuring the dose over different tube potentials (50 to 100 kVp) with 5 kVp increments. Each exposure was repeated three times. With the constructed phantom, different thicknesses were added to match the doses over the range of tube potentials.

The thicknesses from the CT measurements of each child age were used for the dose optimisation studies. The thicknesses of each phantom age for optimisation purposes were taken from CT measurements. The CT measurements varied in thicknesses along the Z-axis of the patient. The variation in thicknesses ranged according to the thicknesses set by Vano et al. (2008) for paediatric AP pelvis examinations, where the AP pelvis equivalent thickness of PMMA for ages <1, 1-5, 6-10 and 11-15 year-old were 7.7, 12.3, 15 and 18.2 cm, respectively (Vano et al., 2008). These thicknesses, along with their ages, were entered into an Excel (Microsoft, Redmond, WA) worksheet. Thus, the thicknesses for the optimisation study were chosen close to the reference by extrapolating an equation of PMMA thicknesses (in cm), depending on the paediatric age (in years). The extrapolated equation (equation 4.2) is as follows. The equation fitting level has a coefficient of determination $R^2=1$.

$$y = 0.0033 x^3 - 0.088 x^2 + 1.2767 x + 7.7 \dots (4.2)$$

y represents the AP thickness of PMMA in cm and x represents the age in years.

Thus, the AP thicknesses used in the phantoms were 9, 12 and 15 cm for the ages 1, 5 and 10 year-old, respectively.

SNR measurements were taken from Regions of Interest (ROIs) - see Figure (4.16). The ImageJ software, version 1.49 (NIH, Maryland, US), was used in the SNR measurements. The ROIs measured on each phantom were from the background and the others were measured from the equivalent bony anatomies across the phantoms. This was done in order to measure similar

responses then calculate the total SNR and compare between each phantom and the commercially available adult anthropomorphic phantom.

The correlation coefficient (r) was measured as an indication of the similarity in the response of SNR measured from each constructed phantom when compared to the SNR measured from the adult anthropomorphic phantom. SPSS software, Version 21 (IBM Inc, Armonk, NY), was used in the statistical analysis. Before statistical analysis of the data (SNR measurements) could be performed, a normality test was done based on the Shapiro-Wilk (p values greater than 0.05 were considered to represent an approximately normal distribution) to determine the type of data acquired during the experiment. Accordingly, the Spearman's Rho correlation was chosen for data with non-normal distribution and the Pearson correlation for data with normal distribution (Field, 2013).

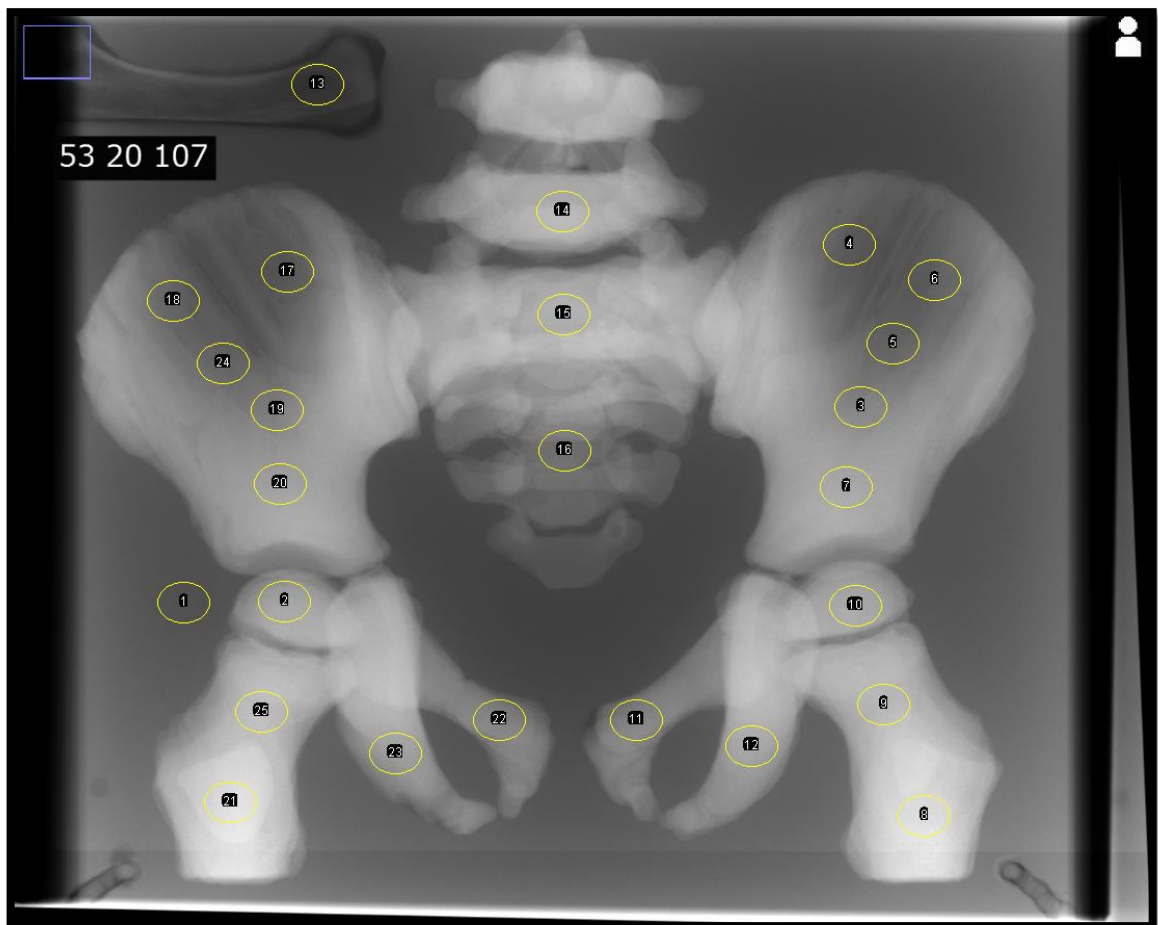


(a)

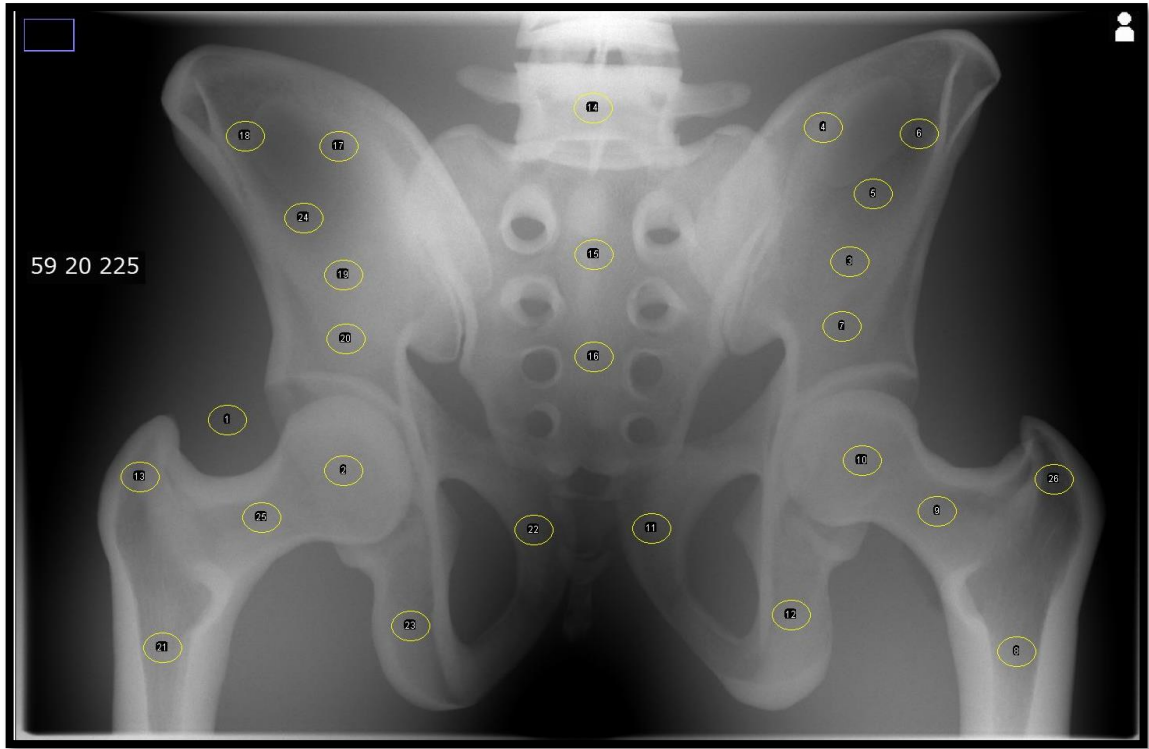


(b)

Figure 4.15: X-ray acquisition set-up for (a), one of the phantoms (5-year-old) and (b) reference phantoms.



(a)



(b)

Figure 4.16: SNR measurements; ROIs placed (a) on each of the constructed phantom X-ray images and (b) on the adult valid phantom X-ray image.

4.3.3 Face Validity: method

This approach includes using a psychometric scale that measures the performance of a scale in evaluating the visual IQ. Once the X-ray images of each phantom are evaluated with this scale, one can determine whether it is possible to evaluate [visual] IQ with the phantom. This psychometric scale was developed by Mraity et al. and includes anatomies usually found within the pelvis from which their visibility can be evaluated by observers when assessing IQ of AP pelvis radiography (Mraity et al., 2016). The images of the constructed phantoms can demonstrate a valid IQ scale by taking the responses from radiographers regarding the anatomical visibility. This means that the X-ray images of the constructed phantoms have an appearance similar to that typically seen in clinical pelvis X-ray images and thus provide a valid way of assessing visual IQ. Therefore, the face validity can be described as the degree to which a scale is visually observed in measuring the intended concept, such as IQ (Mraity et al., 2016). A list of questions (15 questions) was given to observers to evaluate the visual appearance of the X-ray images of the 1, 5 and 10 year-old phantoms. Each question related to the visibility of the different parts of pelvis anatomy. Fourteen of the questions addressed the appearances of pelvic anatomy; these were derived from the psychometric IQ scale developed by Mraity et al.

(2016). A fifteenth question was introduced to ask whether the phantom image would allow the assessment of IQ at different exposure factors. See Table (I-8) in appendix (I).

This list of questions, together with an X-ray image of the 1, 5 and 10 year-old phantoms, were evaluated visually by 34, 32 and 46 second year students in the Directorate of Radiography at University of Salford, respectively,. The students were aware of the radiographic techniques and X-ray image appraisal (see Appendix (IV) for the ethical approval of this work). A 5-point Likert scale was used in the questionnaire (strongly agree, agree, neither agree/disagree, disagree and strongly disagree) and their corresponding values were 2, 1, 0, -1 and -2, respectively.

Regarding to the number of observers used for the face validation, the sample size was taken as the whole Year 2 Diagnostic Radiography BSc (Hons) student cohort. Generally, a calculation of sample size is required to study responses from observers and this is dependent on the total number of observers (Spector, 1992). An example of this is the case for the original subscale validation by Mraity (2015). Others have proposed ‘rules of thumb’, advising that sample sizes between 30 to 500 participants are acceptable for most investigations (Roscoe, 1975; Sekaran & Bougie, 2016). However, the purpose of the observational study (face validation) was not for scale validation. It was for accumulating perspectives from trained observers in their ability to evaluate the visibility of the X-ray image from each phantom. Similar studies used between 5 and 10 observers to evaluate image quality (Allen, Hogg, Ma, & Szczepura, 2013; Lança et al., 2014; Tingberg et al., 2004). In addition to student observers, four experts with more than ten years experience (two radiologists and two radiographers) were included in the study to evaluate the X-ray images of each phantom.

The questionnaire responses from all the participants were taken as mean values for each question (the answers for negative questions- those containing “not”- were taken as mean values then converted to a positive score). If only a limited number of questionnaire items were positively scored (≥ 0.1) by the student in terms of being visible on the resultant phantom X-ray image, these data would be used to propose a modified IQ scale which could be used with the newly developed phantom. Furthermore, a Cronbach’s alpha coefficient would then be calculated to estimate the internal consistency of the modified IQ scale.

Cronbach alpha is defined as a statistical coefficient used to estimate the internal consistency (or reliability) of a specific scale (Spector, 1992). Spector further stated that it connects the number of items in the scale with their inter-correlation values. Cronbach’s alpha ranges from

0 to 1, and a value of 0.6 is considered to be a standard cut off point for each extracted factor (Cronbach, 1951). The values 0.7 to 0.95 are considered to be acceptable values for scale consistency (Tavakol & Dennick, 2011).

The calculation method of Cronbach's alpha was performed by including the IQ criteria (Table I-8 appendix I) that scored visibility for each phantom image by the observers in the scale developed by Mraity et al. (2016). Using SPSS Version V23 software (IBM Inc, Armonk, NY), the Cronbach's alpha coefficient was recalculated for each of the three phantoms with the same method as used in the original work (Mraity et al., 2016), but with the items from the modified scale of each phantom. As the original work included items of IQ criteria that have a total Cronbach's alpha coefficient value of 0.95, removing any of these items would reduce this value according to its weight in the scale. Accordingly, the new scale used in this thesis will have a new value of Cronbach's alpha coefficient, which will act as an estimation of the internal consistency of the new IQ scale. Thus, when applying IQ criteria (scored visible overall) for each constructed phantom, the Cronbach's alpha coefficient can be used to evaluate the performance of the IQ scale of each phantom and its ability to evaluate visual IQ.

4.3.4 Statistical analysis

Throughout the validation study the computer software SPSS Statistics v23 (IBM Inc, Armonk, NY) was used for data analysis. Mean values, together with their respective standard deviations (SD), were reported for data that were approximately normally distributed. For non-parametric data, median values, together with the inter-quartile range, were reported. Normality of the data was established using the Shapiro-Wilk test (p values greater than 0.05 were considered to represent an approximately normal distribution). A Pearson's correlation coefficient was utilised for the comparison of the total SNR values for the adult and the newly constructed phantoms for normally distributed data and Spearman Rho's correlation for non-parametric data (Field, 2013). As previously stated, Cronbach's alpha would be used to calculate the internal consistency of any modified IQ scales (Spector, 1992). The classification for the correlation coefficient value is between -1 and +1. These values are considered to be a perfect negative or positive match between two variables, respectively. In absolute value, an r of 0.1 to 0.3 is considered to be weak, an r of 0.3 to 0.5 is considered to be moderate, and an r of 0.5 to 1 is considered to be large (Cohen, 1988; Field, 2013). Other interpretations of a correlation coefficient reported that an r of 0 to 0.3 and of 0.5 to 0.7 is considered to be a moderate correlation. A value of r in the range 0.7 to 1 is considered to be a strong correlation, and -1 or

+1 is considered to be perfect match (Rumsey, 2011). The last classification for correlation was considered for the phantom validation, as it gives higher predictability threshold.

4.4 Results: Phantom validation

4.4.1 CT validation

The first phase in the evaluation was to determine the equivalent attenuation characteristics of PoP mixing ratios to achieve the CT density of cortical bone. As can be seen in Figure (4.17), all of the mixing ratios took about 7 days to dry completely and the rest of scans were after 7 days and showed similar and consistent results. After comparing the CT density of patient data with those in Table (4.1) and Figure (4.17), the decision was made for the 32/50, 30/50 and 29/50 (water/PoP) ratios for the cortical bone to be used in construction of the 1, 5 and 10 year-old phantoms, respectively. Figure (4.17) clearly demonstrates that 10 days is sufficient for the PoP to dry and become stable.

Table (4.1) shows that, from the means of the measured CT density (HU) and their relatively low SD values, the method of the weight-mixing ratio has suitable repeatability when reviewing the three samples that were used. For each mixing ratio and each CT scanning interval, the standard deviation (SD) varied from 37.2 to 68.6 for all scanning intervals. The averaged CT density varied from 796.6 to 1373.3 HU.

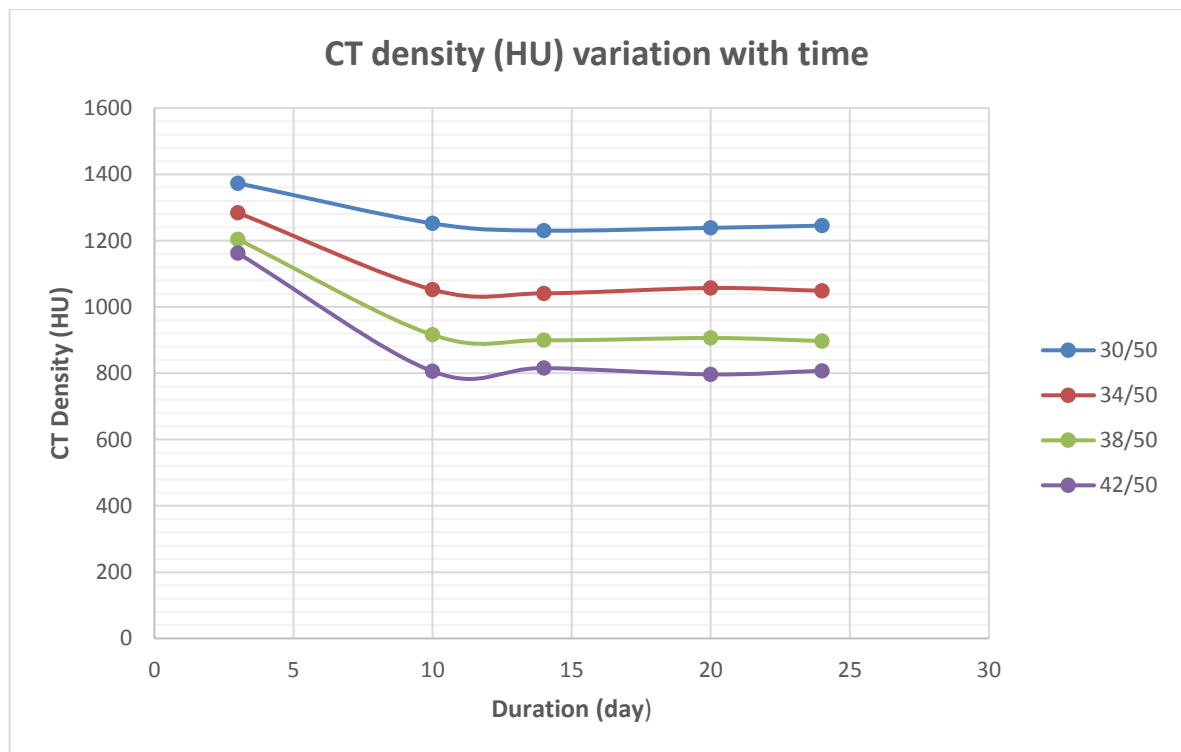


Figure 4.17: CT density variations versus time for the different weight-mixing ratios.

Table 4.1: Mean (SD) CT densities for each of the mix ratios over time.

Date: 10-Oct-2016		
<u>W/PoP</u>	<u>Mean CT Density (HU)</u>	<u>SD</u>
30/50	1373.25	51.75
34/50	1284.08	41.16
38/50	1203.75	51.15
42/50	1162.11	42.88
Date: 17-Oct-2016 (after 7 days)		
<u>W/PoP</u>	<u>Mean CT Density (HU)</u>	<u>SD</u>
30/50	1252.00	68.57
34/50	1052.25	54.98
38/50	915.75	39.88
42/50	805.67	44.44
Date: 21-Oct-2016 (after 14 days)		
<u>W/PoP</u>	<u>Mean CT Density (HU)</u>	<u>SD</u>
30/50	1230.42	47.54
34/50	1041.08	43.51
38/50	899.58	37.18
42/50	815.58	43.55
Date: 27-Oct-2016 (after 21 days)		
<u>W/PoP</u>	<u>Mean CT Density (HU)</u>	<u>SD</u>
30/50	1238.58	58.54
34/50	1057.25	67.06
38/50	906.33	46.68
42/50	796.58	49.52
Date: 1st-Nov-2016 (after 28 days)		
<u>W/PoP</u>	<u>Mean CT Density (HU)</u>	<u>SD</u>
30/50	1245.33	66.84
34/50	1048.67	45.56
38/50	897.25	43.03
42/50	807.42	49.69

After the CT density measurements of the PoP in cups were finished, the next CT density measurements were performed for the phantoms and their corresponding reference patients (phantoms, which were comprised of plaster and the PMMA and; patient data, which were comprised of cortical bone and soft tissue).

CT density measurements were taken of the corresponding anatomies of the patients' cortical bone, except for the L5 area, as there was not enough cortical bone for measures to be acquired- see Tables (I-1-3) in Appendix (I). Measurements over the different anatomical areas showed a range of CT densities, from 810.3 to 1222.8 HU, for the 1 year-old patient. For the 5 year-old patient, the CT density ranged from 1015.4 to 1300.9 HU. The CT density measurements for the 10 year-old showed a range of 1015.9 to 1356.3 HU- see Tables (I-1-3) in Appendix (I). As a result, the mean for different anatomies was taken as a reference HU number in the tissue matching procedure.

The CT densities were measured at time intervals (3-7 days) to ensure the PoP reached a constant and stable density. The data acquisitions for the optimisation study for each phantom started after the last scan was taken. This was done to measure the consistency of the phantom ahead of the data collection. For each scan, the CT density was measured (mean, SD) across different anatomical areas within the PoP in the phantom. The anatomical areas were the femur, pubic, femoral, acetabulum, sacro-iliac joint, iliac crest and the L5 vertebral body. The total CT density value for each phantom was calculated by taking the average for each anatomical location so that the anatomies aforementioned would have similar portions in evaluating the CT density for each phantom- see Tables (I-1-3) in Appendix (I). This calculation method was also applied for the patient CT data.

From the Figures (I-1-3) in Appendix (I), it can be seen that the CT density measurements for the cortical bone substitute showed stable values after 7-10 days of drying, when compared to subsequent scans. The last three CT scans generated CT densities for the bone substitute that were roughly at the same level. This is consistent with the drying time that was found from the PoP cups test. As an additional stability check, the percentage difference and percentage change were calculated between each scan and the one proceeding it in order to quantify the rate of the density change of the PoP for each of the above-mentioned pelvic anatomies. Table (4.2) below illustrates this.

For the 1 year-old, the maximum percentage change and difference were 1.7% and -0.5%, respectively. For the 5 year-old phantom, over the last three scan dates, the maximum percentage difference was -0.2% and the maximum absolute percentage change was 0.6%. For the 10 year-old, the maximum percentage change and difference were 0.3% and -0.3%, respectively. It is important to mention that there is variation within the CT method that might

affect its repeatability to achieve a result with an experimental error of 2% or below. This is explained in the last paragraph of this section (Boone & Chavez, 1996; Hubbell, 1982).

Table 4.2: Percentage difference and percentage change of PoP across the three phantoms.

<u>1-year-old phantom</u>				
Scan date	Period (Day)	Mean HU	% change	% Difference
07-Jul-17		1209.32		
21-Jul-17	+14	1244.65	5.54%	0.72%
31-Jul-18	+24	1221.01	-0.52%	-0.48%
04-Aug-17	+28	1242.45	1.05%	0.44%
11-Aug-17	+35	1254.58	1.70%	0.24%
<u>5-year-old phantom</u>				
Scan date		Mean HU	% change	% Difference
11-Nov-16		1264.77		
21-Nov-16	+10	1258.75	-0.48%	-0.12%
14-Dec-16	+33	1249.85	-0.71%	-0.18%
10-Jan-17	+60	1257.22	0.59%	0.15%
<u>10-year-old phantom</u>				
Scan date		Mean HU	% change	% Difference
21-Jul-17		1248.11		
31-Jul-17	+10	1254.85	0.27%	0.13%
04-Aug-17	+14	1242.37	-0.49%	-0.25%
07-Aug-17	+17	1242.18	-0.01%	0.00%
11-Aug-17	+21	1239.76	-0.10%	-0.05%

The next step was to determine the level of similarity between the phantoms and their corresponding patient ages. The reference quantity from each patient CT datum was compared against the averaged CT density of PoP in each phantom- see Tables (4.3-5) below. Subsequently, the percentage difference between the averaged CT density of a 1 year-old patient cortical bone and the PoP in the one year-old phantom ranged from -27.9% to -26.2%. The same quantity for the 5 and 10 year-old phantoms ranged from -4.7% to -4.1% and from 2.0% to 2.2%, respectively.

The comparison between the patient soft tissue and the phantom PMMA was also recorded (see Tables (3-5)). The average of PMMA CT density and soft tissue with their percentage difference are listed in Tables (3-5) for each phantom. The percentage difference between the PMMA and soft tissue was equal to -30.6%, -23.4% and -20.6% for the 1, 5 and 10 year-old.

The results of the CT density comparisons for the animal bones, when compared to cortical bones, for each patient age, are presented in Tables (4.3-5). The chicken bone (cortical) showed an average value of 1212.4 HU and the percentage difference from the cortical bone of the 5 year-old patient was around -1.1%. Its percentage difference against the 1 year-old patient scored around -25.5%- see Tables (4.3 and 4.4). The lamb bone showed a CT density around 1267.3 HU and its percentage difference with the 10 year-old cortical bone was 2.6%- see Table (4.5). These data demonstrate a good replication of human cortical bone by the X-ray tissue substitutes and justify its use inside the phantom.

Finally, calculations of the ratio of cortical bone to soft tissue for the patient CT density and PoP to PMMA were performed. This included the percentage difference between cortical bone and soft tissue and their equivalent tissue substitutes in each phantom. For the 1 year-old these were 173.5% and 172.8% for the patient cortical bone to soft tissue and PoP to PMMA, respectively. For the 5 year-old, the percentage difference between cortical bone and soft tissue and their equivalent tissue were 176.8% and 172.1%, respectively. The same quantities for the 10 year-old were 178.0% and 172.8% for the cortical to soft tissue and PoP to bone, respectively. Those two quantities reflect similar visibility of the patient's bony anatomies inside soft tissue to the PoP inside the PMMA.

Despite the CT validation method providing accurate and stable results, there remain some limitations in the accuracy of the material used in the phantom simulating the attenuation properties of the target tissue (Homolka et al., 2002). The method described uses the mass attenuation coefficients of photons with an experimental error of <2% for elements with $Z < 30$ across the diagnostic photon energy range (Boone & Chavez, 1996; Hubbell, 1982). In the attenuation measurement process for the tissue substitutes, this error will be cancelled out to some extent since there are some element components that are similar to the bone components and soft tissue from the PMMA and PoP, respectively (International Commission on Radiation Units and Measurements (ICRU), 1989; White, Widdowson, Woodard, & Dickerson, 1991).

Table 4.3: Comparison of CT density for the 1-year-old phantom materials versus human patient tissues.

<u>Material</u>	<u>CT density (SD range), HU</u>	<u>Percentage difference</u>
PoP	1220.0 (16.8-89.1) to 1254.6 (15.7-69.2)	-27.9% to -26.2%
Patient cortical bone	938.0 (5.0-97.8)	
Animal cortical bone	1212.4 (111.4-280.7)	-25.5%
Patient cortical bone	938.0 (5.0-97.8)	
Soft tissue	66.5 (11.0-22.2)	-30.6%
PMMA	90.5 (32.2-49.0)	
Patient cortical bone	938.0 (5.00-97.8)	173.5%
Soft tissue	66.5 (11.00-22.2)	
Averaged PoP	1239.4	172.8%
PMMA	90.5 (32.2-49.0)	
HU: Hounsfield unit; SD: standard deviation; min: minimum; max: maximum.		

Table 4.4: Comparison of CT density for the 5-year-old phantom materials versus human patient tissues.

<u>Material</u>	<u>CT density (SD range), HU</u>	<u>Percentage difference</u>
PoP	1249.9 (50.2-135.5) to 1258.4 (46.1-137.0)	-4.7% to -4.1%
Cortical bone	1200.2 (111.5-297.3)	
Animal bone	1212.4 (111.4-280.7)	-1.0%
Patient cortical bone	1200.2(111.5-297.3)	
Soft tissue	74.0 (20.7-25.4)	-23.4%
PMMA	93.6 (35.2-57.9)	
Cortical bone	1200.2 (111.5-297.3)	176.8%
Soft tissue	74.0 (20.7-25.4)	
Averaged PoP	1255.3	172.2%
PMMA	93.6 (35.2-57.9)	
HU: Hounsfield unit; SD: standard deviation; min: minimum; max: maximum.		

Table 4.5: Comparison of CT density for the 10 year old phantom materials versus human patient tissues.

<u>Material</u>	<u>CT density (SD range), HU</u>	<u>Percentage difference</u>
PoP	1239.8 (56.5-128.3) to 1242.4 (55.0-138.3)	2.0% to 2.2%
cortical bone	1267.3 (8.7-183.9)	
Animal cortical bone	1267.3 (13.6-262.0)	2.6%
Patient cortical bone	1267.3 (8.7-183.9)	
Soft tissue	73.6 (12.8-30.3)	-20.6%
PMMA	90.6 (36.0-58.7)	
Cortical bone	1267.3 (8.7-183.9)	178.0%
Soft tissue	73.6 (12.8-30.3)	
Averaged PoP	1241.4	172.8%
PMMA	90.6 (36.0-58.7)	
HU: Hounsfield unit; SD: standard deviation; min: minimum; max: maximum.		

4.4.2 Pixel value validation

The results from the pixel value validation experiment included measurements of SNR values from each of the three phantoms (with a thickness 21 cm) and the commercially available adult anthropomorphic phantom. The SNR measurements were taken from bony anatomies and the PMMA, and then compared with the corresponding measurements from the adult anthropomorphic phantom. The SNR measurements were taken under a range of tube kVp values and mAs. Correlation tests between each phantom and the adult anthropomorphic phantom were taken. These considered as indication as to the level of similarity in their responding to various qualities and quantities of X-ray radiations.

The correlation coefficients were calculated for each kVp increment over a range of mAs and Vice versa for mAs increments. The sample size for each increment varied depending on the range of tube potentials or mAs values covered. However, the p value of the correlation coefficient varied from being significant ($P < 0.05$) to non-significant ($P \geq 0.05$). A correlation coefficient with a non-significant p value was excluded from the calculation of the averages, as it would complicate the interpretation of the correlation results (Field, 2009).

The results from comparing the SNR values of the adult phantom with the 5 year-old phantom (12 cm thickness) showed a strong positive correlation (mean: PMMA=0.89 and PoP=0.89) in predicting mAs change. For tube potential prediction, the PoP showed a strong correlation at 1 mAs, while the PMMA did so at 1 and 2 mAs. After both these points, the correlation coefficients decreased as mAs increased. They eventually resulted in a negative correlation across the entire range of the mAs values. See Table (I-4) in Appendix (I).

The above results prompted suspicion of dose creep for the digital detector, as the amount of radiation reaching the image detector varied significantly when comparing between adult and children, due to their differences in anatomical thickness. Therefore, the thickness of the 5 year-old phantom was compensated by increasing the thickness of the soft tissue substitute to that equivalent of the adult phantom. An experimental study demonstrated that a PMMA thickness of 21 cm generated an equivalent dose to that of adult anthropomorphic phantom. Consequently, the correlation coefficients between the adult anthropomorphic phantom and the 5 year-old phantom, with calibrated thicknesses (21 cm), were calculated- see Table (4.6). In terms of mAs response, there was a strong positive correlation between SNR values between the phantom construction within this thesis and the commercially available phantom ($r = 0.99$ for all kVps). For kVp response, there was a strong positive correlation between the two phantoms (5 year-old and adult anthropomorphic) for the PMMA and the bone over the range 1 to 8 mAs (mean $r > 0.85$, this was averaged for the PoP and PMMA). This then decreased as the mAs was raised ($r = -0.21$ at 20 mAs; this averaged for PoP and PMMA). For details see Table (I-5) in Appendix (I).

The 21 cm thickness was applied for the validation of 1 and 10 year-old phantoms. The correlation coefficient was then estimated between the SNR values measured from each of the newly constructed phantoms and the adult anthropomorphic phantom for each increment of kVp and mAs. The Pearson correlation and Spearman's Rho were conducted for the normal and non-normal distribution of data, respectively. The normality test showed that there were normal and non-normal distributions of data within the increments. Thus, the calculation of the overall correlation coefficient included a combination of the Pearson's correlation and Spearman's Rho correlations, according to the type of their data. Also, a correlation coefficient with non-significant p values (≥ 0.05) was not included in the overall (average) correlation coefficient. See Tables (I-6&7) in Appendix (I).

The pixel value validation results for the 1 year-old phantom showed a strong correlation with the adult anthropomorphic phantom. This included changing the mAs and kVp (see Table

(4.6)). The kVp response showed a correlation coefficient of about 0.86 and 0.83 for the PMMA and the bone, respectively. The mAs response showed a correlation coefficient of around 0.81 and 0.83 for the PMMA and the bone, respectively. See Table (I-6) in Appendix (I) for more details.

The calculation of correlation coefficients showed strong correlation between the 10 year-old and the adult anthropomorphic phantoms. The correlation coefficients over the kVp response are 0.85 and 0.80 for the PMMA and the bone and, respectively. The mAs response showed a correlation coefficient of 0.80 and 0.78 for the bone and the PMMA, respectively. See Table (I-7) in Appendix (I).

Table 4.6: Mean correlation coefficient from comparing the adult anthropomorphic with each phantom of 21 cm thick.

Correlation coefficient at 21 cm phantom thickness					
(1-year vs adult)					
Changing mAs			Changing kVp		
<u>kVp</u>	<u>PMMA</u>	<u>bone</u>	<u>mAs</u>	<u>PMMA</u>	<u>bone</u>
50-98	0.81	0.83	1-16	0.86	0.83
	0.82			0.85	
(5-year vs adult)					
Changing mAs			Changing kVp		
<u>kVp</u>	<u>PMMA</u>	<u>bone</u>	<u>mAs</u>	<u>PMMA</u>	<u>bone</u>
50-101	0.99	0.99	1-20	0.81	0.60
	0.99			0.71	
			1-8	0.90	0.79
			1-8	0.85	
(10-year vs adult)					
Changing mAs			Changing kVp		
<u>kVp</u>	<u>PMMA</u>	<u>bone</u>	<u>mAs</u>	<u>PMMA</u>	<u>bone</u>
50-101	0.78	0.80	1-20	0.85	0.80
	0.79			0.83	
Only correlation coefficients with P<0.05 were included					

4.4.3 Face validity

Data for each phantom X-ray image were collected from all participants and were then averaged for each question listed in Table (I-8) in the appendix (I) (the answers for negative questions were averaged then converted to positive answers, thereby correcting for affirmation bias). An average answer of more than 0.1 was considered to be an indication of a tendency of agreement with the statements in the questions. The questions with agreement were included in the calculation of Cronbach's Alpha coefficient. This coefficient is considered as an estimation of the internal consistency of the IQ scale. Data from this experiment demonstrates the general applicability of the phantom for visual IQ evaluation and, therefore, dose optimisation studies.

For the 1 year-old phantom, the results of X-ray image questionnaire showed 9 questions- Q1, Q3, Q4, Q6, Q7, Q9, Q11, Q13 and Q14 (from Table I-8, appendix I) with a score range of 0.12-0.85 (see Table (4.7) below and Table (I-12) in appendix (I)). These questions formed the IQ modified scale for the 1 year-old phantom- see Table (I-9) appendix (I). The modified scale showed a valid performance for evaluating visual IQ with a Cronbach's alpha coefficient of 0.83 (range 0.75-0.91). Furthermore, the mean score over all of the questions (Q1 to Q15) was 0.19.

The following questionnaire data arose from the X-ray image of the 5 year-old phantom. Seven questions were selected to be in the IQ scale for the 5 year-old phantom. The modified IQ scale was formed from the questions of the questionnaire (with average answers of 0.53-0.88) - see Table (4.7) and Table (I-13) appendix (I). Accordingly, the questions Q1, Q5, Q7, Q8, Q9, Q11 and Q13 were selected as 'the modified IQ scale' for the 5 year-old phantom, (Table I-10 in appendix (I)). The new (modified) scale showed that the Cronbach's Alpha coefficient for the 6 image sets out of 7 was almost 0.8, except for image set 1 which was 0.7. This suggests that the subscale has valid performance. The questions (Q1 to Q15) scored a mean of 0.5.

The following questionnaire data arose from the X-ray image of the 10 year-old phantom. The questions with scores ranging from 0.13-0.78 were selected as 'the modified IQ scale' for the 10 year-old phantom. Eight questions were selected for this phantom, and can be seen in Table (I-8) appendix (I). These questions were Q1, Q5, Q6, Q7, Q9, Q12, Q13 and Q14. The answers of each question are listed in Table (4.7) and Table (I-14), appendix (I). The modified image quality scale showed a valid performance for the visual evaluation of image quality. These image quality scales are listed in Table (I-11), appendix (I). Cronbach's alpha coefficient

showed a value of 0.77 (0.68-0.86) - a valid performance for the modified IQ scale. Also, the overall mean score over all for the questions (Q1 to Q15) was 0.15.

In addition to the observation studies, four experts with more than ten years of experience (two radiologists and two diagnostic radiographers) showed a positive response in terms of the ability of each phantom image to be acceptable for visual image quality evaluation in dose optimisation research.

Table 4.7: Questionnaire results from the 1, 5 and 10-year-old phantoms.

1-year-old															
ID	Q1	Q2	Q3	Q4	Q5	Q6	Q7	Q8	Q9	Q10	Q11	Q12	Q13	Q14	Q15
Mean	0.85	0.03	0.32	0.41	0.06	0.12	0.15	-0.18	0.44	-0.41	0.24	0.00	0.15	0.21	0.56
SD	0.74	1.06	0.94	1.05	0.97	0.98	1.05	1.00	0.82	1.13	1.05	0.89	0.93	0.91	0.96
Mean Q1-Q15	0.19														
5-year-old															
Mean	0.88	0.03	0.84	0.39	0.55	0.34	0.53	0.52	0.53	0.03	0.75	0.13	0.68	0.35	0.84
SD	0.61	1.00	0.63	0.95	0.89	0.90	0.97	0.96	0.86	1.07	0.80	0.94	0.79	0.91	0.92
Mean Q1-Q15	0.50														
10-year-old															
Mean	0.39	0.24	-0.16	-0.02	0.78	0.13	0.15	0.04	0.46	-0.46	0.02	0.18	0.22	0.22	0.57
SD	0.95	0.96	0.85	1.18	0.79	0.86	0.97	0.97	0.94	1.13	1.01	0.98	1.07	1.01	0.96
Mean Q1-Q15	0.15														
2=strong positive, 1=Positive, 0=not decided, (-1)= Negative and (-2)= Strong Negative															

The questionnaire results for the 1, 5 and 10 year-old phantoms showed a high agreement regarding the ratio of positive/negative answers from the observers on the questions that formed

the modified IQ scale. The number of answer agreements for each question, as well as the ratio of the total positive answers to the total negative answers, is listed in Table (4.8-4.10) below. The questions used in the IQ scale (see the underlined questions (Q) in Tables 4.8-4.10) have almost all their answers on the positive side (1 and 2), wherein 0 is undecided, and negative answers are -1 and -2. The ratios of positive to negative varied from 1.60 to 14.50, 3.80 to 14.00 and 1.50 to 7.20 for the 1, 5 and 10 year-old phantoms, respectively (Tables 4.8-4.10).

Table 4.8: Agreements of answers, number of answers for each question. The underlined questions are the one used for the 1 year old phantom IQ scale.

similar answers agreements															
<u>Likert</u> <u>scale</u>	<u>Q1</u>	Q2	<u>Q3</u>	<u>Q4</u>	Q5	<u>Q6</u>	<u>Q7</u>	Q8	<u>Q9</u>	Q10	<u>Q11</u>	Q12	<u>Q13</u>	<u>Q14</u>	Q15
2	3	1	0	3	1	0	1	0	1	2	2	0	0	1	3
1	26	12	21	19	12	16	17	12	19	6	15	12	16	15	20
0	3	9	4	1	9	8	3	6	8	7	8	11	8	8	5
-1	1	9	8	11	10	8	12	14	6	14	7	10	9	10	5
-2	1	3	1	0	1	2	1	2	0	5	2	1	1	0	1

Table 4.9: Agreements of answers, number of answers for each question. The underlined answers are the one used for the 5 year old phantom image quality scale.

Number of scoring answers															
<u>Likert</u> <u>scale</u>	<u>Q1</u>	Q2	Q3	Q4	<u>Q5</u>	Q6	<u>Q7</u>	<u>Q8</u>	<u>Q9</u>	Q10	<u>Q11</u>	Q12	<u>Q13</u>	Q14	Q15
2	2	1	3	1	2	0	4	3	1	2	3	1	2	2	7
1	26	12	22	18	19	19	13	16	19	10	22	12	21	14	17
0	2	7	6	5	4	6	9	7	6	6	3	10	4	8	4
-1	2	11	1	6	4	6	3	4	3	11	4	8	3	7	3
-2	0	1	0	1	0	1	1	1	1	1	0	1	0	0	0
positive / negative	14.0	1.0	25.0	2.7	5.2	2.7	4.2	3.8	5.0	1.0	6.2	1.4	7.6	2.2	8.0
	0	8	0	1	5	1	5	0	0	0	5	4	7	9	0
positive=(1)+(2), Negative=(-2)+(-1)															

Table 4.10: Agreements of answers, number of answers for each question. The underlined answers are the one used for the 10 year old phantom image quality scale.

similar answers agreements															
<u>Likert</u>	<u>Q1</u>	<u>Q2</u>	<u>Q3</u>	<u>Q4</u>	<u>Q5</u>	<u>Q6</u>	<u>Q7</u>	<u>Q8</u>	<u>Q9</u>	<u>Q10</u>	<u>Q11</u>	<u>Q12</u>	<u>Q13</u>	<u>Q14</u>	<u>Q15</u>
2	1	1	0	4	5	1	0	1	1	1	2	2	2	5	6
1	29	12	12	15	31	16	24	19	30	12	16	18	24	13	23
0	4	8	15	5	5	18	6	7	6	6	9	13	4	16	8
-1	11	23	17	18	5	10	15	19	7	19	17	10	14	11	9
-2	1	1	1	3	0	1	1	0	2	1	1	2	2	1	0

4.5 Phantom validation: Discussion

4.5.1 CT validation

The CT validation demonstrated a number of important outcomes. Starting with the mixing ratios of water with the PoP which showed that they can be combined show equivalent X-ray characteristics to that of paediatric bone. Also, the drying process of the PoP showed that between 7 to 10 days is required to achieve stability. No shrinking of the PoP size was observed in the cups nor in the phantom; there was no need to use vacuum systems, unlike poly- based materials (Homolka & Nowotny, 2002; Watanabe & Constantinou, 2006). On the other hand, there was a possibility of producing air bubbles inside the solid PoP whilst it was drying. To check this, a visual inspection and the standard deviation from CT measurements need to be considered. The visual check showed some air bubbles and black dots (with using CT windowing for bone), but their impact was minor because they were few in size and number. However, the SD range of PoP inside the samples of cups and the phantoms showed a range comparable to the SD range from the measurements of [simulated] patient cortical bone (see Tables 4.1&4.3-4.5). As mentioned by Homolka & Nowotny (2002), the SD from the CT data can be an indication to the homogeneity of the scanned material. This means that the homogeneity of the PoP is proper for the simulation of cortical bone measured against the CT reference data. The soft tissue substitute (PMMA) was not considered for this measurements as it is considered to have a constant density (International Commission on Radiation Units and Measurements (ICRU), 1989).

The level of similarity between the phantoms and their reference CT clinical data, using CT density measurements, showed high acceptability for radiographic simulation- see Tables (4.3-5). The cortical bone, using PoP, showed a maximum percentage difference of -4.74% between the 5 and 10 year-old phantoms and their corresponding patient age reference. The CT density measurements of CT scans provided a reliable indication of the linear attenuation coefficient of X-ray interactions, which is a rigid method for determining substitutes for X-ray imaging (Schaly et al., 2009; Watanabe & Constantinou, 2006; White & Constantinou, 1982). Thus, according to the tissue classification by the International Commission on Radiation Units and Measurements (ICRU) (1989, 1992) and by Watanabe & Constantinou (2006), the PoP is a class A substitute for the cortical bone of 5 and 10 year-old patients and falls within acceptable error range of 5%.

The CT density percentage differences between the substitutes of soft tissues in each phantom and their CT patient reference showed a range of -20% to -30%, which makes PMMA of class B and C for these phantoms, according to the classifications by Watanabe & Constantinou (2006). However, according to ICRU report 44, the PMMA is a class A soft tissue substitute (International Commission on Radiation Units and Measurements (ICRU), 1989). This means that the PMMA used in the phantoms can be of higher density than the one from the literature, or it could be due to differences in soft tissue density in adults. However these percentage differences have less potential effects on the study results as there are different components within the soft tissue, such as the muscle, that reaches 100 HU (Mattsson & Thomas, 2006). Also, another factor that can reduce the effect of these differences is that the thicknesses used for the phantoms are of standard thickness, and were calibrated based on the use of PMMA. The attenuation characteristics of PMMA were considered in the calculation of the corresponding age to PMMA thicknesses (Vano et al., 2008).

The percentage difference between cortical bone to soft tissue (patient) and PoP to PMMA (phantom) showed similar values for each phantom (Tables 4.3-4.5). The differences between the human reference and phantom data were 0.74%, 4.6% and 5.32% for the 1, 5 and 10 year-old phantoms, respectively. These relatively small differences would reflect similar visibility (contrast) of the bony anatomy alongside soft tissue (patient) when compared with PoP alongside PMMA (phantom) and provide further evidence of validity. In addition, the percentage difference between the patient and animal (chicken/lamb) in cortical bone was -1.0%, providing further evidence of validation. This should reduce the effect from having a class C substitute of PMMA, as was the case for using the PoP in the 1 year-old phantom. This

is because the visual contrast of the bone from the soft tissue substitutes is a key parameter associated with visual evaluation of image quality in pelvis radiography (M. Singh et al., 1972; Stieve, 1989).

4.5.2 Pixel value validation

This section considers the correlation between the commercially available adult anthropomorphic pelvis phantom and the three *new* paediatric pelvis phantoms with a thickness of 21 cm. This thickness was found to provide a better comparison than when using the absolute age corresponding thickness for each phantom. The latter approach, without equivalent thickness, shows evidence of dose creep when at high acquisition factors.

The correlation coefficients over the three phantoms scored a minimum 0.78, including the mAs range from 1-8 for the 5 year-old. The data in Table (4.6) shows a strong linear relationship (Rumsey, 2011). The high correlation level for each phantom, with the adult anthropomorphic phantom, can be explained by the high level of structural replication and X-ray characteristic replication of the phantoms and the production of the subsequent X-ray images. Such high correlations demonstrate good validity when compared against the adult anthropomorphic phantom. In addition, this level of correlation can be an indication for undertaking optimisation studies using physical measurements, since the pixel value measurements were SNR values. This can be explained in detail, as follows.

The X-ray attenuation characteristics of the materials determine the brightness of the X-ray image. This is represented by the pixel values. The determination of each pixel value is related to the attenuation of the X-rays that pass through the corresponding body part (Fauber, 2013). Besides what is mentioned in ICRU 44, the threshold visibility for the imaging phantom depends on factors such as the anatomical shape, dimensions and attenuation characteristics of the patient (International Commission on Radiation Units and Measurements (ICRU), 1992). Thus, each level of exposure factor (such as kVp or mAs) represents a specific brightness (or pixel value) within the X-ray image. This means that the correlation of each phantom with the equivalent commercial phantom can be an indication to a valid response of the three phantoms in generating X-ray images when changing energies and intensities of an X-ray beam (changing kVp and mAs). This response can even be generalised for other exposure factors such as filtration and SID, because changing them also results in manipulation of the X-ray beam energy and the intensity reaching the imaging plate (Carroll, 2007).

4.5.3 Face validity

The results for the validity of the IQ scale (the calculations of Cronbach's alpha coefficient) are based on the psychometric scale that was originally validated by Mraity et al. in 2016 (Mraity et al., 2016). This work used X-ray images of different image qualities generated from human cadavers and an anthropomorphic pelvis phantom. Observers scored the visibility of the bony anatomies which are usually found on an AP pelvis X-ray image. Next, a list of the items (anatomies), which were scored with low skewness (or SD), were placed on a psychometric scale. The Cronbach's alpha coefficient was calculated for the images as a measure for the reproducibility of the psychometric scale for assessing the perception of image quality of an AP pelvis radiograph.

When Mraity's psychometric scale was used in this thesis, the positively scored questions resulted in a Cronbach alpha coefficient which suggested that the phantoms are valid. This means that there is adequate visibility of the anatomies within the phantoms for producing a new scale that can evaluate image quality. This is related to the visual radiographic properties that exist in the human pelvis, and these are found within this phantom. The results appear to be reflective of images which adequately represent human pelvis X-ray images. Also, it is highly likely that the IQ subscale, co-incidentally generated as a by-product of this analysis, has valid performance for the visual assessment of image quality in AP pelvis imaging. The high face validity also confirms the perception that the observers had on the high similarity of the geometry of the displayed anatomies and their artificial substitutes' X-ray characteristics. These must therefore be a close match (International Commission on Radiation Units and Measurements (ICRU), 1992).

The results from the face validity experiment showed a mean score (Q1 to Q15) of 0.19, 0.47 and 0.15 for the 1, 5 and 10 year-olds (Table 4.7). The questions listed in the questionnaire are regarding the visibility of anatomies found on the AP pelvis projection. The overall scores' being higher than the midpoint value (zero) indicates that the participants tend to agree that the X-ray imaging characteristics of the phantoms are representative of actual paediatric AP pelvis projections.

Also, the questions included in the IQ scales of the three phantoms are those with high agreement (up to 14 times) between all of the observers (see underlined questions (Q) in Tables 4.8-10). This indicates an overall strong tendency for them to agree on each question that can be used in the visual evaluation of IQ.

4.6 Conclusion: phantom validity

A series of validation experiments were carried out on the three phantoms in order to investigate whether they were capable of generating suitable images for radiographic optimisation studies. From the CT validation work, density measurements showed percentage differences in the contrast between each phantom (newly constructed phantoms and their commercially available equivalents) and their reference patient that were close. Percentage differences between the materials in the phantoms and the tissues in the patients were also similar. These differences mean that the phantom materials would simulate the X-ray radiological properties of a human pelvis of the corresponding age. Pixel value validation also showed a strong correlation with the X-ray images produced from each phantom, at different exposure factors. The phantoms delivered similar responses in terms of pixel values to that of 2D X-ray images generated from a commercially available adult anthropomorphic phantom. The face validity test showed that the phantoms can be used with an IQ scale and this has valid utility for assessing visual image quality (a Cronbach's alpha coefficient about 0.8). This provides an additional indication that the phantoms are fit for purpose, in terms of the visual assessment of image quality.

In terms of accessibility, materials used within these phantoms are widely available and come at a relatively low cost. Manufacturing uses CT data which are, also, readily available and do not require specialist skills to undertake.

Summarising all of the validation tests, they indicate that the phantoms are valid for optimisation purposes, can be made from low cost materials, are relatively simply to construct and are likely to have global utility in areas with limited financial resources and access to phantoms.

4.7 Limitations

The manufacturing of the three phantoms, in general, has many limitations in their procedures. This often leads to limitations in design and representations of human structures. Firstly, the availability of the tissue substitutes and the formation of the complex shapes that are needed to represent the human body. In addition, some materials are also subjected to industrial confidentiality and are not widely available (K. Harrison et al., 2011; Homolka & Nowotny, 2002). Secondly, the complexity in the requirements for manufacturing systems that allow for the preparation of phantom materials, such as vacuum equipment (Watanabe & Constantinou, 2006), which would add extra complexity in the geometrical formation of components, is a potential problem. Those aforementioned limitations have made it necessary for this phantom

to contain a trabecular bone and additional anatomical details from the inclusion of an animal bone. However, this constraint is of limited effect when evaluating the edge of cortical bone against soft tissue- a task that does not require the presence of trabecular bone is also simulated within the phantom. When measuring the estimated surface dose by placing a dosimeter on the phantom surface, it was found that the phantom can also be successfully used in dose optimisation studies. It is also worth mentioning that obtaining lateral projections from the phantoms can be challenging due to the [artefactual] black lines that would appear from the coronal slices that form each phantom. However, the appearance of the bony anatomies would still be visually clear.

4.8 Future Consideration

After going through the manufacturing process of this phantom, a series of improvements to the current phantom design and development can be suggested. Improving the phantom productivity time by using thicker slices may be achieved by using 3D or improved milling technology. 3D printing is an alternative technology that should be considered as it can offer greater replication of individual patient anatomy. New materials are constantly being developed and it is likely that printing filaments will have sufficient densities to replicate a wide range of human tissues and provide much wider phantom construction opportunities. Within the literature, there are reports of the potential role of 3D printing in phantom development and construction (Leng et al., 2017, 2015). It is likely that at present such processes will be expensive and require access to technologies with limited availability. In many parts of the world, logistics and economics would restrict access to 3D printing and alternatives are required, such as our method of phantom construction.

4.9 Chapter summary

Three newly constructed paediatric pelvis phantoms were tested for validity using a three-phase method. Experimental tests covering CT density, resultant X-ray image pixel values and face validity were undertaken. Study data strongly suggests that the three phantoms constructed in this thesis provide a suitable replication of paediatric pelvis X-ray images and would, therefore, be suitable for dose optimisation experiments. Dose optimisation for the three phantoms will be the focus of the remaining chapters.

Chapter Five: Optimisation Methods

5.1 Overview

This chapter provides an explanation and justification for the method used for the optimisation studies that were undertaken using the three constructed and validated phantoms (1, 5 and 10 year-old ages). It starts by presenting the experimental equipment used during data acquisition, accompanied by details on the quality control (QC) tests undertaken. Following this there is an explanation of the experimental set-up used to acquire the image and radiation dose data. Within this there is a full description of the acquisition set-up used for data collection. The chapter then reports on the study design used for data acquisition, including the factorial method used for choosing the exposure factors and their corresponding ranges. After this, the optimisation method is described, as are the approaches used in the evaluation of visual and physical image quality, and of radiation dose measurements. This is followed by an explanation of the observer variability tests, which included determining the intra-class correlation coefficient (ICC) to check the variability of the visual evaluations of IQ. Then, a focus group study that was used to evaluate the level of IQ suitable for diagnosis will be described. The concept of a Figure of Merit (FOM) is presented as an outcome measure for investigating dose optimisation. The statistical analysis will then be presented, including details on the correlation and multiple regression analyses utilised. Finally, the main effect scatterplots are presented in order to illustrate trends between image quality and radiation dose.

5.2 Experimental set-up

5.2.1 X-ray equipment and quality assurance

A series of X-ray exposures were carried out within the Susan Hall Imaging Facility located in the Directorate of Radiography at the University of Salford. The X-ray tube used in this investigation was a Wolverson Arcoma Arco Ceil general radiography system (Arcoma, Annavägen, Sweden), with a high frequency generator and a VARIAN 130 HS X-ray tube. This system has a total filtration of 3 mm Al (i.e. inherent 0.5 and added 2.5 mm). Alongside a fixed anti-scatter grid (10:1 ratio, 40 line/cm frequency), this grid is commonly used in hospitals (Fauber, 2013). Due to the work within this PhD thesis focusing on paediatrics, no grid was used for any data acquisitions, except for on the 10 year-old phantom, as recommended by CEC (1996) and from discussions with experienced radiographers.

Equipment quality assurance testing was performed prior to image acquisition and included an assessment of voltage accuracy, exposure time, field size collimation and AEC sensitivity. In addition, the consistency of the radiation dose output from measuring different KVp and mAs levels were assessed. Testing followed IPEM 91 guidance (Institute of Physics and Engineering in Medicine (IPEM), 2005) and all results were found to be within expected manufacturer tolerances. See Tables (V-1-3) in appendix (V).

5.2.2 Image detector

A Konica Minolta Aero direct digital radiography (DR) imaging system was used in this research (model CS-7; Aero DR System, Konica Minolta Medical Imaging, USA INC, Wayne, NJ). This comprised of a caesium Iodide (CsI) image with a 1,994 x 2,430 pixel matrix. The pixel size was 175µm. The system has an in-built computerised calibration procedure. Within the timeframe of the study there were no error messages generated with regards to the automatic calibration of the Aero DR system. The system was also subject to routine testing by local medical physicists and by the manufacturer and was found to be operating normally.

5.2.3 Display monitors

Two 5 mega-pixel monochrome liquid crystal (LCD) monitors were used in this investigation to display the acquired images (Native resolution; 2560 x 2048). These monitors were DOME E5 (by NDSsi, Santa Rosa, Ca). The viewable image size of both these monitors was 23.2 inches. High resolution monitors were chosen to simulate a clinical reporting situation and improve the displaying conditions recommended for improved detection and interpretation (Norweck et al., 2013). These monitors are beyond the minimum specification suggested by The Royal College of Radiologists (The Royal College of Radiologists, 2012).

Each monitor self-calibrates to the standard grey scale once it is turned on. The Digital Imaging and Communications In Medicine (DICOM) grey scale standard display function (GSDF) was used, with a luminance of >400 cd/m² (National Electrical Manufacturers Association, 2006).

5.2.4 Phantoms

The phantoms used in generating the X-ray images for the optimisation study were the 1, 5 and 10 year-old paediatric pelvis phantoms previously constructed and validated. Full details on these phantoms together with the validation procedures are described in **chapter four**.

5.2.5 Dosimeter

Measurements of radiation dose were carried out using a solid-state dosimeter (Raysafe X2, Unfors Raysafe AB, Billdal, Sweden). The performance of the dosimeter was checked by periodic calibration procedures by local medical physicists (The Christie NHS Foundation Trust) and the results indicated that it was performing within its specification.

5.3 Data acquisition

5.3.1 Factorial study design

For the systematic optimisation of digital paediatric AP pelvis projections, all possible effects or combinations of the different acquisition factors needed to be considered within the study. The literature has identified that a factorial study design would be the most appropriate method for studying the combined effect of a number of different acquisition factors (such as tube potential and additional filtration) (Al Qaroot, Hogg, Twiste, & Howard, 2014; Båth, Håkansson, Hansson, & Månsson, 2005). Factorial designs are more efficient than experiments which focus on one factor at a time. Furthermore, they are necessary when interactions between the exposure factors might exist which could generate misleading conclusions. For example, increasing the SID whilst increasing the mAs would be counterproductive from a dosimetry and image quality perspective. Finally, the benefit of a factorial design is that it allows the estimation of the effects of a single factor whilst considering the influence of several other factors. This approach generally results in more valid conclusions when compared with ‘several experiments’ which attempt to investigate the same aim (Montgomery, 2013).

A previous factorial experiment study has shown a level of predictability for the influence of various parameters affecting image quality and radiation dose (Båth et al., 2005; Norrman & Persliden, 2005). Also, determining the factor with the highest impact on IQ and radiation dose allows for optimisation to be conducted in a more efficient fashion (Matthews & Brennan, 2009). This factorial method is led by the formula, n^k , wherein k represents the number of factors considered in the study (such as kVp, mAs, SID and filtration) and n represents the number of increments for each factor (such as the number of filtration levels used) (Montgomery, 2013; Mraity, 2015).

5.3.2 Experimental study design and procedure

The experimental set-up for acquiring the X-ray images from the three phantoms (1, 5 and 10 years old) is presented under this subheading. Two phantoms (1 and 5 years old), both required similar acquisition set-ups and so their methods are presented together. The 10 year-old

phantom had slightly different acquisition factors, so its method is described separately. The imaging pre-processing algorithm was set as paediatric hip/pelvis throughout the entire experiment.

The 1 and 5 year-old phantoms were placed directly in contact with the DR imaging plate, in an AP pelvis position with the feet positioned towards the anode. An anti-scatter radiation grid was not included for both of these phantoms. Collimation was limited to the pelvic area for each phantom. The exposure factors evaluated included tube potential (kVp), tube current-time (mAs), additional filtration and source to image distance (SID).

For the 1 year-old phantom, tube potential ranged from 50 to 80 kVp in 3 kVp increments. mAs covered the values from 1 to 10 (1, 2, 2.8, 4, 5, 6.3, 7.1, 8, 9 and 10). The SIDs used were 100, 115, 130 and 145 cm and additional filtration was set at three levels: zero, 2 mm Al and 1 mm Al + 0.1 mm Cu filtration. The total number of images generated from this exposure combination was 1320. For the 5 year-old phantom, the filtration and SID were the same as for the 1 year-old phantom, while the tube potential and mAs differed. For the 5 year-old phantom, the tube potential varied from 56 to 89 kVp in 3 kVp increments. The mAs values were from 1 to 16, in increments, and were selected according to those available on the x-ray panel (1, 2, 2.8, 4, 5, 6.3, 7.1, 8, 9, 10, 11, 12.5, 14 and 16). For this phantom the acquisition factor combinations generated 2016 images. Full details on the positioning of the phantoms are illustrated in Figures (5.1) and (5.2) (below).

For the phantom replicating a 10 year-old child, the acquisition parameters which were varied, including the tube potential, additional filtration and SID. The tube potential ranged from 59 to 89 kVp in 3 kVp increments. The additional filtration used was 0, 2 mm Al and 1 mm Al + 0.1 mm Cu. The SID range included 100, 115, 130 and 140 cm. All exposure factors were terminated using automatic exposure control (AEC); this was on the recommendation of radiographers, who stated that this would be common practice for children of this age in clinical practice. When using the AEC within the equipment available, this resulted in the inclusion of an anti-scatter radiation grid (oscillating). These exposure factor combinations were repeated for two different orientations: head away (HA) from the two outer AEC chambers, and head towards (HT) the two outer AEC chambers. For each orientation, three combinations of ionisation chambers were selected- all three chambers, the two outers chambers and the middle chamber. The total number of images generated from this phantom was 792. The full positional details for the imaging of this phantom are illustrated in Figure (5.3) below.

5.3.3 Acquisition factor selection

A factorial analysis was used for selecting the number of exposures produced from the available exposure factor combinations. The range of tube potentials, mAs, SID and additional filtration, were adopted from a paediatric imaging textbook in combination with the exposure factor range typically used in literature/clinical practice (Butler & Brennan, 2009; Knight, 2014). However, the range used in this thesis was developed to try to cover every possibility for reducing the dose whilst maintaining adequate image quality. Also, there were discussions with clinicians for the appropriate range and factor increments along with considerations as to what is available on the X-ray machine.



Figure 5.1: Experimental setup of the 1-year-old phantom, DR detector and X-ray tube.

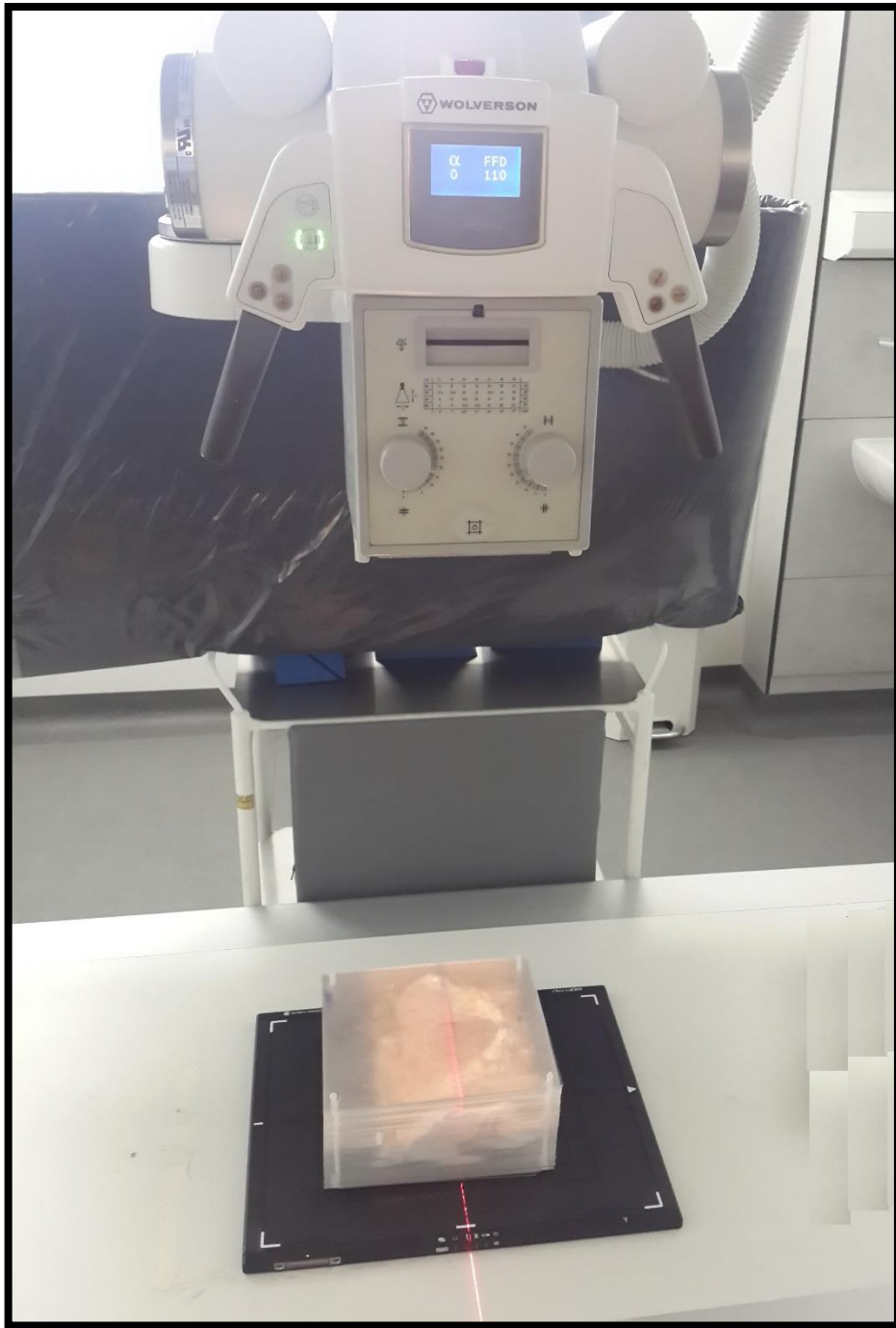


Figure 5.2: Experimental setup of the 5-year-old phantom, DR detector and X-ray tube.



Figure 5.3: Experimental setup of the 10-year-old phantom and X-ray tube. The table Bucky was used for **all** examinations involving this phantom.

5.4 Optimisation method

The optimisation process included assessments of IQ and radiation dose. The dose measurements were undertaken on the surface of each phantom (at the centre of the X-ray field) of each of the corresponding ages- 1, 5 and 10 years old. The image quality assessments used two methods- physical and visual evaluation. The physical image quality measurements involved the calculation of SNR and CNR. The visual image quality included the perceptual evaluation of image sharpness and the noise of the demonstrated bony anatomies in the pelvis

using relative visual grading. Using image quality and radiation dose data, a Figure of Merit (FOM) was drawn for all of the images from each phantom. The exposure/acquisition factor combination which delivered acceptable image quality with the lowest radiation dose was identified for each phantom age (called the optimised technique).

5.5 Dose measurements

The second part of the optimisation study was based around the dose measurements. Many dose quantities were considered before carrying out the respective dose measurements. It is reported in literature that there are large variations in the size of paediatric patients (1 to 15 years old). As reported by Hart and Wall in 2001, paediatric ages are usually grouped as 0, 1, 5, 10 and 15 years. Even within the same age group, children have considerable variation in size and this results in differences in the relationship between ESD and transmitted 'exiting' radiation, or image receptor dose (Hart & Wall, 2001). The effective dose consideration, for example, is limited to standard sizes within each age group (C. J. Martin, 2007a). Therefore, a decision was made to place a solid state dosimeter on the surface of each phantom and measure the incident air kerma dose (IAK) (C. J. Martin, 2007b). This provides a measurement of the dose delivered from each exposure and therefore a comparison can be made between the radiation dose and the image quality for each radiographic exposure (Compagnone, Pagan, & Bergamini, 2005). Since the dose measurements in this thesis are for comparisons between the doses for different exposure factor combinations, there was no need to include effective dose estimations and absolute assessments of radiation risk (Hufton et al., 1998). Also, by including ESD this would require the use of a BSF to convert IAK to ESD. This process can cause error since the BSF can vary in magnitude from 1.01 up to 1.7. Within in the literature there are limited publications covering all BSF possibilities (i.e. different collimation areas and tube potentials) (Petoussi-Hens et al., 1998).

Dose measurements were conducted for each exposure factor combination over the three paediatric pelvis phantoms (1, 5 and 10 years old). A solid-state dosimeter was positioned on the surface of each phantom, at the centre of the X-ray field over all the dose measurements-see Figure (5.4). To minimise random error, each measurement of incident air kerma was repeated three times and then the average and standard deviations were calculated for each exposure. A low standard deviation from each radiographic exposure measurement indicates acceptable reliability levels. This is a method for reliability evaluation that has been used previously (N. Jones et al., 2001).

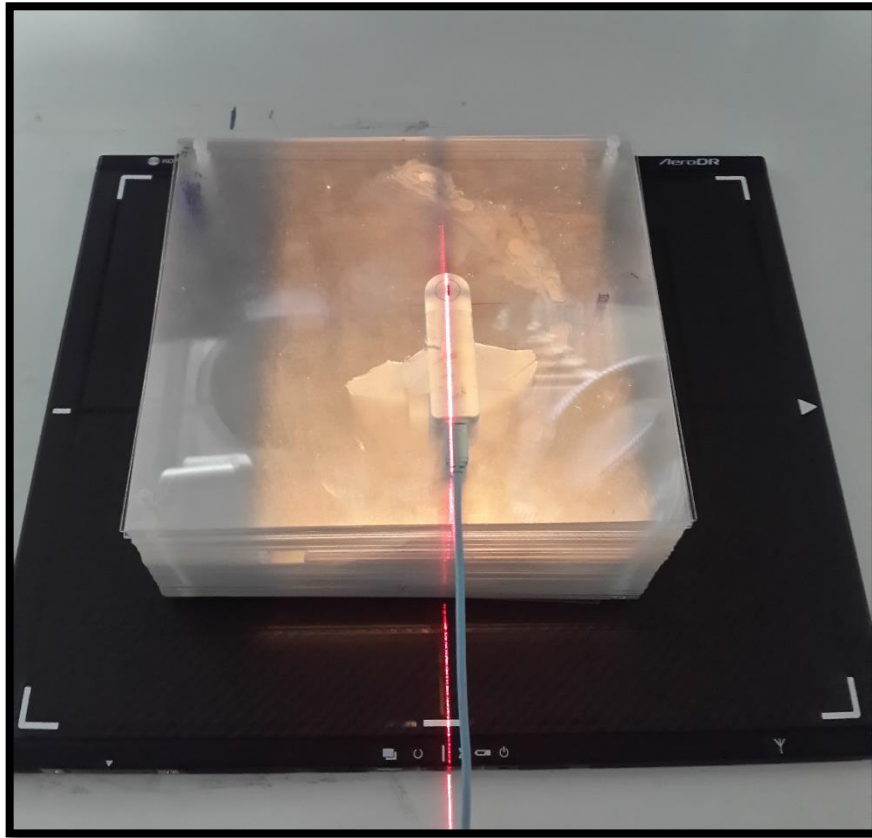


Figure 5.4: Experimental setup for the radiation dose measurements.

5.6 Image quality assessments

The IQ evaluation was undertaken using two methods, physical and visual, since they both evaluate different dimensions of IQ (Mraity, 2015). The physical measurements are represented by calculating SNR and CNR and the visual evaluations are represented by observers evaluating the sharpness and noise on the resultant images. For the visual assessments a relative VGA approach was used (Båth, 2010). Physical IQ was used to support the visual evaluation of IQ by assisting in the selection of the reference image (Bankier, De Maertelaer, Keyzer, & Gevenois, 1999; Mraity, 2015), in addition to examining the relationships between visual and physical IQ (for more details, see “Justification for a VGA approach” in Subsection 2.2.6.2.3, Chapter Two). The IQ clarity was used to refer to the opposite of noise in an X-ray image. This term was used to eliminate any confusion that might come from the opposite scoring that was undertaken during using the IQ scale. Figure (5.5) below provides a diagram explaining the process of assessing IQ.

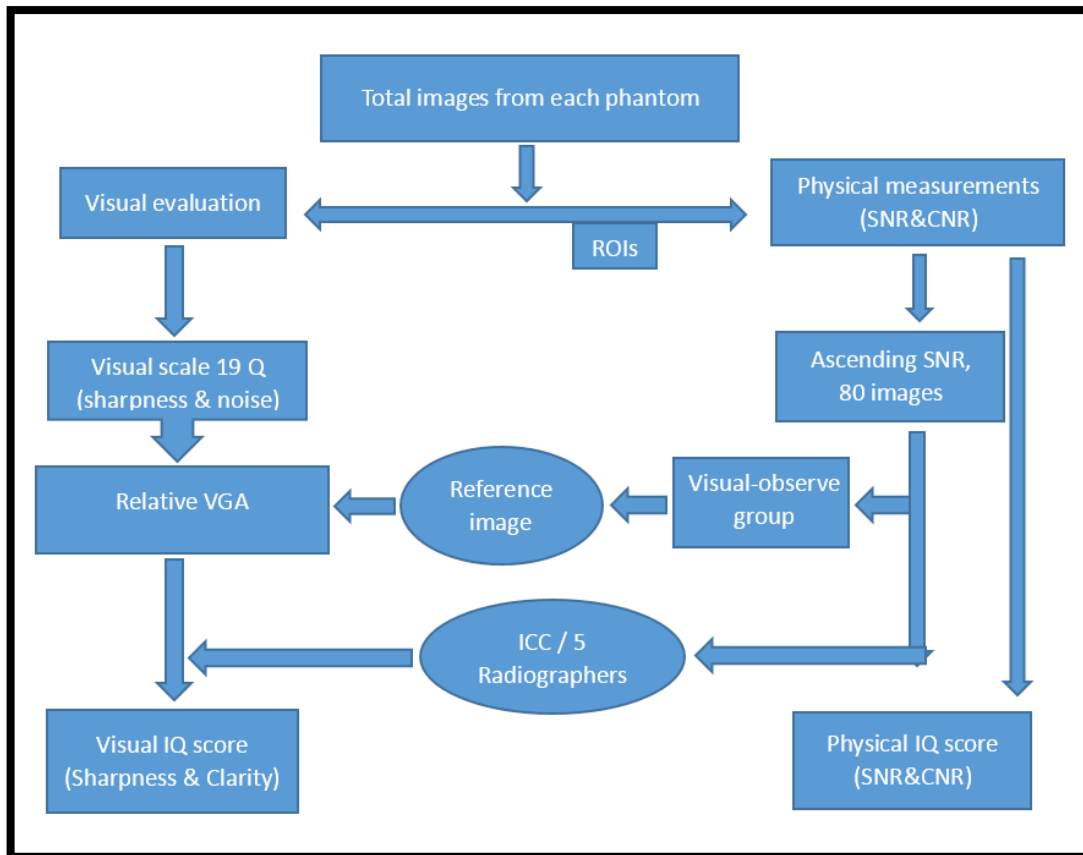


Figure 5.5: This diagram illustrates the processes of assessing the IQ (physical and visual).

5.6.1 Methods used for calculating the net score of image quality

In the literature, IQ scores, including visual and physical, have been used for evaluating X-ray images. In this thesis, the net visual score from each IQ criteria was calculated by taking the sum or average of all IQ criteria as a total IQ score for each image. Finally, the mean was taken from all observers to follow an approach consistent with similar studies reported in the literature (Mraity, 2015; Sandborg et al., 2006b; Tugwell et al., 2014). The same procedure was used for physical measurements. For SNR and CNR, several ROIs were used to calculate the mean as a net SNR and CNR for each image per exposure. Within the analysis, visual IQ data could have been treated as ordinal (Likert scale values). However, based on previous studies (Brennan, McDonnell, & O’Leary, 2004; C. J. Martin, Sharp, & Sutton, 1999; Mraity, 2015) and discussion within the research team, a decision was made to treat the total IQ scores as continuous data.

It is worth noting that IQ criteria are not equally weighted in clinical practice. Some anatomical areas may have a higher impact on the image due to their pathology frequency (Ismailos et al., 1996). For example, the hip joints may be more important than the sacroiliac joints in children.

Accordingly, weighting factors have been applied in some studies to account for this (Brennan & Madigan, 2000; Ismailos et al., 1996). In these studies, the weighting factor criteria were based on opinions' from [only] two radiologists and this is considered to be subjective. Despite the impact of the factoring method on the results, there is also a lack of detail in the literature describing the frequency of pathologies seen within the paediatric pelvis. Consequently, it would be difficult to derive weighting factors based on empirical evidence. In the study carried out by Gänsslen et al. (2013), they provided details of the fractures which can occur in the paediatric pelvis. The study did not report the frequency of pelvic injuries by anatomy. This supports the theory that currently the frequency of paediatric pelvis X-ray pathologies is not quantifiable. Thus, for this thesis, calculating the mean of the individual image quality scores appeared to be the most acceptable approach and the overall SNR evaluation method is similar to previous publications (Lin et al., 2012; Mraity, 2015; Sandborg et al., 2001).

5.6.2 Physical image quality evaluation

Physical measurements were carried out by calculating the SNR and CNR values from each image. In the literature, there are generally two methods for measuring the noise used in SNR calculations- noise from a homogenous background and from the ROIs over the anatomical areas. The measurements of the noise from each ROI itself follows the argument that the visibility of the anatomy might be affected by local 'anatomical' noise, regardless of the noise from the background (Båth et al., 2005; Mraity, 2015). On the other hand, SNR can be calculated from the mean of the signal divided by the surrounding noise (Bushberg et al., 2012; Desai et al., 2010; Rose, 1973). In this thesis, the ImageJ software (NIH, Maryland, US) was used to measure the mean signal (mean pixel value) and the standard deviation was taken as a measure of the noise from an homogenous background region (Bourne, 2010). Measurements of local noise (ROIs) were not included in the evaluation of IQ. This is because the visual image score was based on the anatomical sharpness of the soft tissue interface which considers the effect of background noise more than the noise inside the respective anatomies.

Within this thesis, several ROIs were placed at different pelvic locations on the resultant X-ray images for the 1, 5 and 10 year-old phantoms. In an attempt to evaluate the IQ over many locations, three of the total ROIs were placed in different positions over the soft tissue regions. From the soft tissue ROIs, only the ROI with median standard deviation was considered in the calculations (see Figures 5.6, 5.7 and 5.8 below). For all of the images, the ROIs locations were kept approximately the same so that the same part of the anatomy was measured for the mean signal and the noise. The mean pixel value of each ROI was taken as a measure of the mean

signal. The standard deviation (SD) from each ROI was taken as level of noise. Both mean pixel value and SD were placed in the equations (2.1) and (2.2) (from chapter two) to calculate the CNR and SNR, respectively. The net image quality was calculated by taking the mean of the ROI values for the bony anatomies, as described in the method mentioned in the previous subsection (5.6.1).



Figure 5.6: ROI measurements from the 1-year-old phantom using the ImageJ software.

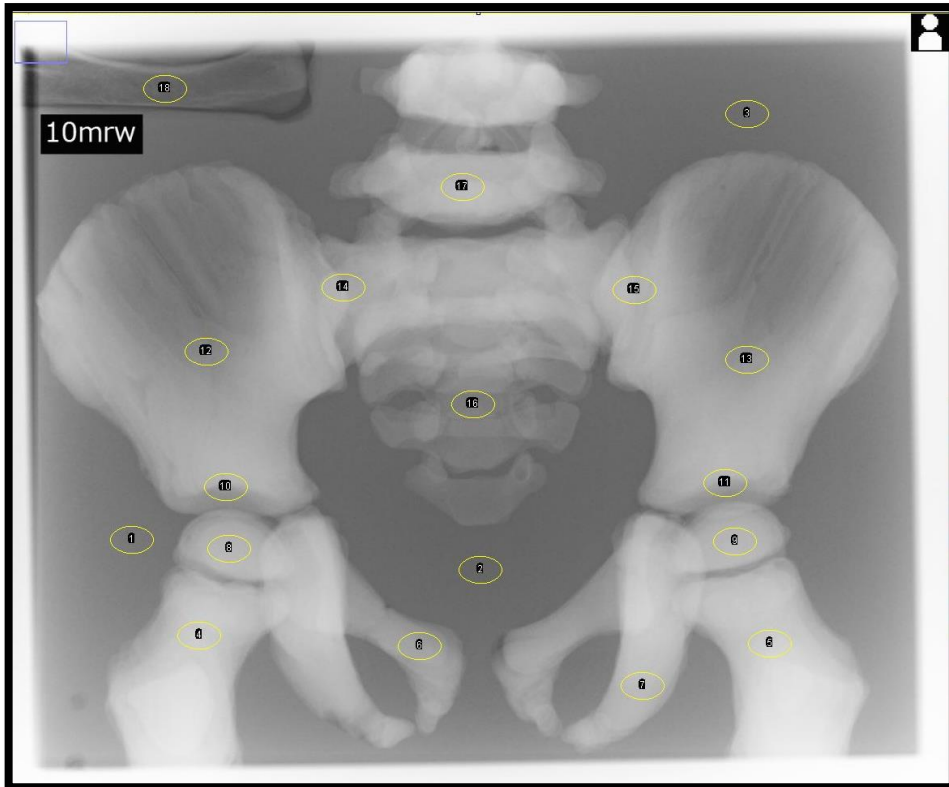


Figure 5.7: ROI measurements from the 5-year-old phantom using the ImageJ software.

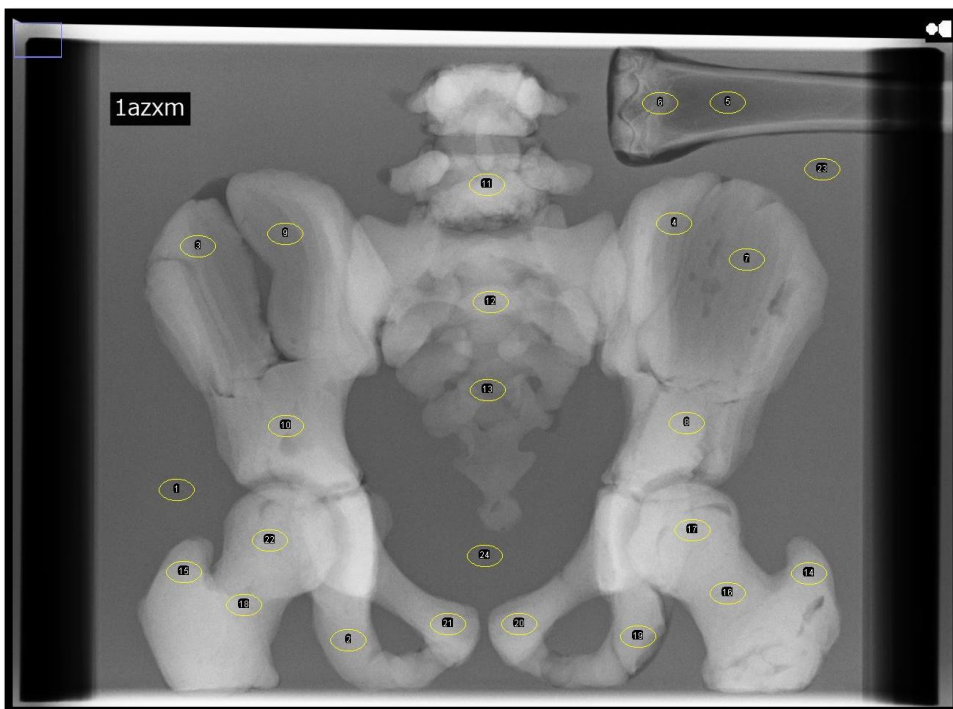


Figure 5.8: ROI measurements from the 10-year-old phantom using the ImageJ software.

5.6.3 Visual image quality evaluation

In this thesis images were coded to ensure that the observers were blinded to the acquisition parameters (the quality of the image). Images were perceptually assessed by means of a relative VGA (Båth, 2010; Mraity, 2015). This approach was selected for several reasons: first, for its high sensitivity to small changes between image quality levels; second, for its help in minimising subjective bias and variability between observers (Pelli & Farell, 1995); third, for its suitability for this thesis because of the questions that are asked in terms of the comparison of sharpness and noise between the ‘reference’ and ‘experimental’ images, which are not related to any pathological investigation.

Regarding the relative VGA method, the images from the paediatric pelvis phantoms were randomly displayed in a DICOM format using the software described by Hogg & Blindell (2012). A 3-point Likert scale was applied to assess the visual image quality. The observers were able to decide whether the sharpness level and noise level of specific regions of interest (pelvic bony anatomies) and the overall IQ were either worse (2), equal to (3), or better (4), than that of the reference image. There are advantages to choosing a 3-point Likert scale over a 5-point system. A 5-point scale might have higher sensitivity, since 5 choices are available to the reader, however, this could generate more inter-observer variability and have a negative effect on the results. Some observers might interpret ‘good’ as ‘excellent’ or ‘worse’ as ‘much worse’. In addition, the assumed symmetry between ‘excellent’ and ‘much worse’ might be affected, as for some observers ‘excellent’ is not as positive as ‘much worse’ is negative and as a result there will be some subjectivity (Keeble, Baxter, Gislason-Lee, Treadgold, & Davies, 2016).

For each of the three phantoms, images were displayed to observers using a set of imaging monitors. On the left-hand monitor there was a fixed reference image with a median IQ and on the right-hand monitor a set of images was randomly applied from the image bank of varying qualities- see Figure (5.9). A total of 19 questions were included in the observational study, considering those on sharpness and the noise of specific bony anatomies. The questions used in this thesis had previously been developed and validated by Mraity et al. (2016) (see Table (II-1) in the appendix (II)).

The reference image was chosen based on two steps: first, using physical IQ; and second, visual evaluation. Using physical measures of IQ (the SNR measurements were explained in the previous section) reduced the subjective bias in choosing a median IQ out of the full image

bank of approximately 2000 images. Selecting the reference image in this way would allow the observer to use the whole of the Likert scale and reduce skewness during scoring (Allen et al., 2013).

This selection procedure for a reference image was undertaken by ranking the images according to their physical IQ (SNR) score. The median for IQ scores was then determined and the image with the equivalent score was chosen as reference image. After this, a subset of 80 images was chosen covering all of the IQ range (lowest to highest). A similar approach was used by Mraity (2015) and it was supported by Lança et al. (2014). The second step involved forming a focus group to perform subjective checking of the 80 images to assess visual IQ. The selected reference image was checked to see whether it had an average image score amongst the 80 images. The aim was to confirm that the identified reference image demonstrated an intermediate level of sharpness and noise. If this was not the case then the choice would be directed to the next SNR score level, and so on until an acceptable middle visual score was found from the reference image. In addition, ambient light was dimmed to a level simulating clinical image evaluations- approximately 30 Lux (Norweck et al., 2013).

Of the 80 images of each phantom, the observer viewed the images and applied the criteria (image quality scale) whilst making a comparison against the reference image. During image viewing, the following were standardised in order to reduce error:

1. Room lighting was similar to that of a radiology reporting room (ambient, 30 Lux).
2. No time limits were imposed on the observers during image scoring task.
3. There were no restrictions on distance between the observer and the monitor.
4. There was no option to use an electronic magnifying glass and change the viewing properties of the image (contrast and brightness).

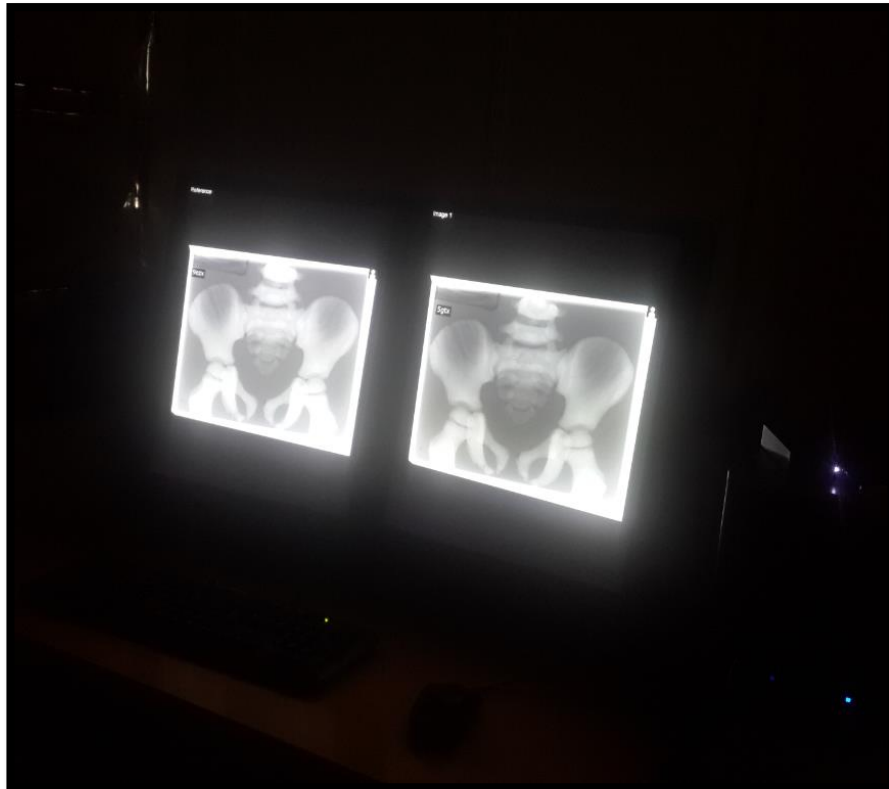


Figure 5.9: The relative VGA monitor set-up for the phantom X-ray images; on the left-hand the reference image and on the right the random image viewed.

5.6.3.1 Observer variability test

As reported in literature, during diagnostic radiology image viewing tasks variability between observations has been a widely reported phenomenon. Variability between observers could have a significant effect on accuracy (Manning, Gale, & Krupinski, 2005). This necessitates the use of several observers in any observational study.

For the 1, 5 and 10 year-old phantoms, data acquisitions yielded 1320, 2016 and 792 images, respectively. For such a large number it is not possible to ask all observers to perform a visual evaluation on all images. As a result, the lead researcher completed this task. Before this, a group of qualified diagnostic radiographers ($n=5$; with more than 5 years of post-qualification experience) undertook two sessions in evaluating IQ on a smaller sub-sample of the images. However, it was still important to make sure that the performance of the lead researcher and the subsequent variability would be within an acceptable range of agreement against the 5 radiographers. In doing so, the 80 images (described previously in subsection 5.6.3) were displayed to five radiographers and their individual responses were compared against the lead researcher's. In order to measure the lead researcher's agreement with the other radiographers, intra-class correlation coefficients (ICC) were calculated between the lead researcher and each

of the five radiographers individually (see Appendix (IV) for the ethical approval of this work). In addition, after the observation had finished, there was a further random sampling of 100 images from all of the images that were scored. This provided a quality assurance mechanism in order to check the performance of the observer at the end of the study (reliability). A series of images were rescored and the ICC was calculated to measure the intra-observer variability. Measurements of ICC were performed with the use of the computer software (SPSS Version 22, IBM corp., Armonk, USA). Guidance from the literature has suggested how ICC values can be interpreted. A value of less than 0.40 shows poor agreement; values of 0.40 to 0.75 show fair to very good agreement; and values greater than 0.75 show excellent agreement (Rosner, 2010).

The ICC results for the ‘sharpness’ criteria varied from 0.827 (95% CI 0.731 to 0.889) to a maximum of 0.937 (95% CI 0.886 to 0.963), while the ‘noise’ criteria showed a minimum ICC value of 0.93 (95% CI 0.874 to 0.959) and a maximum 0.971 (95% CI 0.947 to 0.983). The range of ICC shows, according to Rosner (2010), an excellent agreement against all observers. The results from repeating the scoring of the random sampled images (intra-observer variability) showed ICC values for sharpness at 0.757 (95% CI 0.477 to 0.87) and for noise at 0.847 (95% CI 0.69 to 0.915; see Table (II-2) in appendix (II)) (Rosner, 2010). These intra-observer ICC values are also within the excellent agreement range. The overall results of all the ICC experiments indicated that the lead researcher was competent in evaluating the images and could therefore score all of the images generated in this thesis.

5.6.3.2 Focus group – defining ‘acceptable’ image quality

The steps for defining optimisation were similar for all three phantoms of the corresponding ages; 1, 5 and 10 year-olds. After scoring all AP pelvis X-ray images from each phantom was done by the lead researcher (as explained in subsection 5.6.3), there was a need to determine whether the level of IQ was diagnostically acceptable. This is needed in order to help perform optimisation. The process of choosing an acceptable IQ for diagnostic purposes was undertaken via a focus group, so that observer consensus could be achieved. The aim of the focus group study was to identify the levels of IQ that consultant radiologists would agree on as being ‘diagnostically acceptable’. Two radiologists, with more than 30 years clinical experience each, had to indicate whether an image had adequate quality or not (a binary decision), see Appendix (IV) for the ethical approval of this work. This study consisted of choosing 84 X-ray images from each phantom and inviting the two radiologists to view and comment on them. The selected 84 X-ray images were of different visual IQ levels; ranging from the lowest to the

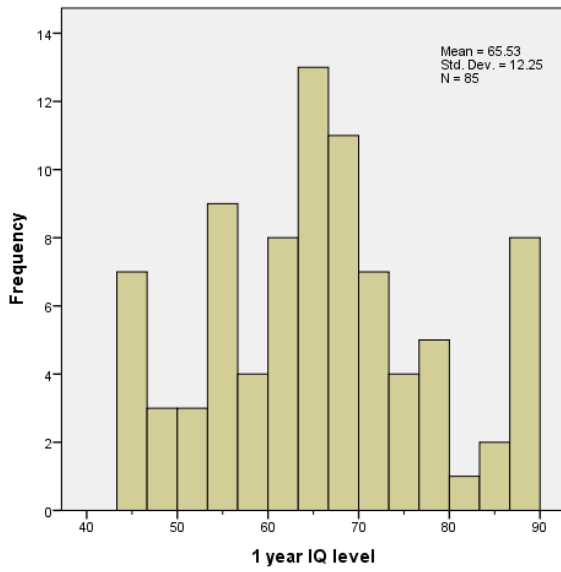
highest according to the visual scale (50% based on sharpness and noise IQ scale). The largest proportion (of the number of images out of the sample) of visual IQ scores represented the intermediate level of IQ. Where the higher and lower visual IQ score were around five images each, the rest were for the middle (intermediate) level. This distribution provided the opportunity for observers to score more images from the levels of IQ with the least consensus, see Figure (5.10) below. Therefore, more robust decisions on diagnostic IQ can be derived from this work.

Images were displayed in a randomised fashion by the use of the software described by Hogg & Blindell (2012), which is for a relative VGA technique, but without showing a reference image. Ambient lighting and the monitor type were kept the same for the visual scoring process.

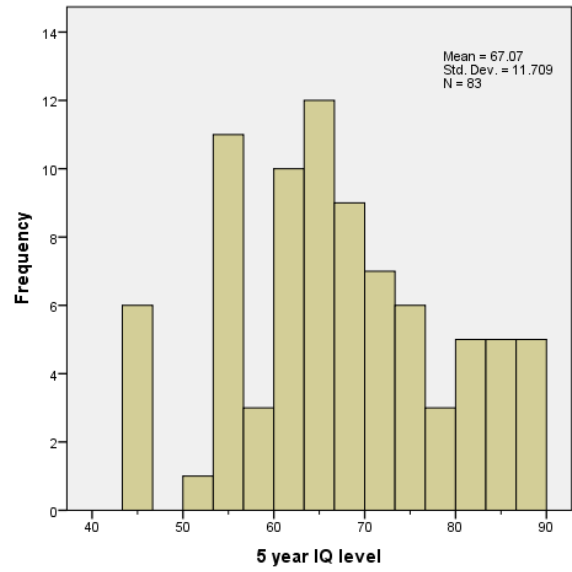
After the scoring of the 80 images from each phantom by the two radiologists, the levels of image quality were grouped into ranges. The percentage of agreement for each IQ group was calculated in order to make a decision on the lowest level of diagnostically acceptable visual IQ- see Table (5.1) below. Figure (5.11) describes the focus group study design in six steps.

Table 5.1: The percentage of agreement by the observers on each level of image quality for the 1, 5 and 10 year-old phantoms.

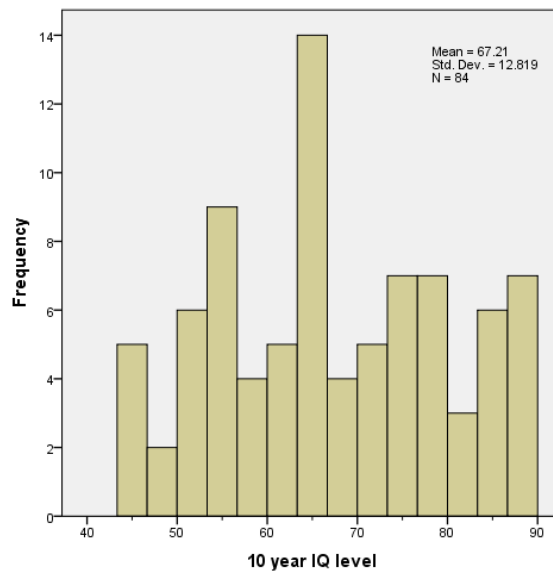
One year-old	Five year-old	Ten year-old
At 44 to 50 IQ level	At 44 to 50 IQ level	At 44 to 50 IQ level
50.00%	60.00%	100.00%
At 50 to 59 IQ level	At 50 to 59 IQ level	At 50 to 59 IQ level
100.00%	92.86%	100.00%
At 60 to 69 IQ level	At 60 to 69 IQ level	At 60 to 69 IQ level
100.00%	100.00%	100.00%
At 70 to 79 IQ level	At 70 to 79 IQ level	At 70 to 79 IQ level
72.73%	81.82%	100.00%
At 80 to 88 IQ level	At 80 to 88 IQ level	At 80 to 88 IQ level
83.33%	100.00%	90.00%



(a)



(b)



(c)

Figure 5.10: Distribution of IQ levels that chosen for the focus group (a), (b) and (c) are for the ages 1, 5 and 10 years, respectively.

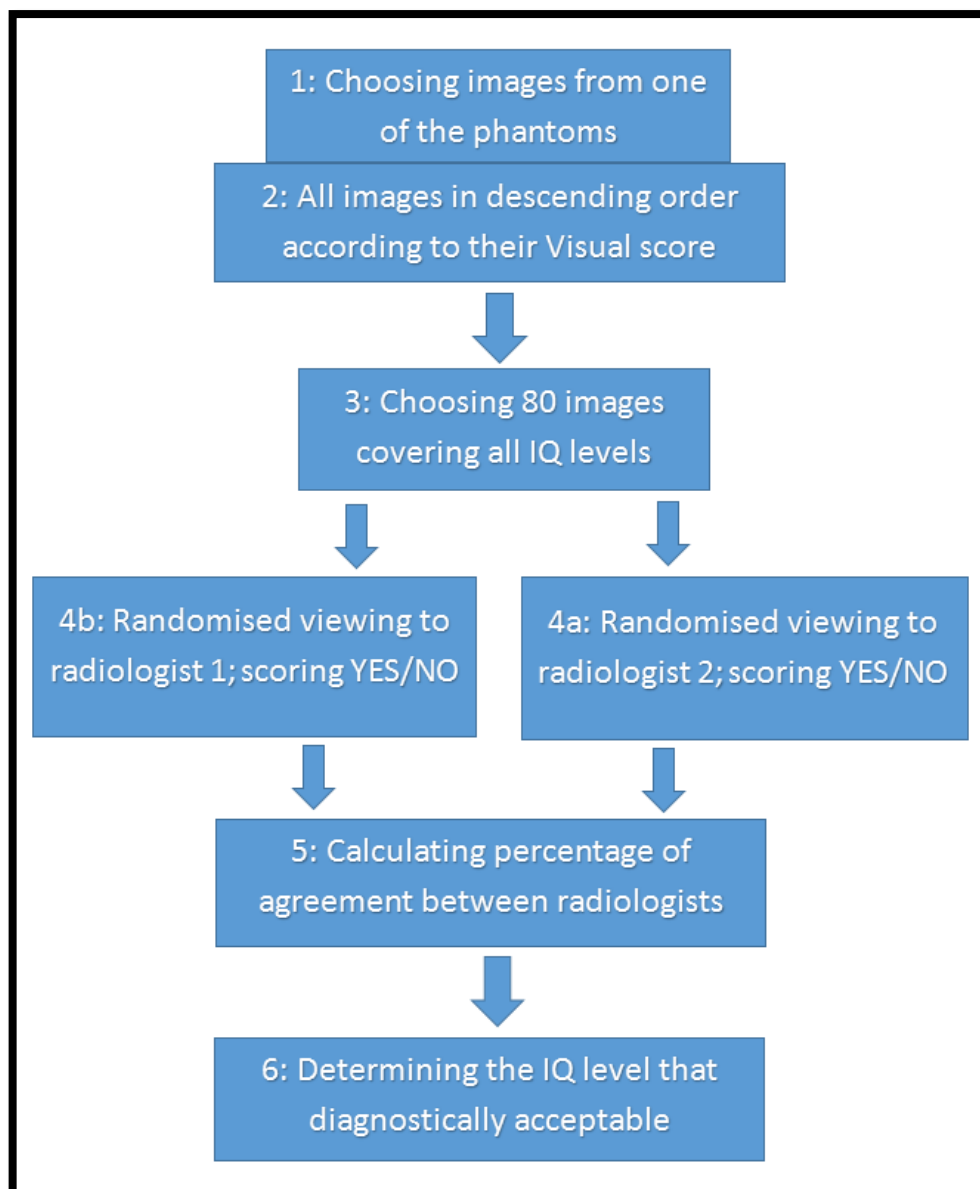


Figure 5.11: Flow diagram for the focus group study design.

5.7 Optimisation and Figure of Merit (FOM)

After undertaking the focus group study with the radiologists to determine which images had [clinically] acceptable IQ for each phantom age, the next step was to identify the images with clinically acceptable IQ levels to be used in the comparison with their doses for defining the optimum technique (lowest dose for acceptable IQ). In addition, an FOM was calculated for the visual and physical (SNR) IQ, since FOM is often described as the end point of the optimisation (Ehsan Samei, Dobbins, Lo, & Tornai, 2005). Initially, FoM can be described as a ratio of IQ to radiation dose, it is a single metric combining IQ and dose. The FOMs can provide an evaluation for assessing IQ to radiation dose trends (Mraity, 2015). The FOMs calculation was performed by dividing the ‘visual IQ score’ by the image’s ‘radiation dose’ - SNR was squared

and divided by the radiation dose (Ehsan Samei et al., 2005; Tugwell, England, & Hogg, 2017). These figures provide information that can be used to identify exposure factors with high IQ and low radiation dose, beside revealing the optimum technique for producing suitable IQ with a low radiation dose (Doyle et al., 2005; Mraity, 2015; Tugwell et al., 2017).

5.8 Data analysis

The statistical analysis included t-tests, correlations, multiple linear regression analyses and main effect scatterplots.

The t-test (or equivalent test) between two groups or, equivalent test for the case of more than two groups, was performed on the radiation dose and IQ metrics. Before conducting the statistical tests, a normality test determined whether to choose parametric or non-parametric testing, dependant on the Shapiro-Wilko P-value (a significant value, $P < 0.05$, meant non-normal distribution) (Field, 2013). The comparisons between similar subjects (such as orientation or ionisation chambers combinations) were considered as paired samples. A similar data categorisation method was undertaken in the literature (Manning-Stanley, Ward, & England, 2012).

Correlation tests were performed between IQ metrics, radiation dose and exposure factors in order to investigate level of coherence (or relationship strength) between them. Before performing the correlation tests, a test for normality was conducted in order to identify the type of correlation necessary. A p value of 0.05 was chosen as the significant level. All of the variables measured had non-normal distribution according to the Shapiro-Wilk statistic. All variables had significant Shapiro-Wilk P-values of < 0.05 . Similar results were found from the Kolmogorov-Smirnov statistics (see Table (II-3) in Appendix (II)). Accordingly, the correlation of Spearman's rho was used (Field, 2013). Correlation coefficient (r) values between -1 to +1 are considered as a perfect negative or positive match between the two variables, respectively. In absolute values, r 0.1 to 0.3 is considered as weak, r 0.3 to 0.5 is considered as moderate and r 0.5 to 1 is considered as large (Cohen, 1988; Field, 2013). Another interpretation of a correlation coefficient reported that r 0 to 0.3 and 0.5 to 0.7 should be considered as a moderate correlation. A value of r in the range 0.7 to 1 is considered as strong correlation and -1 or +1 is considered as a perfect match (Rumsey, 2011). The latter classification for the correlation coefficient was considered for the optimisation study, as it gives higher predictability threshold.

The regression test was conducted for each measured parameter (such as for visual sharpness, SNR and dose) whilst including the exposure factors as dependent variables. This was

performed to identify the size of the impact between the different exposure factors used in this study and to understand the type of relationship when combining them together. For a 10 year-old, a regression method was chosen with a free (non-zero) intercept, unlike the two younger ages (forced intercept with zero). The justification for this is because when the SID increases/decreases, it can reach zero or infinity within manual imaging, while with AEC imaging the generator would compensate to keep the quantity of radiation reaching the image detector the same. Thus, there is no possibility of assuming that the dose approaches zero at an infinite SID. The method used for constructing the regression model was the forced method (or Entry method, in SPSS). All predictors (independent variables) in this method were forced (or entered) simultaneously into the model. Within this approach there is no bias in the decisions regarding the order in which to enter variables and this is an advantage when compared to other methods. Also, this method includes no effect from the order of predictors on the estimation of the regression model (Field, 2013; Field, Miles, & Field, 2012). It is believed by some researchers that this method is the only appropriate method for testing theories (Studenmund & Cassidy, 1987). As stepwise techniques are affected by random variation in the data, they have a very low replicability rate of results when the model is reconstructed (Field et al., 2012). This makes the forced method highly suited to the analysis of this data type. This is because, when altering the exposure parameters (independent variables), there are many factors that can change the prediction of the IQ measures (dependent variables). First, the responses of anatomical visual appearance in X-ray images are influenced by complicated factors, including human vision which is unpredictable to some extent (Bankier et al., 1999). Second, there are the image processing algorithms that manipulate IQ (Körner et al., 2007). Third, the random generation of X-ray beam and random scattering of X-ray radiation, which also contributes to the randomised generation of X-ray images (Carroll, 2011; Menser et al., 2016).

The main effects factorial analysis is a relatively novel data analysis technique and has been used in radiographic IQ studies (Mraity, 2015). The calculations of the main effect of the acquisition factors (mAs, kVp and SID within different filtration levels) were performed, which allowed for the investigation of the impact on different response variables (i.e. IQ and radiation dose) when the settings increased (e.g. kVp from 56 to 89).

The main effect examination enables studying the effect of each level of exposure factor (e.g. mAs) on a dependent variable when the levels of other exposure factors (kVp and/or SID) interacted with a previous level. The main effect test also shows which exposure factor has a higher impact (radiation dose, FOM and IQ) (Mraity, 2015). The output analysis of the main

effect is a plot of dependent variable means against the various levels of each exposure factor increments. All the statistical analysis tests were constructed using the software package SPSS Version 23 (IBM Inc, Armonk, NY).

5.9 Chapter summary

In summary, this chapter presents the method for the optimisation of paediatric pelvic radiography for 1, 5 and 10 year-olds. The method described is using a factorial design for data acquisition. This was performed using a range of different exposure parameters (kVp, mAs, SID and filtration) for each paediatric age. Within the presented method, for all generated images, IQ evaluations were performed (visual and physical) alongside dose measurements for each combination of exposure factors.

After this stage, a figure of merit was calculated for each paediatric age in order to determine the images with diagnostically acceptable IQ and an ‘as low as possible’ radiation dose. Then, the statistical tests, namely correlation, regression and main effect plots for each age, were performed. The correlation test was conducted to find the strength in the relationship between the exposure factors and of the radiation dose, visual and physical IQ, as well as the correlation between the recorded metrics themselves. The regression model was constructed as a statistical method for investigating the impact and the interplay of the exposure factors on IQ metrics and radiation doses. Finally, the main effects factorial analysis was conducted in order to investigate the overall effect from each exposure factor on visual and physical IQ measurements.

Chapter Six: Optimisation Results

6.1 Chapter overview

This chapter contains the results of the dose optimisation study. The results are presented in two main sections: 1) The optimisation of the AP paediatric pelvis radiographic examination and exposure factor effects for paediatric pelvic radiography; 2) main effect analysis, correlation and regression.

The first section describes the data acquired from the optimisation study that identified the optimum techniques (those that produced lowest the possible radiation doses). This includes identifying the optimum acquisition factors (kVp, mAs and SID combined with different additional filtration levels) along with their corresponding radiation doses. In addition, the section also includes an investigation into the reliability of SNR and CNR values in identifying acceptable IQ.

The first part of the second section focuses on understanding general trends between exposure factors and the measured parameters (i.e. IQ or radiation dose). This was undertaken using main effect analysis. Thus, the effect of the exposure factors on IQ measures and radiation dose were shown and explained by main effect plots. Also, a Figure of Merit (FOM) will be included for the evaluation of physical and visual IQ with the resultant radiation dose.

The second part of the second section investigates correlations between exposure factors and the measured parameters (SNR, CNR, visual IQ and radiation dose), and between the measured parameters themselves. Accordingly, correlation tests were conducted to study possible predictions and correlations from the aforementioned variables. The correlation results were classified according to the classification of correlation coefficient ranges- no correlation, weak correlation, intermediate correlation and strong correlation.

The last part in the second section considers the regression analysis constructed for each measured variable (i.e. dose or IQ), as the dependent variable and all the exposure factors were inserted as independent variables. The data from this test were presented in the form of the impact/gradient (β) of each independent variable (exposure factor), and in the form of the β ratio between any two exposure factors, to evaluate their proportions and relative proportions.

The analyses of the aforementioned sections will provide greater understanding as to how to carry out a systematic manipulation of the acquisition factors to optimise the X-ray imaging practice.

6.2 Optimisation of AP paediatric pelvis radiography

As mentioned earlier in the method chapter, the data collection was performed for paediatric 1, 5 and 10 year-olds. The images were acquired using paediatric pelvis phantoms that were specially constructed and validated (see page 89, chapter four). Data acquired for this study included measurements of radiation dose (IAK) and IQ; physical (SNR and CNR) and visual (sharpness and clarity). For the optimisation results, the sharpness and clarity were combined into a single metric. This combination was necessary, since determining diagnostically acceptable IQ for optimisation is linked to clinical practices and is usually a binary decision—either ‘acceptable’ or ‘not acceptable’ (CEC, 1996; Manning-Stanley et al., 2012; L. Martin et al., 2013). For the three phantoms in this thesis, a small focus group study was conducted to identify the level of clinically acceptable IQ for each age group (1, 5 and 10 years).

The optimum exposure combinations for 1, 5 and 10 year-old phantoms are listed in Tables (6.1 to 6.3) along with the next four lowest doses from each age. The reason for providing the lowest five doses is to help in identifying alternative techniques when a case requires for it. The doses of each exposure were included to understand the corresponding level of radiation exposure from each exposure factor combination, as well as to compare them with the dose measurements usually found in practice (such as the DAP). The mean SNR and CNR are also included to investigate whether there is an option to define *acceptable* IQ from the physical IQ metrics. Within clinical practice it is important to understand whether physical IQ metrics are suitable indicators of diagnostic IQ.

6.2.1 Optimisation for a 1 year-old

After finishing the visual scoring of the 1 year-old phantom images, a focus group study was undertaken to determine the minimum IQ level that provided diagnostically acceptable images. The focus group study showed that the lowest mean score of IQ (sharpness & clarity) that can provide clinically acceptable IQ was 50.8 [score range = 44-88] (mean criteria/item score = 2.30 [criteria/item range = 2-4]). This level of IQ was based on the percentage of agreement found from the focus group study— see Table (5.1) in the Optimisation Methods Chapter (see page 156, Chapter Five).

The five optimum (lowest dose) exposure factors with their associated IQ metrics and doses are listed in Table (6.1). Data analysis for the 1 year-old phantom showed that the five dose optimised exposure factor combinations were 53, 59 and 65 kVp, each with 1 mm Al + 0.1 mm

Cu additional filtration. The radiation dose ranged from 15.31 to 25.9 μGy . The exposure factors which produced the lowest dose were 65 kVp, 2 mAs and 115 cm SID.

Also, the optimisation study showed that the minimum SNR and CNR required for optimum image quality can be reliable factors in determining visually acceptable IQ during the imaging of a 1 year-old phantom. This is linked to a statistical test which was conducted to find whether the physical IQ (SNR and CNR) taken from images which were ‘*acceptable*’ when compared to those which were ‘*non-acceptable*’ by the focus group were statistically different. To achieve this, a normality test was conducted, wherein the Shapiro-Wilk test showed an abnormal distribution for the SNR and CNR values ($P < 0.001$). Accordingly, the Mann-Whitney U test was performed; it showed a statistically significant difference ($P < 0.001$) for each of the physical measures when comparing *acceptable* and *non-acceptable* visual IQ. The median and Inter-Quartile Range (IQR) SNR values for acceptable and non-acceptable image quality were 113.1 and 48.88, respectively. The median and IQR CNR for acceptable and non-acceptable image quality were 864 and 454, respectively. In addition, histogram plots comparing SNR and CNR values for acceptable and non-acceptable visual image quality were constructed. A small amount of overlap in SNR and CNR values was seen between the diagnostic and non-diagnostic image qualities (Figure 6.1).

Table 6.1: Exposure factors that scored the five lowest doses with acceptable image quality (1-year-old).

1-year-old													
Dose rank	kVp	mAs	SID (cm)	Filter (mm)	IAK (μGy)	DAP (mGy cm^2)	SNR _{ave}	CNR _{ave}	IQ _{sh}	IQ _{cl}	IQ _{visual}	FOM _{SNR}	FOM _{visual}
1	65	2	115	1 Al + 0.1 Cu	15.31	4	52.77	14.54	4.00	4.00	4.00	181.81	0.26
2	65	5	145	1 Al + 0.1 Cu	23.93	7	67.83	19.18	2.36	3.00	2.68	192.25	0.11
3	53	7.1	145	2 AL	24.64	7	51.53	18.88	3.91	2.00	2.95	107.79	0.12
4	59	6.3	130	1 Al + 0.1 Cu	25.68	8	76.06	23.44	3.00	3.00	3.00	225.29	0.12
5	59	8	145	1 Al + 0.1 Cu	25.9	8	70.15	22.25	3.82	2	2.9	190.02	0.11

IQ_{sh}: IQ clarity, IQ_{cl}: clarity, IQ_{visual}: Average (IQ sharpness and IQ clarity), FOM_{SNR}: SNR²/dose, FOM_{visual}: IQ_{visual}/dose, SNR_{ave}: Average SNR & CNR_{ave}: Average CNR.

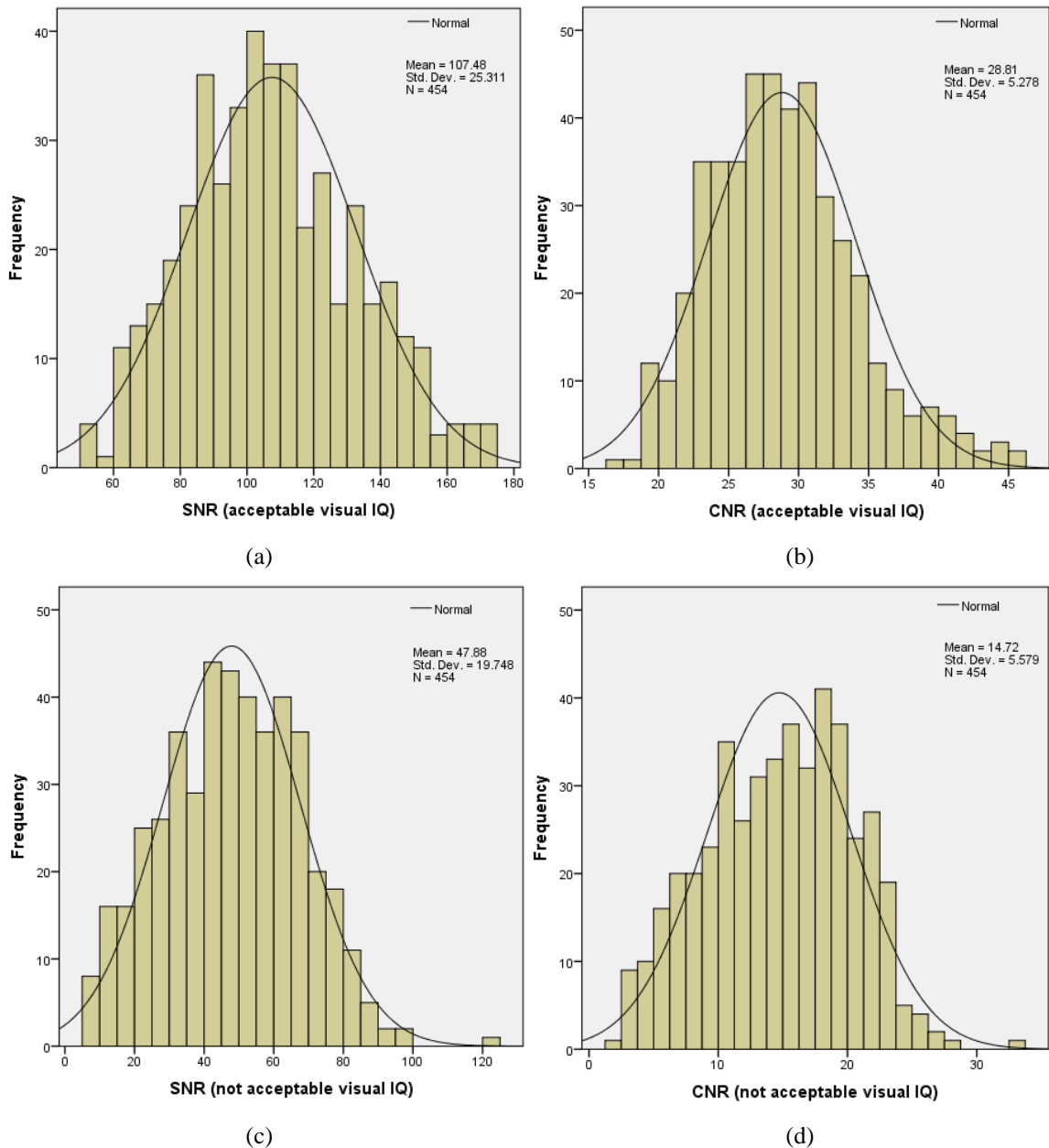


Figure 6.1: Histogram of SNR and CNR overlap between acceptable and non-acceptable image quality (1-year-old); (a) and (b) are measured from acceptable image quality, while (c) and (d) are measured from not acceptable image quality.

6.2.2 Optimisation for a 5 year-old

After finishing the visual scoring for the 5 year-old phantom images using a relative-VGA method, a focus group study was undertaken to determine the diagnostically acceptable level of IQ. The focus group study showed that the lowest mean score of IQ (sharpness & clarity) that can provide clinically acceptable IQ was 50.9 [score range = 44-88] (mean criteria/item score = 2.3 [criteria/item range = 2-4]). This IQ level was chosen through considering the percentage of agreement found between the scores of two expert radiologists- see Table (5.1) in the Optimisation Methods chapter (page 156).

The optimisation study for the five year-old showed that the lowest five radiation doses were 56, 59, 62 and 74 kVp, all with 1 mm Al + 0.1 mm Cu additional filtration. The resultant radiation doses ranged from 42.9 to 49.1 μ Gy and the associated exposure factors are listed in Table (6.2). The lowest dose exposure factor combination was 62 kVp, 8 mAs and 130 cm SID with added filtration of 1 mm Al + 0.1 mm Cu.

The optimisation study showed that defining minimum SNR and CNR values that are required for optimum IQ can be a reliable indicator for determining visually acceptable IQ (5 year-old). This was determined using a statistical test and was conducted to find whether there is a statistically significant difference within the physical IQ measures (SNR and CNR) taken from images with acceptable visual IQ, in comparison to those with non-acceptable visual IQ. The Shapiro-Wilk test showed that the distribution of SNR and CNR values were not normal ($P < 0.001$). Therefore, the Mann-Whitney U test was conducted; this showed a statistically significant difference ($P < 0.001$) in SNR and CNR when compared between acceptable and non-acceptable visual image quality. The median and IQR of SNR for acceptable and non-acceptable image quality were 84.89 and 47.76, respectively, while the median and IQR of CNR for acceptable and non-acceptable IQ were 23.09 and 14.39, respectively. In addition, a histogram (SNR and CNR) compared acceptable and non-acceptable visual IQ. A small overlap in the SNR and CNR values was seen between the diagnostic and non-diagnostic IQ (see Figure 6.2).

Table 6.2: Exposure factors that scored the five lowest doses with acceptable IQ (5 year-old).

Optimum acquisitions: 5 year-old													
Dose rank	kVp	mAs	SID (cm)	Filter (mm)	IAK (μ Gy)	DAP (mGy cm^2)	SNR _{av}	CNR _{av}	IQ _{sh}	IQ _{cl}	IQ _{visual}	FOM _{SNR}	FOM _{visual}
1	62	8	130	1 Al + 0.1 Cu	42.95	14	52.33	18.29	2	3	2.5	63.76	0.06
2	59	10	130	1 Al + 0.1 Cu	44.17	14	51.53	19.52	2	3	2.5	60.12	0.07
3	56	16	145	1 Al + 0.1 Cu	45.38	15	55.09	22.36	3.73	2	2.86	66.88	0.06
4	59	14	145	1 Al + 0.1 Cu	48.27	16	58.06	21.84	2.82	3	2.91	69.85	0.06
5	74	5	130	1 Al + 0.1 Cu	49.12	15	59.78	15.30	2	3	2.5	72.76	0.05

IQ_{sh}: IQ clarity, IQ_{cl}: IQ clarity, IQ_{visual}: Average (IQ sharpness and IQ clarity), FOM_{SNR}: SNR² /dose, FOM_{visual}: IQ_{visual} /dose, SNR_{ave}: Average SNR & CNR_{ave}: Average CNR

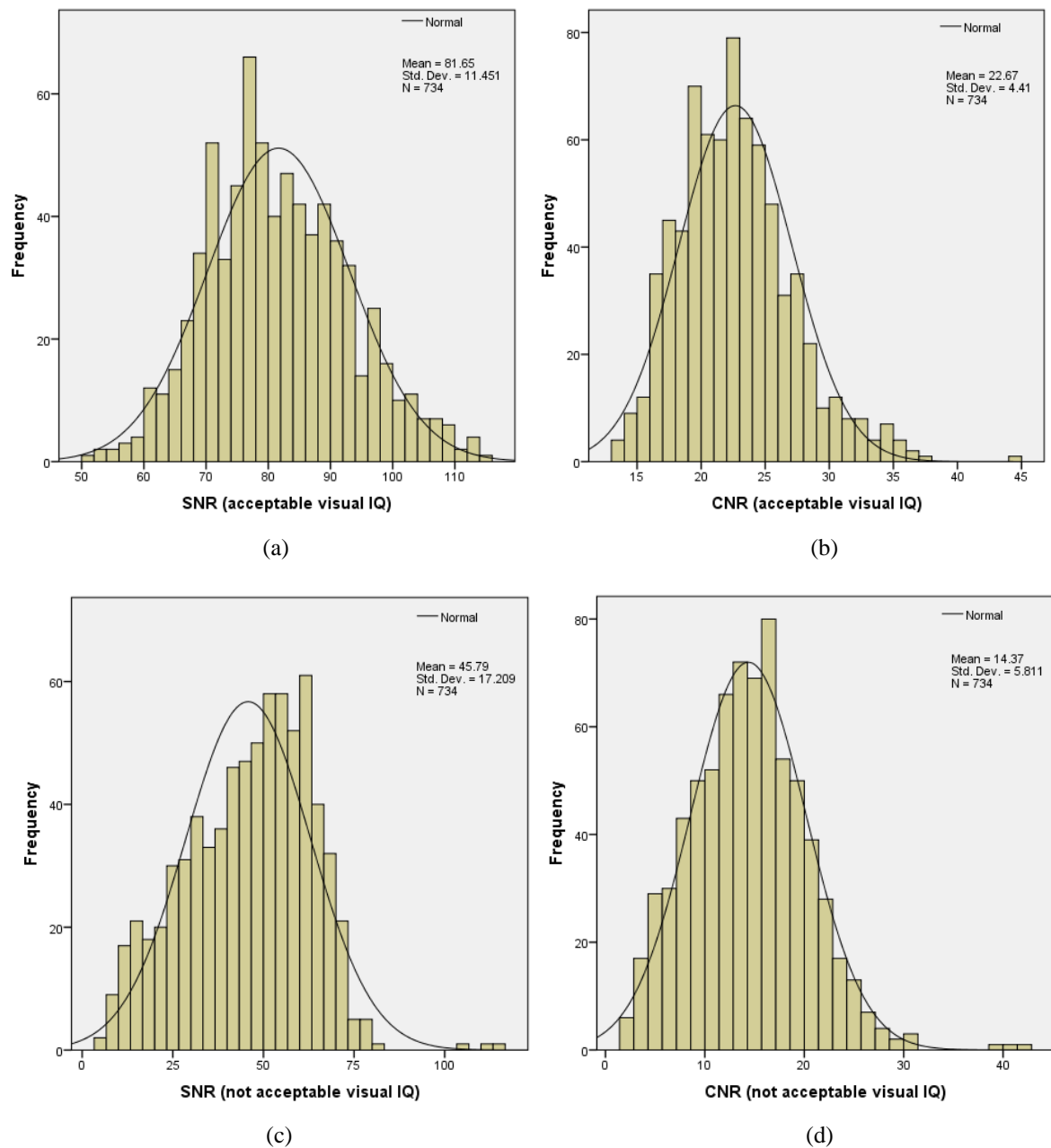


Figure 6.2: Histogram of SNR and CNR overlap between acceptable and non-acceptable image quality (5 year-old); (a) and (b) are measured from acceptable image quality, while (c) and (d) are measured from not acceptable image quality.

6.2.3 Optimisation for a 10 year-old

The focus group study for the 10 year-old phantom imaging optimisation showed that all of the images were of acceptable IQ for diagnostic purposes (Table (5.1), page 156, Optimisation Methods chapter). The optimisation study showed that the five optimum (lowest dose) exposure factor combinations were at 89 kVp, with the lowest one being 89 kVp, 130 cm SID; 1 mm Al + 0.1 mm Cu additional filtration and with the orientation of HT the two outer chambers- see

Table (6.3). The five lowest radiation doses ranged from 178.77 to 193.17 μGy and they had 1 mm Al + 0.1 mm Cu filtration. The optimisation study was undertaken for the two orientations HT and HA, however the lowest doses (up to ninth place) were for the HT orientation. The study also showed that the chamber combinations two outer and all three chambers scored the lowest doses (up to ninth lowest doses).

Table 6.3: Exposure factors that scored the five lowest doses with acceptable IQ (10 year-old).

Optimum acquisitions (AEC): 10 year-old														
Dose rank	kVp	SID	Filter (mm)	Chambers	Or	IAK (μGy)	DAP (mGy cm^2)	SNR _{ave}	CNR _{ave}	IQ _{sh}	IQ _{cl}	IQ _{visual}	FOM _{SNR}	FOM _{Visual}
1	89	130	1 Al + 0.1 Cu	Both outer	HT	178.77	73	50.04	17.92	2.00	2.00	2.00	14.01	0.01
2	89	115	1 Al + 0.1 Cu	Both outer	HT	184.07	74	48.39	16.20	2.00	3.00	2.50	12.72	0.01
3	89	130	1 Al + 0.1 Cu	All	HT	187.53	77	51.51	18.48	2.00	2.00	2.00	14.15	0.01
4	89	140	1 Al + 0.1 Cu	Both outer	HT	188.57	73	49.96	17.26	2.00	2.00	2.00	13.24	0.01
5	89	115	1 Al + 0.1 Cu	All	HT	193.17	78	50.29	16.68	2	2	2	13.09	0.01

Or: Orientation, IQ_{sh}: IQ sharpness, IQ_{cl}: IQ clarity, IQ_{visual}: Average (IQ sharpness and IQ clarity), FOM_{SNR}: SNR² /dose, FOM_{visual}: IQ_{visual} /dose, SNR_{ave}: Average SNR & CNR_{ave}: Average CNR

6.3 Exposure factors effect on paediatric radiography

Following the factorial analysis that was used for the optimisation study, a main effect analysis was used for investigating the effect of each exposure factor (kVp, mAs, SID and additional filtration). For each of the three pelvis phantoms, the trends between exposure factors and IQ, radiation dose and Figure of Merit (FOM) were investigated using main effect plots. The main effect analysis (1 & 5 year-old phantoms) for FOM (SNR and visual) included only the data of acceptable IQ. This was to investigate the indices for optimisation. The main effect plots for IQ and radiation dose included all levels of IQ (acceptable and non-acceptable) to understand the effect on the whole IQ range. The main effect plots for exposure factors of 10-year-old phantoms only included acceptable image qualities (due to the nature of the data collected). The main effect plots contained the mean of each measured parameter such as image quality, radiation dose and Figure of Merit (FOM) versus the exposure factor.

Regarding the study for the 10 year-old phantom, comparison (in term of dose) between the two orientations (HT and HA) was conducted by performing a t-test between two paired samples. This was to eliminate the orientation with the highest dose from main effect, correlation and regression analyses. No comparisons were needed in terms of IQ, as all the images from both orientations were of visually acceptable IQ for the purpose of diagnosis. First, a normality test was performed on each group along with the difference between them; this showed a non-normal distribution (Shapiro-Wilk test, $P < 0.001$). The Wilcoxon signed ranks test showed a significant difference in doses between the two orientations ($p < 0.05$). The HT orientation showed a lower dose than HA in terms of median and percentile values (see Table 6.4). Therefore, the HA orientation was removed from the analysis of the exposure factors' effect on image quality, radiation dose and FOM.

Table 6.4: the 10-year-old radiation doses and image quality produced for each orientation.

		Dose (HT) in μGy	Dose (HA) in μGy
Wilcoxon test		P<0.05	
Mean		421.81	516.63
SD		180.83	237.37
Median		370.25	452.63
Minimum		178.77	204.30
Maximum		1179.33	1760.37
Percentiles	25 th	285.18	336.41
	75 th	513.53	635.75
		Diagnostic IQ (HT)	Diagnostic IQ (HA)
Wilcoxon test		P<0.05	
Mean		3.17	3.42
SD		0.60	0.68
Median		3.05	3.89
Minimum		2.00	2.00
Maximum		4.00	4.00
Percentiles	25 th	2.75	2.84
	75 th	3.66	4.00

In addition, regarding the 10 year-old phantom study, a comparison in terms of the radiation dose between the three chamber combinations was conducted in order to identify which AEC

chamber combination produced the statistically lowest radiation dose (to be included in the main effect, correlation and regression analyses). Since all of the chamber combinations produced acceptable IQ for clinical use, there was no need to perform a test for IQ. Accordingly, statistical tests, in terms of radiation dose, were conducted after testing the distribution of the radiation dose data from each ionisation chamber combination. The normality investigation showed a non-normal distribution (Shapiro-Wilk test; $p < 0.001$). Therefore, a non-parametric paired (Friedman) test was conducted to investigate the difference between the three chamber combinations, and a Wilcoxon signed ranks investigated the differences between each two chamber combinations. The results of the Friedman test showed that there was a significant difference in terms of radiation dose between the three chamber combinations ($p < 0.001$). The results of the Wilcoxon signed ranks test showed that there were significant differences between each of the two chamber combinations ($p < 0.001$). The median (including IQR) radiation doses for the two outer chambers scored the lowest dose amongst the other chamber combinations (see Table 6.5) and hence it was considered when analysing the effect of exposure factors on optimisation.

The exclusion of higher dose techniques from the correlation, main effect and regression analyses (HA orientation and AEC chamber combinations) would draw attention towards the radiographic techniques that matter in terms of dose reduction, which is the central theme of this thesis. The imaging techniques with higher doses would not be recommended for use in clinical practice, according to the results from this thesis.

Table 6.5: the 10-year-old phantom - radiation dose and image quality produced over each combination of ionisation chambers at HT orientation.

		Radiation dose at middle Chamber (μGy)	Radiation dose at two outers (μGy)	Radiation dose at three chambers (μGy)
Mean		473.70	381.92	409.81
SD		207.43	151.43	167.86
Median		414.80	341.38	360.80
Minimum		205.43	178.77	187.53
Maximum		1179.33	907.73	989.43
Percentiles	25 th	314.41	264.02	276.22
	75 th	581.77	464.74	498.13

		Diagnostic IQ at middle Chamber	Diagnostic IQ at two outer chambers	Diagnostic IQ at three chambers
Mean		3.23	3.12	3.16
SD		0.66	0.55	0.58
Median		3.25	3.05	3.00
Minimum		2.00	2.00	2.00
Maximum		4.00	4.00	4.00
Percentiles	25 th	2.66	2.82	2.78
	75 th	3.94	3.50	3.61

6.3.1 Main effect analysis

The main effect analysis was performed for the three phantom ages. For the 1 year old, the analysis of variance showed that all the exposure factors have a significant impact on radiation dose, FOM, visual IQ and physical IQ across all filtration levels ($P < 0.05$). This was with the exception of two cases of mAs main effect analyses which did not impact significantly: first, FOM (SNR) with additional filtration of 0.1 mm Cu + 1 mm Al; and second, FOM (visual IQ) with 2 mm additional Al ($P > 0.05$). For the 5 year-old, the analysis of the variance showed that all the exposure factors have a significant impact on radiation dose, FOM, visual IQ and physical IQ across all filtration levels ($P < 0.05$). Data from both the 1 and 5 year-old phantoms showed that both SID and filtration have a significant impact on IQ and radiation dose (Friedman test; $p < 0.05$).

For the 10 year-old phantom, the results showed that all of the exposure factors have a significant impact on the radiation dose, FOM, visual IQ and physical IQ over all filtration levels ($P < 0.05$). This was with exception of the main effect analysis for the following exposure factors (see Table (6.6) below).

Table 6.6: Exposure factors with a non-significant ($P > 0.05$) impact on measured parameters for the 10-year-old phantom.

<u>Exposure factor</u>	<u>Investigated parameter</u>	<u>Filtration level</u>
kVp	FOM (SNR)	0
kVp	FOM (SNR)	2 mm Al
SID	FOM (visual IQ)	0
SID	FOM (visual IQ)	2 mm Al
SID	IQ (sharpness & clarity)	0

SID	IQ (sharpness & clarity)	2 mm Al
SID	IQ (sharpness & clarity)	0.1 mm Cu + 1 mm Al
SID	IQ (clarity)	0
SID	IQ (clarity)	2 mm Al
SID	IQ (clarity)	0.1 mm Cu + 1 mm Al
SID	IQ (sharpness)	0
SID	IQ (sharpness)	2 mm Al
SID	IQ (sharpness)	0.1 mm Cu + 1 mm Al
SID	DAP	0
SID	DAP	2 mm Al
SID	DAP	0.1 mm Cu + 1 mm Al
SID	Dose	0
SID	Dose	2 mm Al
SID	Dose	0.1 mm Cu + 1 mm Al

6.3.1.1 Main effect from tube potential (kVp)

Data from the 1, 5 and 10 year-old phantoms, and the main effect of kVp on dose at different levels of filtration, are presented in Figures (6.3), (6.4) and (6.5), respectively. Results show, for all the ages, that the filtration combination of 0.1 mm Cu + 1 mm Al had the highest effect on reducing the mean radiation dose. The next was 2 mm of additional aluminium, and the last was no additional filtration. For the 1 and 5 year-old phantoms, the increase rate of radiation dose when increasing kVp at zero filtration was the highest, compared to the 2 mm Al filtration and the filtration combination 1 mm Al + 0.1 mm Cu, which had the lowest dose increase rate.

The main effect analyses showed a linear increase in radiation dose when kVp was increased for 1 and 5 year-old study, and over all filtration levels (Figures 6.3 and 6.4). The main effect for the 10 year-old, including the radiation dose and DAP, showed the opposite (decrease) trend to the younger ages (Figure 6.5).

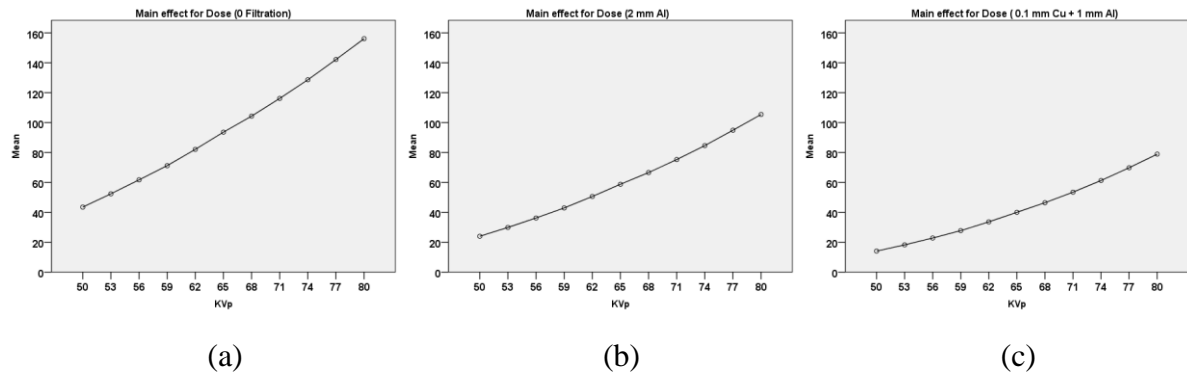


Figure 6.3: **1 year-old** the main effect plot for dose (μGy) when increasing the kVp; (a) at 0 filtration, (b) at 2 mm Al, (c) at 0.1 mm Cu + 1 mm Al.

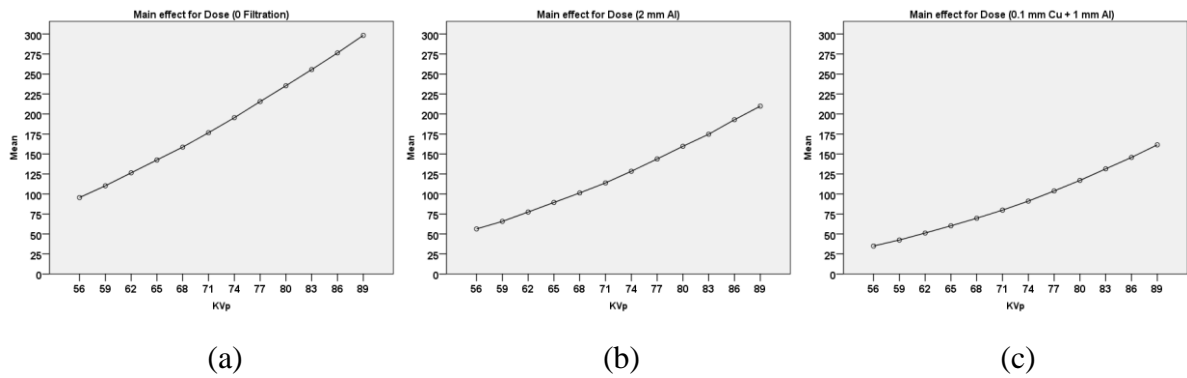


Figure 6.4: **5 year-old** the main effect plot for dose (μGy) when increasing the SID; (a) at 0 filtration, (b) at 2 mm Al, (c) at 0.1 mm Cu + 1 mm Al.

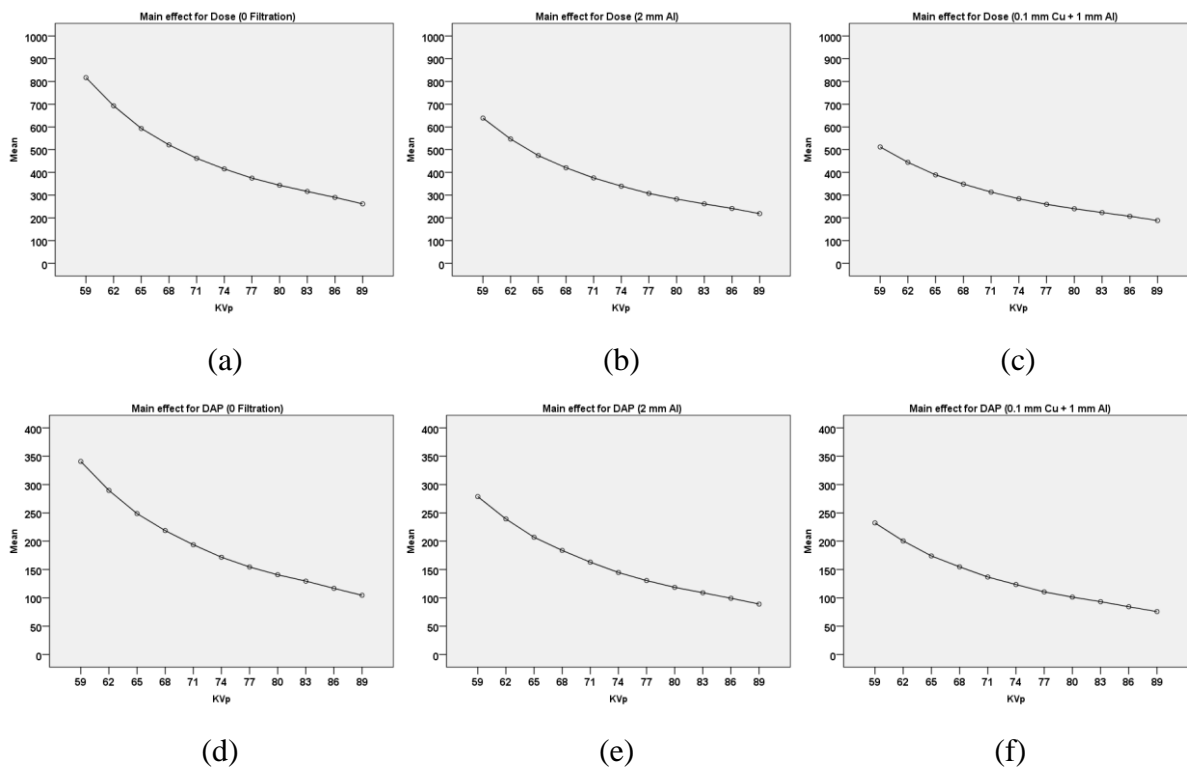


Figure 6.5: **10 year-old** the main effect plot for dose (μGy) and DAP (mGy cm^2) when increasing the SID; (a)&(d) at 0 filtration, (b)&(e) at 2 mm Al, (c)&(f) at 0.1 mm Cu + 1 mm Al.

For the 1, 5 and 10 year-old phantoms, the main effects of tube potential on physical IQ (SNR and CNR), at different levels of filtration, are presented in Figures (6.6), (6.7) and (6.8), respectively. The analysis of the variance showed that, for all the ages, the filtration combination of 0.1 mm Cu + 1 mm Al had the highest effect in reducing the mean physical and visual IQ. The next was 2 mm Al filter and the last was no additional filtration.

Figures (6.6; a-c and 6.7; a-c) show a general increase in SNR when kVp was increased, and this was observed over all filtration levels and for the 1 and 5 year-old phantoms. CNR for the 1 year-old showed a plateau after 65 kVp (see Figure 6.6; d-f). However, for the 5 year-old, a decrease in CNR appeared at no filtration. The CNR then increased slightly with further added levels of filtration. For the 10 year-old phantom (Figure 6.8; a-f) there was a continuous decrease in SNR and CNR when increasing kVp.

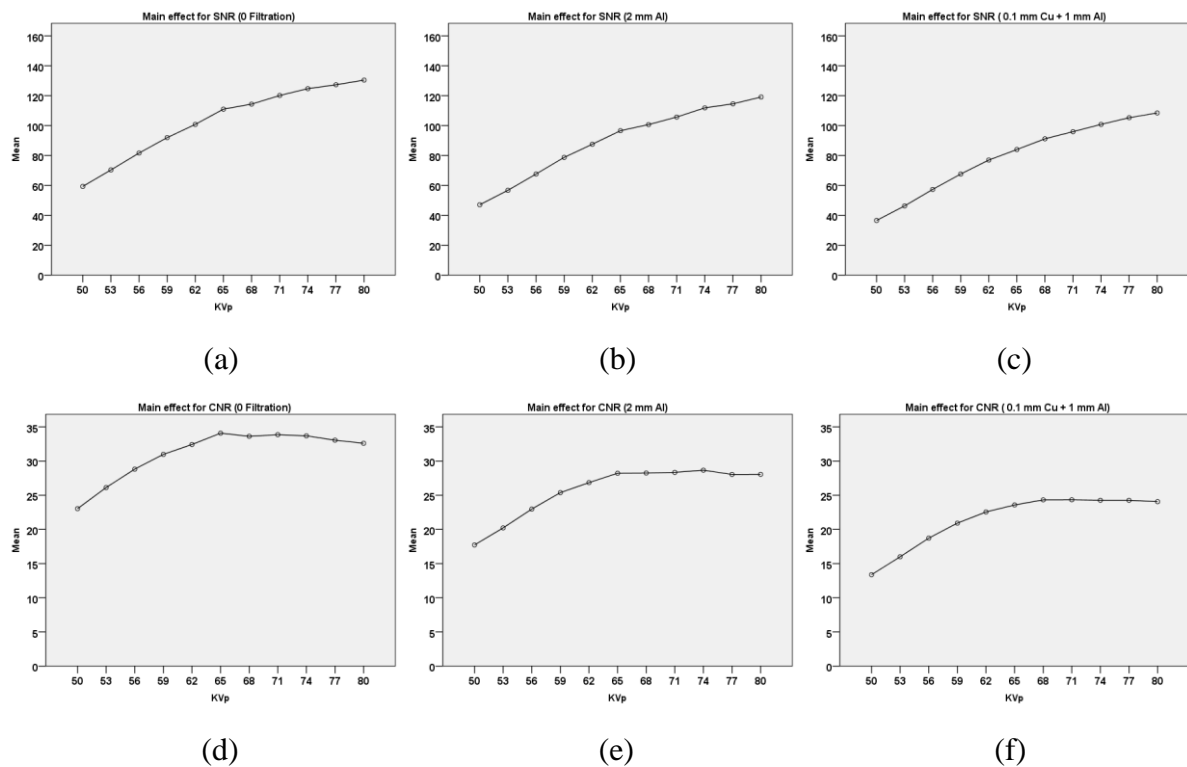


Figure 6.6: **1 year-old** the main effect plot for physical image quality when increasing the kVp: (a-c) for SNR and (d-f) for CNR. (a) & (d) at 0 filtration, (b) & (e) at 2 mm Al and (c) & (f) at 0.1 mm Cu + 1 mm Al.

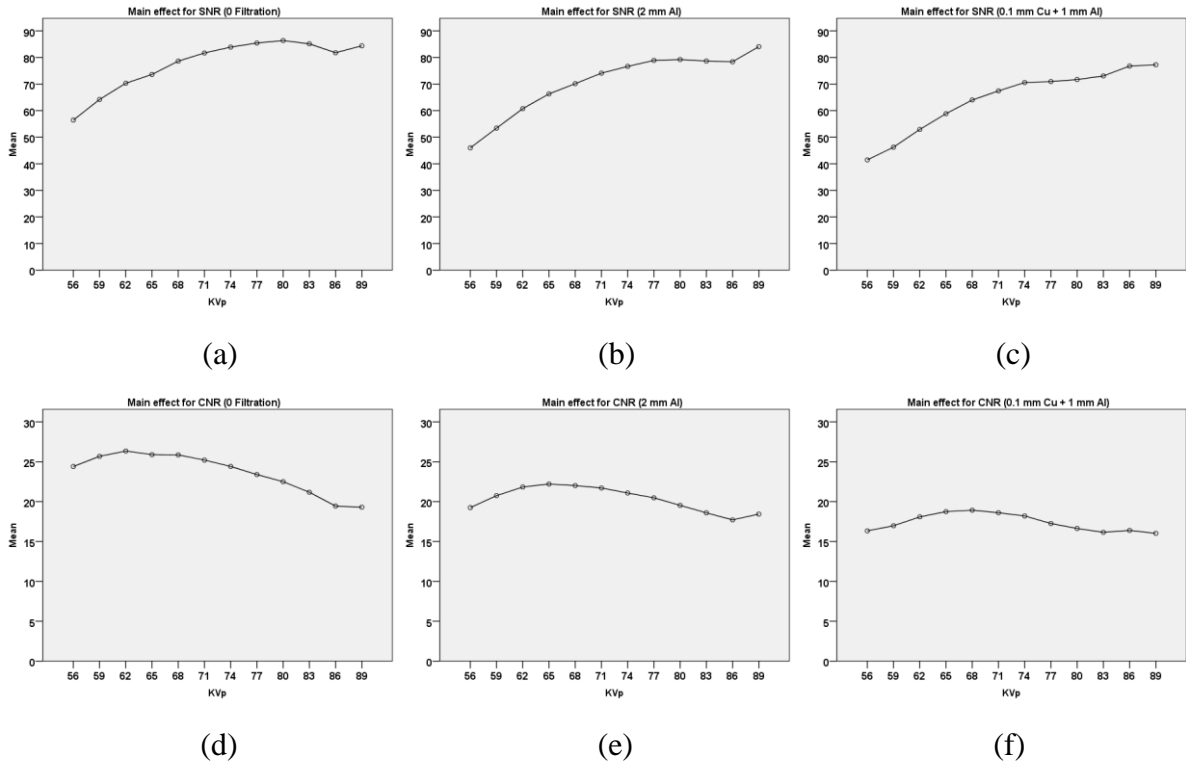


Figure 6.7: **5 year-old** the main effect plot for physical image quality when increasing the kVp: (a-c) for SNR and (d-f) for CNR. (a)& (d) at 0 filtration, (b) &(c) at 2 mm Al and (c) & (f) at 0.1 mm Cu + 1 mm Al.

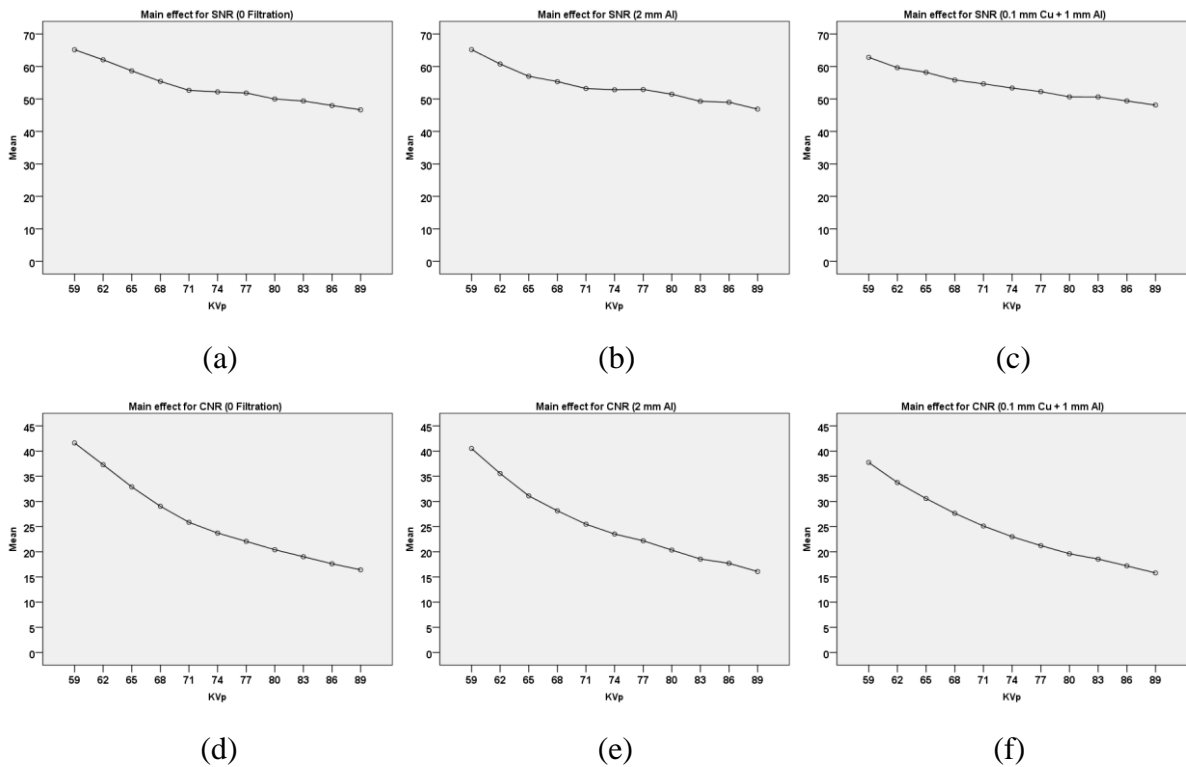


Figure 6.8: **10 year-old** the main effect plot for physical image quality when increasing the kVp: (a-c) for SNR and (d-f) for CNR. (a)& (d) at 0 filtration, (b) &(c) at 2 mm Al and (c) &(f) at 0.1 mm Cu + 1 mm Al.

The main effects of kVp on visual image quality at different levels of filtration are presented in Figures (6.9), (6.10) and (6.11) for the 1, 5 and 10 year-old phantoms, respectively. The analysis of the variance showed, for all the ages, that the filtration combination of 0.1 mm Cu + 1 mm Al had the highest effect on reducing IQ (sharpness). The next was 2 mm Al and the last was no additional filtration. The IQ (clarity) showed similar trends when extra filtration was added. There was an initial incline followed by a decline in IQ (sharpness) for the 1 and 5 year-old when the kVp was increased (see Figures 6.9; a-c and 6.10; a-c). IQ (clarity) for the same ages showed a continuous increase when increasing kVp (Figures 6.9; d-f and 6.10; d-f). The IQ (sharpness) and IQ (clarity) for the 10 year-old showed a continuous decrease when the kVp was increased (Figure 6.11).

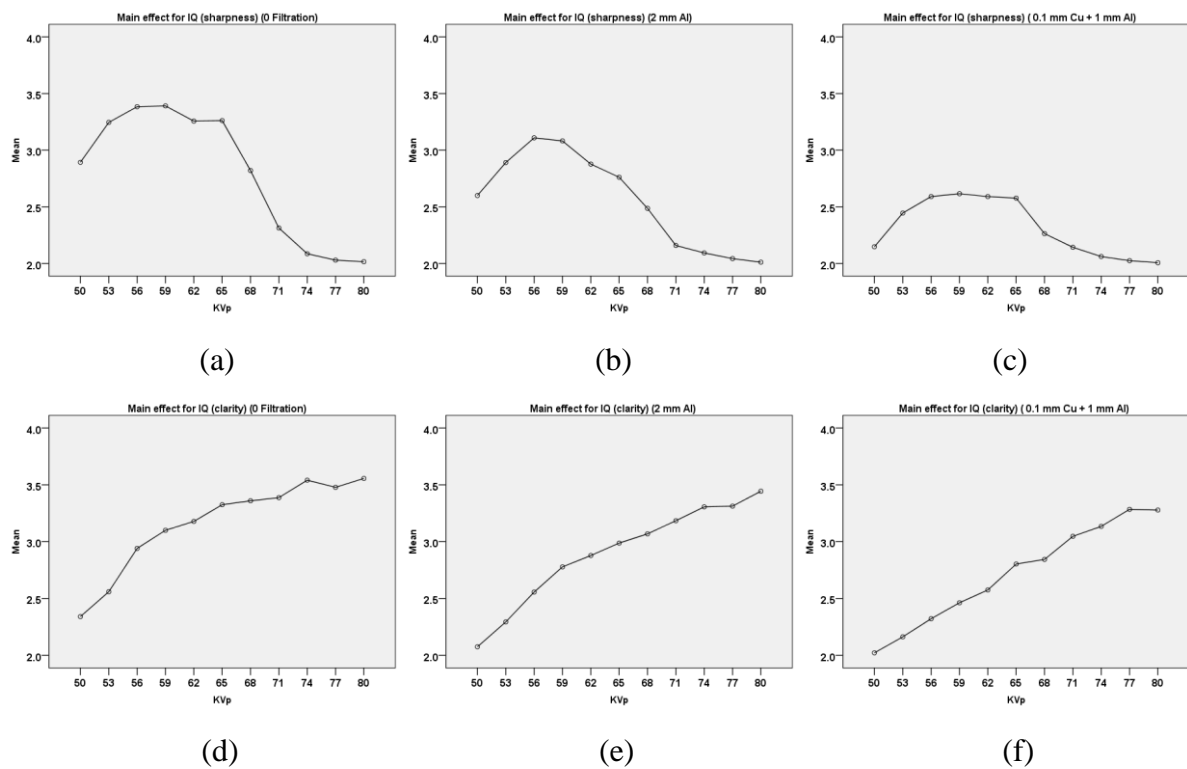


Figure 6.9: **1 year-old** the main effect plot for visual image quality when increasing the kVp; (a-c) for IQ (sharpness) and (d-f) for IQ (clarity). (a)& (d) at 0 filtration, (b) &(c) at 2 mm Al and (c) &(f) at 0.1 mm Cu + 1 mm Al.

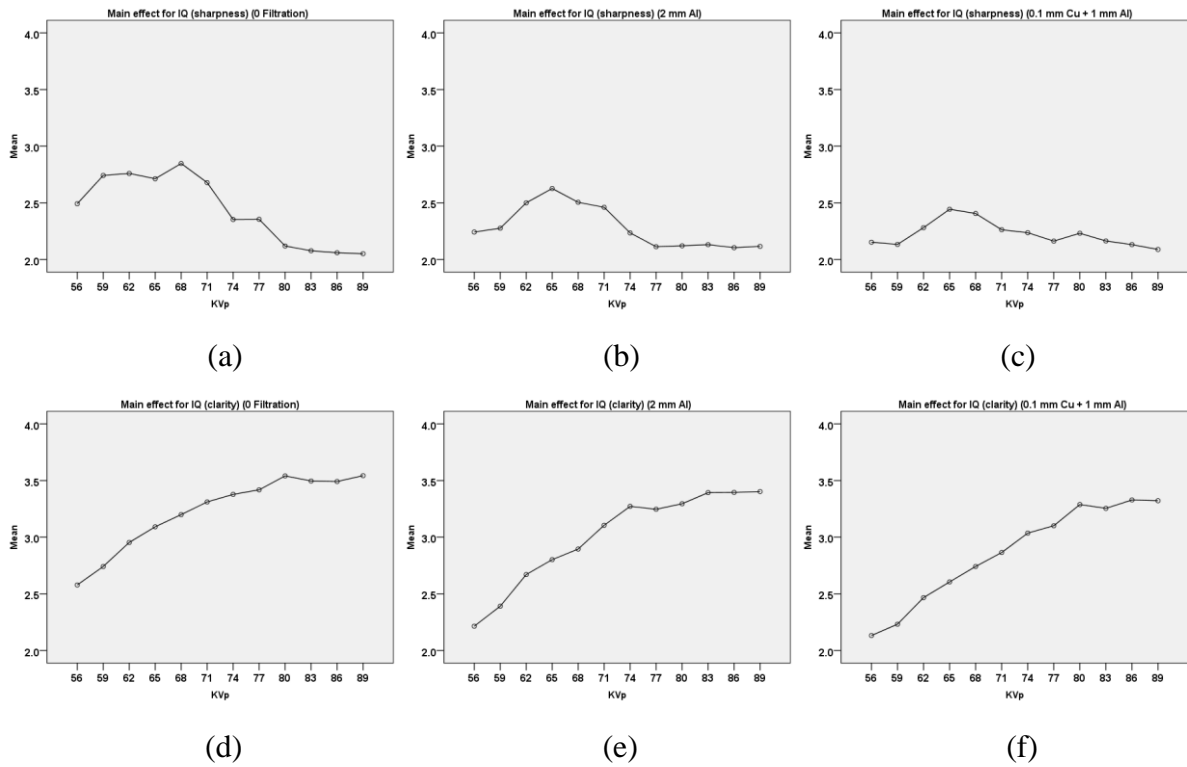


Figure 6.10: **5 year-old** the main effect plot for visual image quality when increasing the kVp; (a-c) for IQ (sharpness) and (d-f) for IQ (clarity). (a)& (d) at 0 filtration, (b) &(c) at 2 mm Al and (c) & (f) at 0.1 mm Cu + 1 mm Al.

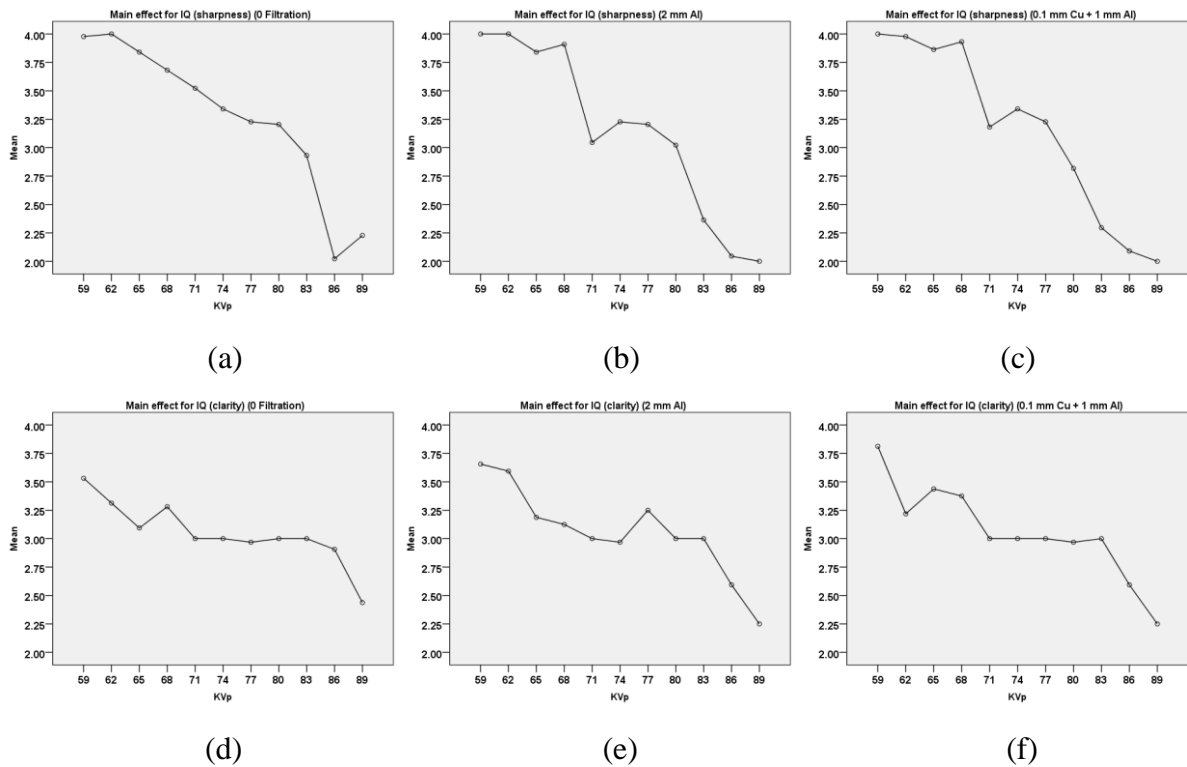


Figure 6.11: **10 year-old** the main effect plot for visual image quality when increasing the kVp; (a-c) for IQ (sharpness) and (d-f) for IQ (clarity). (a)& (d) at 0 filtration, (b) &(c) at 2 mm Al and (c) & (f) at 0.1 mm Cu + 1 mm Al.

The main effects of the tube potential on IQ (sharpness & clarity) at different levels of filtration are presented in Figures (6.12, 6.13 and 6.14) for the 1, 5 and 10 year-old phantoms, respectively. These IQ scores were used in determining the diagnostically acceptable IQ level, which is represented by a horizontal line on each plot. The analysis of variance showed, for all the paediatric ages, that the filtration combination of 0.1 mm Cu + 1 mm Al had the highest effect on reducing IQ (sharpness & clarity). The next was 2 mm Al filter and the last was no additional filtration.

For the 1 year-old, there was an increase in IQ with increasing kVp up to 59 to 65 kVp, after which there was saturation (Figure 6.12) which is followed by a drop in IQ. This behaviour is seen for 0 and 2 mm Al. For the combined filtration of the same age, there was a relatively small increase when increasing tube potential until 59 kVp, and then a saturation was reached beyond this point. The IQ, for the filtration 0 and 2 mm Al, was above the diagnostically acceptable level (Figure 6.12; a & b). For zero filtration, the IQ was under the diagnostically acceptable level at 50 and 53 kVp only (Figure 6.12; c).

For the 5 year-old, the IQ (sharpness & clarity) showed a slight increase and decrease with slight saturation when increasing the kVp. The total range was around the middle of the IQ score (2.6 to 3.8) with no filtration, and this decreased when increasing filtration (Figure 6.13).

For the 10 year-old, image quality was diagnostically acceptable for all images. The IQ (sharpness & clarity) showed a continuous decrease when increasing the kVp (Figure 6.14).

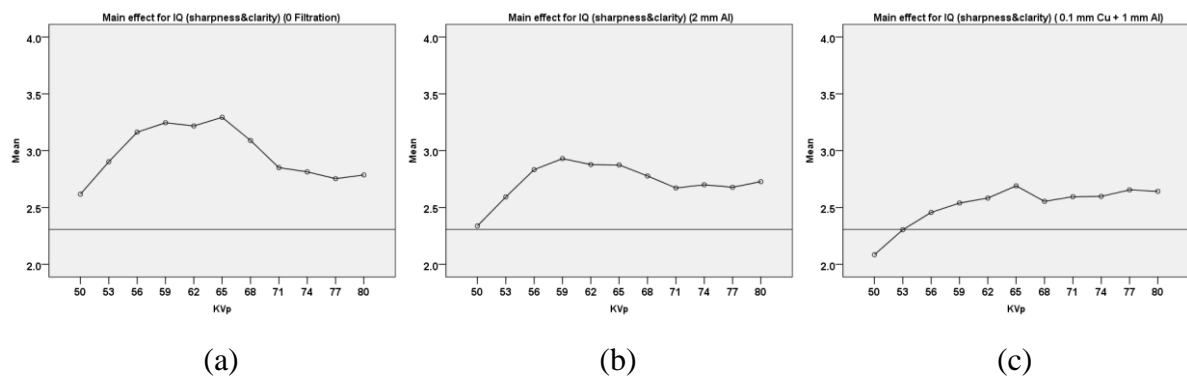


Figure 6.12: **1 year-old** the main effect plot for IQ (sharpness and clarity) when increasing the kVp. (a) at 0 filtration, (b) at 2 mm Al and (c) at 0.1 mm Cu + 1 mm Al.

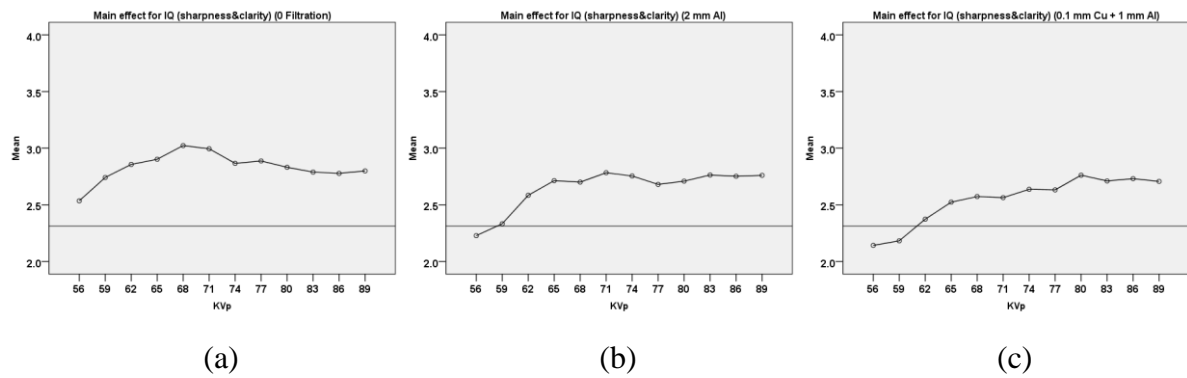


Figure 6.13: **5 year-old** the main effect for IQ (sharpness and clarity) when increasing the kVp. (a) at 0 filtration, (b) at 2 mm Al and (c) at 0.1 mm Cu + 1 mm Al.

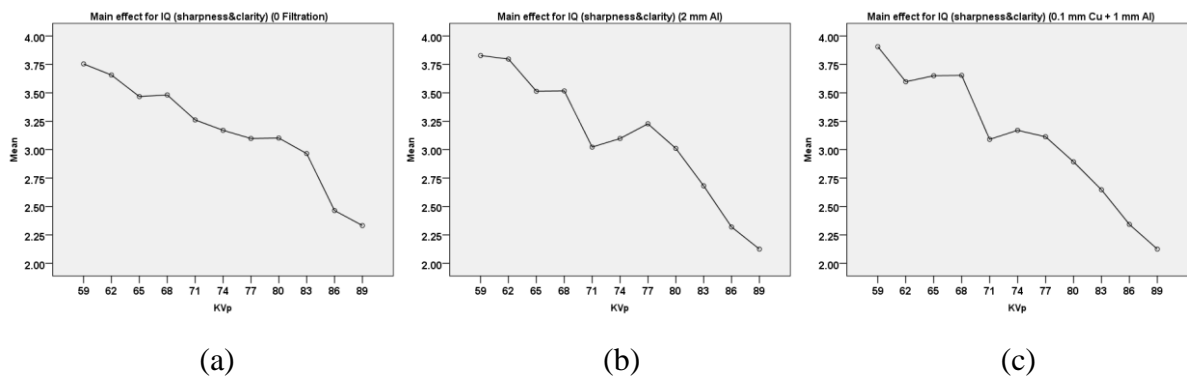


Figure 6.14: **10 year-old** the main effect plot for IQ (sharpness and clarity) when increasing the kVp. (a) at 0 filtration, (b) at 2 mm Al and (c) at 0.1 mm Cu + 1 mm Al.

The main effect plots for FOM versus the tube potential for the three paediatric ages are presented in Figures (6.15), (6.17) and (6.18), below. The IQs used for FOM, including the visual and physical, are diagnostically acceptable. The three ages showed that the higher means for FOM (visual IQ) and FOM (SNR) were with 0.1 mm Cu + 1 mm Al additional filtration. The 2 mm Al filtration was then second, and no filtration showed the lowest mean for both FOMs.

The FOM (SNR) for the 1 year-old (Figure (6.15; a-c)) showed a general increase when kVp was increased. This increase reached a maximum at 65 kVp, before a general decrease started. Unlike the other two filtration options, the maximum point for the 0.1 Cu + 1 mm Al filtration was at 62 kVp. The FOM (visual IQ), however, decreased when kVp was increased Figure (6.15; d-f).

The FOM (SNR) for the 5 year-old showed a slight increase with increasing kVp until 68kVp, then a drop in FOM (SNR) was observed (Figure 6.16; a-c). The FOM (visual IQ) showed an overall decrease with increasing kVp. This was seen over all filtration levels (Figure 6.16; d-f).

The FOM (visual IQ) and FOM (SNR) for the 10 year-old, in contrary to the two other ages, showed a continuous increase when increasing kVp, see Figure (6.17).

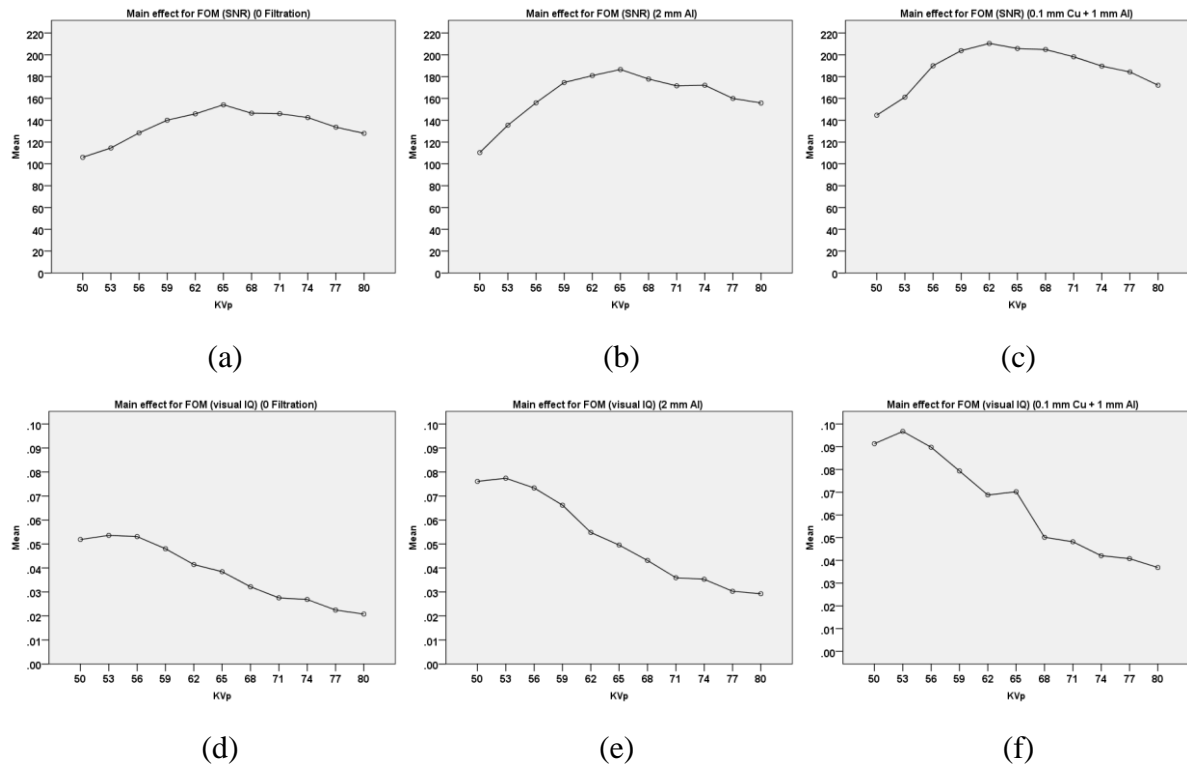


Figure 6.15: **1 year-old** the main effect plot for FOM when increasing the kVp; (a-c) for FOM (SNR) and (d-f) for FOM (visual IQ). (a)& (d) at 0 filtration, (b) &(c) at 2 mm Al and (c) & (f) at 0.1 mm Cu + 1 mm Al.

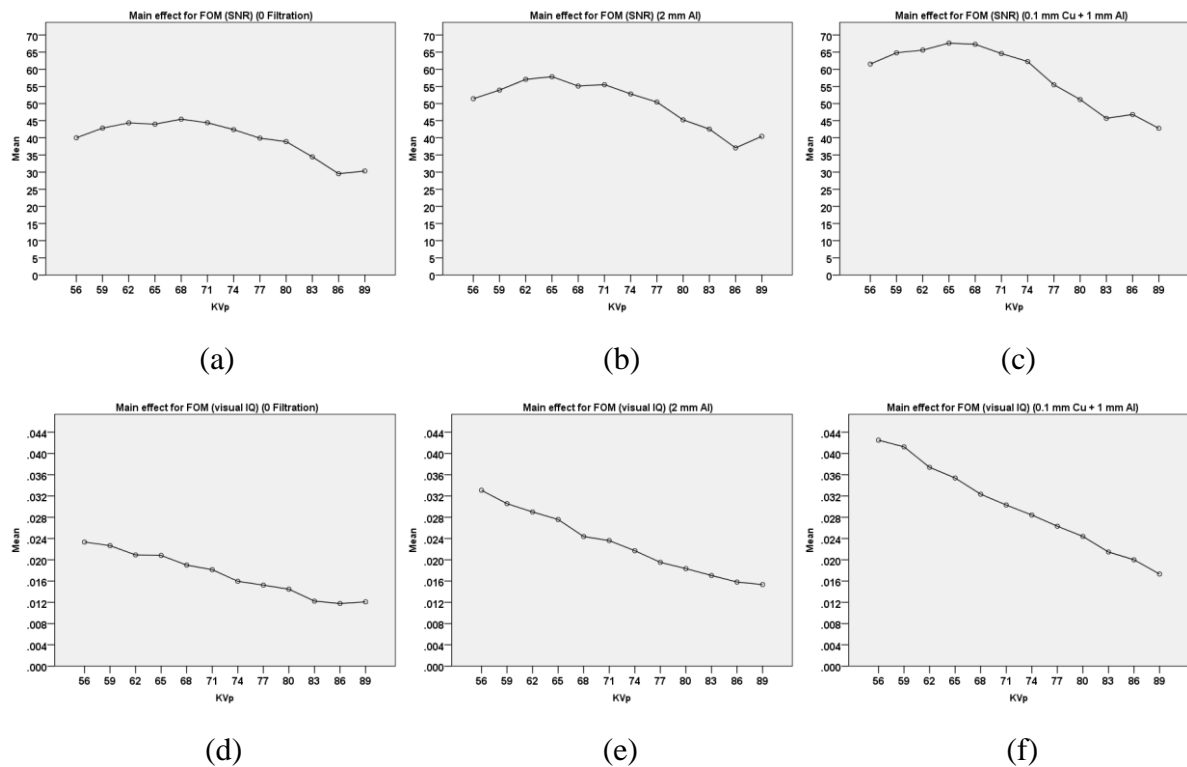


Figure 6.16: **5 year-old** the main effect plot for FOM when increasing the kVp; (a-c) for FOM (SNR) and (d-f) for FOM (visual IQ). (a)& (d) at 0 filtration, (b) &(c) at 2 mm Al and (c) & (f) at 0.1 mm Cu + 1 mm Al.

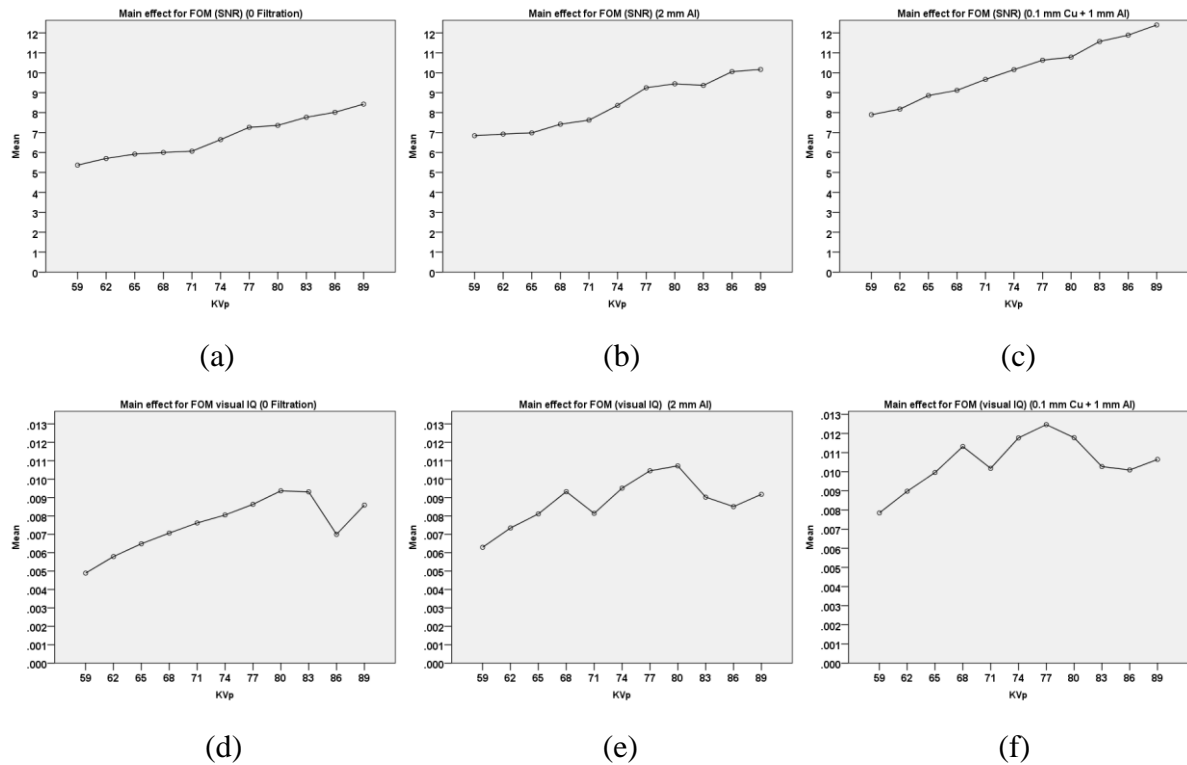


Figure 6.17: **10 year-old** the main effect plot for FOM when increasing the kVp; (a-c) for FOM (SNR) and (d-f) for FOM (visual IQ). (a)& (d) at 0 filtration, (b) &(c) at 2 mm Al and (c) & (f) at 0.1 mm Cu + 1 mm Al.

6.3.1.2 Main effect from mAs

Data for the main effect analysis for mAs were taken for the 1 and 5 year-old phantoms only, since the 10 year-old phantom study was conducted using an AEC. These clinical protocols followed recommendations by the CEC (1996) on film screen, and was indicated in discussions with experienced radiographers to be an up-to-date imaging technique.

The main effect of mAs on radiation dose for the 1 and 5 year-olds, at different levels of filtration, are presented in Figures (6.18) and (6.19) below. The main effect analyses showed a linear increase in radiation dose when the mAs was increased over all filtration levels. The dose rate increased with increasing mAs at zero filtration; this was the highest compared to the 2 mm Al filtration and the filtration combination (0.1 mm Cu + 1 mm Al) which had the lowest dose increase. It also showed, over all mAs values, that the filtration combination of 0.1 mm Cu + 1 mm Al had the lowest mean dose. The next was the 2 mm Al filter and the last was zero filtration.

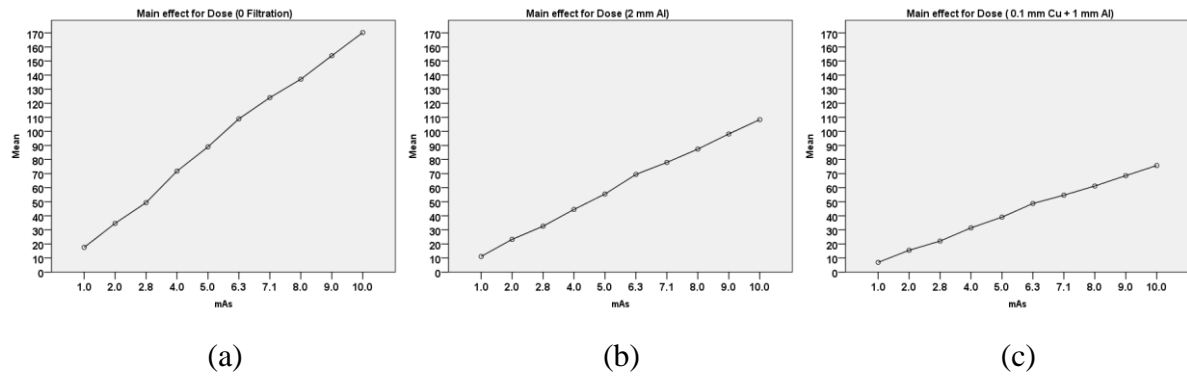


Figure 6.18: **1 year-old** the main effect plot for dose (μGy) when increasing the mAs; (a) at 0 filtration, (b) at 2 mm Al, (c) at 0.1 mm Cu + 1 mm Al.

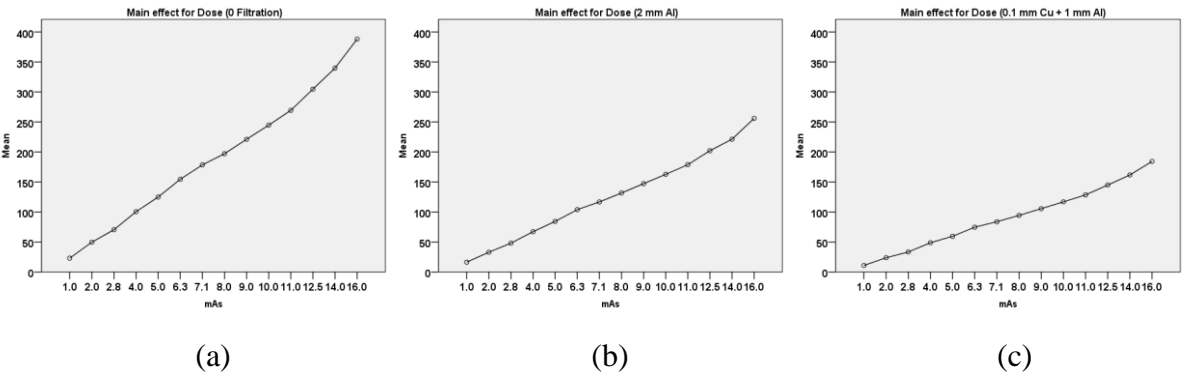
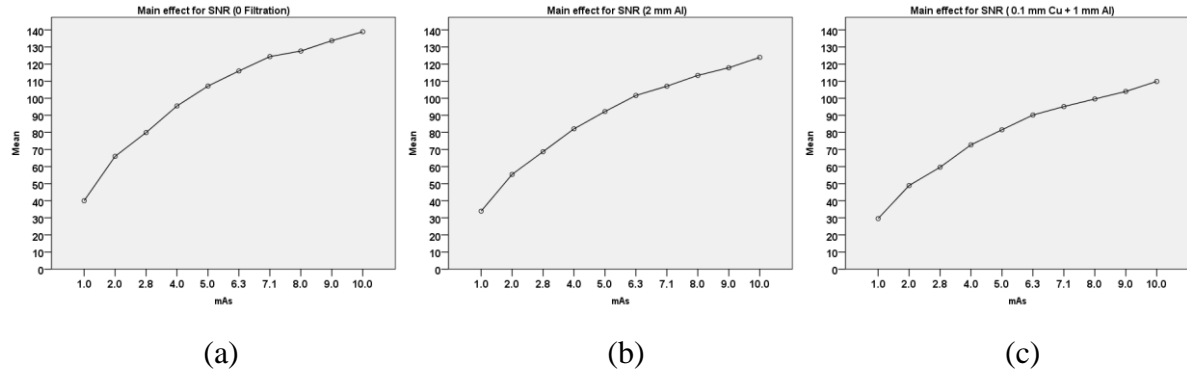


Figure 6.19: **5 year-old** the main effect plot for dose (μGy) when increasing the mAs; (a) at 0 filtration, (b) at 2 mm Al, (c) at 0.1 mm Cu + 1 mm Al.

The main effects of mAs on physical IQ (SNR and CNR) for the 1 and 5 year-old phantoms, at different levels of filtration, are illustrated in Figures (6.20) and (6.21) below. The plots show a continuous increase in SNR and CNR when the mAs was increased. This was observed for the 1 and 5 year-old phantoms across all filtration levels. In addition, for the 1 and 5 year-old, the mean SNR and CNR were lower on average when applying more filtration. This can be seen from the vertical line that represents the mean of SNR and CNR values at each filtration level.



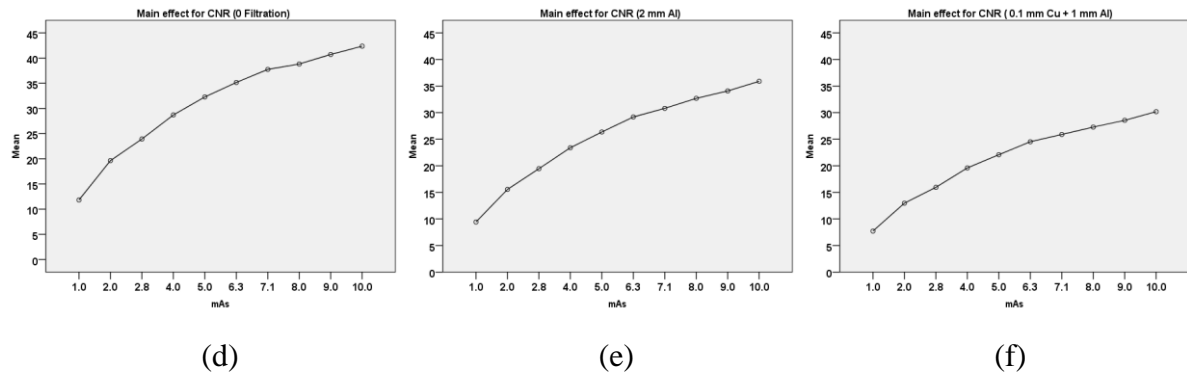


Figure 6.20: **1 year-old** the main effect plot for physical image quality when increasing the mAs: (a-c) for SNR and (d-f) for CNR. (a)& (d) at 0 filtration, (b) &(c) at 2 mm Al and (c) & (f) at 0.1 mm Cu + 1 mm Al.

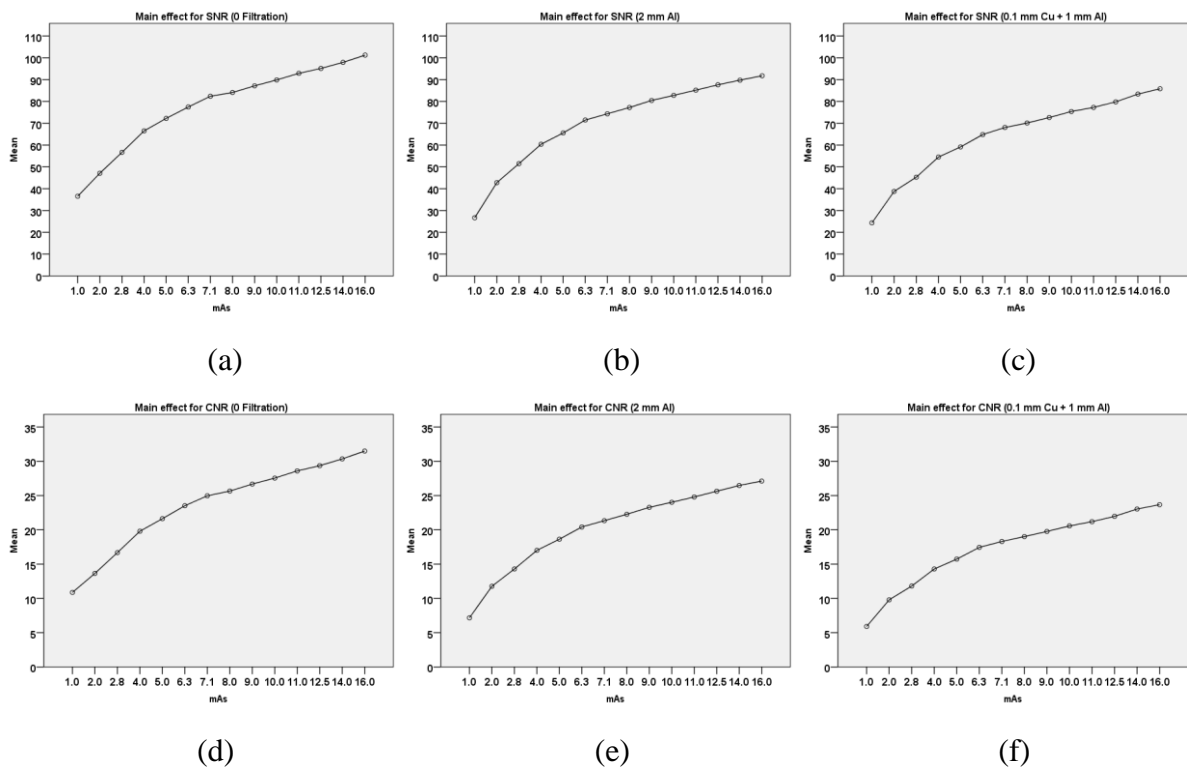


Figure 6.21: **5 year-old** the main effect plot for physical image quality when increasing the mAs: (a-c) for SNR and (d-f) for CNR. (a)& (d) at 0 filtration, (b) &(c) at 2 mm Al and (c) & (f) at 0.1 mm Cu + 1 mm Al.

The main effects of mAs on visual IQ for 1 and 5 year-old phantoms, at different filtration levels, are presented in Figures (6.22) and (6.23). The responses of IQ sharpness and IQ clarity to increasing the mAs both showed an increase. This was observed over the two ages and for all filtrations. Then relatively slower increases were observed at the higher mAs values when the filtration was zero. For the other added filtrations both IQ aspects showed a continuous increase with increasing the mAs.

The analyses of variance, for all 1 and 5 year-old, showed that the filtration combination of 0.1 mm Cu + 1 mm Al had the highest effect on reducing the IQ (sharpness) and IQ (clarity). The next was 2 mm Al filter and the last was zero filtration (Figure 6.10; a-c and d-f).

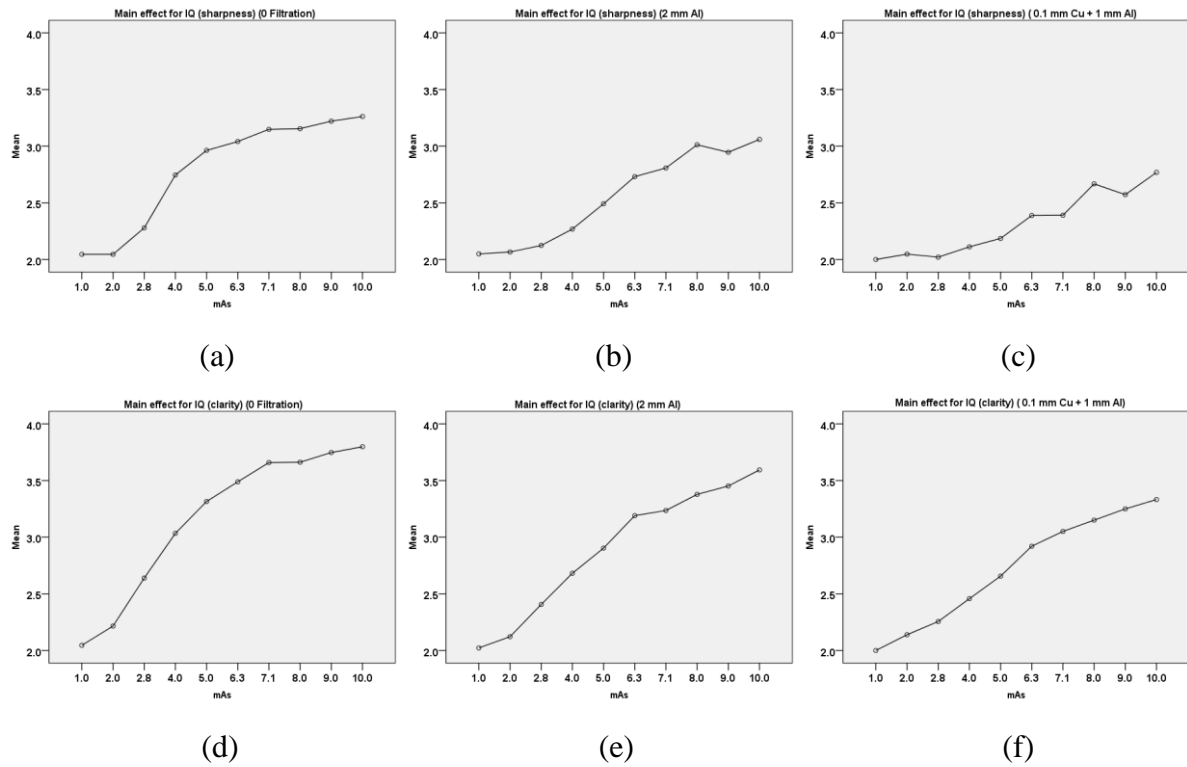
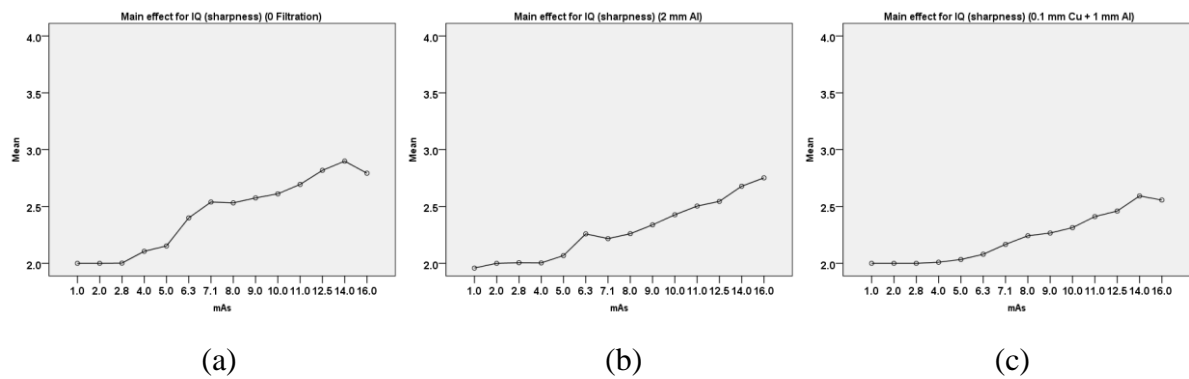


Figure 6.22: **1 year-old** the main effect plot for visual image quality when increasing the mAs; (a-c) for IQ (sharpness) and (d-f) for IQ (clarity). (a)& (d) at 0 filtration, (b) &(c) at 2 mm Al and (c) & (f) at 0.1 mm Cu + 1 mm Al.



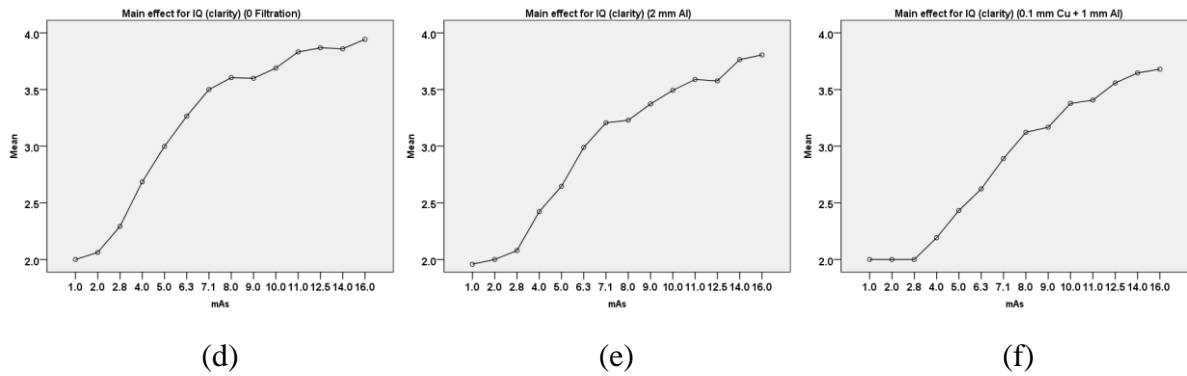


Figure 6.23: **5 year-old** the main effect plot for visual image quality when increasing the mAs; (a-c) for IQ (sharpness) and (d-f) for IQ (clarity). (a) & (d) at 0 filtration, (b) & (c) at 2 mm Al and (c) & (f) at 0.1 mm Cu + 1 mm Al.

The main effects of mAs on IQ (sharpness & clarity) for 1 and 5 year-old phantom, at different levels of filtration, are presented in Figures (6.25) and (6.26). This IQ score was used in determining the diagnostically acceptable IQ level, which is represented by a horizontal line on each plot.

The plots show a continuous increase in the IQ with increasing mAs for the 1 and 5 year-old phantom data. For the 1 year-old, the IQ was above the diagnostically acceptable IQ level when ≥ 2.8 mAs was used (when the filtration was zero). The minimum mAs value moved up to 4 and 5 mAs for each increase in additional filtration (Figure 6.24; a-d). Similarly, for the 5 year-old, diagnostically acceptable IQ was produced at a minimum of 4 mAs with zero filtration; this then required an increase in mAs for each extra level of added filtration.

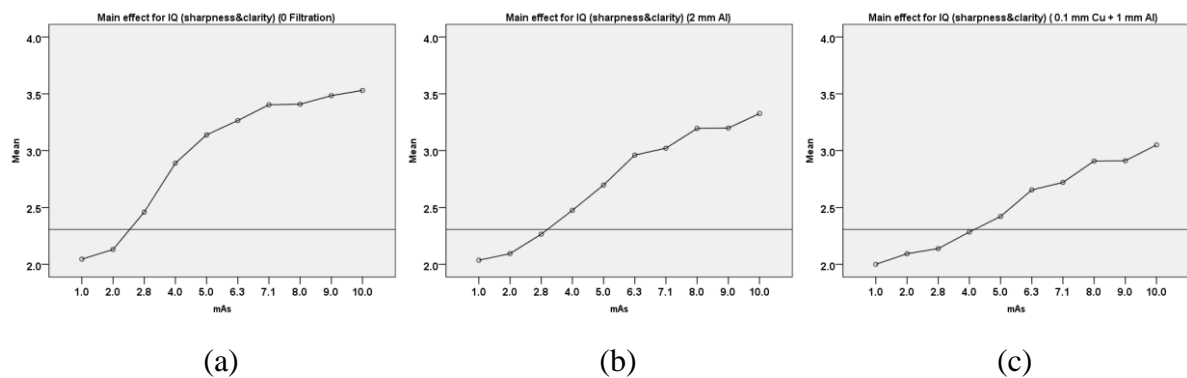


Figure 6.24: **1 year-old** the main effect plot for IQ (sharpness and clarity) when increasing the mAs. (a) at 0 filtration, (b) at 2 mm Al and (c) at 0.1 Cu + 1 mm Al.

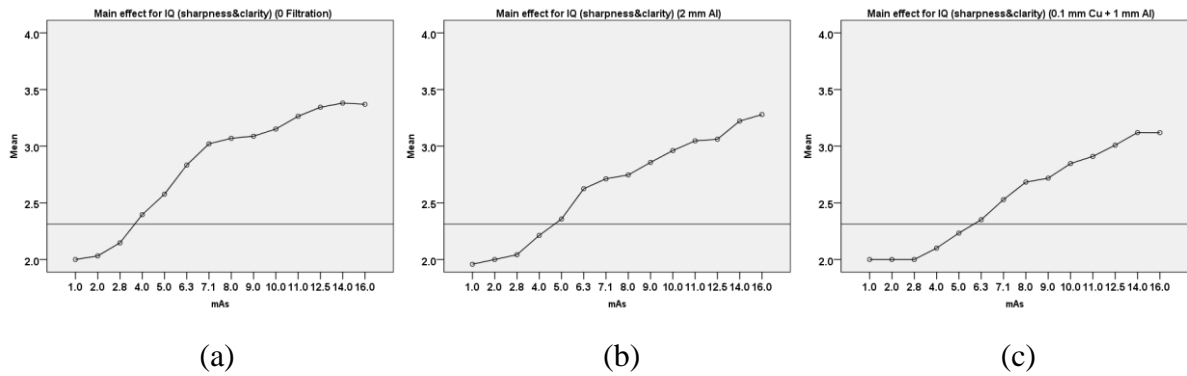


Figure 6.25: **5 year-old** the main effect plot for IQ (sharpness and clarity) when increasing the mAs. (a) at 0 filtration, (b) at 2 mm Al and (c) at 0.1 Cu + 1 mm Al.

The main effect plots for FOM versus mAs for the 1 and 5 year-old phantoms are presented in Figures (6.26) and (6.27), below. The IQ level used in the calculation of FOM includes both the visual and physical measures for images which were of diagnostically acceptable IQ. For the 1 and 5 year-olds, the mean of the FOM for SNR and the FOM for visual IQ scored higher when more filtration was added.

The FOM for SNR and the FOM for visual IQ showed a continuous decrease when increasing kVp for the two ages and over all filtrations (Figures 6.26 & 6.27). A high FOM value was recorded at 2 mAs and 0.1 mm Cu + 1 mm Al filtration (Figure 6.26; f). There is an exception for a 1 year-old at zero and 2 mm Al additional filtration, wherein a very low FOM for SNR was observed at 1 mAs (Figure 6.26; a & b).

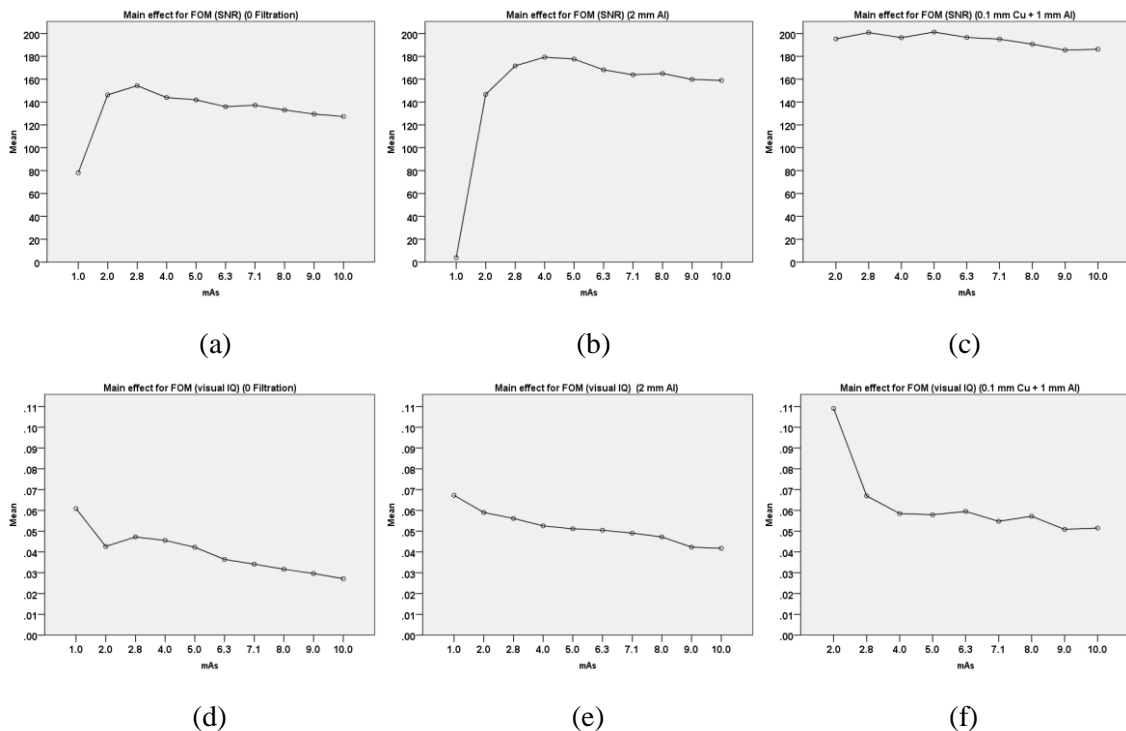


Figure 6.26: **1 year-old** the main effect plot for FOM when increasing the mAs; (a-c) for FOM (SNR) and (d-f) for FOM (visual IQ). (a)&(d) at 0 filtration, (b)&(e) at 2 mm Al and (c)&(f) at 0.1 mm Cu + 1 mm Al.

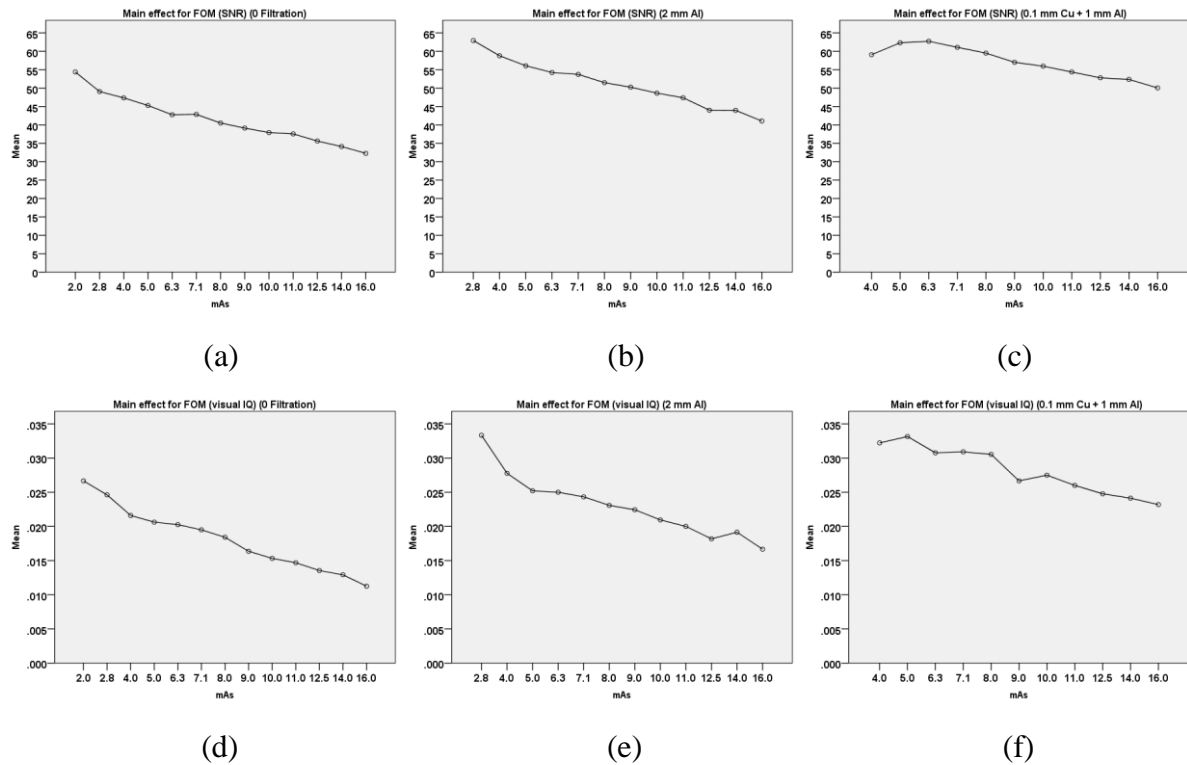


Figure 6.27: **5 year-old** the main effect plot for FOM when increasing the mAs; (a-c) for FOM (SNR) and (d-f) for FOM (visual IQ). (a)&(d) at 0 filtration, (b) & (c) at 2 mm Al and (c) & (f) at 0.1 mm Cu + 1 mm Al.

6.3.1.3 Main effect from SID

The main effect of SID on radiation dose for 1, 5 and 10 year-old phantoms, at different levels of filtration, are presented in Figures (6.27), (6.29) and (6.30). The DAP (mGy cm^2) is included in the Figure (6.30; d-f) for the 10 year-old. A filtration combination of 0.1 mm Cu + 1 mm Al had the highest impact on reducing the mean radiation dose. The next was 2 mm Al and the last was zero filtration.

The radiation doses for the three ages showed a linear decrease in radiation dose when SID increased. This was observed over all filtration levels. It also showed that the filtration combination of 0.1 mm Cu + 1 mm Al had the highest impact on reducing the mean radiation dose. The next was 2 mm Al and last was zero filtration. There is an exceptional case for the radiation dose in the 10 year-old study, which showed an increase after 130 cm SID (Figure 6.30; a-c).

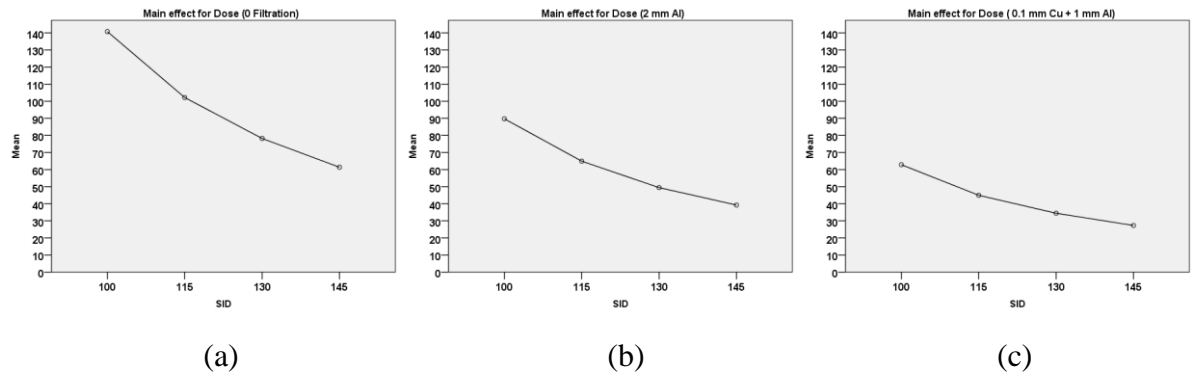


Figure 6.28: **1 year-old** the main effect plot for dose (μGy) when increasing the SID; (a) at 0 filtration, (b) at 2 mm Al, (c) at 0.1 mm Cu + 1 mm Al.

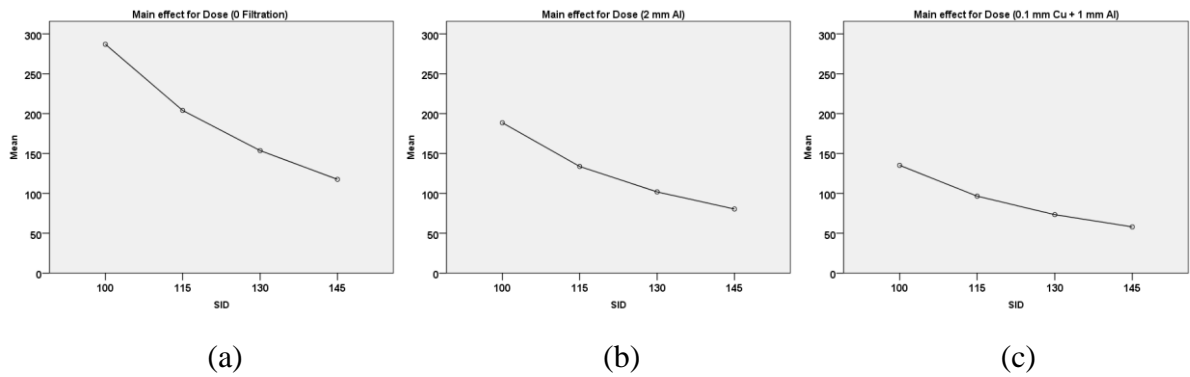


Figure 6.29: **5 year-old** the main effect plot for dose (μGy) when increasing the SID; (a) at 0 filtration, (b) at 2 mm Al, (c) at 0.1 mm Cu + 1 mm Al.

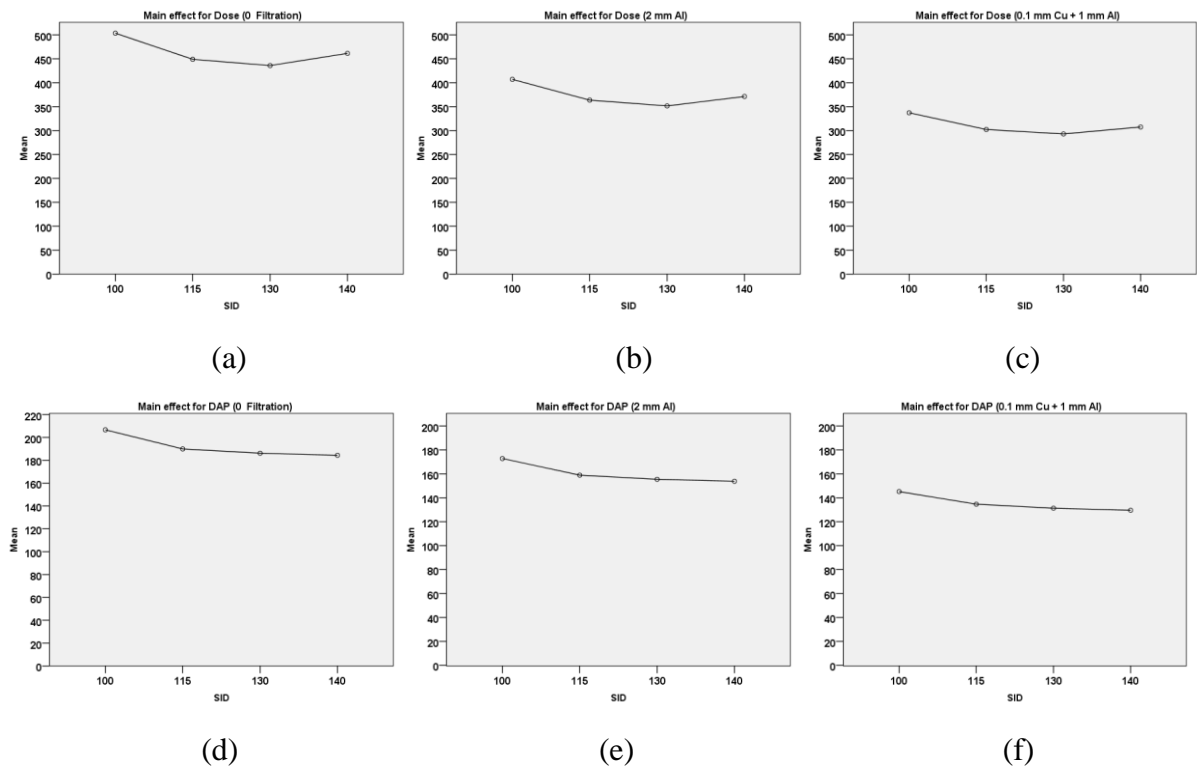


Figure 6.30: **10 year-old** the main effect plot for dose (μGy) and DAP (mGy cm^2) when increasing the SID; (a)&(d) at 0 filtration, (b)&(e) at 2 mm Al, (c)&(f) at 0.1 mm Cu + 1 mm Al.

The main effects of SID on physical IQ (SNR and CNR) for the 1, 5 and 10 year-old phantoms, at different levels of filtration, are presented in Figures (6.31), (6.32) and (6.33). The mean SNR and CNR levels, for the 1 and 5 year-olds, were lower on average when applying more filtration, this can be seen from the vertical line that represent the mean SNR and CNR values at each filtration level. For the 10 year-old phantom, the two aspects of physical IQ maintained relatively equal means over all the filtration levels (Figure 6.33).

The plots show a continuous decrease in SNR and CNR when SID was increased. This was observed for the 1 year-old and over all filtration levels- see Figure (6.31). The 5 year-old study showed a decrease in both physical IQ aspects, however after the 130 cm SID there was an increase observed across all of the filtration levels (Figure 6.32). The 10 year-old phantom demonstrated a totally opposite trend to the other two ages, wherein an increase in SNR and CNR was observed over all filtration stages (Figure 6.33).

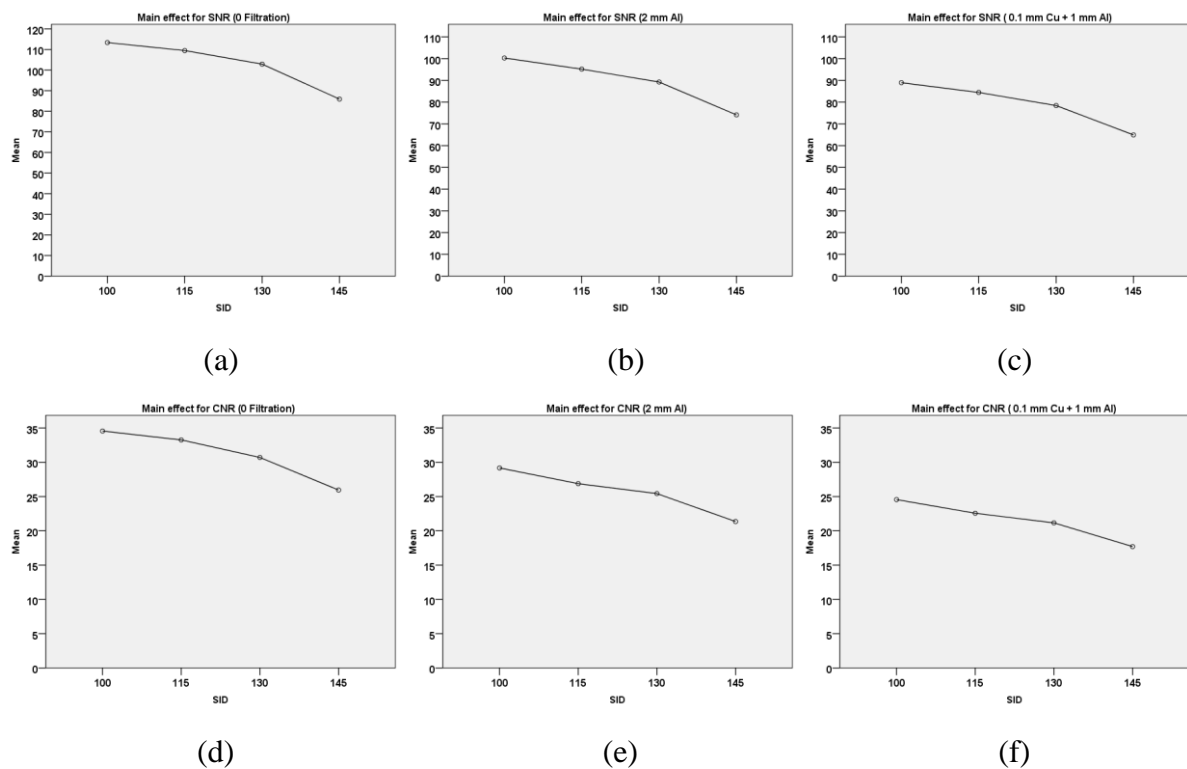


Figure 6.31: **1 year-old** the main effect plot for physical image quality when increasing the SID: (a-c) for SNR and (d-f) for CNR. (a)&(d) at 0 filtration, (b)&(c) at 2 mm Al and (c)&(f) at 0.1 mm Cu + 1 mm Al.

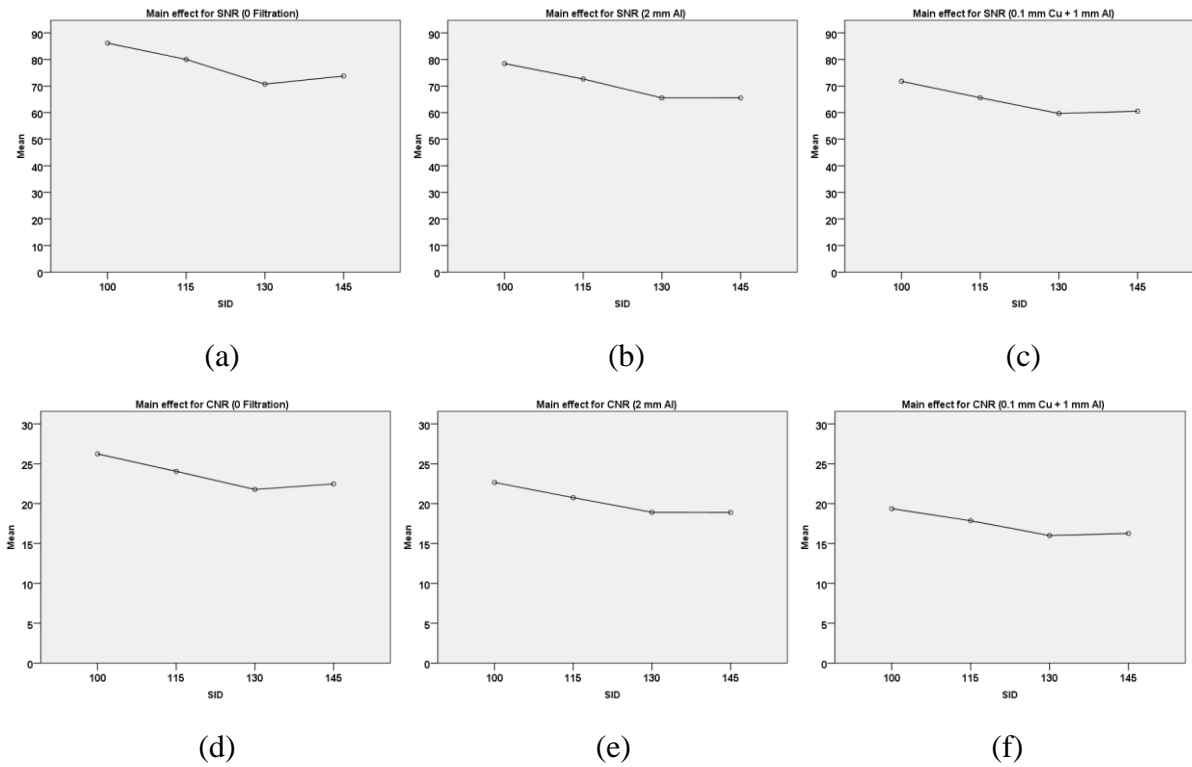


Figure 6.32: **5 year-old** main effect plot for physical image quality when increasing the SID: (a-c) for SNR and (d-f) for CNR. (a)&(d) at 0 filtration, (b)&(c) at 2 mm Al and (c)&(f) at 0.1 mm Cu + 1 mm Al.

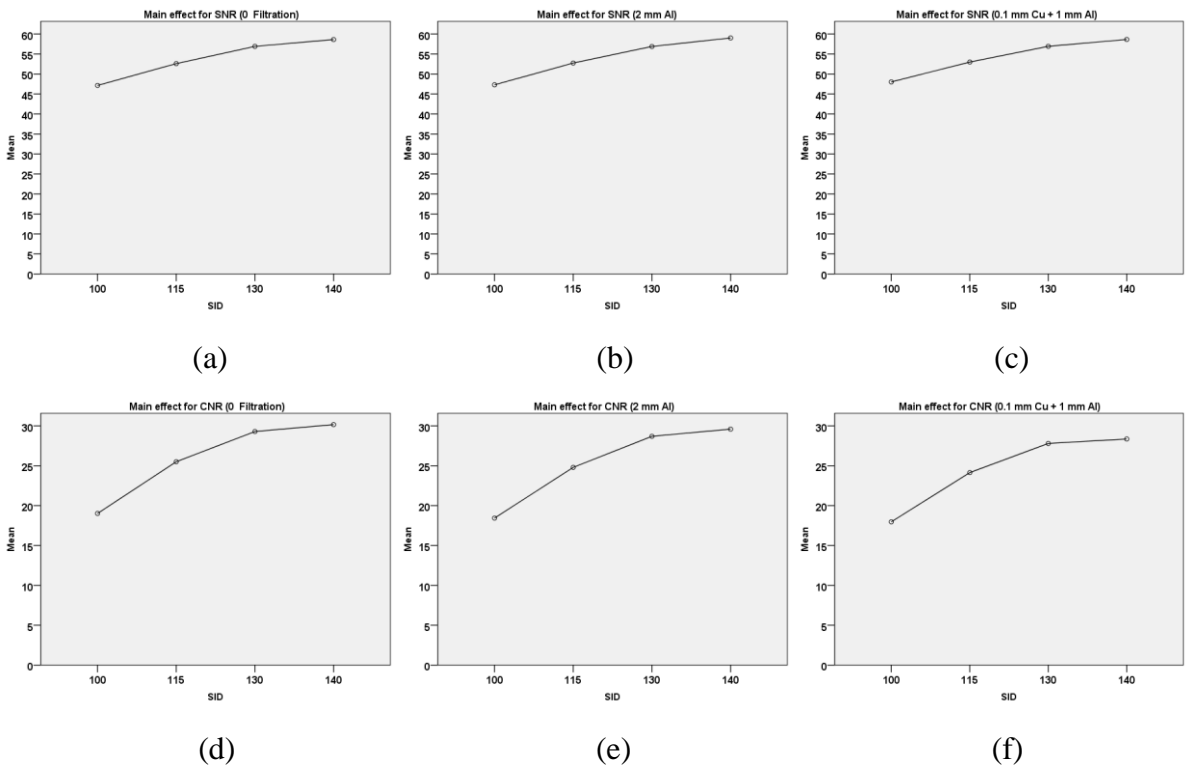


Figure 6.33: **10 year-old** main effect plot for physical image quality when increasing the SID: (a-c) for SNR and (d-f) for CNR. (a)&(d) at 0 filtration, (b)&(c) at 2 mm Al and (c)&(f) at 0.1 mm Cu + 1 mm Al.

The main effect of SID on IQ sharpness and IQ clarity for 1, 5 and 10 year-old phantoms, at different filtration levels, are presented in Figures (6.34), (6.35) and (6.36). The analysis of the variance for IQ sharpness and IQ clarity showed that the filtration combination of 0.1 mm Cu + 1 mm Al had the lowest means. The next was 2 mm Al filter and the last was zero filtration. This was observed for the 1 year-old phantom only (Figure 6.34). For the 5 and 10 year-old phantoms, there was no observable difference across different levels of additional filtration (Figures 6.35 and 6.36).

The plots show a continuous decline in both aspects of visual image quality (sharpness and clarity) for 1 and 5 year-olds when increasing SID (Figure 6.34 & 6.35). This was excluding for 5-year-old IQ sharpness, wherein the biggest drop was observed at 130 cm SID (Figure 6.35; a-d). For the 10 year-old phantom, there was an increase in IQ sharpness which started after the 115 cm SID (Figure 6.36; a-c). The IQ clarity maintained only small changes (Figure 6.36; d-f).

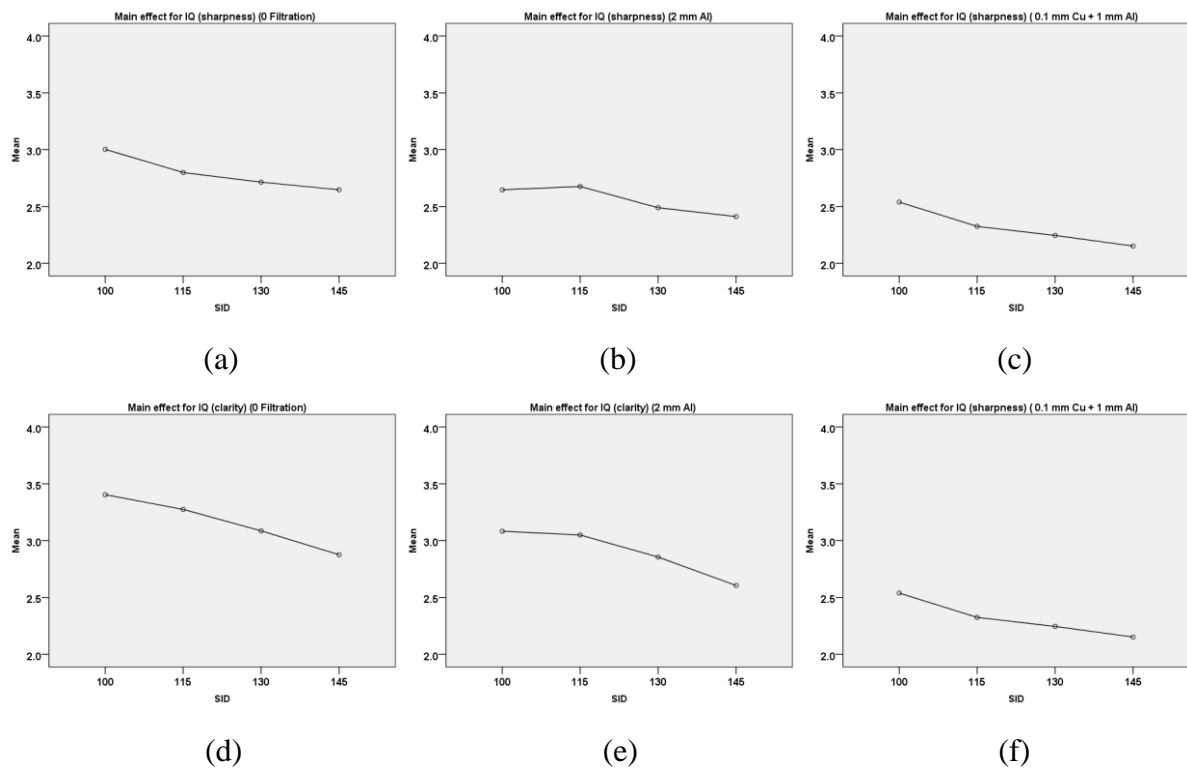


Figure 6.34: **1 year-old** main effect plot for visual image quality when increasing the SID; (a-c) for IQ (sharpness) and (d-f) for IQ (clarity). (a)&(d) at 0 filtration, (b)&(c) at 2 mm Al and (c)&(f) at 0.1 mm Cu + 1 mm Al.

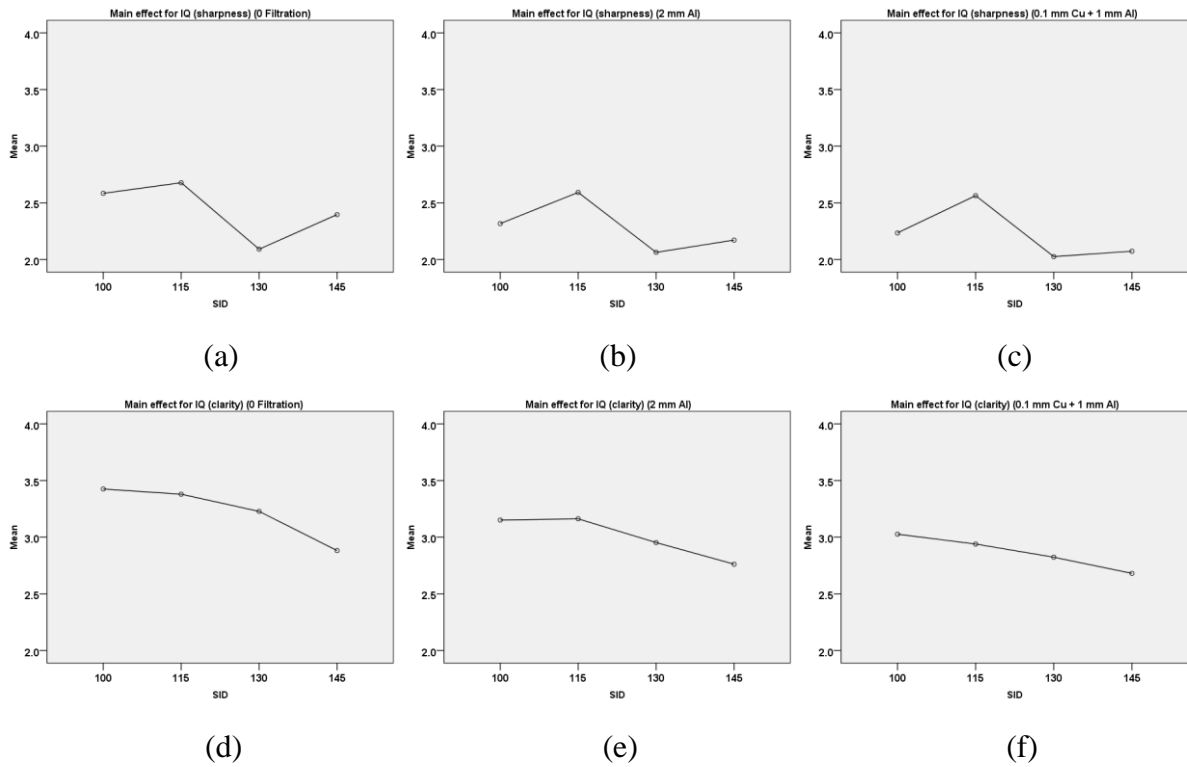


Figure 6.35: **5 year-old** main effect plot for visual image quality when increasing the SID; (a-c) for IQ (sharpness) and (d-f) for IQ (clarity). (a)&(d) at 0 filtration, (b)&(c) at 2 mm Al and (c)&(f) at 0.1 mm Cu + 1 mm Al.

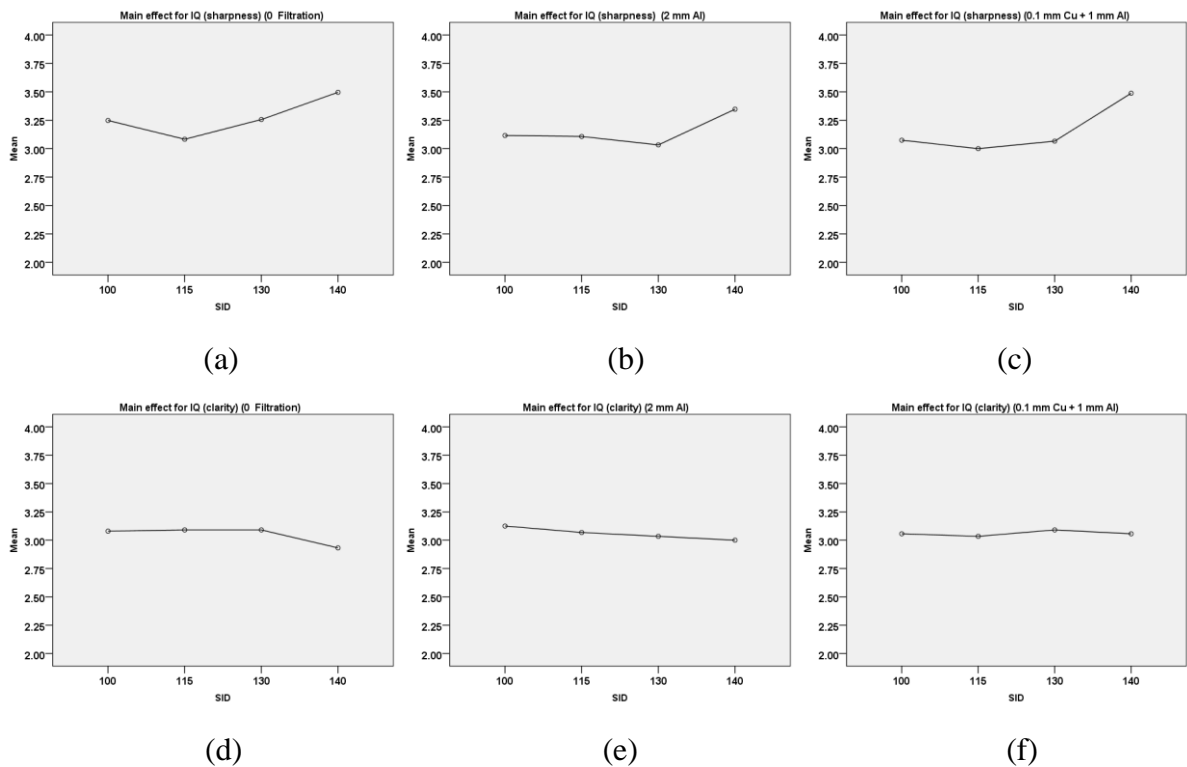


Figure 6.36: **10 year-old** main effect plot for visual image quality when increasing the SID; (a-c) for IQ (sharpness) and (d-f) for IQ (clarity). (a)&(d) at 0 filtration, (b)&(c) at 2 mm Al and (c)&(f) at 0.1 mm Cu + 1 mm Al.

The main effects of SID on IQ (sharpness & clarity) for 1, 5 and 10 year-old phantoms, at different levels of filtration, are presented in Figures (6.37), (6.38) and (6.39). This IQ score was used to determine the diagnostically acceptable IQ level, which is represented by a horizontal line in each plot.

The 1- and 5-year-old mean IQ scores showed that the highest filtration (0.1 mm Cu + 1 mm Al) scored the lowest IQ (sharpness & clarity), the second lowest was 2 mm Al and the higher mean IQ was at zero filtration. Also, the IQ means were above the diagnostically acceptable IQ level for all the ages and filtration aspects.

The plots for the 1 and 5 year-old phantoms show a continuous decrease in IQ when increasing SID, however the 115 cm SID for the 5 year-old phantom scored the highest IQ (sharpness & clarity),- see Figures (6.37; a-c) and (6.38; a-c). The plots for the 10 year-old showed stable IQ (both sharpness & clarity)- see Figure (6.39; a-c).

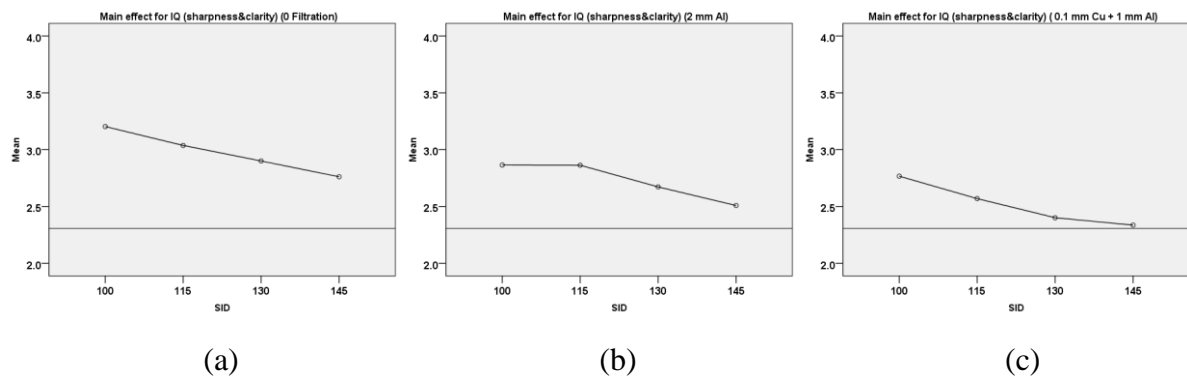


Figure 6.37: **1 year-old** the main effect plots for IQ (sharpness and clarity) when increasing the mAs. (a) at 0 filtration, (b) at 2 mm Al and (c) at 0.1 Cu + 1 mm Al.

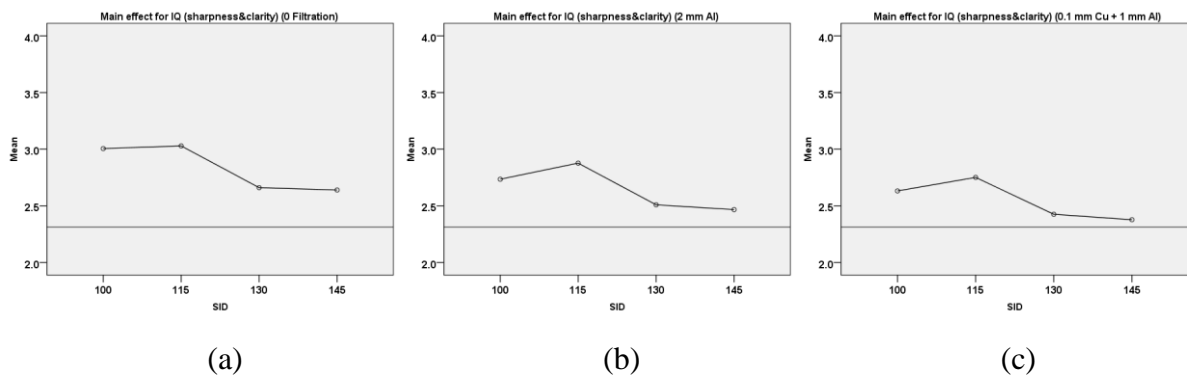


Figure 6.38: **5 year-old** the main effect plots for IQ (sharpness and clarity) when increasing the mAs. (a) at 0 filtration, (b) at 2 mm Al and (c) at 0.1 Cu + 1 mm Al.

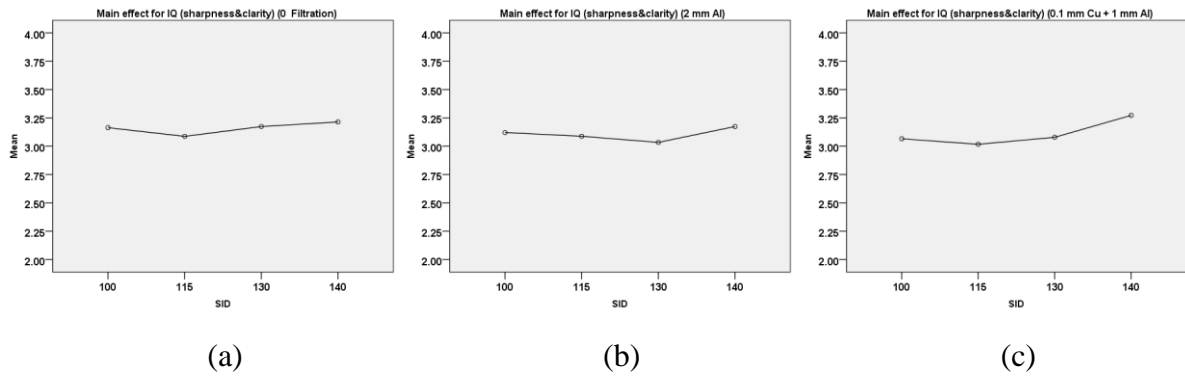
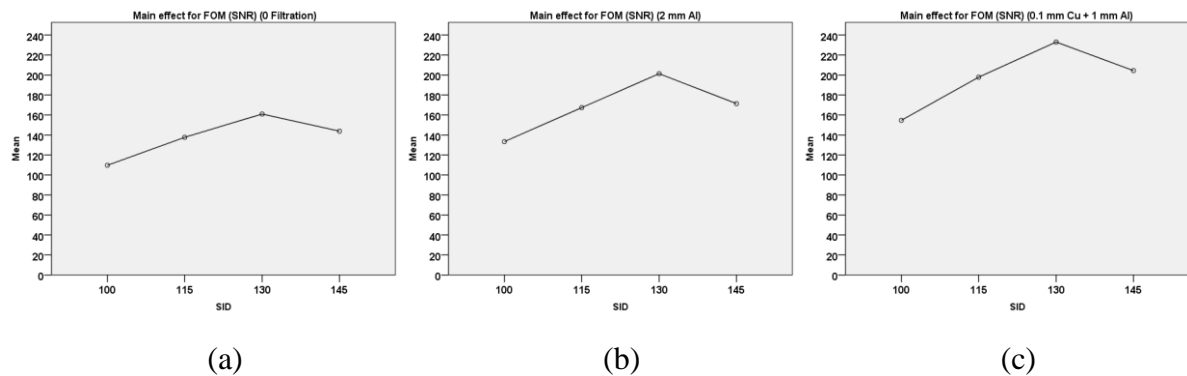


Figure 6.39: **10 year-old** the main effect plots for IQ (sharpness and clarity) when increasing the mAs. (a) at 0 filtration, (b) at 2 mm Al and (c) at 0.1 Cu + 1 mm Al.

The main effect plots for FOM (SNR) and FOM (visual IQ) versus SID for the 1, 5 and 10 year-old phantoms are presented in Figures (6.40), (6.41) and (6.42). The IQ levels used, based on visual and physical metrics, are for images of diagnostically acceptable quality. Similar to FOM (SNR), the higher mean for FOM (visual IQ) was the filtration combination (0.1 mm Cu + 1 mm Al). The 2 mm Al was second, and zero filtration scored the lowest. This was observed over the three phantom ages.

Figures (6.40-6.42; a-c) show an increase in FOM (SNR) when SID was increased for the 1, 5 and 10 year-old phantoms. This increase included an exceptional FOM (SNR) for the 1 year-old phantom at SID 130 cm, which scored the highest (Figure 6.40; a-c). The FOM (visual IQ), for 1, 5 and 10 year-olds, showed a continuous increase when increasing SID. This was seen over all filtration levels (Figures 6.40-6.42; d-f).



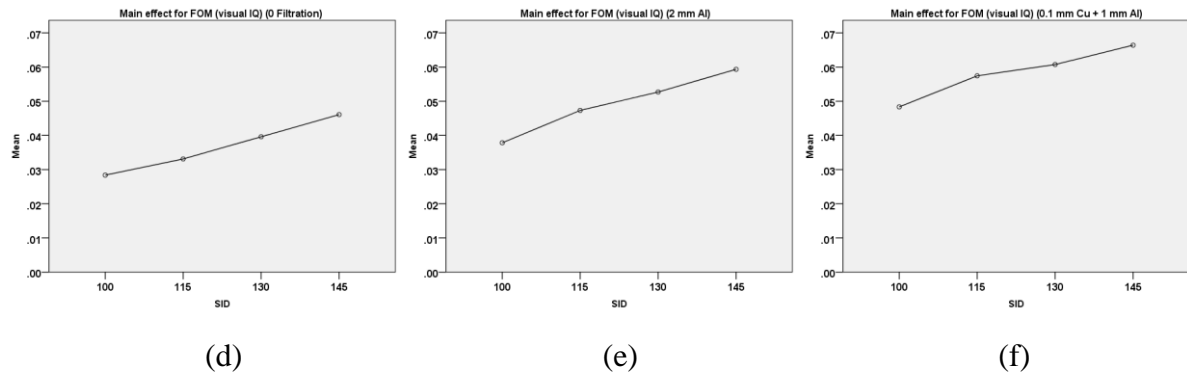


Figure 6.40: **1 year-old** the main effect plot for FOM when increasing the mAs; (a-c) for FOM (SNR) and (d-f) for FOM (visual IQ). (a)&(d) at 0 filtration, (b)&(c) at 2 mm Al and (c)&(f) at 0.1 mm Cu + 1 mm Al.

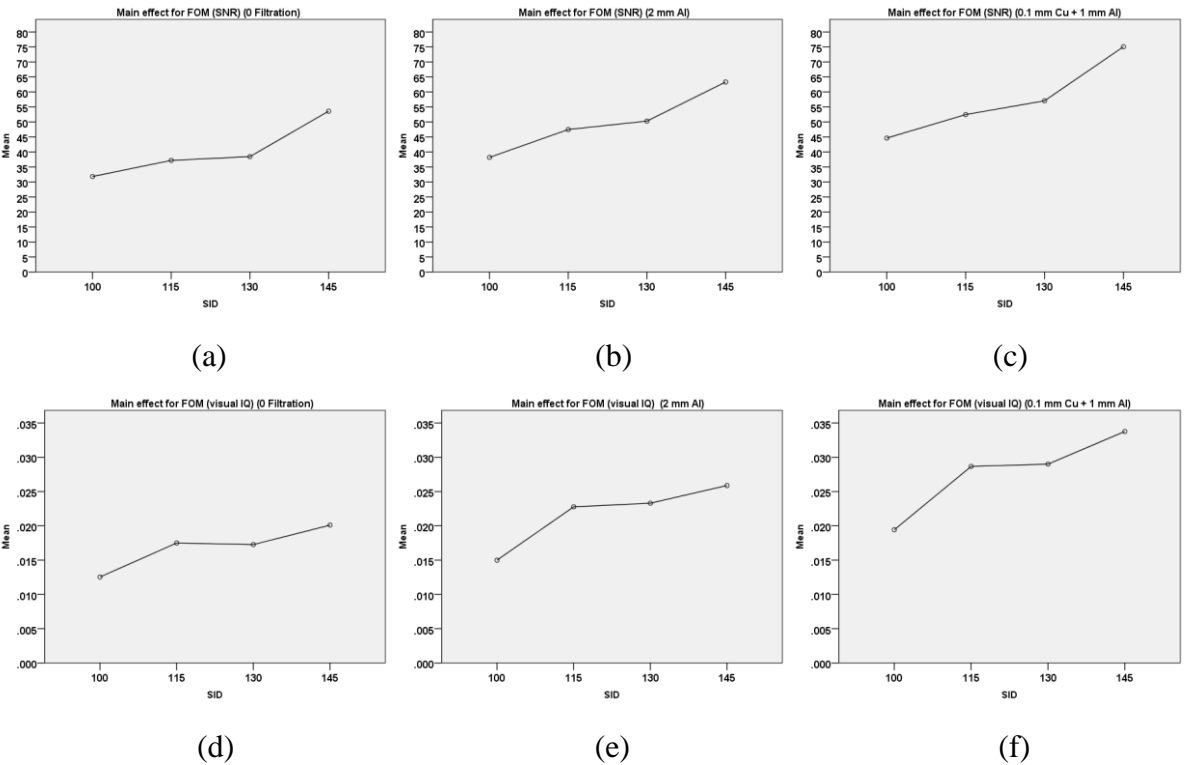
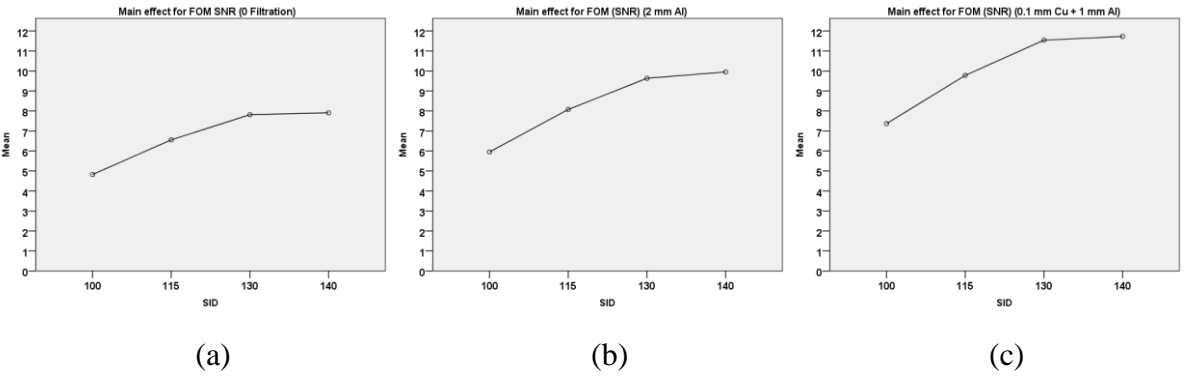


Figure 6.41: **5 year-old** the main effect plot for FOM when increasing the mAs; (a-c) for FOM (SNR) and (d-f) for FOM (visual IQ). (a)&(d) at 0 filtration, (b)&(c) at 2 mm Al and (c)&(f) at 0.1 mm Cu + 1 mm Al.



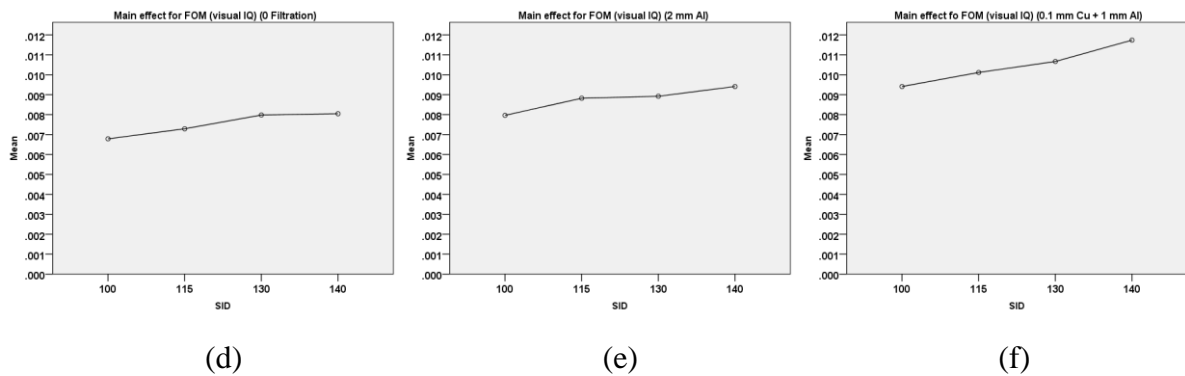


Figure 6.42: **10 year-old** the main effect plot for FOM when increasing the mAs; (a-c) for FOM (SNR) and (d-f) for FOM (visual IQ). (a)&(d) at 0 filtration, (b)&(c) at 2 mm Al and (e)&(f) at 0.1 mm Cu + 1 mm Al.

6.3.2 Correlations

Correlation tests were performed between all of the parameters that were considered in this study within each age group. Before performing the correlation test between the dependent and independent variables, a normality test was conducted in order identify the type of correlation statistic necessary. All of the variables measured had non-normal distributions, according to Shapiro-Wilk test ($p < 0.05$). Accordingly, the correlation of Spearman's rho was considered for all the paediatric ages.

The classification of the correlation coefficient was reported for each age, instead of its actual values. The reason for not reporting the actual values is that the correlation coefficient is useful to describe how strong (depending on the r value) the relationship is between two different variables. As a result, its true meaning can be seen through understanding its interpretation (Taylor, 1990). Also, the correlation coefficients that scored just below or above the correlation range threshold were reported.

For each phantom age, the classification of the correlation coefficient between each exposure factor and the measured variables was reported according to (Rumsey, 2011)- see page 159, section 5.8, in the Optimisation Methods chapter. Also, the correlation coefficient between the variables themselves was reported. This included the correlation between physical and visual IQ and radiation dose with both IQ aspects (sharpness and clarity) - see Table (6.7). The actual correlations (with their corresponding p values) for each age are listed Tables (II-4), (II-5) and (II-6) and in appendix (II). It is worth mentioning that all correlations for 1 and 5 year-olds were statistically significant ($p < 0.05$). The 10 year-old phantom showed correlations with significant p values. This was with the exception of SID correlation with radiation dose, IQ sharpness, IQ clarity, and both IQ aspects together (sharpness & clarity); and also of filtration against SNR,

CNR, IQ sharpness, IQ clarity and both IQ aspects together sharpness & clarity)- see Table (II-6) in appendix (II). The non-significant correlation coefficients can be related to the sample size, as the 10 year-old had only kVp and SID available in the form of continuous data, while filtration (three levels) was ordinal data which breaks down the number of increments and, thus, reduces the sample size.

From the Table (6.7), the range of the correlation coefficients for the kVp for 1 and 5 year-old phantoms were similar except for SNR. For the 1 year-old phantom, SNR scored a moderate correlation, while the rest scored either weak or no correlation. The kVp correlations for the 10 year-old phantom were all different, where they all, except for SNR (which showed a moderate correlation), showed a strong correlation with kVp.

The mAs showed overall moderate correlations for the 1 year-old phantom, except for the CNR which was strong. For the 5 year-old, mAs demonstrated strong relationships with all parameters except for IQ sharpness, which produced a moderate correlation ($r = 0.65$).

The correlation of SID for the 1 and 5 year-old phantoms showed similar correlations (all demonstrated 'no correlations', except for radiation dose which was weak). For the 10 year-old phantom, the SID showed no correlations, except for SNR and CNR which were moderate and weak, respectively.

For the correlations of filtration- filtration being ordinal data-, there is a methodological limitation when measuring correlations between continuous and ordinal/categorical data. As a result, the measured parameters showed either weak correlations or no relationship for all of the paediatric ages. The ages 1 and 5 showed similar correlation data, wherein no correlations existed except for radiation dose and CNR (which were weak). For the 10 year-old phantom, there were no correlations with filtration, except for radiation dose and DAP, but these were weak.

All the three ages showed positive correlations between the measured parameters. The dose correlations with other measured parameters showed a strong correlation with SNR, IQ clarity and both aspects of IQ together (sharpness & clarity). This is for both 1 and 5 year-olds. The dose for the 1 year-old phantom scored both strong and weak correlations with CNR and IQ sharpness, respectively, while both of them scored moderate within 5-year-old phantom ($r = 0.68$ for CNR). The 10 year-old dose correlations showed a strong relationship with DAP, CNR, IQ sharpness and both aspects of IQ together (sharpness & clarity). Moderate correlations between SNR and IQ clarity were seen with dose.

The DAP correlation, within the 10-year-old study, showed a strong correlation with IQ sharpness and both aspects of IQ together (sharpness & clarity), but it showed only a moderate correlation with IQ clarity ($r = 0.65$).

The relationship between physical and visual image quality showed a positive range of correlations. The SNR showed strong correlation with IQ clarity and both aspects of IQ together (sharpness & clarity), for both the 1 and 5 year-old phantoms. However it showed only weak and moderate correlations ($r = 0.69$ for 5-year-old) with IQ sharpness for the 1 and 5 year-olds, respectively. The 10 year-old SNR correlations showed moderate correlations with DAP, IQ sharpness and both aspects of IQ together (sharpness & clarity). It produced strong and weak correlations against CNR and IQ clarity, respectively.

The CNR correlations for the 1 year-old phantom showed a moderate correlation with IQ sharpness and a strong correlation with both IQ clarity and both aspects of IQ together (sharpness & clarity). The correlations associated with the data from the 5 year-old phantom demonstrated that CNR had strong correlations with all visual image quality aspects. For the 10 year-old phantom, CNR showed strong correlation with DAP, IQ sharpness and both aspects of IQ together (sharpness & clarity), while with IQ (clarity) it showed moderate correlation ($r = 0.53$).

The correlation between IQ clarity and IQ sharpness showed a strong relationship within the 5 year-old study, but within the 1 and 10 year-old datasets the correlation was weak ($r = 0.45$) and moderate ($r = 0.65$), respectively.

Table 6.7: Range of exposure factor correlation coefficients for each paediatric age.

	Age (years)	Dose	DAP	SNR	CNR	IQ (sharpness)	IQ (clarity)	IQ (sharpness & clarity)
kVp	1	Weak (+)	-	Moderate (+)	No (-)	No (-)	Weak (+)	No +
	5	Weak (+)	-	Weak (+)	No (-)	No	Weak (+)	No (+)
	10	Strong (-)	Strong (-)	Moderate (-)	Strong (-)	Strong (-)	Strong (-)	Strong (-)
mAs	1	Moderate (+)	-	Moderate (+)	strong (+)	Moderate (+)	Moderate (+)	Moderate (+)
	5	Strong (+)	-	Strong (+)	Strong (+)	Moderate (+)	Strong (+)	Strong (+)
	10	-	-	-	-	-	-	-
SID	1	Weak (-)	-	No (-)	No (-)	No (-)	No (-)	No (-)
	5	Weak (-)	-	No (-)	No (-)	No (-)	No (-)	No (-)
	10	No (-)	No (-)	Moderate (+)	Weak (+)	No (+)	No (-)	No
Filtration	1	Weak (-)	-	No (-)	Weak (-)	No (-)	No (-)	No (-)
	5	Weak (-)	-	No (-)	Weak (-)	No (-)	No (-)	No (-)
	10	Weak (-)	Weak (-)	No	No	No	No	No
Dose	1		-	Strong (+)	Strong (+)	Weak (+)	Strong (+)	Strong (+)
	5		-	Strong (+)	Moderate (+)	Moderate (+)	Strong (+)	Strong (+)
	10		Strong (+)	Moderate (+)	Strong (+)	Strong (+)	Moderate (+)	Strong (+)
SNR	1	Strong (+)	-		Strong (+)	Weak (+)	Strong (+)	Strong (+)
	5	Strong (+)	-		Strong (+)	Moderate (+)	Strong (+)	Strong (+)
	10	Moderate (+)	Moderate (+)		Strong (+)	Moderate (+)	Weak (+)	Moderate (+)
CNR	1	Strong (+)	-	Strong (+)		Moderate (+)	Strong (+)	Strong (+)
	5	Moderate (+)	-	Strong (+)		Moderate (+)	Moderate (+)	Moderate (+)
	10	Strong (+)	Strong (+)	Strong (+)		Strong (+)	Moderate (+)	Strong (+)
IQ (sharpness)	1		-	Weak (+)	Moderate (+)		Weak (+)	Strong (+)
	5		-	Moderate (+)	Moderate (+)		Strong (+)	Strong (+)
	10		Strong (+)	Moderate (+)	Strong (+)		Moderate (+)	Strong (+)
IQ (clarity)	1	Strong (+)	-	Strong (+)	Strong (+)	Weak (+)		Strong (+)
	5	Strong (+)	-	Strong (+)	Moderate (+)	Strong (+)		Strong (+)
	10	Moderate (+)	Moderate (+)	Weak (+)	Moderate (+)	Moderate (+)		Strong (+)

IQ (sharpness & clarity)	1	Strong (+)	-	Strong (+)	Strong (+)	Strong (+)	Strong (+)	
	5	Strong (+)	-	Strong (+)	Moderate (+)	Strong (+)	Strong (+)	(+)
	10	Strong (+)	Strong (+)	Moderate (+)	Strong (+)	Strong (+)	Strong (+)	
(+); negative correlation, (-); positive correlation, 0-0.3; No correlation, 0.3-0.5; Weak correlation, 0.5-0.7; moderate correlation and 0.7-1; strong correlation.								

6.3.3 Regression analysis

Regression provides an equation combining the dependent variable with independent variable(s) that are each multiplied by a factor called the regression coefficient (β). The regression coefficient represents the amount of change in the dependent variable for each unit change in each independent variable. The β represents the impact/gradient/slope, and is also called the standardised (or unstandardized for multi) regression coefficient in the regression equation. β can therefore represent the impact of the exposure factor when it is placed as the independent variable in the regression model for image quality or for radiation dose. Furthermore, when a multi linear regression is constructed with independent variables such as kVp, mAs, SID and additional filtration, a comparison between the impacts of each exposure factor becomes possible. Thus, the purpose of regression analysis is to investigate the proportional effect when changing the exposure parameters. In addition, we can understand the type of relationship that combines IQ (or radiation dose) with variations in exposure factors.

The information reported from this regression test includes the p value for F-test and β , which confirm the significant suitability (prediction) of the multi linear model and the significance of the gradient value, respectively. Also, the confident interval (CI) of β and R squared values were included, see Tables (6.5), (6.6) and (6.7) for the 1, 5 and 10 year-old, respectively.

The regression analysis showed that the R squared value, for the 1, 5 and 10 year-old phantoms, ranged from 0.91 to 0.99, 0.91 to 0.98 and 0.86 to 0.99, respectively. All of the phantom ages showed significant p values for the F-test ($P < 0.001$). The gradient (β) showed statistical significance for the 1 and 5 year-old phantom datasets, except for a case within the 1 year-old study which was the kVp in the IQ sharpness regression model.

The full radiation dose regression models from the 1 and 5 year-old phantoms showed that kVp and mAs have a positive impact on radiation dose. SID and filtration have a negative impact on the 1 and 5 year-olds' data, except for SID (on IQ sharpness and IQ (sharpness and clarity)) and

SID (on CNR) wherein they showed a positive impact. For the 10 year-old, the regression model demonstrated that SID, kVp and filtration have positive impact on radiation dose. While SID showed positive impact, kVp and filtration showed negative impact on IQ (sharpness & clarity) - see Tables (II-7), (II-8) and (II-9) in appendix I.

The regression models of all the measured parameters for the 1 and 5 year-old showed that addition of extra filtration had the highest gradient (impact) on radiation dose, and that the next three impacts were mAs, kVp and SID. Only, the IQ sharpness regression model for the 5 year-old study showed mAs slightly higher than filtration ($|\beta|$ ratio 1.21)- see Tables (6.8) and (6.9). The 10 year-old dose regression model of the measured parameters showed filtration had the highest impact, similarly to that of the other ages. The kVp and SID had the second most and third most impact, respectively. The SNR regression showed that kVp, SID and filtration had the first, second and third lowest impact - see Table (6.10).

There were wide variations in terms of $|\beta|$ value for each exposure factor and their ratios over all measured parameter in each age. The $|\beta|$ ratios of each exposure factor ranged from (1.1 to 82.8), (1.1 to 148.9) and (1.1 to 10.8) for the 1, 5 and 10 year-old, respectively. These ranges indicate to a large manipulability in the measured parameters, including IQ or radiation dose and, thus, to the potential of optimisation. Due to the many values shown in the Tables (6.8), (6.9) and (6.10), only the outstanding impact ratios affecting optimisation are described in detail, such as radiation dose and the score that defines the diagnostically acceptable IQ, which are both aspects of IQ together (sharpness and clarity).

1 year-old regression models

The regression models within the 1 year-old phantom showed that additional filtration and mAs had the highest impact on radiation dose and image quality (visual and physical), while the lowest impact was by SID. This was with the exception of IQ sharpness, wherein the tube potential was the third highest impacting variable and SID was the fourth.

In the dose regression model, the largest gradient ratio was additional filtration to SID (21.3). The absolute gradient ratio of filtration to kVp was 9.6 closely followed by the gradient ratio of mAs to SID which was 9.3. The last and lowest two impact ratios were mAs to kVp and kVp to SID which were 4.2 and 2.2, respectively.

The largest two variables to impact on the IQ (sharpness and clarity) regression model were filtration to SID (63.5) and mAs to SID (58.0). The gradient ratios of kVp to SID and filtration

to kVp were close and were 8.4 and 7.6, respectively. The mAs to kVp impact ratio was 6.9, while filtration and mAs showed relatively close gradients, wherein their ratio was 1.1 (Table 6.8).

The gradient ratios that scored more than three times than that of the other ratios in the SNR and CNR models were filtration to SID (17.4 and 43.5), mAs to SID (12.7 and 26.9), filtration to kVp (5.8 and 10.8), mAs to kVp (4.2 and 6.7) and kVp to SID (3.0 and 4.0), respectively. While filtration and SID in SNR and CNR regression models showed relatively close β values, their ratios were 1.4 and 1.6, respectively (Table 6.8).

The two biggest impact ratio variables in the regression model of IQ sharpness and IQ clarity were the same- filtration to SID (82.8 and 26.4) and mAs to SID (77.5 and 23.6), respectively. In the IQ sharpness, the gradient ratios of filtration to kVp and mAs to kVp were 12.0 and 11.2, respectively. The impact ratio for kVp to SID was 6.9. In the IQ clarity regression model, the gradient ratios of the filtration to kVp, mAs to kVp and kVp to SID were 4.4, 4.0 and 6.0, respectively. The filtration and mAs showed a relatively close $|\beta|$ value in both the regression model of IQ sharpness (1.1) and IQ clarity (1.1), this case is similar to the regression model for both aspects of IQ together (sharpness and clarity) (Table 6.8).

Table 6.8: Absolute β values (descending order) for each exposure factor along with their ratios for the **1-year-old** phantom.

Regression (1 year old)											
Radiation dose		SNR		CNR		IQ (sharpness)		IQ (clarity)		IQ (sharpness & clarity)	
Exposure factor	$\pm \beta $	Exposure factor	$\pm \beta $	Exposure factor	$\pm \beta $	Exposure factor	$\pm \beta $	Exposure factor	$\pm \beta $	Exposure factor	$\pm \beta $
Filter	-26.76	Filter	-12.46	Filter	-4.61	Filter	-0.17	Filter	-0.21	Filter	-0.19
mAs	11.70	mAs	9.10	mAs	2.86	mAs	0.15	mAs	0.19	mAs	0.17
kVp	2.80	kVp	2.16	kVp	0.43	SID	0.01	kVp	0.05	kVp	0.02
SID	-1.25	SID	-0.71	SID	-0.11	kVp	0.002	SID	-0.01	SID	0.003
Exposure factor β ratio											
Dose		SNR		CNR		IQ (sharpness)		IQ (clarity)		IQ (sharpness & clarity)	
Filter / mAs	2.29	Filter / mAs	1.37	Filter / mAs	1.62	Filtration / mAs	1.07	Filter / mAs	1.12	Filter / mAs	1.09
Filter / kVp	9.55	Filter / kVp	5.76	Filter / kVp	10.79	Filtration / SID	12.00	Filter / kVp	4.41	Filter / kVp	7.59
Filter /SID	21.34	Filter /SID	17.42	Filter /SID	43.45	Filtration / kVp	82.76	Filter /SID	26.35	Filter /SID	63.47

mAs / kVp	4.18	mAs / kVp	4.20	mAs / kVp	6.68	mAs / SID	11.24	mAs / kVp	3.95	mAs / kVp	6.93
mAs / SID	9.33	mAs / SID	12.73	mAs / SID	26.90	mAs / kVp	77.54	mAs / SID	23.59	mAs / SID	58.00
kVp / SID	2.23	kVp / SID	3.03	kVp / SID	4.03	SID / kVp	6.90	kVp / SID	5.98	kVp / SID	8.36

5 year-old regression models

The regression models within the 5 year-old phantom showed that kVp and SID had the third and fourth highest impact on radiation dose and measurements of IQ, while the first and second highest impact variables were filtration and mAs, respectively. This was with the exception of IQ sharpness, wherein the tube current was the highest impacting variable and filtration was the second.

In the dose regression model, the largest impact ratio was filtration to SID (19.6); the next biggest gradient ratio was filtration to kVp (9.9); and the third biggest gradient ratio was for mAs to SID (6.8). The impact of mAs was about three times the impact of kVp (their ratio was 3.5). The filtration to mAs impact ratio was 2.9, and the lowest impact ratio was for kVp to SID (2.0) (Table 6.9).

The gradient ratio of filtration to SID was similar to the dose regression model, and showed the largest impact ratio (148.9) in the regression model for both aspects of IQ together (sharpness and clarity). The second largest impact ratio was mAs to SID (135.8). The third biggest impact ratio (about a quarter of the second biggest) was kVp to SID (32.2). When considering the size of the impact ratio, filtration to kVp and mAs to kVp, were about the same- 4.6 and 4.2, respectively. The filtration and mAs showed similarity, where their ratio was 1.1 (Table 6.9).

The gradient ratios that scored more than three times that of the other ratios in SNR and CNR were filtration to SID (27.9 and 57.1), mAs to SID (16.8 and 28.0), filtration to kVp (6.3 and 28.8), kVp to SID (4.5 and 2.0), mAs to kVp (3.8 and 14.1) and filtration to mAs (1.7 and 2.0), respectively. The impact of filtration and mAs were relatively close (their gradient ratio was 1.7) in the SNR regression model, while in the CNR regression model kVp and SID were relatively close (their gradient ratio was 2.0) (Table 6.9).

The exposure factor impact ratios in the regression model of IQ sharpness, in descending order, were mAs to SID (8.9), filtration to SID (7.3), mAs to kVp (6.5) and filtration to kVp (5.4). The mAs and filtration showed similar impacts (their ratio was 1.2). kVp and SID were also of

similar impacts (1.4). In the IQ clarity regression model, the gradient ratios, from biggest to smallest, were filtration to SID (27.2), mAs to SID (22.1), kVp to SID (6.2), filtration to kVp (4.4) and mAs to kVp (3.6). The impact of filtration and mAs on IQ clarity were relatively close, wherein their ratio was 1.2 (Table 6.9).

Table 6.9: Absolute β values (descending order) for each exposure factor along with their ratios for the **5-year-old** phantom.

Regression (5-year-old)											
Radiation dose		SNR		CNR		IQ (sharpness)		IQ (clarity)		IQ (sharpness & clarity)	
Exposure factor	$\pm \beta $	Exposure factor	$\pm \beta $	Exposure factor	$\pm \beta $	Exposure factor	$\pm \beta $	Exposure factor	$\pm \beta $	Exposure factor	$\pm \beta $
Filter	-49.62	Filter	-6.50	Filter	-2.69	mAs	0.07	Filter	-0.18	Filter	-0.12
mAs	17.27	mAs	3.92	mAs	1.32	Filter	-0.06	mAs	0.14	mAs	0.11
kVp	4.99	kVp	1.04	kVp	0.09	kVp	0.01	kVp	0.04	kVp	0.03
SID	-2.54	SID	-0.23	SID	0.05	SID	0.008	SID	-0.006	SID	0.001
Exposure factor β ratio											
Dose		SNR		CNR		IQ (sharpness)		IQ (clarity)		IQ (sharpness & clarity)	
Filter / mAs	2.87	Filter / mAs	1.66	Filter / mAs	2.04	mAs / Filter	1.21	Filter / mAs	1.23	Filter / mAs	1.10
Filter / kVp	9.94	Filter / kVp	6.26	Filter / kVp	28.77	mAs / kVp	6.53	Filter / kVp	4.41	Filter / kVp	4.63
Filter /SID	19.56	Filter /SID	27.90	Filter /SID	57.06	mAs /SID	8.88	Filter /SID	27.22	Filter /SID	148.88
mAs / kVp	3.46	mAs / kVp	3.78	mAs / kVp	14.10	Filter / kVp	5.39	mAs / kVp	3.59	mAs / kVp	4.22
mAs / SID	6.81	mAs / SID	16.83	mAs / SID	27.96	Filter / SID	7.33	mAs / SID	22.13	mAs / SID	135.76
kVp / SID	1.97	kVp / SID	4.45	kVp / SID	1.98	kVp / SID	1.36	kVp / SID	6.17	kVp / SID	32.17

10 year-old regression models

The regression models within the 10 year-old study showed the first, second and third highest impacting variables on radiation dose were filtration, kVp and SID, respectively. The first, second and the third highest impacting variables on image quality measures, except for SNR, were kVp, filtration and SID, respectively. The factors that had the first, second and third highest impact on SNR were kVp, SID and filtration, respectively.

In the dose regression model, the largest impact ratio was filtration to SID (79.2), and the second largest was kVp to SID (5.7), respectively. Filtration to kVp had the lowest impact ratio (5.7) (Table 6.10).

The regression model for both aspects of IQ together (sharpness & clarity) showed that the largest impact ratio on this image quality scale was kVp to SID (22.5), and that the second largest impact ratio was filtration to SID (11.3). The kVp showed approximately twice the impact of filtration- their ratio was 2.0.

The regression models for SNR and CNR, similarly, showed that the biggest gradient ratios were kVp to filtration- 3.1 and 2.8. The second biggest for SNR and CNR were kVp to SID (1.81) and filtration to SID (2.6), respectively. The lowest impact ratios of the SNR and CNR regression models were from SID to filtration (1.7) and kVp to filtration (1.1), respectively (Table 6.10).

The largest impact ratio in the IQ sharpness model was kVp to SID (10.9). The next largest was filtration to SID (8.9), while kVp and filtration were about the same impact (1.2). Within the IQ clarity regression model, kVp to SID showed the biggest impact ratio (17.5). The next biggest was the gradient ratio of kVp to filtration (5.7) and the lowest impact ratio was filtration to SID- about three times (3.08) (Table 6.10).

Table 6.10: Absolute β values (descending order) for each exposure factor along with their ratios for the **10-year-old** phantom.

Regression (10 year old) (free intercept)											
Radiation dose		SNR		CNR		IQ (sharpness)		IQ (clarity)		IQ (sharpness & clarity)	
Exposure factor	$\pm \beta $	Exposure factor	$\pm \beta $	Exposure factor	$\pm \beta $	Exposure factor	$\pm \beta $	Exposure factor	$\pm \beta $	Exposure factor	$\pm \beta $
Filter	-76.24	kVp	-0.51	kVp	-0.76	kVp	-0.07	kVp	-0.03	kVp	-0.05
kVp	-13.44	SID	0.28	Filter	-0.71	Filter	-0.06	Filter	0.006	Filter	-0.03
SID	-0.96	Filter	0.16	SID	0.28	SID	0.006	SID	-0.002	SID	0.002
Exposure factor β ratio											
Radiation dose		SNR		CNR		IQ (sharpness)		IQ (clarity)		IQ (sharpness & clarity)	
Filter / kVp	5.67	kVp / SID	1.81	kVp / Filter	1.06	kVp / Filter	1.23	kVp / Filter	5.69	kVp / Filter	1.99
Filter / SID	79.18	kVp / Filter	3.14	kVp / SID	2.75	kVp / SID	10.93	kVp / SID	17.52	kVp / SID	22.52
kVp / SID	13.96	SID / Filter	1.73	Filter / SID	2.59	Filter / SID	8.92	Filter / SID	3.08	Filter / SID	11.30

6.4 Chapter Summary

This chapter presented the results of the systematic optimisation study which was undertaken for paediatric AP pelvis radiography. Firstly, it included identifying dose optimum acquisition factors for the three phantom ages- 1, 5 and 10 year-olds. The results showed that 65 kV, 2 mAs, 115cm SID and 2 mm Al additional filtration produced images with diagnostic quality at the lowest radiation dose (15 μ Gy) for the 1 year-old. For the 5 year-old, 62 kV, 8 mAs, 130 cm SID and 1 mm Al + 0.1 mm Cu additional filtration produced images with diagnostic quality and with the lowest radiation dose (43 μ Gy). For a 10 year-old, 89 kV, 130 cm SID and 1 mm Al + 0.1 mm Cu additional filtration, within HT orientation and two AEC outer chambers, produced the lowest radiation dose (179 μ Gy). Optimisation data also showed that physical IQ (SNR and CNR) data can be used to help in identifying diagnostically acceptable IQ via investigating the correlation for each metric against diagnostic IQ. Secondly, it demonstrated linear and nonlinear relationships with exposure factors (using main effect plots), with plateauing points being observed. Thirdly, it examined the ability to predict radiation dose, and visual/physical IQ from controlling exposure factors or radiation dose. This was through regression analysis that also estimated and compared the impact magnitude of each exposure factor on the radiation dose and IQ measures. Lastly, work within this chapter presented the impact from each exposure factor on radiation dose, physical IQ and visual IQ. In addition, it described the relative proportional effect of each exposure factor from regression with one another.

Chapter Seven: Discussion

7.1 Chapter overview

This chapter includes a discussion of the optimisation results obtained within this thesis. Within this chapter, conclusions from the results are given as are the study's limitations and the potential for future work. The structure of this chapter is similar to the results chapter on the optimisation of paediatric pelvis radiography (page 138). Mirroring the structure helped to simplify the discussion.

This chapter is divided into two main parts. The first part considers the optimisation of AP paediatric pelvis radiography, which includes the optimised exposure techniques that produced the lowest radiation dose. This part of the discussion brings together the results from the dose optimised exposure work together with the results from the regression and main effect analysis in order to explore dose reduction strategies further. The results are also compared against existing literature regarding paediatric optimisation studies.

The second part considers the effect of exposure factors on paediatric pelvis radiography, wherein the effect from each of the exposure factors is discussed in terms of main effect, when using correlation and regression analyses. The main effect analysis results are discussed in terms of whether there is a plateauing or a continuous increase/decrease with each increase in exposure factor on radiation dose, IQ and FOMs within the different paediatric ages. The trends of the main effect analysis are then compared with the trends reported in the literature. The regression analysis results are discussed in terms of the impact of each exposure factor on IQ and radiation dose; these are then compared to the impact of other exposure factors. The results from the regression analyses are then compared with similar regression studies within literature. Lastly, the correlation results are discussed to consider whether correlations might be promising as visual IQ predictors, such as exposure factors or physical measures of image quality.

Conclusions are made about which exposure factors result in the lowest radiation dose for each age. Conclusions are also drawn regarding the use of exposure factors that have a higher/lower impact on radiation dose than on image quality. Such investigations can be useful when considering dose reduction strategies.

7.2 Optimisation of AP paediatric pelvis radiography

This section combines the optimisation results section (page 163) with the other analyses (page 168) conducted within the results chapter such as main effect (page 171), correlation (page 196) and regression (page 200). This was undertaken in order to interpret each analysis and to help find the exposure factor combination that produces the lowest radiation dose with acceptable IQ.

7.2.1 Optimisation for 1 year-old phantom

Using a manual exposure mode for the 1 year-old, the results determined that the optimum technique was 65 kV, 2 mAs, 115cm SID and 0.1 mm Cu + 1 mm Al additional filtration. This combination produced images with diagnostic quality at the lowest radiation dose (15 μ Gy). The following will discuss separately each optimised exposure factor.

kVp

With respect to kVp, the most important function of tube potential is to provide at least partial penetration through all of the tissues that need to be imaged (Carroll, 2007, 2011). Increasing the kVp increases the average energy and intensity of the X-ray beam (Fauber, 2013; Graham et al., 2011). The 1 year-old dose optimised images that produced the lowest doses with acceptable IQ used 53, 59 and 65 kVp (Table 6.1, page 164). A possible explanation regarding this low kVp range can be offered by making a comparison with adult pelvis examinations wherein there is the need for higher kVp ranges to sufficiently penetrate thicker body parts (Mraity et al., 2016). The low kVp range can be related to the thinner pelvis associated with a 1 year-old which as such requires lower penetrability (Alzen & Benz-Bohm, 2011; L. Martin et al., 2013).

Linking the main effect analysis (Figure 6.12, page 178) with optimum kVp trends, there was an increase in diagnostic IQ (sharpness & clarity) which plateaued at 59 to 65 kVp (depending on filtration level), after which the mean IQ generally started to decrease. This means that IQ can be at its highest level within the range of 59-65 kVp. This can be explained by the k-edge related to the materials of the image detector, which showed that there is a specific energy range that, within which, the X-ray absorption is at its maximum level (Honey et al., 2005; Uffmann & Schaefer-Prokop, 2009). The literature suggests (Alzen & Benz-Bohm, 2011; Khong et al., 2013; Sj et al., 2015) that using a higher kVp with higher additional filtration levels could be considered as a dose reduction strategy. Findings from this thesis suggests using 1 mm Al + 0.1 mm Cu with 65 kVp being optimum. No further increases in IQ (sharpness & clarity) were

evident beyond 65 kVp (Figure 6.12; c, page 178). Comparing with the literature, a study found that 55 kVp should be used with 0.3 mm Cu filtration as a dose optimised exposure technique for a 1 year-old AP pelvis in DR imaging (McEntee & Doherty, 2011). The difference in results in this thesis compared to the aforementioned study can be related to the limited exposure factors (i.e. SID) these researchers used (only 0.3 mm Cu additional filtration). This can limit the findings to the tube potentials and filtrations used. In addition, the researchers used dosimetry phantoms which may limit their assessment of IQ since the phantoms use average bone density (cortical and trabecular bone) to simulate bone tissue (CIRS Tissue Simulation and Phantom Technology, 2011).

A hospital study by Martin et al. aimed to identify initial exposure factors for paediatric AP pelvis examinations at an acute hospital in the UK. They found an optimum tube potential for a 1 year-old AP pelvis radiography to be around 60 kVp, giving a dose of 120 μ Gy (L. Martin et al., 2013). Despite the close outcomes to this thesis (kVp was 65), there are limitations associated with the aforementioned study which has a relatively high kVp. This, together with the weight and age ranges which would vary within clinical studies, limits the outcomes from such studies (Billinger et al., 2010; Brosi et al., 2011). In addition, other limitations can be identified within Martin's work due to possible variations in the exposure factors tested (i.e. mAs, SID and filtration) in comparison to the work reported in this thesis.

mAs

Regarding the optimum setting with low mAs, the minimum mAs that showed a visually acceptable image quality was 2 (Table 6.1, page 164). A lower mAs value of 1 mAs was possible (radiation dose 31.41 μ Gy) but the images were not considered diagnostically acceptable since the extremely low radiation intensity reaching the image detector did not provide sufficient anatomical information (signal) compared to noise (Carroll, 2011). In addition, mAs showed a significant effect (from the main effect analysis) on diagnostic IQ (sharpness & clarity) and radiation dose. This is because of the direct relation of mAs to the amount of radiation (signal) reaching the image detector and contributing to the dose and IQ (Fauber, 2013).

The effect of mAs showed (from regression analysis) a higher impact ($+\beta$) than the impact of kVp ($+\beta$) and SID ($-\beta$) on both radiation dose and diagnostic IQ. This means that mAs plays a more dominant role in the optimisation of radiation dose and IQ compared to kVp and SID. However, investigating dominance in dose reduction does not provide a clear understanding as

to which exposure parameters are needed to provide the best balance between IQ and radiation dose. Following this, a comparison in terms of the impact ratios of each exposure factor to another on diagnostic IQ and radiation dose revealed which one was affected the most, and thus which one should take priority (increased or decreased) when attempting to achieve the best balance between IQ and radiation dose. Accordingly, the impact ratios of mAs to kVp and mAs to SID were both higher on IQ (sharpness & clarity) than on radiation dose (Table 6.8, page 202). Where the impact ratios of mAs to SID on diagnostic image quality was 58.0 while on radiation dose was 9.3, the division of the two is 6.2 (about six times). This means that the effect from mAs compared to SID is six times higher on diagnostic IQ than on radiation dose. The same effect from mAs and kVp was about one and half times (1.7). This indicates a closer effect. Thus, this study suggests increasing SID and lowering mAs as low as possible to be the most appropriate option for maintaining high IQ and with the lowest possible dose. Regarding balancing mAs and kVp, the regression model showed that kVp versus mAs manipulation had an approximately equal effect on radiation dose and diagnostic IQ. This regression showed no preference for changing mAs or kVp. However, the study has shown there is a kVp range that gives the highest diagnostic image quality (from main effect analysis) with mAs as low as possible, and can be used as to reduce radiation dose.

Comparing with the literature, the lowest mAs associated with the optimum techniques found in this thesis was 2 mAs. This is lower than 6.3 mAs at 60 kVp reported in a study which used a lamb's femur representing a 5 year-old child hip (H. Precht et al., 2014). The difference in mAs can be related to the size difference between the 1 year-old pelvis phantom, which is smaller than the femur of lamb representing a 5 year-old, or the difference in filtration and kVp used that would require a lower mAs (C. J. Martin, Farquhar, Stockdale, & Macdonald, 1994).

SID

Regarding SID, an advantage of increasing it during imaging is the subsequent reduction in radiation dose to the patient. There is also a reduction to the penumbra and magnification; overall this increases image sharpness (Carroll, 2011; Graham et al., 2011). The 1 year-old optimisation study showed that SID had a significant effect on IQ and radiation dose (from Friedman test, see subsection 6.3.1, page 171). In addition, images with diagnostically acceptable quality and the five lowest doses appeared at 115, 130 and 145 cm SID. The impact proportion of SID scored the lowest among the other exposure factors (see Table 6.8, page 202). This can be attributed to the level of radiation reduction associated with an increase of SID from 100 cm to 145 cm in comparison with the other exposure factors.

A study by Karami et al. used clinical data to investigate SID when optimising CR imaging systems (Karami et al., 2017). Their study found that increasing the SID from 100 to 130 cm reduced the radiation dose for AP pelvis projections by 30.6%, with no significant effect on IQ ($P>0.05$). Despite the similarity in producing a statistically significant dose reduction within data reported in this thesis, the difference in SID effect on IQ was significant but not in the work by Karami and colleagues. SID changes within this thesis showed significant effects on diagnostic IQ for the 1 year-old phantom. The non-significant effect of SID on IQ from the study by Karami et al. can possibly be related to the lower kVp range used in their study. This is in addition to the variation in the size of the patients included and the exposure factors, which would have a major impact on the IQ and radiation dose outcomes (Agarwal & Newbery, 2016; Brennan & Johnston, 2002). In addition, results from this hospital study were generalised over a wide paediatric age range (0 to 14 year-old for pelvis), which also would introduce significant size variations (Varchena, 2002). There was also a small sample size (24-32 images) used for all of the paediatric ages included.

Additional filtration

Filtration techniques involve removing the lower energy spectrum of x-ray photons by placing a sheet of material in the path of the X-ray beam (Carroll, 2007; Fauber, 2013). The dose optimised images of the 1 year-old pelvis study showed that filtration of 1 mm Al + 0.1 mm Cu was dominant among the other filtration levels examined. A few images at 2 mm Al were also recorded with optimum (lowest) dose. The main effect (and Friedman test) showed that filtration had a significant effect on radiation dose and IQ, this can be related to the fact that filtration reduces the quantity of the X-ray beam reaching the image detector, along with increasing its average energy (Fauber, 2013). Work within this thesis agreed with the study by Brosi et al. that found a significant difference in IQ and the radiation dose (ESD) for AP paediatric pelvis using a manual imaging mode (Brosi et al., 2011).

There are, however, some conflicting results between work reported in this thesis and other studies (Butler & Brennan, 2009; McEntee & Doherty, 2011). These studies found a significant difference on radiation dose from adding filtration, but with no difference on IQ. Differences between studies could be related to the differences in filtration combinations, kVp settings and limitations in the imaging phantoms used in both aforementioned studies, wherein the phantoms used were either test objects or ATOM dosimetry phantoms. Test object phantoms, such as the CDRAD, lack the anatomical representation and do not consider anatomical noise. As such, they provide a limited representation of clinical images (Veldkamp et al., 2006). ATOM

dosimetry phantoms contain bone density that are averaged for both the cortical and trabecular bone (CIRS Tissue Simulation and Phantom Technology, 2011).

Filtration showed the highest impact ($-\beta$) on radiation dose and diagnostic IQ among all the other exposure factors in the regression analysis. In order to determine whether IQ or radiation dose is affected more when changing filtration, when considering other exposure factors the impact ratios of filtration against each exposure factor were calculated (Table 6.8, page 202). The absolute impact ratio of filtration to mAs in the radiation dose regression model was 2.29, while for IQ (sharpness & clarity) it was about half (1.09) (Table 6.8, page 202). Thus, the filtration has almost double the impact of mAs on radiation dose than on diagnostic IQ scores. As a result, the data in this thesis suggests that using high filtration has an advantage over decreasing mAs as a technique to reduce patient dose. This agrees with the suggestion by Alzen and Benz-Bohm (2011) and by the CEC (1996) that tube filtration of 1 mm Al with 0.1 to 0.2 mm Cu must be used for paediatric and adult radiography (Alzen & Benz-Bohm, 2011; CEC, 1996).

Regarding the physical IQ (SNR and CNR), the acceptable IQ with lowest dose showed SNR and CNR mean values to be 52.77 and 14.54, respectively. Within the lowest five doses (Table 6.1, page 164), as doses went higher, the SNR and CNR showed an 'increasing' trend. This can be related to the strong correlation between them (Table 6.7, page 199). Also, significant differences were found (The Mann-Whitney U test and Wilcoxon test, $P < 0.001$) for SNR and CNR when compared between acceptable and non-acceptable visual image qualities. This means that the values of physical IQ (SNR and CNR) can be used to [statistically] predict visually acceptable IQ.

7.2.2 Optimisation for 5 year-old phantom

Using manual mode, similar to the 1 year-old, this dose optimisation study demonstrated the exposure techniques that would produce acceptable IQ with lowest radiation dose. The dose optimised exposure technique had exposure factors of: 62 kV, 8 mAs, 130 cm SID and 1 mm Al + 0.1 mm Cu additional filtration. These factors produced images with diagnostic quality and with the lowest radiation dose (43 μ Gy). The following will discuss separately each dose optimised exposure factor.

kVp

The 5 year-old phantom optimisation study showed that the lowest five radiation doses had 56, 59, 62 and 74 kVp (Table 6.2, page 166). This kVp range is higher on average than the kVp

range from the 1 year-old phantom. This finding is in agreement with the literature which demonstrates the need for higher kVp ranges for sufficient penetration of thicker body parts in paediatric imaging (Alzen & Benz-Bohm, 2011; Bloomfield et al., 2015b).

Regarding trends for optimising kVp, the main effect analysis showed an inflexion point (peak IQ), wherein the diagnostic IQ started to increase until it reached saturation between 65-77 kVp for all filtration levels (Figure 6.13, page 179). This makes the kVp range 65-77 the most suitable for achieving acceptable diagnostic IQ. This can be explained by the absorption sensitivity of the image detector which relates to the k-edge characteristics of the detector material (Seeram et al., 2013; Uffmann & Schaefer-Prokop, 2009). In relation to producing the lowest dose possible, the literature suggests that using a higher kVp with a lower mAs is a successful dose reduction technique (C. Martin et al., 1993). This is in addition to the use of 1 mm Al with 0.1 or 0.2 mm Cu added filtration (Alzen & Benz-Bohm, 2011; Khong et al., 2013). Thus, the aforementioned kVp range can be used in production the best IQ possible alongside added filtration of 1 mm Al + 0.1 mm Cu which can be used in optimum dose reduction, both the exposure factors can be implemented in solving the difficulty in balancing IQ with radiation dose.

McEntee & Doherty (2011) recommended 90 kVp and 45 kVp with 0.3 mm Cu filtration for imaging a 5 year-old AP pelvis, DR and CR, respectively (McEntee & Doherty, 2011). Their study showed discrepancies in tube potential between DR (90) and CR (45). Their use of limited exposure factors (i.e. SID) may be the result of such discrepancies, along with using phantoms designed for dosimetry purposes which have average bone density from cortical and trabecular bone (CIRS Tissue Simulation and Phantom Technology, 2011). Additionally, this work was a poster presented at an international scientific meeting and as such the IQ evaluation was only briefly described. This makes it hard to determine the level of rigour applied within their work. The mAs values were not reported in the work by McEntee & Doherty and this also limits any comparisons. Within the radiographic community, questions could also arise about their study regarding the dose implications of imaging with low kVp (45).

Another comparison with the literature can be made with the hospital study by Martin et al. which identified initial exposure factors in an acute hospital in the UK. They reported an optimum kVp for a 5 year-old AP pelvis as 65 with a resultant ESD of 130 μ Gy (L. Martin et al., 2013). In this study they increased kVp and mAs, forming different sets of exposure factors for each paediatric age (1, 5 and 10 year-old), whilst maintaining an 'adequate' dose received

by the CR detector. The generated sets of exposure factors were applied as subsequent protocols (each at a time) within each X-ray unit in the hospitals. However, their method had limitations, such as that their study did not consider any added filtration and changes to SID. Such acquisition factors have demonstrated a significant effect on IQ and radiation dose, as reported by Brosi et al. (Brosi et al., 2011), and would thus affect their outcomes. Also, there were limitations from the size and thickness variations which existed within each paediatric age range (Hart, Wall, Shrimpton, et al., 2000). Thus, their exposure factors were applied on different patient sizes (within each age group) and subsequently a range of image qualities and doses were produced (C. J. Martin, 2007a). In addition, Martin et al. also used a different IQ evaluation scoring system (absolute scale) which may be less sensitive to variations in IQ when compared to the relative VGA method used in this thesis (Månsson, 2000).

mAs

The minimum mAs found within the lowest 5 doses that produced visually acceptable IQ was 5 at 74 kVp (Table 6.2, page 166). Lower mAs values (4, 2.8, 2 and 1) that produced acceptable IQ were rare, except for 4 mAs that appeared as the 7th lowest dose protocol (ESD 50.7 μ Gy) at 80 kVp, 130 cm SID and with filtration of 1 mm Al + 0.1 mm Cu. The reason for an absence of lower mAs values is related to the corresponding thickness of the 5 year-old phantom that attenuates a certain amount of radiation before it reaches the imaging plate. Thus, a higher radiation intensity is needed (from higher mAs) for the signal, rather than noise, to reach the image detector. This is needed to supply sufficient anatomical information (Carroll, 2011). Compared to the mAs from the 1 year-old optimisation study, the higher mAs for the 5 year-old can be attributed to the thicker body parts. In addition, the main effect analysis showed that mAs has a significant effect on IQ (sharpness & clarity) and radiation dose. This is likely due to the direct relation of mAs to the amount of radiation (signal) reaching the image detector and its contributing to the dose and IQ (T. Herrmann et al., 2012; Johnston & Fauber, 2011).

Similar to the 1 year-old phantom, the regression analysis for the 5 year-old phantom showed that mAs, after filtration impact, has a higher impact ($+\beta$) than kVp ($+\beta$) and SID ($-\beta$) on both radiation dose and diagnostic IQ. This means that mAs is dominant compared to kVp and SID in controlling diagnostic IQ and radiation dose. Comparing impact ratios for one exposure factor to another on both diagnostic IQ and radiation dose can determine which one is affected the most, thus, can help to find the best balance between IQ and radiation dose. The impact ratios for mAs to kVp and mAs to SID were both higher on IQ (sharpness & clarity) than on radiation dose (Table 6.9, page 204). The impact ratios of mAs to SID on diagnostic IQ and

radiation dose were 135.8 and 6.8, Respectively, their ratio is 19.97 (about 20 times). The corresponding effect from mAs and kVp was about 1.2 times, which is a closer effect. This means that mAs (compared to SID) can affect the diagnostic IQ about 20 times more than the radiation dose. While mAs and kVp affect diagnostic IQ and radiation dose relatively equally. Thus, this thesis suggests prioritising the increase of SID in favour of decreasing the mAs, as mAs (compared to SID) affects IQ higher than radiation dose and gives a greater balance between keeping acceptably high IQ with as low a dose as possible (ALARP). Since the impact ratios of the mAs and kVp on radiation dose and IQ were about equal, the regression analysis proposes no preference to increasing kVp or mAs. However, the data suggests using the kVp range (65-77 kVp) would give the highest IQ.

In comparison to literature, the lowest mAs associated with optimum techniques was 5 (ESD 49.12 μ Gy), which is lower than the mAs found in the study by Precht et al. which was 6.3 with a skin dose of 125 μ Gy (at 60 kVp and 5.2 mm Al) for a 6 month-old lamb femur representing a 5 year-old child's hip (H. Precht et al., 2014). This higher mAs and radiation dose can be attributed to the thicker lamb hip (20 cm), which would require a higher mAs to reach an acceptable IQ. Still, the skin dose is far higher than the optimised radiation dose that was recorded in this thesis; this relates to the limitations of Precht's study, as it only used a narrow range of exposure factors.

SID

Regarding the effect of changing the SID, the main effect analysis and Friedman test for the 5 year-old phantom optimisation study demonstrated a significant effect of SID on IQ and radiation dose. The optimised techniques showed that images with acceptable IQ and the lowest doses appeared at larger SIDs, i.e. 130 and 145 cm (Table 6.2, page 166). This can be linked to the advantage of increasing SID during imaging which reduces the radiation dose to the patient. It also reduces the penumbra in the image and increases the sharpness of the recorded details, as noted earlier. A larger SID also results in less image magnification (Carroll, 2011; Graham et al., 2011).

From the regression analysis, the SID showed the lowest impact proportion on radiation dose and on diagnostic IQ among the other exposure factors (see Table 6.9, page 204). Also, when SID is increased, there is no effect on 'diagnostically acceptable' IQ scores (main effect analysis; Figure 6.38, page 193). This is likely to be related to the fact that the SID range (100-145 cm) does not reduce the X-ray radiation dose as much as the other exposure factors studied.

When comparing these findings with the literature, Karami and colleagues undertook a clinical study to examine the effect of SID when optimising AP pelvis CR imaging systems (Karami et al., 2017). They found a significant dose reduction for AP pelvis protocols with no significant effect on IQ when using an SID range of 100-130 cm. There is some similarity with the findings in this thesis as the dose reduction was significant, however the effect on IQ was not similar. Image differences between the work in this thesis and the results from Karami et al. could have arisen from 1) differences in the imaging systems used, i.e. DR versus CR; 2) differences in the image evaluation methods used; and 3) variations in exposure factors that usually affect IQ outcomes (Agarwal & Newbery, 2016; Brennan & Johnston, 2002). Furthermore, a wide paediatric age range (0 to 14 years old for pelvis), was used in the above-mentioned study which can limit the reliability of these results due to significant size variations (Varchena, 2002). In addition, there was a small sample size (24-32 images) used across a wide range of paediatric ages. However in this study, 2016 images were acquired using the 5-year old phantom.

Additional filtration

With regards to additional filtration, all of the diagnostically acceptable images with the lowest dose in the 5 year-old optimisation study (Table 6.2, page 166) had 1 mm Al + 0.1 mm Cu filtration. This can be explained by the ability of filtration to remove the low energy X-ray photons and, hence, reduce radiation doses (Fauber, 2013). Similar results were found by Brosi et al who found a significant difference in the radiation dose (ESD) and partial differences in IQ (depending on body part thickness) when increasing additional filtration during AP paediatric pelvis radiography (Brosi et al., 2011).

The main effect analysis and Friedman test showed a significant effect of additional filtration on radiation dose and IQ. This can be explained by the reduction in the amount of X-ray photons reaching the image detector, along with increasing the average beam energy (Fauber, 2013). Both would decrease IQ and radiation dose.

Other studies' results agree with this thesis' conclusion that a statistically significant decrease from additional filtration was demonstrated for radiation dose only. These studies disagree with this thesis by showing no significant effect on IQ from applying extra filtration (Brosi et al., 2011; Butler & Brennan, 2009; McEntee & Doherty, 2011). There are some differences which could explain the reason for their showing different results, such as: different filtration levels were studied; a different range of tube potentials were used and limitations exist in the imaging phantoms used; and the authors typically used either test objects or ATOM dosimetry phantoms,

both of which have limitations for representing bony anatomical shapes and soft tissues. Test objects lack anatomical detail and anatomical noise and as such provide a limited representation of clinical images (Veldkamp et al., 2006). ATOM dosimetry phantoms contain bone density equal to average of both the cortical and trabecular bone, but not to the real density of bone (CIRS Tissue Simulation and Phantom Technology, 2011).

Regarding the regression model, filtration scored the highest impact ($-\beta$) amongst the other exposure factors on diagnostic IQ and radiation dose. In order to determine whether IQ or radiation dose is affected more than the other from each exposure factor when compared to filtration, the impact ratios of filtration to each exposure factor were calculated (Table 6.9, page 204). The filtration to mAs impact ratio was 2.87 for radiation dose and 1.10 for IQ. Thus, changing filtration and mAs has about twice the impact (2.60) on radiation dose than on diagnostic IQ. One can conclude that increasing filtration when decreasing mAs has advantages in reducing the radiation dose to patient whilst maintaining acceptable IQ. There is agreement in the literature to support this (Alzen & Benz-Bohm, 2011; CEC, 1996). Several studies have recommended adding additional filtration of 1 mm Al with 0.1 to 0.2 mm Cu for paediatric examinations.

Concerning the measurements of physical IQ (SNR and CNR), the images which scored acceptable IQ with the lowest five radiation doses had mean SNR and CNR, values of 51.53 and 15.30, respectively (Table 6.2, page 166). Within the lowest five doses, as radiation doses went higher, there was a similar trend between increasing dose and SNR. This can be related to the strong correlation between these two variables (Table 6.7, page 199). Also, a significant difference was found between acceptable and non-acceptable visual IQ (Mann-Whitney U test and Wilcoxon test, $P < 0.001$) for each of the SNR and CNR values. This means that the values of SNR and CNR, as physical image quality metrics, can statistically predict visual (from observers) IQ acceptability.

7.2.3 Optimisation for 10 year-old phantom

Within the 10 year-old age phantom category, unlike the two younger ages, dose optimisation was undertaken using AEC and with the inclusion of an anti-scatter radiation grid. All of the images produced using these techniques had visually acceptable IQ. The study included variations of kVp, SID, additional filtration, AEC orientation and chamber combinations. The lowest radiation dose was 178.8 μ Gy, while the lowest SNR and CNR were 48.4 and 16.2, respectively.

Comparison between orientations

Comparisons between HT (head toward the two AEC outer chambers) and HA (head away the two AEC outer chambers) orientations for the 10 year-old phantom were performed for radiation dose and diagnostic IQ. In terms of dose reduction between the two orientations, the comparison between HT and HA orientation for the 10 year-old phantom showed a significant difference (Wilcoxon, $P < 0.05$). Higher doses were demonstrated for the HA orientation than for the HT orientation (Table 6.4, page 169). This can be explained by the position of the ionisation chambers under the bony anatomies, which require more radiation to the threshold value for the termination of the AEC (Carroll, 2011). Opposite results were found in adult pelvis optimisation studies (Harding et al., 2014; Manning-Stanley et al., 2012; Mraity, 2015), which undertook radiation dose comparisons between the two orientations. They found that the radiation dose in HA was lower than in the HT orientation (head towards the anode; or caudal AEC orientation, otherwise known as head away from the two outer AEC chambers). This difference could be related to the size of the 10 year-old pelvis, specifically the iliac crest and sacrum, which is not sufficiently large enough, unlike adults' are, to lie over the two outer chambers in HT orientation. This issue was mentioned in the report of the Council of the European Communities (1996) with respect to the size of the AEC chambers, shape and position not being satisfactory for paediatric use (CEC, 1996).

Regarding results reported within this thesis for comparing the IQ of the two orientations, all of the images from both orientations were diagnostically acceptable; this agrees with the other studies (Harding et al., 2014; Manning-Stanley et al., 2012; Mraity, 2015). However, the actual IQ scores between the two orientations showed significant differences (Wilcoxon, $P < 0.05$) within this thesis. Where HA had higher IQ (Table 6.4, page 169), this would relate to the higher mean dose associated with this HA orientation and the subsequent increase in SNR. The aforementioned results disagree with the results by Mraity, who found that IQ and radiation dose were higher in the HT orientation for adult AP pelvis imaging (Mraity, 2015). The difference in results presented in this thesis could be related to the size of the bony pelvis that covers the ionisation chambers for adult patients. As previously mentioned, this might not be large enough in children to achieve the same coverage. Results from this thesis also support the results of Manning-Stanley and colleagues who examined IQ differences between the two orientations and found that IQ remained adequate during AEC adult pelvis radiography

(Manning-Stanley et al., 2012). The differences in IQ, between the two orientations, reported in this thesis were statistically significant ($P < 0.05$), while Manning-Stanley's study found IQ reduction but no statistically significant differences. On the other hand, there is agreement in the outcomes between this thesis and a study by Harding et al. who found that IQ in HT orientation was slightly lower than HA orientation, but not statistically significant (Harding et al., 2014).

Comparison between the AEC chambers combinations

A comparison between the AEC chamber combinations was performed in terms of diagnostic IQ and radiation dose, within the HT orientation. In term of radiation dose, this revealed that examinations using the two outer chambers had the lowest radiation dose and those with the middle AEC chamber produced images with the highest dose, while those acquired with the three outer chambers were in between (Table 6.5, page 170). This can be explained by the two outer ionisation chambers in the HT orientation not being covered by the iliac crest, while the other chamber was not active (Manning-Stanley et al., 2012). Thus, less radiation is required to reach the cut-off (threshold) point during imaging using AECs. Different results from studies investigating the adult pelvis (Hawking & Elmore, 2009; Manning-Stanley et al., 2012) found that, with HA orientation, using the two outer chambers showed the lowest dose, using three chambers was second lowest, and using the middle chamber had the highest radiation dose (ESD). This can be explained by the bony component of the pelvis, within the above studies, not covering the two outer AEC chambers in the HA orientation. Within this thesis, the two outer chambers were not covered by bony anatomy in the HT orientation and thus resulted in a lower radiation dose.

Concerning the IQ between the three chamber combinations, the middle chamber showed the highest diagnostic IQ. This is likely to be related to the amount of radiation received, as the middle chamber combination showed the highest radiation dose (median) (Table 6.5, page 170). The results of this thesis are similar to what was found by Manning-Stanley et al. regarding IQ scores for the middle chamber configuration (Manning-Stanley et al., 2012).

kVp

Regarding kVp, the effect of using higher kVp results in an increase in the average energy of the X-ray beam, besides increasing the amount of X-ray radiation reaching the detector (Fauber, 2013; Graham et al., 2011). Since the AEC mode is used in this study, the radiation reaching the image detector is compensated to maintain an adequate amount of radiation (T. Herrmann

et al., 2012). As a result, the effect from kVp is only its increasing the penetrability of the X-ray beam. Thus, increasing kVp for AEC imaging would decrease the radiation dose reaching the patient. Such reasons can limit comparisons between studies using AEC and those using manual exposures.

Results from this thesis suggest using high tube potential (89 kVp) for dose optimised imaging. This agrees with the literature wherein a high kVp is supported as a dose reduction technique (T. Herrmann et al., 2012). A decrease in radiation dose when increasing kVp was observed in the main effect plots. Also, the main effect analysis showed a significant effect from increasing kVp on reducing both radiation dose and the diagnostic IQ for each orientation and AEC chamber combination studied. However, all images were acquired with acceptable IQ. This means that the penetrability of kVp alone has a significant effect even when the AEC compensates for the radiation intensity. Similar results were reported by Mraity (2015) in a similar study investigating adult AP pelvis imaging.

In the literature, a study by McEntee and Doherty found that 65 kVp with 0.2 mm Cu of filtration could be considered as the dose optimised exposure technique for a 10 year-old AP pelvis examination (McEntee & Doherty, 2011). Unlike this thesis, their study used a manual imaging mode which limits direct comparisons. Nevertheless, there are other sources of variations including the exposure range and the type of phantoms used (dosimetry) (CIRS Tissue Simulation and Phantom Technology, 2011).

With regards to hospital based studies, a group of researchers (Paulo, Santos, Moreira, & Figueiredo, 2011) undertook a hospital study using 70, 81 and 90 kVp for patients with a weight range of <20, 20-40 and >40 kg, respectively. This was instead of using the routine 60 kVp across the whole weight range together with AEC imaging. They found significant dose reduction and maintained diagnostic IQ when applying weight-specific protocols. These findings were similar to what was found in this thesis regarding the dose optimised exposure techniques with relatively higher tube potentials (89 kVp) and diagnostic IQ.

SID

The effect of increasing SID is that it generally decreases the radiation dose reaching the patient (Graham et al., 2011). However, this was not the case for AEC imaging. The reason for this relates to the fact that when SID is increased, the ionisation chambers increase the exposure time to achieve the threshold amount of radiation needed (T. Herrmann et al., 2012). Thus, the effect of the inverse square law is negated. The greatest effect from increasing the SID is on IQ

by reducing the penumbra (increasing the sharpness of the recorded details) and decreasing image magnification (Carroll, 2011; Graham et al., 2011). This can limit comparison with other studies in the literature which have used manual modes, as the effect from reducing radiation dose on IQ is eliminated by the AEC imaging mode. It was observed from the Friedman test that no significant difference was recorded from changing the SID (100-140 cm) on diagnostic IQ, however there was a significant difference in radiation dose for the both orientations with all AEC chamber combinations. The low effect on diagnostic IQ could be related to the low sensitivity of human perception to subtle differences which can be generated from the continuous compensation of the AEC chambers (Smith & Webb, 2010).

Amongst all the exposure factors investigated, the SID showed the lowest impact on radiation dose ($-\beta$) and on diagnostic IQ ($+\beta$) in the regression models (Table 6.10, page 205). The lowest impact of SID on radiation dose and IQ can be justified by the compensation of the ionisation chambers during the AEC imaging mode. Thus, dose reduction is almost cancelled by the AEC function. While filtration and kVp have a higher impact as they both increase the average energy of the X-ray beam, in addition to changing the amount of radiation, the AEC is not capable of stopping the effect on radiation dose and IQ of changing the X-ray energy.

kVp to SID impact proportions in the regression model were 14 for radiation dose and 22.5 for diagnostic IQ. This means that the effect of changing both kVp and SID are about the same (their ratios are about 1.6 times for both kVp and SID) on radiation dose and diagnostic IQ. However, the SID showed a positive impact on diagnostic IQ and a negative impact on radiation dose. Thus, the results suggest increasing SID as a preferred choice for dose reduction. For 'additional filtration' to 'SID manipulation', the impact ratio on radiation dose (79.2) was larger than on diagnostic IQ (11.3) by about seven times. This means that the effect of changing filtration (compared to SID) has approximately seven times more effect on radiation dose than on diagnostic IQ. This makes filtration a preferred change, when compared to SID, however the SID showed a positive impact on diagnostic IQ (Table 6.10, page 205). Thus, the results suggest using a larger SID and higher filtration levels.

In the literature, the effect from increasing SID was studied for an adult anthropomorphic phantom to obtain AP pelvis images under AEC imaging (Brennan et al., 2004; Tugwell et al., 2014). They found a significant reduction in ESD while no significant reduction in IQ was observed. These results agree with the results within this thesis.

As mentioned earlier, limitations arise when comparisons are made with other studies which used manual imaging, however it can be useful to compare differences in the outcomes between the two imaging modes (manual and AEC). Karami et al. undertook a clinical study to examine the effect of increasing the SID (100-130 cm) when optimising AP pelvis CR imaging systems (Karami et al., 2017). They found a significant dose reduction in AP pelvis protocols with no significant effect on IQ. These studies also agree with the results found in this thesis.

Additional filtration

All the diagnostically acceptable images with the five lowest doses (Table 6.3, page 168) were with 1 mm Al + 0.1 mm Cu additional filtration. This can be explained by the ability of filtration to remove the low energy X-ray photons and, hence, reduce radiation doses (Fauber, 2013). This is done whilst maintaining visually acceptable IQ. Also, from the Friedman test, the added filtration showed a significant effect (reduction) on radiation dose but no significant effect on diagnostic IQ. This was observed for HT orientation for all AEC chamber combinations. The significant effect of reducing the radiation dose can be related to the beam hardening that causes a reduction in the dose. The non-significant effect from added filtration on IQ can be related to the effect from beam hardening. This reduces IQ whilst the radiation dose is compensated by the AEC mode. The effect of increased average energy on IQ is reduced by the wide dynamic range of the digital imaging system that maintains image contrast (J. Hansson et al., 2005). Thus, the effect of additional filtration on IQ is small (not significant).

Concerning the regression analysis for the 10-year-old phantom, additional filtration showed the highest impact on reducing radiation dose ($-\beta$), while also showing the second highest impact after the kVp on diagnostic IQ ($-\beta$). The comparison between filtration and kVp effect's on IQ can be explained by the level at which image contrast is decreased, wherein kVp can increase average X-ray energy more than filtration. On the other hand, the impact ratio of filtration to kVp on radiation dose (5.67) is bigger than that of diagnostic IQ (1/1.99) by about eleven times (11.28). This means that increasing filtration (compared to kVp) has an eleven times bigger effect on radiation dose than it does on diagnostic IQ. Thus, the results suggest using higher filtration rather than increasing kVp. This agrees with that which is recommended in the literature, wherein it is suggested that 1 mm Al with 0.1 to 0.2 mm Cu be used for paediatric and adult imaging (Alzen & Benz-Bohm, 2011).

Comparison with literature, as mentioned earlier, is limited due to the AEC imaging mode which compensates for the reduced radiation when adding additional filtration, unlike the

manual mode. Thus, the effect of filtration for AEC imaging is different when compared to manual imaging, which makes comparisons difficult.

A number of publications agree with the findings in this thesis, wherein a statistically significant effect was seen when increasing additional filtration on radiation dose, with no significant effect on IQ (Butler & Brennan, 2009; McEntee & Doherty, 2011). There are, however, instances of disagreement found in the literature. A study by Brosi et al. showed partial differences regarding the effect of adding filtration on IQ (due to the different body part thickness evaluated) (Brosi et al., 2011). Differences in the results can be explained by the different imaging mode used in their studies. The IQ in manual mode is more affected by dose reduction and X-ray beam energy increase when increasing filtration and both of these, unlike in AEC, affect IQ. There are other reasons for such differences, and these would include: the specific filtration levels selected, the kVp ranges and the limitations associated with using PMMA and CDRAD imaging phantoms, both of which have well documented anatomical/clinical limitations (Veldkamp et al., 2006).

7.3 Effect of exposure factors on paediatric pelvis radiography

A correlation test was performed between all of the parameters measured for each phantom age (1, 5 and 10 years old). Correlation statistics were calculated between the exposure factors and the dose and IQ, as well as between the measured metrics themselves (physical and visual IQ). The classification of correlation coefficients was reported for each phantom age in order to investigate the prediction level between the exposure factors and measured parameters, as well as between the measured parameters themselves. Also, a main effect analysis was performed in order to plot the responses from IQ, radiation dose and FOM when each exposure factor increased. In addition, a regression model was developed for each measured parameter containing all of the exposure factors so that their individual impact could be determined. Accordingly, the regression analysis will determine how much each exposure factor contributes to each measured parameter, and their contribution compared to one another.

Combining these three tests (main effect, correlation and regression) will produce a fuller understanding of the abilities and limitations of controlling IQ and radiation dose within pelvis paediatric radiography.

7.3.1 Main effect

The analysis of the main effect was performed for each exposure factor and for each phantom age (Figures 6.3-6.42).

kVp effect

Within the main effect analysis for the 1 and 5 year-old phantoms, increasing the kVp showed a continuous increase in the radiation dose, SNR and IQ (clarity) (Figures 6.3-6.4, 6.6-6.7; a-c and 6.9-6.10; d-f). IQ aspects such as CNR, IQ sharpness and both aspects of IQ (sharpness & clarity) began to plateau when kVp increased (Figures 6.6-6.7; d-f, 6.9-6.10; a-c). The continuous increase in the measured parameters relates to their nature of depending on the quantity of the X-ray photons, which increases with increasing kVp. The plateauing regions can be related to the effect of increasing kVp, however it also increases radiation intensity and energy/penetrability. Therefore, it decreases the contrast which starts appearing at higher kVp levels due to the k-edge of the image detector materials (Seeram et al., 2013). Also, it can be noted that an increase in filtration level leads to a decrease in radiation dose and IQ (a significant decrease). This is likely due to the decrease in radiation intensity. Regarding the kVp effect within the 10 year-old phantom, all parameters showed a continuous decrease when increasing the kVp. This can be attributed to the continuous increase in the penetrability of the X-ray beam and the consistency in the radiation levels received by the detector because of the AEC. Thus, an increase in kVp causes a continuous increase in X-ray penetrability (decreasing contrast) and the amount of scatter (noise) reaching the image receptor (Al Khalifah & Brindhavan, 2004; T. Herrmann et al., 2012). Therefore, the radiation dose will decrease as well as image quality.

The effect of kVp on FOM for the 1 and 5 year-old phantoms showed that the FOM (visual) decreased as kVp increased. The FOM (SNR) for 1 and 5 year-old phantoms began to plateau when the FOM (SNR) increased at the lower kVp range, and decreased at the higher kVp range, starting from 62 kVp. This can be explained by two reasons: first, the continuous increase in radiation dose that appears when increasing kVp (Figure (6.3), page 173 and Figure (6.4), page 173); and second, the detector efficiency that is related to the k-edge absorption for the detector materials. The latter makes the image detector more sensitive within a specific range (mid kVp). The Inflexion point appeared more visible for the FOM of SNR than the visual FOM. The reason for this can be attributed to the high sensitivity of SNR measurements compared to visual (perceptual) assessments (Smith & Webb, 2010; Tugwell et al., 2014). Furthermore, the FOM of the SNR was calculated by taking the squared SNR.

On the other hand, the visual FOM and SNR FOM of the 10 year-old phantom when using AEC imaging showed a continuous decrease when kVp was increased. The difference between the two imaging techniques can be related to the fact that the radiation dose in AEC imaging, unlike

in manual, showed a continuous decrease in radiation dose when increasing kVp. In addition, the SNR value might show small variations due to the radiation compensation by the AEC.

As mentioned earlier (chapter two), there is a lack of literature regarding paediatric optimisation studies in general, and specifically for pelvic anatomy. However, there is still some potential there for comparing trends between this thesis and other studies that used different ages or anatomical parts. Comparing the 10 year-old phantom data with AEC studies, there is agreement in the outcome with that published by Mraity and Lança et al., wherein both studies found a decrease in visual IQ along with increasing the kVp (Lança et al., 2014; Mraity, 2015). Also, results were found in the literature that demonstrated an increase in physical FOM with increasing the kVp when using AEC, similarly to this study (Mraity, 2015). A study by Sandborg et al. found a continuous decrease in SNR, similar to the data in this thesis (AEC), with increasing the kVp (Sandborg et al., 2006a). A study by Jones et al. investigated the effect of beam quality by changing tube potential on CNR and clinical IQ during infant lateral ankle projections (A. Jones et al., 2015). Their imaging techniques were similar in that they manipulated mAs with increasing kVp to keep radiation dose at a fixed level. The authors reported an improvement in the scores of clinical IQ and CNR at lower beam energies. This is similar to the effect of increasing kVp on diagnostic IQ and CNR found within this thesis, also using AEC. Comparing results from this thesis and manual studies within the literature, Martin et al. evaluated paediatric AP pelvis imaging for 1 and 5 year-olds (L. Martin et al., 2013). They found, using manual a imaging mode, an increase in visual IQ came with an increased kVp as was found in this thesis.

mAs effect

The main effect plots for manual imaging only contained data from the 1 and 5 year-old phantom optimisation studies. These studies showed a continuous increase in radiation dose and IQ aspects when increasing the mAs. This increase can be explained by the proportional increase in radiation intensity associated with increasing mAs. The SNR FOM and the visual FOM decreased when the mAs increased. This behaviour can be explained due to a continuous increase in the radiation dose. For IQ, saturation appeared at higher mAs levels. This response can be due to the image processing algorithm, which tries to maintain the IQ (T. Herrmann et al., 2012). Similar results have been observed by Lanca & Hogg, wherein saturations in SNR and CNR were observed when the mAs was increased (Lanca & Hogg, 2016).

A similar result was found in literature from a study for a 5 year-old DP/AP projection of wrist and ribs, demonstrating an increase in IQ parameters (including contrast, sharpness and noise) and radiation dose (ESD) with increasing the mAs (Lança et al., 2018a). Also, in comparing the behaviour of the visual FOM and the SNR FOM within the literature, similar results were found by Mraity regarding the effect of increasing mAs during non-AEC adult AP pelvis imaging (Mraity, 2015).

SID effect

The main effect plots for SID within the three ages studied are presented in Figures (6.28-6.42). The SID main effect on radiation dose and IQ showed that increasing SID reduced radiation dose and IQ for the 1 and 5 year-old phantoms. This is with the exception of IQ sharpness) within the 5 year-old phantom which showed an increase at an SID of 115 cm. This decrease in IQ can be explained by the decrease in the amount of radiation reaching the image detector during manual exposure. The score for IQ sharpness at 115 cm SID for the 5 year-old phantom can be highlighted as the optimum balance of penumbra and magnification, also bringing the radiation reduction associated with increasing the SID.

The main effect analysis for the 10 year-old phantom data showed that increasing the SID caused a decrease in radiation dose and an increase in physical IQ (SNR and CNR), while visual IQ aspects remained unchanged. The difference between physical and visual IQ can be attributed to the high sensitivity of physical image quality metrics compared to the human eye, which cannot detect small differences in image quality (Tugwell et al., 2014). The visual FOM and the SNR FOM for all the ages showed an increase with increasing the SID. This behaviour can be related to the decrease in radiation dose that was observed with increasing SID.

Regarding the effect of SID reported in the literature for studies using the AEC, similar results were found by Tugwell et al. and Mraity, who all showed that increasing the SID caused a decrease in ED (Mraity, 2015; Tugwell et al., 2014). Also, the IQ in this thesis showed a similar response to that in the work by Mraity and Lança et al. who found a decrease in perceptual IQ when the kVp was increased (Lança et al., 2014; Mraity, 2015). Lastly, the effect of SID on both visual FOM and SNR FOM showed similar results to Mraity for the AEC imaging of an AP adult pelvis (Mraity, 2015).

The FoMs values between the three phantoms, showed a decrease in FoM with older ages (see Tables 6.1, 6.2 and 6.3), this difference can be related to the differences in phantom size (as the age increases) which requires a higher radiation dose.

7.3.2 Correlation

kVp

Regarding the response of all the measured parameters when increasing kVp, the 1 and 5 year-old phantom showed only weak or no correlations (positive), with the exception of SNR which for the 1 year-old phantom was moderate (Tables 6.7, page 199). The reason for this can be attributed to the effect of increasing kVp on X-ray radiation. The intensity and average energy of the X-ray beam increases with increasing the kVp, and both have the opposite effect on IQ and radiation dose (T. Herrmann et al., 2012; C. J. Martin, Sutton, et al., 1999). Thus, the effect on IQ and radiation dose of increasing the energy of the X-ray beam is reduced by the increase in X-ray intensity when increasing kVp. For the 10 year-old phantom, the increase in kVp showed strong negative correlations, except for SNR which had a moderate negative correlation. This is because of the fact that increasing the kVp during AEC would increase the average energy of the X-ray beam, while at the same time the AEC chambers compensate for the amount of radiation (T. Herrmann et al., 2012). Thus, this can yield decreases in IQ (physical and visual) and radiation dose. As a result, for kVp correlation the difference between the 1 and 5 year-old phantom experiments and the 10 year-old phantom experiment can be related to the manual and AEC mode used in studies, respectively. This difference demonstrates that the radiation quantity is the determinant of IQ and radiation dose in AEC imaging.

mAs

mAs, radiation dose and IQ, for the 1 and 5 year-old phantoms, showed positive moderate and strong correlations. For the 1 year-old phantom data, most variables showed moderate correlations except for CNR which was strong. The 5 year-old phantom data demonstrated strong positive correlations, except for IQ sharpness which was moderate. These levels of positive correlation can be explained by the direct relationship between mAs and radiation intensity which increases both IQ and radiation dose.

Radiation dose

The radiation dose correlations with diagnostic IQ showed positive strong correlations for the three paediatric ages. The correlation between radiation dose and the other physical IQ aspects showed relationships which were positive strong /moderate across the three paediatric ages. These correlations can be explained by the relationship between the radiation dose and the amount of radiation or signal that reaches the image detector and contributes to the signal to noise ratio within the image. This also reflects on visual IQ, but not on the IQ sharpness for the 1 year-old phantom which showed a positive weak correlation ($r = 0.47$). The level of

correlation between radiation dose and IQ sharpness for the 1 year-old phantom can be attributed to the smaller size of the 1 year-old, compared to the other phantom ages/sizes that require less radiation in order to achieve an adequate signal level reaching the image detector. As explained in the literature, implementing higher radiation dose does not necessarily produce better IQ, as there are complex effects from many factors (C. J. Martin, Sutton, et al., 1999). This can explain the various correlation levels found between the radiation dose and IQ aspects.

Physical and visual image quality

The SNR showed a positive strong correlation with IQ clarity and with both aspects of IQ together (sharpness & clarity). It also showed a weak positive and a weak moderate correlation with IQ sharpness for both the 1 and 5 year-old phantom data, respectively. This can be related to the fact that SNR is positively affected by the amount of information compared to the noise and thus enables better clarity (less noise). This could be the reason for the above strong positive correlations. The high correlation here reflects the direct relationship between the ratio of the signal to noise compared with the perceived noise. This has been reported in literature (Hasegawa, 1991) as the perceptibility inside the image being limited by noise. The correlation between SNR and visual sharpness can be explained thus: the more signal, the more appealing the overall IQ. Conversely with the noise; the higher the fluctuation in the signal, the noisier the image appears. This means that increasing the SNR can improve overall IQ. At the same time the presence of visual noise to some degree can reduce the visual sharpness of the image. This was found in this thesis and agrees with what was stated about the Rose model by Burgess (Burgess, 1999). For the 10 year-old phantom, the positive weak correlation between the SNR and IQ clarity can be related to the nature of AEC imaging that produced the images with minimal visual noise. Moderate and strong positive correlations were observed between CNR and the visual IQ aspects. The justification for such correlations is similar to that of the SNR. However, the calculation of CNR, which includes the signal from the background (see equation (2.1), subsection 2.2.6.1 in Chapter Two (page 24)), could be the reason for the improvement in its correlation with IQ sharpness in the 1 year-old phantom, compared to SNR. This is because sharpness is a relative measure similar to the CNR. The outcomes from this thesis demonstrated high levels of correlations regarding visual IQ with radiation dose and physical IQ. The proper use of these correlations can help predict the clinical IQ, as well as system performance for producing clinical images (Sund et al., 2004).

There were many attempts in the literature to investigate the level of correlation between exposure factors and/or IQ and radiation dose. Similar to this thesis, strong positive correlations

between radiation dose and visual IQ have been found by Bloomfield et al. within paediatric AP pelvis X-ray images produced from dosimetry phantoms (Bloomfield et al., 2015a). A study on paediatric lateral ankle imaging by Jones et al. found similar results to this thesis. These similarities were regarding the strength of correlation (intermediate) between sharpness and noise, and also its strong correlation between sharpness and the acceptability of images (A. Jones et al., 2015). Another study with similar results to this thesis is a study by Lança et al. who found a moderate positive correlation between CNR and fracture visibility within paediatric AP, lateral wrist and AP rib projections (Lança et al., 2018b).

Regarding adult studies, a study by Moore et al. investigated the correlation between visual and physical IQ within adult chest radiography using images reconstructed from CT scans (Moore et al., 2013). Similarly to this thesis, they found that clinical and physical IQ (CNR) metrics showed strong correlation. A study by Tugwell, England, & Hogg investigated the correlation level between effective dose, CNR and visual IQ within adult AP pelvis radiography undertaken using a trolley (Tugwell et al., 2017). Their results showed similarities to the results presented in this thesis. These similarities were regarding the strong positive correlation between the IQ and radiation dose within a 10 year-old phantom, Found in this thesis, using AEC. They also reported a close correlation between CNR and visual IQ. Also, the aforementioned study showed similar results in terms of its positive correlation between CNR and radiation dose. However, the strength of the correlations was higher than those reported in this thesis. This can be attributed to the set of acquisition parameters used by Tugwell and colleagues, which only varied SID and thus would not result in as much variation in CNR as changing the kVp and mAs would. Besides, the type of radiation dose that was considered in this study (ED) is less sensitive to acquisition parameter changes than the surface dose used within this thesis (IAK) (C. J. Martin, Sutton, et al., 1999). Similar results to this thesis regarding its positive correlation between SNR and visual IQ were found by Sandborg et al. and Mraity who used the Monte Carlo simulation software and an anthropomorphic pelvis phantom, respectively, to produce AP pelvis X-ray images (Mraity, 2015; Sandborg et al., 2006a).

On the other hand, some researchers found no correlation between radiation dose and visual IQ within paediatric chest radiography, acquired using hospital images (Jacob et al., 2009). The difference between the results of Jacob's study and this thesis can be related to the age/size variations and the associated exposure factors variation that exist in the hospital setting. These variations might mask the relationship between radiation dose and IQ.

7.3.3 Regression analysis

This section will be discussed in two parts: the manual imaging mode and the AEC imaging mode.

Manual imaging

The regression analysis showed that additional filtration and mAs showed the first and second highest impact on radiation and IQ aspects (physical and visual) within the 1 and 5 year-old phantom studies (manual imaging mode). kVp had the third highest absolute impact amongst the exposure factors on radiation dose and IQ aspects within the 1 and 5 year-old phantom studies (Tables 6.8, page 202 and 6.9, page 204). This was with the exception of the IQ sharpness regression for 1-year-old study, wherein kVp had the lowest impact instead of SID. The impact order of exposure factors from the regression analysis can be related to the nature of these effects being associated with changing each exposure factor, and the proportion of the effect that each one has compared to the others. To explain further, filtration and kVp each have two effects regarding the X-ray intensity and its average energy, while for mAs and SID each one affects only the intensity of the X-ray beam. In addition, there is an added effect from the DR system. This are explained in detail below.

Within the manual imaging mode (1 and 5 year-old phantoms), the increase of filtration decreases the amount of radiation and increases the average energy of X-ray beam, and both decrease radiation dose and IQ (C. J. Martin, Sutton, et al., 1999). As a result, the effect from added filtration is maximised and this is a possible reason for its having the largest impact on both IQ and radiation dose. While increasing kVp increases radiation intensity and the average energy of the X-ray photons, in this case both are acting in opposite directions toward IQ and radiation dose. Thus, the effect of increasing radiation intensity is to some degree cancelled out by the increase in the average energy of the X-ray beam. This could be the reason for kVp having a lower impact than filtration and mAs.

Contrarily, the effect of increasing the mAs and SID is only their increasing and decreasing the X-ray intensity, respectively. Thus, they contribute to the amount of signal reaching the patient and the signal to noise ratio reaching the image detector, both of which can affect the SNR and CNR, and accordingly the visual IQ (Carroll, 2011). However, an increased SID can improve IQ by reducing magnification and penumbra (Carroll, 2011; Graham et al., 2011). This could be the reason for its producing a positive impact of SID on IQ sharpness and on both aspects of IQ (sharpness & clarity), but not on SNR, CNR and IQ clarity. Thus, the effect of an increased

SID on IQ, in terms of radiation intensity reaching the image detector, is reduced by the improvements to certain aspects of visual IQ caused by improvements to magnification and geometric unsharpness. This besides the possible effect from the image processing algorithms that maintain image quality.

It is worth mentioning that there is an effect on IQ from the DR system, and this includes the wide dynamic range and image processing algorithm. Both of these features might contribute to the impact of each exposure factor within the IQ regression model. Regarding the image processing, which is a distinctive feature in DR systems, the continuous increase in radiation is scaled down by the algorithms based within the system. These keep the IQ within a fixed level, however such compensatory effects can result in dose creep (Al Khalifah & Brindhaban, 2004). Also, the dynamic range of the DR systems allows the storage of a wide range of grey shades. Thus, IQ can be manipulated in terms of contrast (Uffmann & Schaefer-Prokop, 2009). However, the ability of the digital systems to make up for the lack of amount of radiation is limited to the level of noise present, as there is no possibility to process and recover missing information (noise) (E. Samei et al., 2009).

It worth pointing out that filtration and SID both showed a negative effect on CNR, SNR, IQ (clarity) and radiation dose. This is related to the nature of their effects which reduce the amount of radiation during the manual imaging mode. The opposite was observed from mAs and kVp, which showed positive effects on radiation dose and IQ. This can be related to the increase in radiation intensity. It was observed that, despite increases in kVp and filtration and the average X-ray energy, their effects adhered to the fact that reducing the amount of radiation would reduce radiation dose and IQ aspects, and vice versa. One can conclude that reducing or increasing the amount of radiation is what makes the difference in the manual imaging mode. The effect from increasing X-ray beam energy (i.e. effect on contrast) can be minimised by the image processing of the digital imaging system (Uffmann & Schaefer-Prokop, 2009).

To summarise, when comparing the absolute impacts of the different variables during manual exposure, the effect of reducing the intensity and increasing the average X-ray energy by adding filtration produces a higher effect (as an absolute) on radiation dose and IQ than by only increasing the amount of radiation which is represented by increasing mAs. Also, the increase of the intensity and energy of the X-ray beam, through increasing kVp, shows a bigger effect on IQ and radiation dose than decreasing the amount of radiation and improving IQ through

using a larger SID. Consideration must be taken towards the range of each exposure factor that was used when statements are made about which impact was bigger/smaller.

Examining the literature about the impact on radiation dose of using a manual imaging mode, Mraity found that kVp had the highest impact on ED compared to mAs and SID, which had the second and third highest impact, respectively (Mraity, 2015). Another study by Norrman and Persliden found similar results regarding the effect of mAs on radiation dose (KAP). It was found to have the highest impact among kVp and filtration, while the effect from the filtration was lower than kVp (Norrman & Persliden, 2005). The differences between the outcomes of the two above studies and those in this thesis (where additional filtration showed the highest impact) can be related to the use of surface dose (IAK) in this thesis. This dose can be directly affected by increasing the X-ray energy and decreasing the intensity of X-ray beam, such as when adding extra filtration. Unlike IAK, the ED (used in the above studies) is affected by the amount of the low energy which is absorbed at the patient's surface and not counted in ED calculations (C. J. Martin, Sutton, et al., 1999). In addition, the Monte Carlo simulation used in calculating ED is limited in terms of estimating scatter radiation, which is significant within diagnostic X-ray imaging (Menser et al., 2016; Ullman, 2008).

The impact on IQ, using a manual imaging mode, showed similar outcomes to the study by Mraity wherein mAs showed the highest impact on perceptual IQ, while SID had the lowest impact (Mraity, 2015). On the other hand, Norman and Persliden found that the highest impact on IQ came from tube current and the second highest comes from kVp, while additional filtration was the third (Norrman & Persliden, 2005). The difference from the previous study is the impact of filtration being the lowest, whereas in this thesis it was the highest. The difference can be related to the type of phantom that was used, being CDRAD such phantom contains holes and lacks anatomical representation (Veldkamp et al., 2006). Thus, the contrast of bony anatomy in the phantom used in this thesis would have higher contrast when compared to the holes in the CDRAD phantom, due to the higher attenuation and size of the bony anatomies.

AEC imaging mode

Regarding the dose regression model for the AEC imaging mode (10 year-old phantom), it was shown that the biggest impact on radiation dose was filtration, while kVp had the second highest impact and SID had the lowest impact. On the other hand, the IQ aspects in regression models for the 10 year-old phantom showed that kVp had the highest impact, while filtration had second highest impact and SID had the lowest impact (Table 6.10, page 205). This can be related to

the effect of increasing the average energy, which is larger for kVp than for filtration. Thus, the measured dose on the surface is reduced more with added filtration. The justification for kVp having the highest effect on IQ, while the highest effect on dose was from filtration is that the increase in filtration increases the average energy and the AEC does not fully compensate for the radiation dose (filtration showed significant effect on dose). Thus, the effect of filtration on dose is doubled (from increase energy and not fully compensation for dose by the AEC), such effect was noticed as increasing SID in AEC resulted in significant reduction to the dose. Now, having the highest effect on IQ from kVp is related to the amount of scatter radiation (more than from increase filtration) and, thus, noise that makes kVp having higher effect on IQ.

In the literature, similar results were found by Mraity, who compared kVp and SID's effects on ED using AEC imaging for the AP adult pelvis (Mraity, 2015). Also, similar results were found by Norrman and Persliden who found that the tube potential had a bigger impact than filtration on radiation dose during AEC mode (Norrman & Persliden, 2005). However, their results contradict the results from this thesis in terms of their reported effects on radiation dose. They found that kVp had a bigger effect than filtration on KAP and ED. This difference can be related to the higher kVp range used in their study, which can increase the effect from tube potential. Furthermore, the dose measurements method that referenced KAP, which includes the area product of Air kerma at the patient surface (for adult size) (B. Hansson, Finnbogason, Schuwert, & Persliden, 1997; Huda, 2014), can produce outcome differences from different paediatric sizes.

Regarding studies for assessing impacts on IQ, a study by Mraity reported similar results about kVp being of a higher impact on IQ than SID. Also, similar results were found by Norrman and Persliden who found, using AEC imaging, that kVp has a bigger impact than filtration on IQ (Norrman & Persliden, 2005).

Regarding the nature of the effect of each exposure factor, increasing the SID showed a negative effect on radiation dose. This raises a question about the efficiency of AEC chambers in their compensation for reduced radiation intensity. Similar results were found in the literature (Brennan et al., 2004; Mraity, 2015; Tugwell et al., 2014). Also, increasing the SID had a negative effect on IQ clarity, which is related to the subsequent reduction in the radiation dose. This reduction in radiation dose showed no effect on the rest of the IQ aspects, as they showed general positive effect with increasing SID. This positive effect could be due to the image processing that maintains the image quality, as well as a reduction in the magnification and

penumbra due to an increased SID. Filtration and kVp showed negative effects on radiation dose and IQ. These effects on the IQ aspects could be related to the effect of the increasing noise ratio and decreased contrast that are associated with increasing kVp and the filtration level. Their effects on radiation dose could be related to increasing the penetrability of X-ray as the kVp and filtration level increased.

7.4 Conclusion

Conclusions can be made regarding the construction and validation of paediatric AP pelvis phantoms along with their applicability in dose optimisation studies (See section 4.5 in Chapter Four, page 132). A series of factorial experimental design studies were undertaken in this study to provide a systematic optimisation for the radiation doses within digital paediatric AP pelvis radiography. This study design was adopted based on reports in the literature in order to answer the main thesis question, which investigated the dose optimised exposure factors for different ages/sizes paediatric AP pelvis. Two types of imaging modes were used based on their clinical utility. The first was manual mode imaging, which was used for the 1 and 5 year-old phantoms; and the second was AEC mode imaging, which was used for the 10 year-old phantom. For each age, the evaluation of visual IQ and physical IQ along with radiation dose were conducted to answer the thesis question. Consequently, for each phantom age, exposure factor combinations were identified according to their ability to produce diagnostically acceptable X-ray images with the lowest possible radiation dose (see Table 7.1);

Table 7.1: Dose optimised exposure factor combination for 1, 5- and 10-year-old pelvis radiography.

	1-year-old	5-years-old	10-years-old
Technique	Manual	Manual	AEC – HA (2 outer chambers)
Tube potential	65 kVp	62 kVp	89 kVp
Tube current-time product	2 mAs	8 mAs	AEC
Source-to-image distance	115 cm	130 cm	130 cm
Additional filtration	1 mm Al + 0.1 mm Cu	1 mm Al + 0.1 mm Cu	1 mm Al + 0.1 mm Cu
Radiation dose	15.31 μ Gy	52.33 μ Gy	178.77 μ Gy

From the optimisation studies there is a unified conclusion for the three phantom ages. That conclusion is that the use of additional filtration (1 mm Al + 0.1 mm Cu) universally reduces dose whilst maintaining IQ. There are a number of further conclusions that can be made from the main effect, regression and correlation analyses, and are described below.

First, the main effect analysis showed, within both imaging techniques, that a continuous increase of the exposure factors can yield a continuous increase (manual imaging: when increasing mAs) or a continuous decrease (AEC imaging: when increasing kVp, SID and filtration / manual imaging: when increasing SID and filtration) in either or both of radiation dose and diagnostic IQ. However, the kVp, within manual imaging, showed different results (inflexion points) as there was a kVp range that contained almost the highest IQ within a specific range for each age. That kVp range was 59-65 and 65-77 for 1 and 5 year-old phantoms, respectively. The main effect analysis showed that FOMs within manual and AEC imaging modes depend on the response of the trend of radiation dose when changing exposure factors (inflexion points also affect FOMs).

Second, the regression analysis within the manual imaging of the 1 and 5 year-old phantoms revealed two advantageous strategies for reducing dose. The first strategy is increasing the SID and compensating it with mAs; and the second is increasing the level of additional filtration and increasing the mAs to compensate. Within the AEC imaging of the 10 year-old phantom, the regression analysis highlighted two points for reducing dose. First, it demonstrated that increasing the SID would be advantageous, as it reduced the radiation dose with no significant effect on diagnostic IQ; and second, increasing the filtration level is a priority over increasing the kVp.

Third, the correlation test showed that kVp can be a promising predictor of IQ and radiation dose using the AEC imaging mode for the 10 year-old phantom. This result was not consistent within manual imaging for the 1 and 5 year-old phantom. The correlation of mAs within the manual imaging mode highlighted its capability for controlling IQ and radiation dose for the 1 and 5 year-old phantoms. However, a better predictive ability was observed for the 5 year-old phantom. Radiation dose showed its ability for being the indicator for diagnostic IQ within both the manual and AEC imaging modes across the three phantom ages. In addition, the physical IQ (SNR and CNR) showed high predictability for diagnostic IQ using both imaging techniques. This means that there is applicability using physical IQ in evaluating and predicting the performance of a system for producing images with clinical diagnostic quality.

Finally, the factorial study was able to undertake a comprehensive study of many exposure factor effects at the same time. It also provided a full understanding of the influence of each exposure factor on IQ or radiation dose in comparison to the other exposure factors. In addition, this study's design has provided the opportunity to investigate the main effect from each exposure factor wherein the other exposure factors are duly considered. One last advantage for a factorial study is its ability to predict the radiation dose and IQ aspects through a multiple regression model that contains all exposure factors together. The aforementioned conclusions demonstrate the need for a factorial study design in systematic dose optimisation studies, and that these should be applied to other anatomical areas.

7.5 Limitations

Within the experimental work presented in this thesis there were a number of limitations. The limitations were related to some of the data collection methods, including those focused around IQ and radiation dose assessments.

The first limitation relates to the construction and appropriateness of the paediatric pelvis phantoms. The paediatric pelvis phantoms differ from children in that they only represent one size for each age and only contain two tissue substitutes (bone and soft tissue). Children in reality have different sizes associated with their ages (1, 5, 10 and 15), and, in addition to this, there are differences in their sizes for those of the same age. These differences have a small effect on the population in hospitals as they were the standard size per age, and organ sizes vary no more than 15% within each age group (Varchena, 2002). In this thesis, the variation in paediatric phantoms were based on age. However there are other size references such as studies based on weight or size variations and several has also recommended considering the utilisation of growth charts (Billinger et al., 2010; European Commission, 2018). For example, it is possible that both a 5 and 10 year-old child could be of the same size and weight. The paediatric ages considered in this study did not include 15 year-olds. The reason for this was due to this size being close to an adult, for which there are many commercially available anthropomorphic/dosimetry phantoms and there are also adult AP pelvis optimisation studies reported in the literature.

On the other hand, there are a limited number of simulated tissues in each pelvis phantom, such as the soft tissue and cortical bones. Tissues like trabecular bone and other soft tissues (Bladder, testis or ovary) were not included. However, the included tissues in the three phantoms used within this thesis are the ones that are typically represented on paediatric AP pelvis X-ray

images to visualise the edges of bony anatomies. They are also considered to be a key imaging priority (M. Singh et al., 1972; Stieve, 1989). Also, the phantoms in question lack the pathological variability, and optimisation is therefore limited to normal cases only. This identifies a potential need for clinical studies (patient or cadaver based) and these could be considered as a follow-on for confirming the results of this study. In addition, there is an emerging trend towards possible ‘indication’ based optimisation studies (such as those for fracture follow-up). A collaboration in Europe, under the banner of EuroSafe ⁷, are currently working on such an initiative. As a result, there could have been the possibility of including a fracture within animal bone to undertake a fracture-based optimisation study. This should be the focus of future work, but it is noted that some authors believe that optimisation can be undertaken when based solely on ‘normal’ imaging appearances.

There are other limitations related to the devices used for data collection. For example, the DR imaging plate was supplied by Konica Minolta. There are other types of imaging systems available, and each may have different materials and algorithms for image processing, even though all algorithms are clinically based. The findings presented here are acquired from single DR detector and image processing algorithms from a single manufacturer and thus DQE, dynamic range, kV sensitivity and processed image quality might be different from other commercial products. As a result, further multi-vendor comparison studies are needed and should be undertaken in due course. Also, it is important to note that both automatic image processing and post-processing options could influence optimisation. These variables are rarely considered within optimisation studies and should be considered moving forward. The difficulty is that the precise mechanisms for image processing can be vendor specific and as such there could also be differences between DR systems.

Lastly, the types of radiation dose measurements (IAK) considered in this thesis are not the only dosimetry methods available. There are other approaches for estimating radiation dose, such as effective dose calculations or individual organ dose measurements. However, these measurements require time and equipment (such as a suitable phantom, TLDs and a reading system), and there was no time available. Regarding the evaluation of visual IQ, it should be acknowledged that the handling of the VGA data (treating ordinal data as continuous) is stated to be suboptimal (Chakraborty, 2017). Therefore, there is suggested improvement to the VGA

⁷ www.eurosafeimaging.org

analysis can be achieved by using Visual Grading Regression Analysis, which can be used in future study (Keeble et al., 2016; Smedby & Fredrikson, 2010).

7.6 Recommendations

Several recommendations to maintain IQ and reduce dose were found within this study for manual and AEC imaging techniques separately, and are detailed as follows:

For manual imaging:

- 1- Identify the 'image quality' effective range when selecting kVp, which relates to specific paediatric age groups.
- 2- Use higher SID and additional filtration as a dose reduction strategy.
 - If not producing acceptable IQ compensate by increasing mAs.
- 3- Use mAs to control IQ and radiation dose.

For AEC imaging:

- 1- To decrease radiation dose, use higher kVp, SID and additional filtration (AECs automatically compensate to maintain IQ by increasing mAs).

7.7 Future work

There are many steps which can be undertaken in the future as an extension to the work reported within this thesis or as new studies. These include:

- 1- Studies evaluating the potential for look-up table-based imaging- i.e., selecting the desired IQ or radiation dose prospectively and then determining which exposure factor combinations to use.
- 2- There can be optimisation for other bony anatomical areas using the same approach, such as dose optimisation for paediatric spine radiography.
- 3- Clinical studies seeking to confirm the proposed optimisation parameters for clinical practice.
- 4- Studies considering the paediatric ages in-between the ages considered in this thesis (1, 5 and 10 year-olds). In addition, there could be studies considering dose optimisation for obese and underweight paediatric patients based on patient weight/body habitus, rather than on age.
- 5- Dose optimisation studies including pathological imaging. This could be applied via simulating bone fractures or lesions within the paediatric pelvis. Also, there could be

extra studies using ROC methods to evaluate lesion detection performance. A full evaluation of optimised parameters should consider lesion detection performance alongside radiation dose.

References

- Agarwal, V., & Newbery, S. (2016). Paediatric radiation dose measurements undergoing X-ray examination in Tasmania. *Radiation Protection Dosimetry*, *174*(3), 382–386. <https://doi.org/10.1093/rpd/ncw143>
- Ahn, S. H., Montero, M., Odell, D., Roundy, S., & Wright, P. (2002). Anisotropic material properties of fused deposition modeling ABS. *Rapid Prototyping Journal*, *8*(4), 248–257. <https://doi.org/10.1108/13552540210441166>
- Aichinger, H., Dierker, J., Joite-Barfuß, S., & Säbel, M. (2012). *Radiation Exposure and Image Quality in X-Ray Diagnostic Radiology. The effects of brief mindfulness intervention on acute pain experience: An examination of individual difference* (Vol. 1). Berlin, Heidelberg: Springer Berlin Heidelberg. <https://doi.org/10.1007/978-3-642-11241-6>
- Akahane, K., Kai, M., Kusama, T., Mitarai, T., Ono, K., Hada, M., ... Kato, Y. (2000). Development of Neonate Phantom for Estimating Medical Exposure Phantom development Phantom development. *IRPA-10 Proceedings of the 10th International Congress of the International Radiation Protection Association on Harmonization of Radiation, Human Life and the Ecosystem*. Japan Health Physics Society.
- Akhlaghi, P., Miri-Hakimabad, H., & Rafat-Motavalli, L. (2015). Determination of tissue equivalent materials of a physical 8-year-old phantom for use in computed tomography. *Radiation Physics and Chemistry*, *112*, 169–176. Retrieved from <http://linkinghub.elsevier.com/retrieve/pii/S0969806X15001188>
- Al Khalifah, K., & Brindhaban, A. (2004). Comparison between conventional radiography and digital radiography for various kVp and mAs settings using a pelvic phantom. *Radiography*, *10*(2), 119–125. <https://doi.org/10.1016/j.radi.2004.02.006>
- Al Qaroot, B., Hogg, P., Twiste, M., & Howard, D. (2014). A systematic procedure to optimise dose and image quality for the measurement of inter-vertebral angles from lateral spinal projections using Cobb and superimposition methods. *Journal of X-Ray Science and Technology*, *22*(5), 613–625. <https://doi.org/10.3233/XST-140449>
- Allen, E., Hogg, P., Ma, W., & Szczepura, K. (2013). Fact or fiction: An analysis of the 10 kVp ‘rule’ in computed radiography. *Radiography*, *19*(3), 223–227. <https://doi.org/10.1016/j.radi.2013.05.003>
- Alsleem, H., & Davidson, R. (2012). Quality parameters and assessment methods of digital radiography images. *Journal of Medical Radiation Sciences*, *59*(2), 46–55. <https://doi.org/10.1002/j.2051-3909.2012.tb00174.x>
- Alves, A. F. F., Alvarez, M., Ribeiro, S. M., Duarte, S. B., Miranda, J. R. A., & Pina, D. R. (2016). Association between subjective evaluation and physical parameters for radiographic images optimization. *Physica Medica*, *32*(1), 123–132. <https://doi.org/10.1016/j.ejmp.2015.10.095>
- Alves, A. F. F., Miranda, J. R. A., Neto, F. A. B., Duarte, S. B., & Pina, D. R. (2015). Construction of pediatric homogeneous phantoms for optimization of chest and skull radiographs. *European Journal of Radiology*, *84*(8), 1579–1585. <https://doi.org/10.1016/j.ejrad.2015.05.015>
- Alves, A. F. F., Pina, D. R., Neto, F. A. B., Ribeiro, S. M., & Miranda, J. R. A. (2014). Quantification of biological tissue and construction of patient equivalent phantom (skull

- and chest) for infants (1-5 years old). *SPIE Medical Imaging*, 9033(2012), 90334T. <https://doi.org/10.1117/12.2043310>
- Alzen, G., & Benz-Bohm, G. (2011). Radiation Protection in Pediatric Radiology. *Deutsches Ärzteblatt Online*, 108(24), 407–414. <https://doi.org/10.3238/arztebl.2011.0407>
- Alzimami, K., Sassi, S., Alkhorayef, M., Britten, A. J., & Spyrou, N. M. (2009). Optimisation of computed radiography systems for chest imaging. *Nuclear Instruments and Methods in Physics Research, Section A: Accelerators, Spectrometers, Detectors and Associated Equipment*, 600(2), 513–518. <https://doi.org/10.1016/j.nima.2008.12.023>
- Anderson, J. R., Diaz, O., Klucznik, R., Zhang, Y. J., Britz, G. W., Grossman, R. G., ... Karmonik, C. (2014). Validation of computational fluid dynamics methods with anatomically exact, 3D printed MRI phantoms and 4D pcMRI. *Conference Proceedings : ... Annual International Conference of the IEEE Engineering in Medicine and Biology Society. IEEE Engineering in Medicine and Biology Society. Annual Conference, 2014*, 6699–6701. <https://doi.org/10.1109/EMBC.2014.6945165>
- Andria, G., Attivissimo, F., Guglielmi, G., Lanzolla, A. M. L., Maiorana, A., & Mangiantini, M. (2016). Towards patient dose optimization in digital radiography. *Measurement*, 79, 331–338. <https://doi.org/10.1016/j.measurement.2015.08.015>
- Andria, G., Attivissimo, F., Nisio, A., Lanzolla, A., Guglielmi, G., & Terlizzi, R. (2014). Dose Optimization in Chest Radiography: System and Model Characterization via Experimental Investigation. *IEEE Transactions on Instrumentation and Measurement*, 63(5), 1163–1170. <https://doi.org/10.1109/TIM.2013.2282411>
- Atiyah, H., Powell, J., Petring, D., Stoyanov, S., & Voisey, K. T. (2018). Fiber laser cutting: The use of carbon-filled acrylic as a qualitative and quantitative analysis tool. *Journal of Laser Applications*, 30(3), 032009. <https://doi.org/10.2351/1.5045349>
- Aufrichtig, R. (1999). Comparison of low contrast detectability between a digital amorphous silicon and a screen-film based imaging system for thoracic radiography. *Medical Physics*, 26(7), 1349–1358. <https://doi.org/10.1118/1.598630>
- Aufrichtig, R., & Xue, P. (2000). Dose efficiency and low-contrast detectability of an amorphous silicon x-ray detector for digital radiography. *Physics in Medicine and Biology*, 45(9), 2653–2669. <https://doi.org/10.1088/0031-9155/45/9/316>
- Bacher, K., Smeets, P., Bonnarens, K., De Hauwere, A., Verstraete, K., & Thierens, H. (2003). Dose Reduction in Patients Undergoing Chest Imaging: Digital Amorphous Silicon Flat-Panel Detector Radiography Versus Conventional Film-Screen Radiography and Phosphor-Based Computed Radiography. *American Journal of Roentgenology*, 181(4), 923–929. <https://doi.org/10.2214/ajr.181.4.1810923>
- Bankier, a a, De Maertelaer, V., Keyzer, C., & Gevenois, P. a. (1999). Pulmonary emphysema: subjective visual grading versus objective quantification with macroscopic morphometry and thin-section CT densitometry. *Radiology*, 211(3), 851–858. <https://doi.org/10.1148/radiology.211.3.r99jn05851>
- Båth, M. (2010). Evaluating imaging systems: practical applications. *Radiation Protection Dosimetry*, 139(1–3), 26–36. <https://doi.org/10.1093/rpd/ncq007>
- Båth, M., Håkansson, M., Hansson, J., & Månsson, L. G. (2005). A conceptual optimisation strategy for radiography in a digital environment. *Radiation Protection Dosimetry*, 114(1–

- 3), 230–235. <https://doi.org/10.1093/rpd/nch567>
- Båth, M., & Månsson, L. G. (2007). Visual grading characteristics (VGC) analysis: A non-parametric rank-invariant statistical method for image quality evaluation. *British Journal of Radiology*, *80*(951), 169–176. <https://doi.org/10.1259/bjr/35012658>
- Båth, M., Sund, P., & Månsson, L. G. (2002). Evaluation of the imaging properties of two generations of a CCD-based system for digital chest radiography. *Medical Physics*, *29*(10), 2286–2297. <https://doi.org/10.1118/1.1507781>
- Baumeister, L., & Rocky, H. (1923). Roentgen-Ray Measurements. *Acta Radiologica*, *2*(4–5), 418–429. <https://doi.org/10.3109/00016922309133874>
- Bewick, V., Cheek, L., & Ball, J. (2004). Statistics review 13: Receiver operating characteristic curves. *Critical Care*, *8*(6), 508. <https://doi.org/10.1186/cc3000>
- Bibb, R., & Winder, J. (2010). A review of the issues surrounding three-dimensional computed tomography for medical modelling using rapid prototyping techniques. *Radiography*, *16*(1), 78–83. <https://doi.org/10.1016/j.radi.2009.10.005>
- Bijwaard, H., de Vries, G., Scheurleer, J., Roding, T., Erenstein, H., Ravensbergen, W., ... van Welie, F. (2017). Compliance to Diagnostic Reference Levels for radiation exposure in common radiological procedures in Dutch hospitals: A nation-wide survey carried out by medical imaging students. *Radiography*, *23*(3), 197–201. <https://doi.org/10.1016/j.radi.2017.03.005>
- Billinger, J., Nowotny, R., & Homolka, P. (2010). Diagnostic reference levels in pediatric radiology in Austria. *European Radiology*, *20*(7), 1572–1579. <https://doi.org/10.1007/s00330-009-1697-7>
- BIR. (1989). *Optimization of Image Quality and Patient Exposure in Diagnostic Radiology*. *British Institute of Radiology, Report 20*. <https://doi.org/10.1148/radiology.177.1.72>
- Bliznakova, K. (2016). THE USE OF 3D PRINTING IN MANUFACTURING ANTHROPOMORPHIC PHANTOMS FOR BIOMEDICAL APPLICATIONS. *REVIEWS Scripta Scientifica Medicinae Dentalis*, *2*(1), 23–31.
- Bloomfield, C., Boavida, F., Chabloz, D., Crausaz, E., Huizinga, E., Hustveite, H., ... Visser, R. (2015a). *Experimental article – Reducing effective dose to a paediatric phantom by using different combinations of kVp, mAs and additional filtration whilst maintaining image quality*. OPTIMAX 2014 – radiation dose and image quality optimisation in medical imaging. Lisbon, Portugal: OPTIMAX 2014 – radiation dose and image quality optimisation in medical imaging.
- Bloomfield, C., Boavida, F., Chabloz, D., Crausaz, E., Huizinga, E., Hustveite, H., ... Visser, R. (2015b). *Review article – A narrative review on the reduction of effective dose to a paediatric patient by using different combinations of kVp, mAs and additional filtration whilst maintaining image quality*. OPTIMAX 2014 – radiation dose and image quality optimisation in medical imaging. Lisbon, Portugal.
- Bochud, F. O., Valley, J.-F., Verdun, F. R., Hessler, C., & Schnyder, P. (1999). Estimation of the noisy component of anatomical backgrounds. *Medical Physics*, *26*(7), 1365–1370. <https://doi.org/10.1118/1.598632>
- Boone, J. M., & Chavez, A. E. (1996). Comparison of x-ray cross sections for diagnostic and therapeutic medical physics. *Medical Physics*, *23*(12), 1997–2005.

<https://doi.org/10.1118/1.597899>

- Borisova, R., Ingilizova, C., & Vassileva, J. (2008). Patient dosimetry in paediatric diagnostic radiology. *Radiation Protection Dosimetry*, *129*(1–3), 155–159. <https://doi.org/10.1093/rpd/ncn003>
- Bourne, R. (2010). *Fundamentals of Digital Imaging in Medicine. Igarss 2014*. London: Springer London. <https://doi.org/10.1007/978-1-84882-087-6>
- Bower, M. W. (1997). *A Physical Anthropomorphic Phantom of a One-Year-Old Child with Real-Time Dosimetry*. University of Florida.
- Brennan, P., & Johnston, D. (2002). Irish X-ray departments demonstrate varying levels of adherence to European guidelines on good radiographic technique. *British Journal of Radiology*, *75*(891), 243–248. <https://doi.org/10.1259/bjr.75.891.750243>
- Brennan, P., & Madigan, E. (2000). Lumbar spine radiology: Analysis of the posteroanterior projection. *European Radiology*, *10*(7), 1197–1201. <https://doi.org/10.1007/s003309900272>
- Brennan, P., McDonnell, S., & O’Leary, D. (2004). Increasing film-focus distance (FFD) reduces radiation dose for x-ray examinations. *Radiation Protection Dosimetry*. <https://doi.org/10.1093/rpd/nch029>
- Brindhavan, A. (2004). Radiation dose to premature infants in neonatal intensive care units in kuwait. *Radiation Protection Dosimetry*, *111*(3), 275–281. <https://doi.org/10.1093/rpd/nch338>
- Brindhavan, A., & Al Khalifah, K. (2005). Radiation dose in pelvic imaging. *Radiologic Technology*, *77*(1), 32–40. Retrieved from <http://www.ncbi.nlm.nih.gov/pubmed/16218020>
- Brindhavan, A., Al Khalifah, K., Al Wathiqi, G., & Al Ostath, H. (2005). Effect of x-ray tube potential on image quality and patient dose for lumbar spine computed radiography examinations. *Australasian Physics & Engineering Sciences in Medicine*, *28*(4), 216–222. <https://doi.org/10.1007/BF03178721>
- Brindhavan, A., & Eze, C. U. (2006). Estimation of radiation dose during diagnostic X-ray examinations of newborn babies and 1-year-old infants. *Medical Principles and Practice*, *15*(4), 260–265. <https://doi.org/10.1159/000092987>
- Brosi, P., Stuessi, A., Verdun, F., Vock, P., & Wolf, R. (2011). Copper filtration in pediatric digital X-ray imaging: Its impact on image quality and dose. *Radiological Physics and Technology*, *4*(2), 148–155. <https://doi.org/10.1007/s12194-011-0115-4>
- Burgess, A. (1999). The Rose model, revisited. *Journal of the Optical Society of America A*, *16*(3), 633. <https://doi.org/10.1364/JOSAA.16.000633>
- Burgess, A., Jacobson, F., & Judy, P. (2001). Human observer detection experiments with mammograms and power-law noise. *Medical Physics*, *28*(4), 419–437. <https://doi.org/10.1118/1.1355308>
- Busch, H. P. (2004). *Image Quality and Dose Management For Digital Radiography. Radiography*. <https://doi.org/http://dx.doi.org/10.1093/rpd/nci728>
- Bushberg, J.T., Seibert, J.A., Leidholdt Jr, E. and Boone, J. (2002). *The essential of physics of*

- medical imaging* (second ed.). Lippincott Williams & Wilkins.
- Bushberg, J. T., Seibert, J. A., Leidholdt, E. M., & Boone, J. M. (2012). *The Essential Physics of Medical Imaging* (3rd ed.). Philadelphia: Lippincott Williams and Wilkins.
- Bushberg, J. T., Seibert, J. A., Leidholdt, E. M., Boone, J. M., & Goldschmidt, E. J. (2003). *The Essential Physics of Medical Imaging*. Lippincott Williams & Wilkins (Vol. 30). <https://doi.org/10.1118/1.1585033>
- Bushong, S. C. (2013). *Radiologic science for technologists : physics, biology, and protection* (10th ed.). St. Louis, Mo. : Elsevier Mosby.
- Butler, M.-L., & Brennan, P. (2009). Nonselective Filters Offer Important Dose-Reducing Potential in Radiological Examination of the Paediatric Pelvis. *Journal of Medical Imaging and Radiation Sciences*, 40(1), 15–23. <https://doi.org/10.1016/j.jmir.2008.11.002>
- Cabibihan, J. J. (2011). Patient-Specific Prosthetic Fingers by Remote Collaboration—A Case Study. *PLoS ONE*, 6(5), e19508. <https://doi.org/10.1371/journal.pone.0019508>
- Carroll, Q. (2007). *Practical Radiographic Imaging* (8th Editio). Charles C Thomas Pub Ltd.
- Carroll, Q. (2011). *Radiography in the Digital Age: Physics, Exposure, Radiation Biology*. Springfield, Illinois: Charles C. Thomas.
- CEC. (1996). *European Guidelines on quality criteria for diagnostic radiographic images in paediatrics*. Eur 16261EN. Retrieved from <ftp://ftp.cordis.lu/pub/fp5-euratom/docs/eur16261.pdf>
- Ceh, J., Youd, T., Mastrovich, Z., Peterson, C., Khan, S., Sasser, T., ... Leevy, W. (2017). Bismuth infusion of ABS enables additive manufacturing of complex radiological phantoms and shielding equipment. *Sensors (Switzerland)*, 17(3), 1–11. <https://doi.org/10.3390/s17030459>
- Chakraborty, D. P. (2002). Statistical Power in Observer-Performance Studies. *Academic Radiology*, 9(2), 147–156. [https://doi.org/10.1016/S1076-6332\(03\)80164-2](https://doi.org/10.1016/S1076-6332(03)80164-2)
- Chakraborty, D. P. (2010). Clinical relevance of the ROC and free-response paradigms for comparing imaging system efficacies. *Radiation Protection Dosimetry*, 139(1–3), 37–41. <https://doi.org/10.1093/rpd/ncq017>
- Chakraborty, D. P. (2011). New Developments in Observer Performance Methodology in Medical Imaging. *Seminars in Nuclear Medicine*, 41(6), 401–418. <https://doi.org/10.1053/j.semnuclmed.2011.07.001>
- Chakraborty, D. P. (2017). *Observer Performance Methods for Diagnostic Imaging*. *Observer Performance Methods for Diagnostic Imaging*. Boca Raton, FL : CRC Press, Taylor & Francis Group, [2017] |: CRC Press. <https://doi.org/10.1201/9781351228190>
- Chakraborty, D. P., & Berbaum, K. S. (2004). Observer studies involving detection and localization: Modeling, analysis, and validation. *Medical Physics*, 31(8), 2313–2330. <https://doi.org/10.1118/1.1769352>
- Chakraborty, D. P., & Winter, L. H. (1990). Free-response methodology: alternate analysis and a new observer-performance experiment. *Radiology*, 174(3), 873–881. <https://doi.org/10.1148/radiology.174.3.2305073>
- Chakraborty, D. P., Yoon, H.-J., & Mello-Thoms, C. (2007). Spatial Localization Accuracy of

- Radiologists in Free-Response Studies: Inferring Perceptual FROC Curves from Mark-Rating Data. *Academic Radiology*, 14(1), 4–18. <https://doi.org/10.1016/j.acra.2006.10.015>
- Chan, C. T. P., & Fung, K. K. L. (2015). Dose optimization in pelvic radiography by air gap method on CR and DR systems – A phantom study. *Radiography*, 21(3), 214–223. <https://doi.org/10.1016/j.radi.2014.11.005>
- Chapple, C. L., Faulkner, K., & Hunter, E. W. (1994). Energy imparted to neonates during X-ray examinations in a special care baby unit. *British Journal of Radiology*, 67(796), 366–370. <https://doi.org/10.1259/0007-1285-67-796-366>
- Chen, X., Shen, J., & Zhou, M. (2016). Rapid fabrication of a four-layer PMMA-based microfluidic chip using CO₂-laser micromachining and thermal bonding. *Journal of Micromechanics and Microengineering*, 26(10), 107001. <https://doi.org/10.1088/0960-1317/26/10/107001>
- Choudhury, I. A., & Shirley, S. (2010). Laser cutting of polymeric materials: An experimental investigation. *Optics and Laser Technology*, 42(3), 503–508. <https://doi.org/10.1016/j.optlastec.2009.09.006>
- Christensen, E., Dietz, G., Murry, R., & Moore, J. (1980). in proceedings of a symposium on optimization of chest radiography. *Madison, WI, HHS Publ. (FDA)*, 80(8124), 249.
- CIRS Tissue Simulation and Phantom Technology. (2011). ATOM ® Dosimetry Phantoms: Models 701-706, 16. Retrieved from <http://www.cirsinc.com/products/modality/33/atom-dosimetry-verification-phantoms/?details=resources>
- Cohen, J. (1988). *Statistical Power Analysis for the Behavioral Sciences* (2nd ed.). Lawrence Erlbaum Associates. Retrieved from <http://linkinghub.elsevier.com/retrieve/pii/B9780121790608500128>
- Compagnone, G., Pagan, L., & Bergamini, C. (2005). Comparison of six phantoms for entrance skin dose evaluation in 11 standard X-ray examinations. *Journal of Applied Clinical Medical Physics / American College of Medical Physics*, 6(1), 13. <https://doi.org/10.1120/jacmp.2003.25326>
- Constantinou, C. (1978). *Tissue substitutes for particulate radiations and their use in radiation dosimetry and radiotherapy*. University of London. Retrieved from <https://qmro.qmul.ac.uk/xmlui/handle/123456789/1718>
- Constantinou, C., Cameron, J., DeWerd, L., & Liss, M. (1986). Development of radiographic chest phantoms. *Medical Physics*, 13(6), 917–921. <https://doi.org/10.1118/1.595818>
- Conway, B. J., Butler, P. F., Duff, J. E., Fewell, T. R., Gross, R. E., Jennings, R. J., ... Showalter, C. K. (1984). Beam quality independent attenuation phantom for estimating patient exposure from x-ray automatic exposure controlled chest examinations. *Medical Physics*, 11(6), 827–832. <https://doi.org/10.1118/1.595611>
- Cristy, M. (1980). *Mathematical phantoms representing children of various ages for use in estimates of internal dose. (No. NUREG/CR-1159; ORNL/NUREG/TM-367)*. Oak Ridge National Lab., TN (USA). Retrieved from <http://web.ornl.gov/info/reports/1980/3445605812234.pdf>
- Cronbach, L. J. (1951). Coefficient alpha and the internal structure of tests. *Psychometrika*, 16(3), 297–334. <https://doi.org/10.1007/BF02310555>

- Davey, E., & England, A. (2015). AP versus PA positioning in lumbar spine computed radiography: Image quality and individual organ doses. *Radiography*, 21(2), 188–196. <https://doi.org/10.1016/j.radi.2014.11.003>
- De Crop, A., Bacher, K., Van Hoof, T., Smeets, P. V, Smet, B. S., Vergauwen, M., ... Thierens, H. (2012). Correlation of contrast-detail analysis and clinical image quality assessment in chest radiography with a human cadaver study. *Radiology*, 262(1), 298–304. <https://doi.org/10.1148/radiol.11110447>
- Dendy, P. P., & Heaton, B. (2011). *Physics for Diagnostic Radiology*. CRC Press (Third).
- Desai, N., Singh, A., & Valentino, D. J. (2010). Practical evaluation of image quality in computed radiographic (CR) imaging systems. In *Physics of Medical Imaging* (Vol. 1, p. 76224Q). <https://doi.org/10.1117/12.844640>
- Dhawan, A. P. (2011). *Medical Image Analysis* (Second Edn). Hoboken, NJ, USA: John Wiley & Sons, Inc. <https://doi.org/10.1002/9780470918548>
- Don, S. (2004). Radiosensitivity of children: Potential for overexposure in CR and DR and magnitude of doses in ordinary radiographic examinations. *Pediatric Radiology*, 34(SUPPL. 3), 167–172. <https://doi.org/10.1007/s00247-004-1266-9>
- Doubrovski, Z., Verlinden, J., & Geraedts, J. (2011). Optimal Design for Additive Manufacturing: Opportunities and Challenges. In *Volume 9: 23rd International Conference on Design Theory and Methodology; 16th Design for Manufacturing and the Life Cycle Conference* (pp. 635–646). ASME. <https://doi.org/10.1115/DETC2011-48131>
- Doyle, P., Martin, C. J., & Gentle, D. (2005). Dose-image quality optimisation in digital chest radiography. *Radiation Protection Dosimetry*, 114(1–3), 269–272. <https://doi.org/10.1093/rpd/nch546>
- Ekpo, E. U., Hoban, A. C., & McEntee, M. F. (2014). Optimisation of direct digital chest radiography using Cu filtration. *Radiography*, 20(4), 346–350. <https://doi.org/10.1016/j.radi.2014.07.001>
- European Commission. (1996). *European Guidelines on Quality Criteria for Diagnostic Radiographic Images (UR 16260 EN)*.
- European Commission. (2014). Diagnostic Reference Levels in Thirty-six European Countries. Part 2/2. *Radiation Protection N° 180*, 1–73.
- European Commission. (2018). *European Guidelines on Diagnostic Reference Levels for Paediatric Imaging*. Luxembourg. <https://doi.org/10.2833/486256>
- Fauber, T. (2013). *Radiographic Imaging and Exposure* (4th ed.). Elsevier Health Sciences.
- Field, A. (2009). *Discovering Statistics Using SPSS* (3rd Editio). London: Sage Publications Ltd.
- Field, A. (2013). *Discovering Statistics Using IBM SPSS Statistics* (4th ed.). London: Sage Publications Ltd.
- Field, A., Miles, J., & Field, Z. (2012). *DISCOVERING STATISTICS USING R*. Sage Publications Ltd.
- Fraass, B., Doppke, K., Hunt, M., Kutcher, G., Starkschall, G., Stern, R., & Van Dyke, J. (1998). American Association of Physicists in Medicine Radiation Therapy Committee

- Task Group 53: quality assurance for clinical radiotherapy treatment planning. *American Association of Physicists in Medicine*, 25(10), 1773–1829.
- Frayre, A. S., Torres, P., Gaona, E., Rivera, T., Franco, J., & Molina, N. (2012). Radiation dose reduction in a neonatal intensive care unit in computed radiography. *Applied Radiation and Isotopes*, 71(SUPPL.), 57–60. <https://doi.org/10.1016/j.apradiso.2012.04.015>
- Fritz, S., & Jones, A. (2014). Guidelines for anti-scatter grid use in pediatric digital radiography. *Pediatric Radiology*, 44(3), 313–321. <https://doi.org/10.1007/s00247-013-2824-9>
- Gammex Inc. Middleton WI. (2013). Neonatal chest phantom Gammex 610. *Madison, WI: Gammex RMI.*
- Gänsslen, A., Heidari, N., & Weinberg, A. M. (2013). Fractures of the pelvis in children: A review of the literature. *European Journal of Orthopaedic Surgery and Traumatology*, 23(8), 847–861. <https://doi.org/10.1007/s00590-012-1102-0>
- George, J., Eatough, J. P., Mountford, P. J., Koller, C. J., Oxtoby, J., & Frain, G. (2004). Patient dose optimization in plain radiography based on standard exposure factors. *The British Journal of Radiology*, 77(922), 858–863. <https://doi.org/10.1259/bjr/21484847>
- Giacco, G., Cannata, V., Furetta, C., Santopietro, F., & Fariello, G. (2001). On the use of pediatric phantoms in the dose evaluation during computed tomography (CT) thorax examinations. *Medical Physics*, 28(2), 199. <https://doi.org/10.1118/1.1344205>
- Gibson, D., & Davidson, R. (2012). Exposure Creep in Computed Radiography. *Academic Radiology*, 19(4), 458–462. <https://doi.org/10.1016/j.acra.2011.12.003>
- Gislason, A. J., Davies, A. G., & Cowen, A. R. (2010). Dose optimization in pediatric cardiac x-ray imaging. *Medical Physics*, 37(10), 5258–5269. <https://doi.org/10.1118/1.3488911>
- Goitein, M. (1982). Applications of Computed Tomography in Radiotherapy Treatment Planning. In *Progress in Medical Radiation Physics* (pp. 195–293). Boston, MA: Springer US. https://doi.org/10.1007/978-1-4615-7691-4_4
- Goodman, L. (1969). A modified tissue equivalent liquid. *Health Physics*, 16(763).
- Graham, D., Cloke, P., & Vosper, M. (2011). *Principles and Applications of Radiological Physics* (6th ed.). Churchill Livingstone/Elsevier, 2011.
- Green, D. M., & Swets, J. A. (1966). *Signal detection theory and psychophysics*. Wiley.
- Groenewald, A., & Groenewald, W. A. (2014). In-house development of a neonatal chest simulation phantom. *Journal of Applied Clinical Medical Physics / American College of Medical Physics*, 15(3), 4768. <https://doi.org/10.1120/jacmp.v15i3.4768>
- Guerra, a Del. (2004). *Ionizing Radiation Detectors for Medical Imaging*. World Scientific Publishing Co. Re. Ltd. Retrieved from <http://books.google.com/books?hl=en&lr=&id=UzOxXhBKpYEC&oi=fnd&pg=PA1&q=Ionizing+Radiation+Detectors+for+Medical+Imaging&ots=5GV6emfaN3&sig=XsaB WkvLXJa3E8BXhwMXZ7AQvyg>
- Guo, H., Liu, W. Y., He, X. Y., Zhou, X. S., Zeng, Q. L., & Li, B. Y. (2013). Optimizing imaging quality and radiation dose by the age-dependent setting of tube voltage in pediatric chest digital radiography. *Korean Journal of Radiology*, 14(1), 126–131. <https://doi.org/10.3348/kjr.2013.14.1.126>

- Gur, D., Bandos, A. I., Fuhrman, C. R., Klym, A. H., King, J. L., & Rockette, H. E. (2007). The Prevalence Effect in a Laboratory Environment. *Academic Radiology*, *14*(1), 49–53. <https://doi.org/10.1016/j.acra.2006.10.003>
- Hall, J. G., Froster-Iskenius, U. G., & Allanson, J. E. (1989). *Handbook of normal physical measurements*. Oxford: Oxford University Press.
- Hansson, B., Finnbogason, T., Schuwert, P., & Persliden, J. (1997). Added copper filtration in digital paediatric double-contrast colon examinations: effects on radiation dose and image quality. *European Radiology*, *7*(7), 1117–1122. <https://doi.org/10.1007/s003300050265>
- Hansson, J., Båth, M., Håkansson, M., Grundin, H., Bjurklint, E., Orvestad, P., ... Månsson, L. G. (2005). An optimisation strategy in a digital environment applied to neonatal chest imaging. *Radiation Protection Dosimetry*, *114*(1–3), 278–285. <https://doi.org/10.1093/rpd/nch528>
- Harding, L., Manning-Stanley, A., Evans, P., Taylor, E., Charnock, P., & England, A. (2014). Optimum patient orientation for pelvic and hip radiography: A randomised trial. *Radiography*, *20*(1), 22–32. <https://doi.org/10.1016/j.radi.2013.09.002>
- Hardy, M., & Boynes, S. (2003). *Paediatric Radiography*. Blackwell Publishing. Retrieved from <https://www.dawsonera.com:443/abstract/9781405147682>
- Harris, J., Tuddenham, W., Stanton, L., Glauser, F., & Pendergrass, E. (1956). The Development of a Chest Phantom for Use in Radiologic Dosimetry. *Radiology*, *67*(6), 805–814. <https://doi.org/10.1148/67.6.805>
- Harris, M., Huckle, J., Anthony, D., & Charnock, P. (2017). The Acceptability of Iterative Reconstruction Algorithms in Head CT: An Assessment of Sinogram Affirmed Iterative Reconstruction (SAFIRE) vs. Filtered Back Projection (FBP) Using Phantoms. *Journal of Medical Imaging and Radiation Sciences*, 1–11. <https://doi.org/10.1016/j.jmir.2017.04.002>
- Harrison, K., Ebert, M., Kron, T., Howlett, S., Cornes, D., Hamilton, C., & Denham, J. (2011). Design, manufacture, and evaluation of an anthropomorphic pelvic phantom purpose-built for radiotherapy dosimetric intercomparison. *Medical Physics*, *38*(10), 5330–5337. <https://doi.org/10.1118/1.3626573>
- Harrison, R. (1982). Backscatter factors for diagnostic radiology (1-4 mm Al HVL). *Physics in Medicine and Biology*, *27*(12), 1465–1474.
- Hart, D., Hillier, M., & Wall, B. (2007). *Doses to Patients from Radiographic and Fluoroscopic X-ray Imaging Procedures in the UK – 2010 Review*. Health Protection Agency (UK). Retrieved from <http://www.hpa.org.uk/Publications/Radiation/CRCEScientificAndTechnicalReportSeries/HPACRCE034>
- Hart, D., Hillier, M., & Wall, B. (2009). National reference doses for common radiographic, fluoroscopic and dental X-ray examinations in the UK. *British Journal of Radiology*, *82*(973), 1–12. <https://doi.org/10.1259/bjr/12568539>
- Hart, D., Jones, D., & Wall, B. (1996). *Coefficients for Estimating Effective Doses from Paediatric X-ray Examinations*. National Radiological Protection Board.
- Hart, D., & Wall, B. (2001). *Development of Diagnostic Reference Levels in Paediatric Radiology*.

- Hart, D., Wall, B., & Shrimpton, P. (2000). *Reference doses and patient size in paediatric radiology*. Didcot (United Kingdom).
- Hart, D., Wall, B., Shrimpton, P., & Dance, D. (2000). The Establishment of Reference Doses in Paediatric Radiology as a Function of Patient Size. *Radiation Protection Dosimetry*, 90(1), 235–238. <https://doi.org/10.1093/oxfordjournals.rpd.a033127>
- Hasegawa, B. H. (1991). *The physics of medical X-ray imaging*.
- Hawking, N., & Elmore, A. (2009). Effects of AEC chamber selection on patient dose and image quality. *Radiologic Technology*, 80(5), 411–419. Retrieved from <http://www.radiologictechnology.org/content/80/5/411.long>
- Hazelaar, C., Eijnatten, M., Dahele, M., Wolff, J., Forouzanfar, T., Slotman, B., & Verbakel, W. (2018). Using 3D printing techniques to create an anthropomorphic thorax phantom for medical imaging purposes. *Medical Physics*, 45(1), 92–100. <https://doi.org/10.1002/mp.12644>
- Heath, R., Bs, H., England, A., Bs, H., C, P., Evans, P., ... C, P. (2011). Digital Pelvic Radiography: Increasing Distance to Reduce Dose. *RADIOLOGIC TECHNOLOGY*, 83(1).
- Hendee, W. R., & O'Connor, M. K. (2012). Radiation Risks of Medical Imaging: Separating Fact from Fantasy. *Radiology*, 264(2), 312–321. <https://doi.org/10.1148/radiol.12112678>
- Hermann, K. P., Geworski, L., Hatzky, T., Lietz, R., & Harder, D. (1986). Muscle- and fat-equivalent polyethylene-based phantom materials for x-ray dosimetry at tube voltages below 100 kV. *Physics in Medicine and Biology*, 31(9), 1041–1046. <https://doi.org/10.1088/0031-9155/31/9/009>
- Hermann, K. P., Geworski, L., Muth, M., & Harder, D. (1985). Polyethylene-based water-equivalent phantom material for x-ray dosimetry at tube voltages from 10 to 100 kV. *Physics in Medicine and Biology*, 30(11), 1195–1200. <https://doi.org/10.1088/0031-9155/30/11/002>
- Herrmann, K., Bonél, H., Stäbler, A., Kulinna, C., Glaser, C., Holzknecht, N., ... Reiser, M. (2002). Chest imaging with flat-panel detector at low and standard doses: comparison with storage phosphor technology in normal patients. *European Radiology*, 12(2), 385–390. <https://doi.org/10.1007/s00330-001-1166-4>
- Herrmann, T., Fauber, T. L., Gill, J., Hoffman, C., Orth, D. K., Peterson, P. a, ... Odle, T. G. (2012). Best practices in digital radiography. *Radiologic Technology*, 84(1), 83–89. <https://doi.org/84/1/83> [pii]
- HH, R., & G, F. (1956). TISSUE-EQUIVALENT IONIZATION CHAMBERS. *Nucleonics*, 14(32).
- Hintenlang, K., Williams, J., & Hintenlang, D. (2002). A survey of radiation dose associated with pediatric plain-film chest X-ray examinations. *Pediatric Radiology*, 32(11), 771–777. <https://doi.org/10.1007/s00247-002-0734-3>
- Hogg, P., & Blindell, P. (2012). Software for image quality evaluation using a forced choice method. *Paper Presented at the UKRC, Manchester, UK*.
- Homolka, P., Gahleitner, a, Prokop, M., & Nowotny, R. (2002). Optimization of the composition of phantom materials for computed tomography. *Physics in Medicine and*

- Biology*, 47(16), 2907–2916. <https://doi.org/10.1088/0031-9155/47/16/306>
- Homolka, P., & Nowotny, R. (2002). Production of phantom materials using polymer powder sintering under vacuum. *Physics in Medicine and Biology*, 47(3), N47-52. Retrieved from <http://www.ncbi.nlm.nih.gov/pubmed/11848127>
- Honey, I., & Hogg, P. (2012). Balancing radiation dose and image quality in diagnostic imaging. *Radiography*, 18, e1–e2. <https://doi.org/10.1016/j.radi.2011.10.005>
- Honey, I., MacKenzie, A., & Evans, D. (2005). Investigation of optimum energies for chest imaging using film-screen and computed radiography. *British Journal of Radiology*, 78(929), 422–427. <https://doi.org/10.1259/bjr/32912696>
- Hubbell, J. H. (1982). Photon mass attenuation and energy-absorption coefficients. *The International Journal Of Applied Radiation And Isotopes*, 33(11), 1269–1290. [https://doi.org/10.1016/0020-708X\(82\)90248-4](https://doi.org/10.1016/0020-708X(82)90248-4)
- Hubbell, J. H. (1995). Tables of X-Ray Mass Attenuation Coefficients and Mass Energy-Absorption Coefficients from 1 keV to 20 MeV for Elements Z = 1 to 92 and 48 Additional Substances of Dosimetric Interest. *NISTIR 5632. Natl Inst Standards Technol, USA*. Retrieved from <http://www.nist.gov/pml/data/xraycoef/>
- Huda, W. (2014). Kerma-Area Product in Diagnostic Radiology. *American Journal of Roentgenology*, 203(6), W565–W569. <https://doi.org/10.2214/AJR.14.12513>
- Hufton, A., Doyle, S., & Carty, H. (1998). Digital radiography in paediatrics: Radiation dose considerations and magnitude of possible dose reduction. *British Journal of Radiology*, 71(FEB.), 186–199. <https://doi.org/10.1259/bjr.71.842.9579183>
- IAEA. (2013). Human Health Series 24: Dosimetry In Diagnostic Radiology for Paediatric Patients. *Human Health Series*, (24), 176. Retrieved from http://www-pub.iaea.org/MTCD/publications/PDF/Pub1609_web.pdf%5Cnhttp://www.vomfi.univ.kiev.ua/assets/files/IAEA/Pub1462_web.pdf
- ICRP. (1974). *Report of the task group on reference man. Annals of the ICRP*. Retrieved from [http://ani.sagepub.com/lookup/doi/10.1016/0146-6453\(79\)90123-4](http://ani.sagepub.com/lookup/doi/10.1016/0146-6453(79)90123-4)
- ICRP. (2002). *Basic Anatomical and Physiological Data for Use in Radiological Protection: Reference Values. ICRP PUBLICATION 89*. <https://doi.org/10.1016/j.icrp.2006.06.001>
- ICRP. (2004a). *Managing Patient Dose in Digital Radiology. A Report of the International Commission on Radiological Protection*.
- ICRP. (2004b). *MANAGING PATIENT DOSE IN DIGITAL RADIOLOGY. A report of the international commission on radiological protection (Publication 93)*.
- ICRP. (2007). ICRP 103: The 2007 Recommendations of the International Commission on Radiological Protection. *Annals of the ICRP*, 37, 330. <https://doi.org/10.1016/j.icrp.2007.10.001>
- ICRP. (2017). *Diagnostic reference levels in medical imaging. ICRP Publication 135 (Vol. 46)*. <https://doi.org/10.1016/j.icrp.2006.06.001>
- ICRU. (1996). *ICRU Report 54: Medical imaging—the assessment of image quality. ICRU 54*. Retrieved from <http://linkinghub.elsevier.com/retrieve/pii/S1078817497900389>
- Illers, H., Buhr, E., & Hoeschen, C. (2005). Measurement of the detective quantum efficiency

- (DQE) of digital X-ray detectors according to the novel standard IEC 62220-1. *Radiation Protection Dosimetry*, 114(1–3), 39–44. <https://doi.org/10.1093/rpd/nch507>
- Institute of Physics and Engineering in Medicine (IPEM). (2005). *IPEM report 91 recommended standards for the routine performance testing of diagnostic X-ray imaging systems*. York.
- International Commission on Radiation Units and Measurements (ICRU). (1989). *Tissue substitutes in radiation dosimetry and measurement. ICRU Report 44*. Bethesda, Maryland.
- International Commission on Radiation Units and Measurements (ICRU). (1992). *Phantoms and Computational Models in Therapy, Diagnosis and Protection. ICRU Report 48*. Bethesda, Maryland. Retrieved from <https://academic.oup.com/jicru/article/2923832/1>.
- IRMER. (2017). *Ionising radiation medical exposure regulations*. Retrieved from http://www.legislation.gov.uk/ukxi/2017/1322/pdfs/ukxi_20171322_en.pdf
- IRMER. (2018). *The Ionising Radiation (Medical Exposure) (Amendment) Regulations 2018*.
- Ismailos, E., Mastorakou, I., Kelekis, N. L., Papadopoulos, K. P., Efstathopoulos, E. P., Panayiotakis, G., & Kelekis, D. a. (1996). Clinical evaluation of manual and automatic exposure control techniques in film-based chest radiography. *The British Journal of Radiology*, 69(823), 650–654. <https://doi.org/10.1259/0007-1285-69-823-650>
- Iwashita, Y. (2000). Basic study of the measurement of bone mineral content of cortical and cancellous bone of the mandible by computed tomography. *Dentomaxillofac Radiol*, 29(4), 209–215. <https://doi.org/10.1038/sj/dmfr/4600541>
- Jacob, R., Vano-Galvan, E., Vano, E., Ruiz, N., Soto, J., Barrio, D., & Prieto, C. (2009). Optimising the Use of Computed Radiography in Pediatric Chest Imaging. *Journal of Digital Imaging*, 22(2), 104–113. <https://doi.org/10.1007/s10278-007-9071-2>
- Jahnke, P., Limberg, F., Gerbl, A., P., A., Braun, V., Hamm, B., & Scheel, M. (2017). Radiopaque Three-dimensional Printing: A Method to Create Realistic CT Phantoms. *Radiology*, 282(2), 569–575. <https://doi.org/10.1148/radiol.2016152710>
- Jahnke, P., Schwarz, S., Ziegert, M., Schwarz, F., Hamm, B., & Scheel, M. (2019). Paper-based 3D printing of anthropomorphic CT phantoms: Feasibility of two construction techniques. *European Radiology*, 29(3), 1384–1390. <https://doi.org/10.1007/s00330-018-5654-1>
- Jana, M., Nair, N., Gupta, A., Kabra, M., & Gupta, N. (2017). Pelvic radiograph in skeletal dysplasias: An approach. *Indian Journal of Radiology and Imaging*, 27(2), 187. https://doi.org/10.4103/ijri.IJRI_367_16
- Jessen, K. A. (2004). Balancing image quality and dose in diagnostic radiology. *European Radiology Supplements*, 9–18. <https://doi.org/10.1007/s10406-004-0003-7>
- Jha, P., Stein-Wexler, R., Coulter, K., Seibert, A., Li, C.-S., & Wootton-Gorges, S. (2013). Optimizing bone surveys performed for suspected non-accidental trauma with attention to maximizing diagnostic yield while minimizing radiation exposure: utility of pelvic and lateral radiographs. *Pediatric Radiology*, 43(6), 668–672. <https://doi.org/10.1007/s00247-012-2614-9>
- John, S., Moore, Q., Herrmann, T., Don, S., Powers, K., Smith, S., ... Goske, M. (2013). The image gently pediatric digital radiography safety checklist: Tools for improving pediatric

- radiography. *Journal of the American College of Radiology*, 10(10), 781–788. <https://doi.org/10.1016/j.jacr.2013.02.026>
- Johnston, J., & Fauber, T. L. (2011). *Essentials of Radiographic Physics and Imaging* (1 edition). Mosby.
- Jones, A. (2006). *Dose Versus Image Quality in Pediatric Radiology: Studies Using a Tomographic Newborn Physical Phantom with an Incorporated Dosimetry System*. University of Florida. Retrieved from <http://arxiv.org/abs/1011.1669>
- Jones, A., Ansell, C., Jerrom, C., & Honey, I. (2015). Optimization of image quality and patient dose in radiographs of paediatric extremities using direct digital radiography. *The British Journal of Radiology*, 88(1050), 20140660. <https://doi.org/10.1259/bjr.20140660>
- Jones, A., Hintenlang, D. E., & Bolch, W. E. (2003). Tissue-equivalent materials for construction of tomographic dosimetry phantoms in pediatric radiology. *Medical Physics*, 30(8), 2072–2081. <https://doi.org/10.1118/1.1592641>
- Jones, A., Simon, T., Bolch, W., Holman, M., & Hintenlang, D. (2006). Tomographic physical phantom of the newborn child with real-time dosimetry I. Methods and techniques for construction. *Medical Physics*, 33(10). <https://doi.org/10.1118/1.2256686>
- Jones, N., Palarm, T., & Negus, I. (2001). Neonatal chest and abdominal radiation dosimetry: a comparison of two radiographic techniques. *The British Journal of Radiology*, 74(886), 920–925. <https://doi.org/10.1259/bjr.74.886.740920>
- Jones, T., Brennan, P., & Ryan, E. (2017). the Impact of Digital Technology on Dose Reduction in Paediatric Cardiac Catheterisation Within a Large Metropolitan Children'S Hospital. *Radiation Protection Dosimetry*, (January), 1–6. <https://doi.org/10.1093/rpd/ncx294>
- Kalender, W. A., & Suess, C. (1987). A new calibration phantom for quantitative computed tomography. *Medical Physics*, 14(5), 863–866. <https://doi.org/10.1118/1.596013>
- Karami, V., Zabihzadeh, M., Danyaei, A., & Shams, N. (2016). Efficacy of Increasing Focus to Film Distance (FFD) for Patient's Dose and Image Quality in Pediatric Chest Radiography. *Int J Pediatr*, 49(33). <https://doi.org/10.22038/ijp.2016.7319>
- Karami, V., Zabihzadeh, M., Shams, N., & Gilavand, A. (2017). Optimization of radiological protection in pediatric patients undergoing common conventional radiological procedures: Effectiveness of increasing the film to focus distance (FFD). *International Journal of Pediatrics*, 5(4), 4771–4782. <https://doi.org/10.22038/ijp.2017.22010.1841>
- Keeble, C., Baxter, P., Gislason-Lee, A., Treadgold, L., & Davies, A. (2016). Methods for the analysis of ordinal response data in medical image quality assessment. *The British Journal of Radiology*, (January), 20160094. <https://doi.org/10.1259/bjr.20160094>
- Khong, P.-L., Ringertz, H., Donoghue, V., Frush, D., Rehani, M., Appelgate, K., & Sanchez, R. (2013). ICRP Publication 121: Radiological Protection in Paediatric Diagnostic and Interventional Radiology. *Annals of the ICRP*, 42(2), 1–63. <https://doi.org/10.1016/j.icrp.2012.10.001>
- Kienbock, R. (1906). On the Quantimetric Method. *Archives of The Roentgen Ray*, 11(1), 17–20. <https://doi.org/10.1259/arr.1906.0005>
- Kiljunen, T., Tietavainen, A., Parviainen, T., Viitala, A., & Kortenesniemi, M. (2009). Organ doses and effective doses in pediatric radiography: Patient-dose survey in Finland. *Acta*

- Radiologica*, 50(1), 114–124. <https://doi.org/10.1080/02841850802570561>
- Knight, S. P. (2014). A paediatric X-ray exposure chart. *Journal of Medical Radiation Sciences*, 61(3), 191–201. <https://doi.org/10.1002/jmrs.56>
- Korir, G. K., Wambani, J. S., & Ochieng, B. O. (2010). Optimisation of Patient Protection and Image Quality in Diagnostic Radiology. *East African Medical Journal*, 87(3), 127–133.
- Körner, M., Weber, C., Wirth, S., Pfeifer, K.-J., Reiser, M., & Treitl, M. (2007). Advances in Digital Radiography: Physical Principles and System Overview. *RadioGraphics*, 27(3), 675–686. <https://doi.org/10.1148/rg.273065075>
- Kostova-Lefterova, D., Taseva, D., Hristova-Popova, J., & Vassileva, J. (2015). Optimisation of paediatric chest radiography. *Radiation Protection Dosimetry*, 2(January), 1–4. <https://doi.org/10.1093/rpd/ncv119>
- Kwok, M. Y., Yen, K., Atabaki, S., Adelgais, K., Garcia, M., Quayle, K., ... Holmes, J. F. (2015). Sensitivity of plain pelvis radiography in children with blunt torso trauma. *Annals of Emergency Medicine*, 65(1), 63–71. <https://doi.org/10.1016/j.annemergmed.2014.06.017>
- Lagisetty, J., Slovis, T., Thomas, R., Knazik, S., & Stankovic, C. (2012). Are routine pelvic radiographs in major pediatric blunt trauma necessary? *Pediatric Radiology*, 42(7), 853–858. <https://doi.org/10.1007/s00247-011-2341-7>
- Lança, L., Bowdler, M., Creedon, J., Dayer, V., N., S., V.H., S., ... Pires Jorge, J. A. (2018a). Paediatric Phantom Dose Optimization Using Digital Radiography with Paediatric Phantom Dose Optimisation Using Digital Radiography with Variation of Exposure Parameters and Filtration whilst minimising Image Quality Impairment . In *Optimax2018* (pp. 77–92).
- Lança, L., Bowdler, M., Creedon, J., Dayer, V., N., S., V.H., S., ... Pires Jorge, J. A. (2018b). Paediatric phantom dose study using digital radiography with variation of exposure parameters and filtration, (March), 0–18. <https://doi.org/10.1594/ecr2018/C-0986>
- Lança, L., Franco, L., Ahmed, A., Harderwijk, M., Marti, C., Nasir, S., ... Hogg, P. (2014). 10kVp rule - An anthropomorphic pelvis phantom imaging study using a CR system: Impact on image quality and effective dose using AEC and manual mode. *Radiography*, 20(4), 333–338. <https://doi.org/10.1016/j.radi.2014.04.007>
- Lança, L., & Hogg, P. (2016). Are physical measures good indicators of clinical image quality at low dose levels? A pilot study, (March).
- Lança, L., & Silva, A. (2013). *Digital Imaging Systems for Plain Radiography. Statewide Agricultural Land Use Baseline 2015* (Vol. 1). New York, NY: Springer New York. <https://doi.org/10.1007/978-1-4614-5067-2>
- Lança, L., & Silva, A. (2008). Digital radiography detectors – A technical overview: Part 2. *Radiography*, 15(2), 134–138. <https://doi.org/10.1016/j.radi.2008.02.005>
- Leary, M., Babae, M., Brandt, M., & Subic, A. (2013). Feasible Build Orientations for Self-Supporting Fused Deposition Manufacture: A Novel Approach to Space-Filling Tesselated Geometries. *Advanced Materials Research*, 633, 148–168. <https://doi.org/10.4028/www.scientific.net/amr.633.148>
- Leary, M., Kron, T., Keller, C., Franich, R., Lonski, P., Subic, A., & Brandt, M. (2015).

- Additive manufacture of custom radiation dosimetry phantoms: An automated method compatible with commercial polymer 3D printers. *Materials and Design*, 86, 487–499. <https://doi.org/10.1016/j.matdes.2015.07.052>
- Leblans, P., Vandenbroucke, D., & Willems, P. (2011). Storage phosphors for medical imaging. *Materials*, 4(6), 1034–1086. <https://doi.org/10.3390/ma4061034>
- Lee, Choonik. (2006). *Development of the voxel computational phantoms of pediatric patients and their application to organ dose assessment*. University of Florida. Retrieved from http://etd.fcla.edu/UF/UFE0013660/lee_c.pdf?origin=publication_detail
- Lee, Choonsik, Lodwick, D., Hurtado, J., Pafundi, D., Williams, J. L., & Bolch, W. E. (2010). The UF family of reference hybrid phantoms for computational radiation dosimetry. *Physics in Medicine and Biology*, 55(2), 339–363. <https://doi.org/10.1088/0031-9155/55/2/002>
- Leng, S., Chen, B., Vrieze, T., Kuhlmann, J., Yu, L., Alexander, A., ... McCollough, C. (2016). Construction of realistic phantoms from patient images and a commercial three-dimensional printer. *Journal of Medical Imaging*, 3(3), 033501. <https://doi.org/10.1117/1.JMI.3.3.033501>
- Leng, S., McGee, K., Morris, J., Alexander, A., Kuhlmann, J., Vrieze, T., ... Matsumoto, J. (2017). Anatomic modeling using 3D printing: quality assurance and optimization. *3D Printing in Medicine*, 3(1), 6. <https://doi.org/10.1186/s41205-017-0014-3>
- Leng, S., Yu, L., Vrieze, T., Kuhlmann, J., Chen, B., & McCollough, C. (2015). Construction of realistic liver phantoms from patient images using 3D printer and its application in CT image quality assessment. In C. Hoeschen, D. Kontos, & T. G. Flohr (Eds.), *HHS Public Access* (Vol. 21, p. 94124E). <https://doi.org/10.1117/12.2082121>
- Liaparinos, P., & Kandarakis, I. (2011). Overestimations in zero frequency DQE of x-ray imaging converters assessed by Monte Carlo techniques based on the study of energy impartation events. *Medical Physics*, 38(7), 4440–4450. <https://doi.org/10.1118/1.3603190>
- Lin, Y., Luo, H., Dobbins, J. T., Page McAdams, H., Wang, X., Sehnert, W. J., ... Samei, E. (2012). An image-based technique to assess the perceptual quality of clinical chest radiographs. *Medical Physics*, 39(11), 7019–7031. <https://doi.org/10.1118/1.4760886>
- Linnet, M., Slovis, T., Miller, D., Kleinerman, R., Lee, C., Rajaraman, P., & Berrington de Gonzalez, A. (2012). Cancer risks associated with external radiation from diagnostic imaging procedures. *CA: A Cancer Journal for Clinicians*, 62(2), 75–100. <https://doi.org/10.3322/caac.21132>
- Ludewig, E., Richter, A., & Frame, M. (2010). Diagnostic imaging - Evaluating image quality using visual grading characteristic (VGC) analysis. *Veterinary Research Communications*, 34(5), 473–479. <https://doi.org/10.1007/s11259-010-9413-2>
- Ludwig, K., Ahlers, K., Sandmann, C., Gosheger, G., Kloska, S., Vieth, V., ... Heindel, W. (2003). Dosisreduktion bei röntgenaufnahmen des kindlichen Beckenskelettes zur Diagnostik der Hüftgelenksdysplasie unter Verwendung eines digitalen Flachdetektorsystems. *RoFo Fortschritte Auf Dem Gebiet Der Röntgenstrahlen Und Der Bildgebenden Verfahren*, 175(1), 112–117. <https://doi.org/10.1055/s-2003-36597>
- Ludwig, K., Ahlers, K., Wormanns, D., Freund, M., Bernhardt, T., Diederich, S., & Heindel,

- W. (2003). Lumbar Spine Radiography: Digital Flat-Panel Detector versus Screen-Film and Storage-Phosphor Systems in Monkeys as a Pediatric Model. *Radiology*, 229(1), 140–144. <https://doi.org/10.1148/radiol.2291020717>
- Ma, W. K., Hogg, P., Tootell, A., Manning, D., Thomas, N., Kane, T., ... Kitching, J. (2013). Anthropomorphic chest phantom imaging - The potential for dose creep in computed radiography. *Radiography*, 19(3), 207–211. <https://doi.org/10.1016/j.radi.2013.04.002>
- Manning-Stanley, A. S., Ward, A. J., & England, A. (2012). Options for radiation dose optimisation in pelvic digital radiography: A phantom study. *Radiography*, 18(4), 256–263. <https://doi.org/10.1016/j.radi.2012.06.002>
- Manning, D. J., Gale, A., & Krupinski, E. A. (2005). Perception research in medical imaging. *British Journal of Radiology*, 78(932), 683–685. <https://doi.org/10.1259/bjr/72087985>
- Månsson, L. G. (2000). Methods for the Evaluation of Image Quality: A Review. *Radiation Protection Dosimetry*, 90(1–2), 89–99. Retrieved from <http://rpd.oxfordjournals.org/content/90/1-2/89>
- Markus, B. (1956). The concept of tissue equivalence and several water-like phantom substances for energies of 10 KeV to 100 MeV as well as fast electrons. *Strahlentherapie*, 101(1), 111–131.
- Martin, C., Darragh, C., McKenzie, G., & Bayliss, A. (1993). Implementation of a programme for reduction of radiographic doses and results achieved through increases in tube potential. *British Journal of Radiology*, 66(783), 228–233. <https://doi.org/10.1259/0007-1285-66-783-228>
- Martin, C. J. (2007a). Optimisation in general radiography. *Biomedical Imaging and Intervention Journal*, 3(2). <https://doi.org/10.2349/bij.3.2.e18>
- Martin, C. J. (2007b). The importance of radiation quality for optimisation in radiology. *Biomedical Imaging and Intervention Journal*, 3(2), 1–14. <https://doi.org/10.2349/bij.3.2.e38>
- Martin, C. J., Farquhar, B., Stockdale, E., & Macdonald, S. (1994). A study of the relationship between patient dose and size in paediatric radiology. *The British Journal of Radiology*. <https://doi.org/10.1259/0007-1285-67-801-864>
- Martin, C. J., Sharp, P. F., & Sutton, D. G. (1999). Measurement of image quality in diagnostic radiology. *Applied Radiation and Isotopes*, 50(1), 21–38. [https://doi.org/10.1016/S0969-8043\(98\)00022-0](https://doi.org/10.1016/S0969-8043(98)00022-0)
- Martin, C. J., Sutton, D., & Sharp, P. (1999). Balancing patient dose and image quality. *Applied Radiation and Isotopes*, 50(1), 1–19. [https://doi.org/10.1016/S0969-8043\(98\)00021-9](https://doi.org/10.1016/S0969-8043(98)00021-9)
- Martin, L., Ruddlesden, R., Makepeace, C., Robinson, L., Mistry, T., & Starritt, H. (2013). Paediatric x-ray radiation dose reduction and image quality analysis. *Journal of Radiological Protection*, 33(3), 621–633. <https://doi.org/10.1088/0952-4746/33/3/621>
- Matthews, K., & Brennan, P. (2009). Optimisation of X-ray examinations: General principles and an Irish perspective. *Radiography*, 15(3), 262–268. <https://doi.org/10.1016/j.radi.2008.07.002>
- Matthews, K., Brennan, P., & McEntee, M. (2014). An evaluation of paediatric projection radiography in Ireland. *Radiography*. <https://doi.org/10.1016/j.radi.2013.10.001>

- Mattsson, S., & Thomas, B. (2006). Development of methods for body composition studies. *Phys. Med. Biol. Phys. Med. Biol*, *51*(51), 203–228. <https://doi.org/10.1088/0031-9155/51/13/R13>
- Mc Fadden, S., Roding, T., de Vries, G., Benwell, M., Bijwaard, H., & Scheurleer, J. (2017). Digital imaging and radiographic practise in diagnostic radiography: An overview of current knowledge and practice in Europe. *Radiography*, 8–12. <https://doi.org/10.1016/j.radi.2017.11.004>
- McCollough, C. H., Bruesewitz, M. R., & Kofler, J. M. (2006). CT Dose Reduction and Dose Management Tools: Overview of Available Options. *RadioGraphics*, *26*(2), 503–512. <https://doi.org/10.1148/rg.262055138>
- McEntee, M., & Doherty, P. (2011). Optimisation of the pediatric pelvis radiographic examination. *ECR 2011 (Poster No: C-0265)*, 1–7. <https://doi.org/10.1594/ecr2011/C-0265>
- Menser, B., Manke, D., Mentrup, D., & Neitzel, U. (2016). A Monte Carlo simulation framework for joint optimisation of image quality and patient dose in digital paediatric radiography. *Radiation Protection Dosimetry*, *169*(1), 371–377. <https://doi.org/10.1093/rpd/ncv483>
- Montgomery, D. (2013). *Design and Analysis of Experiments Eighth Edition* (8th ed.). John Wiley & Sons, Inc.
- Moore, C., Wood, T., Beavis, A., & Saunderson, J. (2013). Correlation of the clinical and physical image quality in chest radiography for average adults with a computed radiography imaging system. *British Journal of Radiology*, *86*(1027). <https://doi.org/10.1259/bjr.20130077>
- Morrison, G., John, S. D., Goske, M. J., Charkot, E., Herrmann, T., Smith, S. N., ... Carbonneau, K. (2011). Pediatric digital radiography education for radiologic technologists: Current state. *Pediatric Radiology*, *41*(5), 602–610. <https://doi.org/10.1007/s00247-010-1904-3>
- Mothiram, U., Brennan, P., Lewis, S., Moran, B., & Robinson, J. (2014). Digital radiography exposure indices: A review. *Journal of Medical Radiation Sciences*, *61*(2), 112–118. <https://doi.org/10.1002/jmrs.49>
- Mraity, H. (2015). *Optimisation of radiation dose and image quality for AP pelvis radiographic examination*. University of Salford.
- Mraity, H., & Alrowilly, M. (2016). Visual image quality assessment methods. In *optimax2015* (pp. 32–37).
- Mraity, H., England, A., Cassidy, S., Eachus, P., Dominguez, A., & Hogg, P. (2016). Development and validation of a visual grading scale for assessing image quality of AP pelvis radiographic images. *The British Journal of Radiology*, *89*(1061), 20150430. <https://doi.org/10.1259/bjr.20150430>
- Murphey, M. D., Quale, J. L., Martin, N. L., Bramble, J. M., Cook, L. T., & Dwyer, S. J. (1992). Computed radiography in musculoskeletal imaging: state of the art. *American Journal of Roentgenology*, *158*(1), 19–27. <https://doi.org/10.2214/ajr.158.1.1727344>
- National Electrical Manufacturers Association. (2006). *Digital Imaging and Communications in Medicine (DICOM) Part 14 : Grayscale Standard Display Function*. Rosslyn, Virginia

22209 USA. Retrieved from <http://www.ncbi.nlm.nih.gov/pubmed/2188123>

- Neitzel, U. (1992). Grids or air gaps for scatter reduction in digital radiography: a model calculation. *Medical Physics*. <https://doi.org/10.1118/1.596836>
- Neitzel, U. (2000). Recent Technological Developments and Their Influence. *Radiation Protection Dosimetry*, *90*(1), 15–20. <https://doi.org/10.1093/oxfordjournals.rpd.a033107>
- Nickoloff, E. (2002). Current adult and pediatric CT doses. *Pediatric Radiology*, *32*(4), 250–260. <https://doi.org/10.1007/s00247-002-0677-8>
- Norrmann, E., & Persliden, J. (2005). A factorial experiment on image quality and radiation dose. *Radiation Protection Dosimetry*, *114*(1–3), 246–252. <https://doi.org/10.1093/rpd/nch557>
- Norweck, J., Seibert, J., Andriole, K., Clunie, D., Curran, B., Flynn, M., ... Wyatt, M. (2013). ACR–AAPM–SIIM Technical Standard for Electronic Practice of Medical Imaging. *Journal of Digital Imaging*, *26*(1), 38–52. <https://doi.org/10.1007/s10278-012-9522-2>
- Nyathi, T. (2013). *Dose optimization in diagnostic radiology*. (Doctoral thesis). University of the Witwatersrand.
- Oakley, J. (2003). *Digital Imaging: A Primer for Radiographers, Radiologists and Health Care Professionals* (1st ed.). Cambridge University Press.
- Obuchowski, N. A. (1994). Computing Sample Size for Receiver Operating Characteristic Studies. *Investigative Radiology*, *29*(2), 238–243. <https://doi.org/10.1097/00004424-199402000-00020>
- Orton, C. G. (Ed.). (1982). *Progress in Medical Radiation Physics*. Boston, MA: Springer US. <https://doi.org/10.1007/978-1-4615-7691-4>
- Palareti, G., Legnani, C., Cosmi, B., Antonucci, E., Erba, N., Poli, D., ... Tosetto, A. (2016). Comparison between different D-Dimer cutoff values to assess the individual risk of recurrent venous thromboembolism: Analysis of results obtained in the DULCIS study. *International Journal of Laboratory Hematology*, *38*(1), 42–49. <https://doi.org/10.1111/ijlh.12426>
- Paliwal, B. R., Ritter, M. A., McNutt, T. R., Mackie, T. R., Thomadsen, B. R., Purdy, J. A., & Kinsella, T. J. (1998). A solid water pelvic and prostate phantom for imaging, volume rendering, treatment planning, and dosimetry for an RTOG multi-institutional, 3-D dose escalation study. *International Journal of Radiation Oncology Biology Physics*, *42*(1), 205–211. [https://doi.org/10.1016/S0360-3016\(98\)00187-4](https://doi.org/10.1016/S0360-3016(98)00187-4)
- Park, H. S., Kim, Y. S., Park, O. S., Kim, S. T., Jeon, C. W., & Kim, H. J. (2014). Effective DQE (eDQE) and dose to optimize radiographic technical parameters: A survey of pediatric chest X-ray examinations in Korea. *Radiologia Medica*, *119*(4), 231–239. <https://doi.org/10.1007/s11547-013-0337-0>
- Paulo, G., Vaño, E., & Rodrigues, A. (2016). Diagnostic reference levels in plain radiography for paediatric imaging: A Portuguese study. *Radiography*, *22*(1), e34–e39. <https://doi.org/10.1016/j.radi.2015.07.002>
- Paulo, Graciano, Santos, J., Moreira, A., & Figueiredo, F. (2011). Transition from screen-film to computed radiography in a paediatric hospital: the missing link towards optimisation. *Radiation Protection Dosimetry*, *147*(1–2), 164–167. <https://doi.org/10.1093/rpd/ncr355>

- Pearce, J. G., Gillan, G., & Rock, W. (1980). In preceeding of a symposium on Optimisation of chest phantom. *Madison, WI, HHS Publ. (FDA)*, 80(8124), 255.
- Pelli, D. G., & Farell, B. (1995). Chapter 29 Psychophysical Methods. In *Handbook of optics: Fundamentals, techniques, and design (2 ed., Vol. 1)*.
- Perks, T. D., Dendere, R., Irving, B., Hartley, T., Scholtz, P., Lawson, A., ... Douglas, T. S. (2015). Filtration to reduce paediatric dose for a linear slot-scanning digital X-ray machine. *Radiation Protection Dosimetry*, 167(4), 552–561. <https://doi.org/10.1093/rpd/ncu339>
- Petoussi-Henss, N., Zankl, M., Drexler, G., Panzer, W., & Regulla, D. (1998). Calculation of backscatter factors for diagnostic radiology using Monte Carlo methods. *Physics in Medicine and Biology*, 43(8), 15. Retrieved from <http://www.ncbi.nlm.nih.gov/pubmed/9725601>
- Pina, D. R. (2002). *Metodologia para otimização de imagens radiográfica*. University of Sao Paulo, USP, Brazil.
- Pina, D. R., Duarte, S. B., Ghilardi Netto, T., & Morceli, J. (2009). Phantom development for radiographic image optimization of chest, skull and pelvis examination for nonstandard patient. *Applied Radiation and Isotopes*, 67(1), 61–69. <https://doi.org/10.1016/j.apradiso.2008.07.018>
- Pina, D. R., Duarte, S. B., Ghilardi Netto, T., Trad, C. S., Brochi, M. A., & de Oliveira, S. C. (2004). Optimization of standard patient radiographic images for chest, skull and pelvis exams in conventional x-ray equipment. *Physics in Medicine and Biology*, 49(14), N215–N226. <https://doi.org/10.1088/0031-9155/49/14/N02>
- Precht, H., Gerke, O., Rosendahl, K., Tingberg, A., & Waaler, D. (2012). Digital radiography: Optimization of image quality and dose using multi-frequency software. *Pediatric Radiology*, 42(9), 1112–1118. <https://doi.org/10.1007/s00247-012-2385-3>
- Precht, H., Gerke, O., Rosendahl, K., Tingberg, A., & Waaler, D. (2014). Large dose reduction by optimization of multifrequency processing software in digital radiography at follow-up examinations of the pediatric femur. *Pediatric Radiology*, 44(2), 239–240. <https://doi.org/10.1007/s00247-013-2854-3>
- Precht, Helle, Tingberg, A., Waaler, D., & Outzen, C. B. (2014). New developed DR detector performs radiographs of hand, pelvic and premature chest anatomies at a lower radiation dose and/or a higher image quality. *Journal of Digital Imaging*, 27(1), 68–76. <https://doi.org/10.1007/s10278-013-9635-2>
- Quick, T. J., & Eastwood, D. M. (2005). Pediatric fractures and dislocations of the hip and pelvis. *Clinical Orthopaedics and Related Research*, (432), 87–96. <https://doi.org/10.1097/01.blo.0000155372.65446.40>
- Rajapakshe, R., Luchka, K., & Shalev, S. (1996). A quality control test for electronic portal imaging devices. *Medical Physics*, 23(7), 1237–1244. <https://doi.org/10.1118/1.597866>
- Roberts, J. a, Evans, S. C., & Rees, M. (2006). Optimisation of imaging technique used in direct digital radiography. *Journal of Radiological Protection: Official Journal of the Society for Radiological Protection*, 26(3), 287–299. <https://doi.org/10.1088/0952-4746/26/3/003>
- Roscoe, J. T. (1975). *Fundamental research statistics for the behavioral sciences* (2nd editio). New York: Holt, Rinehart and Winston.

- Rose, A. (1948). The sensitivity performance of the human eye on an absolute scale. *Journal of the Optical Society of America*, 38(2), 196–208. <https://doi.org/10.1364/JOSA.38.000196>
- Rose, A. (1973). *Vision-Human and Electronic*. Plenum Press, New York, N.Y., 1973.
- Rosner, B. (2010). *Fundamentals of Biostatistics* (7th ed.). Cengage Learning, Inc.
- Rumsey, D. J. (2011). *Statistics For Dummies* (2nd ed.). Hoboken, New Jersey: Wiley Publishing, Inc.
- RV, G., AL, A., & PN, D. (1976). Further realistic torso phantom development. *University of California Research Laboratory*, 76(1).
- Sæther, H., Lagesen, B., Martinsen, A., Holsen, E., & Øvrebø, K. (2010). Dose levels from thoracic and pelvic examinations in two pediatric radiological departments in Norway – a comparison study of dose-area product and radiographic technique. *Acta Radiologica*, 51(10), 1137–1142. <https://doi.org/10.3109/02841851.2010.515616>
- Salmi, M. (2013). *Medical applications of additive manufacturing in surgery and dental care*. (PhD thesis), Aalto University, Helsinki, Finland.
- Samei, E., Ranger, N., MacKenzie, A., Honey, I., Dobbins, J., & Ravin, C. (2009). Effective DQE (eDQE) and speed of digital radiographic systems: an experimental methodology. *Medical Physics*, 36(8), 3806–3817. <https://doi.org/10.1118/1.3171690>
- Samei, Ehsan, Dobbins, J. T., Lo, J. Y., & Tornai, M. P. (2005). A framework for optimising the radiographic technique in digital X-ray imaging. *Radiation Protection Dosimetry*, 114(1–3), 220–229. <https://doi.org/10.1093/rpd/nch562>
- Sandborg, M., McVey, G., Dance, D. R., & Carlsson, G. A. (2000). Comparison of Model Predictions of Image Quality with Results of Clinical Trials in Chest and Lumbar Spine Screen-film Imaging. *Radiation Protection Dosimetry*, 90(1), 173–176. <https://doi.org/10.1093/oxfordjournals.rpd.a033112>
- Sandborg, M., Tingberg, A., Dance, D., Lanhede, B., Almén, A., McVey, G., ... Carlsson, G. (2001). Demonstration of correlations between clinical and physical image quality measures in chest and lumbar spine screen–film radiography. *The British Journal of Radiology*, 74(882), 520–528. <https://doi.org/10.1259/bjr.74.882.740520>
- Sandborg, M., Tingberg, A., Ullman, G., Dance, D., & Carlsson, G. (2006a). Comparison of clinical and physical measures of image quality in chest and pelvis computed radiography at different tube voltages. *Medical Physics*, 33(11), 4169–4175. <https://doi.org/10.1118/1.2362871>
- Sandborg, M., Tingberg, A., Ullman, G., Dance, D., & Carlsson, G. (2006b). Comparison of clinical and physical measures of image quality in chest and pelvis computed radiography at different tube voltages. *Medical Physics*, 33(11), 4169–4175. <https://doi.org/10.1118/1.2362871>
- Schaefer-Prokop, C., De Boo, D., Uffmann, M., & Prokop, M. (2009). DR and CR: Recent advances in technology. *European Journal of Radiology*, 72(2), 194–201. <https://doi.org/10.1016/j.ejrad.2009.05.055>
- Schaefer-Prokop, C., & Neitzel, U. (2006). Computed Radiography/Digital Radiography: Radiologist Perspective on Controlling Dose and Study Quality. Retrieved from

https://www.researchgate.net/profile/Ulrich_Neitzel/publication/236609268_Computed_Radiography_Digital_Radiography_Radiologist_Perspective_on_Controlling_Dose_and_Study_Quality/links/5464a0140cf2837efdb47a8e/Computed-Radiography-Digital-Radiography-Radiolo

- Schaefer-Prokop, C., Neitzel, U., Venema, H., Uffmann, M., & Prokop, M. (2008). Digital chest radiography: an update on modern technology, dose containment and control of image quality. *European Radiology*, 18(9), 1818–1830. <https://doi.org/10.1007/s00330-008-0948-3>
- Schaly, B., Varchena, V., Au, P., & Pang, G. (2009). Evaluation of an anthropomorphic male pelvic phantom for image-guided radiotherapy. *Reports in Medical Imaging*, (January), 69–78. Retrieved from <http://www.dovepress.com/getfile.php?fileID=5090>
- Schettini, M., Maia, M., & Campos, T. (2007). The development of an anthropomorphic and anthropometric thorax female phantom for experimental radiodosimetry. *International Journal of Low Radiation*, 4(2), 124. <https://doi.org/10.1504/IJLR.2007.015437>
- Schneider, K. (1995). Evolution of Quality Assurance in Paediatric Radiology. *Radiation Protection Dosimetry*, 57(1–4), 119–123. <https://doi.org/10.1093/oxfordjournals.rpd.a082507>
- Schueler, B. A. (1998). Clinical applications of basic x-ray physics principles. *Radiographics : A Review Publication of the Radiological Society of North America, Inc*, 18(3), 731–744; quiz 729. <https://doi.org/10.1148/radiographics.17.5.9308113>
- Seeram, E., & Brennan, P. (2006). Diagnostic Reference Levels In Radiology. *Radiologica Technology*, 77, 373–384.
- Seeram, E., Davidson, R., Bushong, S., & Swan, H. (2013). Radiation dose optimization research: Exposure technique approaches in CR imaging - A literature review. *Radiography*, 19(4), 331–338. <https://doi.org/10.1016/j.radi.2013.07.005>
- Seeram, E., Davidson, R., Bushong, S., & Swan, H. (2014). Image Quality Assessment Tools for Radiation Dose Optimization in Digital Radiography: An Overview. *Radiologic Technology*, 85(5), 555–562. Retrieved from <http://www.radiologicstechnology.org/content/85/5/555.short>
- Seggern, H. von. (1999). Photostimulable X-ray storage phosphors: a review of present understanding. *Brazilian Journal of Physics*, 29(2), 254–268. <https://doi.org/10.1590/S0103-97331999000200008>
- Seibert, J. A. (2004). Tradeoffs between image quality and dose. *Pediatric Radiology*, 34(SUPPL. 3), 183–195. <https://doi.org/10.1007/s00247-004-1268-7>
- Seibert, J. A., & Morin, R. L. (2011). The standardized exposure index for digital radiography: An opportunity for optimization of radiation dose to the pediatric population. *Pediatric Radiology*, 41(5), 573–581. <https://doi.org/10.1007/s00247-010-1954-6>
- Sekaran, U., & Bougie, R. (2016). *Research methods for business: A skill building approach*. Wiley (7th Edditi). John Wiley & Sons Ltd.
- Shah, ., Jones, A., & Willis, C. (2008). Consequences of modern anthropometric dimensions for radiographic techniques and patient radiation exposures. *Medical Physics*, 35(8), 3616–3625. <https://doi.org/10.1118/1.2952361>

- Sheridan, N., & McNulty, J. P. (2016). Computed radiography versus indirect digital radiography for the detection of glass soft-tissue foreign bodies. *Radiography*, 22(3), 223–227. <https://doi.org/10.1016/j.radi.2016.02.003>
- Shet, N., Chen, J., & Siegel, E. L. (2011). Continuing challenges in defining image quality. *Pediatric Radiology*, 41(5), 582–587. <https://doi.org/10.1007/s00247-011-2028-0>
- Shonka, F.R. ; Rose, J.E. ; Failla, G. (1958). CONDUCTING PLASTIC EQUIVALENT TO TISSUE, AIR, AND POLYSTYRENE. *Progress in Nuclear Energy*.
- Singh, M., Riggs, B. L., Beabout, J. W., & Jowsey, J. (1972). Femoral Trabecular-Pattern Index for Evaluation of Spinal Osteoporosis. *Annals of Internal Medicine*, 77(1), 63–67. <https://doi.org/10.7326/0003-4819-77-1-63>
- Singh, V. P., Badiger, N. M., & Kucuk, N. (2014). Determination of Effective Atomic Numbers Using Different Methods for Some Low- Z Materials. *Journal of Nuclear Chemistry*, 2014, 1–7. <https://doi.org/10.1155/2014/725629>
- Sj, J., Kuhl, H., Hons, L. A., Hons, X. G., Hons, P. R., & Hons, P. (2015). Optimum tube voltage for pelvic direct radiography : a phantom study. *The South African Radiographer*, 53(2), 15–19.
- Smedby, Ö., & Fredrikson, M. (2010). Visual grading regression: Analysing data from visual grading experiments with regression models. *British Journal of Radiology*, 83(993), 767–775. <https://doi.org/10.1259/bjr/35254923>
- Smith, N. B., & Webb, A. (2010). *Introduction to Medical Imaging: Physics, Engineering and Clinical Applications*. Cambridge University Press.
- Solomon, J., Ba, A., Bochud, F., & Samei, E. (2016). Comparison of low-contrast detectability between two CT reconstruction algorithms using voxel-based 3D printed textured phantoms. *Medical Physics*, 43(12), 6497–6506. <https://doi.org/10.1118/1.4967478>
- Spahn, M. (2005). Flat detectors and their clinical applications. *European Radiology*, 15(9), 1934–1947. <https://doi.org/10.1007/s00330-005-2734-9>
- Spector, P. E. (1992). *Summated Rating Scale Construction: An Introduction*. Sage Publications, Inc.
- Stieve, F. E. (1989). Radiological requirements for the specification of image quality criteria. *Optimization of Image Quality and Patient Exposure in Diagnostic Radiology, BIR Report*, 20, 221–238.
- Studenmund, A. H., & Cassidy, H. J. (1987). *Using Econometrics: A Practical Guide*. Boston: Little Brown.
- Suess, C., Kalender, W. A., & Coman, J. M. (1999). New low-contrast resolution phantoms for computed tomography. *Medical Physics*, 26(2), 296–302. <https://doi.org/10.1118/1.598516>
- Sun, Z., Lin, C., Tyan, Y., & Ng, K.-H. (2012). Optimization of chest radiographic imaging parameters: a comparison of image quality and entrance skin dose for digital chest radiography systems. *Clinical Imaging*, 36(4), 279–286. <https://doi.org/10.1016/j.clinimag.2011.09.006>
- Sund, P., Båth, M., Kheddache, S., & Månsson, L. G. (2004). Comparison of visual grading

- analysis and determination of detective quantum efficiency for evaluating system performance in digital chest radiography. *European Radiology*, 14(1), 48–58.
- Sund, P., Herrmann, C., Tingberg, A., Kheddache, S., Månsson, L. G., Almén, A., & Mattsson, S. (2000). Comparison of two methods for evaluating image quality of chest radiographs. *Proceedings of SPIE*, 3981(April), 251–257.
- Tavakol, M., & Dennick, R. (2011). Making sense of Cronbach's alpha. *International Journal of Medical Education*, 2, 53–55. <https://doi.org/10.5116/ijme.4dfb.8dfd>
- Taylor, R. (1990). Interpretation of the Correlation Coefficient: A Basic Review. *Journal of Diagnostic Medical Sonography*, 6(1), 35–39. <https://doi.org/10.1177/875647939000600106>
- The National Imaging Board. (2009). *Delivering Quality Imaging Services for Children*.
- The Royal College of Radiologists. (2012). Picture archiving and communication systems (PACS) and guidelines on diagnostic display devices. *IT Guidance Documents*. Retrieved from [https://www.rcr.ac.uk/sites/default/files/docs/radiology/pdf/BFCR\(12\)16_PACS_DDD.pdf](https://www.rcr.ac.uk/sites/default/files/docs/radiology/pdf/BFCR(12)16_PACS_DDD.pdf)
- The Royal College of Radiologists. (2017). *RCR iRefer Guidelines: making the best use of clinical radiology, eighth edition*. London.
- Thijssen, M. A. O., & Bijkerk, K. R. (1998). MANUAL CONTRAST-DETAIL PHANTOM ARTINIS CDRAD type 2.0. *University Hospital Nijmegen, St. Radboud, The Netherlands*, 1–18.
- Thompson, J. D. (2014). *The role of the free-response receiver operating characteristic method for dose and image quality optimisation*. University of Salford.
- Thorsen, J. B. B., Precht, H., Steen, T., Hellfritsch, M. B., Aagesen, H., Lindequist, S., ... Rasmussen, L. (2015). Software Optimization on multi-frequency imaging software of pediatric pelvic DR lowdose examinations, 1–10. <https://doi.org/10.1594/ecr2015/C-1238>
- Tingberg, A. (2000). *Quantifying the quality of medical x-ray images. An evaluation based on normal anatomy for lumbar spine and chest radiography*. Lund University, Lund.
- Tingberg, A., Herrmann, C., Lanhede, B., Almen, A., Besjakov, J., Mattsson, S., & Sund, P. (2000). Comparison of two methods for evaluation of image quality of lumbar spine radiographs. *Radiation Protection Dosimetry*, 90(Nos 1–2), 165–168.
- Tingberg, A., Herrmann, C., Lanhede, B., Almén, A., Sandborg, M., McVey, G., ... Zankl, M. (2004). Influence of the characteristic curve on the clinical image quality of lumbar spine and chest radiographs. *The British Journal of Radiology*, 77(915), 204–215. <https://doi.org/10.1259/bjr/22642890>
- Tucker, D. M., Souto, M., & Barnes, G. T. (1993). Scatter in computed radiography. *Radiology*, 188(1), 271–274. <https://doi.org/10.1148/radiology.188.1.8511311>
- Tugwell, J., England, A., & Hogg, P. (2017). Antero-posterior (AP) pelvis x-ray imaging on a trolley: Impact of trolley design, mattress design and radiographer practice on image quality and radiation dose. *Radiography*, 23(3), 242–248. <https://doi.org/10.1016/j.radi.2017.04.002>

- Tugwell, J., Everton, C., Kingma, A., Oomkens, D. M., Pereira, G. A., Pimentinha, D. B., ... Hogg, P. (2014). Increasing source to image distance for AP pelvis imaging - Impact on radiation dose and image quality. *Radiography*, 20(4), 351–355. <https://doi.org/10.1016/j.radi.2014.05.012>
- Tung, C. J., Tsai, H. Y., Shi, M. Y., Huang, T. T., Yang, C. H., & Chen, I. J. (2007). A phantom study of image quality versus radiation dose for digital radiography. *Nuclear Instruments and Methods in Physics Research, Section A: Accelerators, Spectrometers, Detectors and Associated Equipment*, 580(1 SPEC. ISS.), 602–605. <https://doi.org/10.1016/j.nima.2007.05.232>
- Tuomi, J., Paloheimo, K. S., Vehviläinen, J., Björkstrand, R., Salmi, M., Huutilainen, E., ... Mäkitie, A. (2014). A Novel Classification and Online Platform for Planning and Documentation of Medical Applications of Additive Manufacturing. *Surgical Innovation*, 21(6), 553–559. <https://doi.org/10.1177/1553350614524838>
- Uffmann, M., Neitzel, U., Prokop, M., Kabalan, N., Weber, M., Herold, C., & Schaefer-Prokop, C. (2005). Flat-panel-detector chest radiography: effect of tube voltage on image quality. *Radiology*, 235(2), 642–650. <https://doi.org/10.1148/radiol.2352031730>
- Uffmann, M., & Schaefer-Prokop, C. (2009). Digital radiography: The balance between image quality and required radiation dose. *European Journal of Radiology*, 72(2), 202–208. <https://doi.org/10.1016/j.ejrad.2009.05.060>
- Ullman, G. (2008). *Quantifying image quality in diagnostic radiology using simulation of the imaging system and model observers*. Linköping University, Sweden.
- Ullman, G., Sandborg, M., Tingberg, A., Dance, D. R., Hunt, R., & Carlsson, G. A. (2004). Comparison of Clinical and Physical Measures of Image Quality in Chest PA and Pelvis AP Views at Varying Tube Voltages. *Isrn*, 98, 1102–1799.
- Valentin, J. (2004). *Managing patient dose in digital radiology*. *Annals of the ICRP* (Vol. 64). <https://doi.org/10.1016/j.icrp.2004.02.001>
- Vano, E. (2005). ICRP recommendations on ‘Managing patient dose in digital radiology.’ *Radiation Protection Dosimetry*, 114(1–3), 126–130. <https://doi.org/10.1093/rpd/nch533>
- Vaño, E., Fernández, J. M., Ten, J. I., Prieto, C., González, L., Rodríguez, R., & de Las Heras, H. (2007). Transition from Screen-Film to Digital Radiography: Evolution of Patient Radiation Doses at Projection Radiography. *Radiology*, 243(2), 461–466. <https://doi.org/10.1148/radiol.2432050930>
- Vano, E., Martinez, D., Fernandez, J., Ordiales, J., Prieto, C., Floriano, A., & Ten, J. (2008). Paediatric entrance doses from exposure index in computed radiography. *Physics in Medicine and Biology*, 53(12), 3365–3380. <https://doi.org/10.1088/0031-9155/53/12/020>
- Varchena, V. (2002). Pediatric phantoms. *Pediatric Radiology*, 32(4), 280–284. <https://doi.org/10.1007/s00247-002-0681-z>
- Varchenya, V., Gubatova, D., Sidorin, V., & Kalnitsky, S. (1993). Children’s Heterogeneous Phantoms and Their Application in Röntgenology. *Radiation Protection Dosimetry*, 49(1–3), 77–78. <https://doi.org/10.1093/rpd/49.1-3.77>
- Vassileva, J. (2002). A phantom for dose-image quality optimization in chest radiography. *British Journal of Radiology*, 75(898), 837–842. <https://doi.org/10.1259/bjr.75.898.750837>

- Veldkamp, W. J. H., Kroft, L. J. M., Boot, M. V., Mertens, B. J. A., & Geleijns, J. (2006). Contrast-detail evaluation and dose assessment of eight digital chest radiography systems in clinical practice. *European Radiology*, *16*(2), 333–341. <https://doi.org/10.1007/s00330-005-2887-6>
- Vergara, J., Romero, A., Fernandez, C., Gomez, S., Vazquez, J., & Olivares, M. (1999). Dose Measurements in a Phantom Simulating Neonates by Using Different TL Materials: LiF:Mg,Cu,P and LiF:Mg,Ti. *Radiation Protection Dosimetry*, *85*(1), 345–348. <https://doi.org/10.1093/oxfordjournals.rpd.a032867>
- Waite, B. L., & Krabak, B. J. (2008). Examination and Treatment of Pediatric Injuries of the Hip and Pelvis. *Physical Medicine and Rehabilitation Clinics of North America*, *19*(2), 305–318. <https://doi.org/10.1016/j.pmr.2007.12.005>
- Waran, V., Narayanan, V., Karuppiah, R., Owen, S., & Aziz, T. (2014). Utility of multimaterial 3D printers in creating models with pathological entities to enhance the training experience of neurosurgeons. *Journal of Neurosurgery*, *120*(2), 489–492. <https://doi.org/10.3171/2013.11.JNS131066>
- Watanabe, Y., & Constantinou, C. (2006). Phantom Materials in Radiology. In *Encyclopedia of Medical Devices and Instrumentation* (pp. 252–269). Hoboken, NJ, USA: John Wiley & Sons, Inc. <https://doi.org/10.1002/0471732877.emd201>
- Welton, K. L., Jesse, M. K., Kraeutler, M. J., Garabekyan, T., & Mei-Dan, O. (2018). The Anteroposterior Pelvic Radiograph. *The Journal of Bone and Joint Surgery*, *100*(1), 76–85. <https://doi.org/10.2106/JBJS.17.00500>
- White, D. (1974). *The formulation of substitute materials with predetermined characteristics of radiation absorption and scattering*. Queen Mary, University of London.
- White, D. (1978). Tissue substitutes in experimental radiation physics. *Medical Physics*, *5*(6), 467–479. <https://doi.org/10.1118/1.594456>
- White, D., Buckland-Wright, J., Griffith, R., Rothenberg, L., Showwalter, C., Williams, G., ... Zankl, M. (1992a). 3. Selection Requirements for Phantoms. *Journal of the International Commission on Radiation Units and Measurements*, *os25*(1), 16–20. <https://doi.org/10.1093/jicru/os25.1.16>
- White, D., Buckland-Wright, J., Griffith, R., Rothenberg, L., Showwalter, C., Williams, G., ... Zankl, M. (1992b). 5. Phantoms in Diagnostic Procedures. *Journal of the International Commission on Radiation Units and Measurements*, *os25*(1), 26–30. <https://doi.org/10.1093/jicru/os25.1.26>
- White, D., & Constantinou, C. (1982). Anthropomorphic Phantom Materials. In *Progress in Medical Radiation Physics* (Vol. 1, pp. 133–193). Boston, MA: Springer US. https://doi.org/10.1007/978-1-4615-7691-4_3
- White, D., Constantinou, C., & Martin, R. (1986). Foamed epoxy resin-based lung substitutes. *The British Journal of Radiology*, *59*(704), 787–790. <https://doi.org/10.1259/0007-1285-59-704-787>
- White, D., Widdowson, E., Woodard, H., & Dickerson, J. (1991). The composition of body tissues. (II) Fetus to young adult. *British Journal of Radiology*. <https://doi.org/10.1259/0007-1285-64-758-149>
- Willis, C. E. (2009). Optimizing digital radiography of children. *European Journal of*

Radiology, 72(2), 266–273. <https://doi.org/10.1016/j.ejrad.2009.03.003>

- Wimpenny, D. I., Pandey, P. M., & Kumar, L. J. (2017). *Advances in 3D Printing & Additive Manufacturing Technologies*. (D. I. Wimpenny, P. M. Pandey, & L. J. Kumar, Eds.), *Advances in 3D Printing & Additive Manufacturing Technologies*. Singapore: Springer Singapore. <https://doi.org/10.1007/978-981-10-0812-2>
- Winslow, J. F., Hyer, D. E., Fisher, R. F., Tien, C. J., & Hintenlang, D. E. (2009). Construction of anthropomorphic phantoms for use in dosimetry studies. *Journal of Applied Clinical Medical Physics*, 10(3), 195–204. <https://doi.org/10.1120/jacmp.v10i3.2986>
- Wits, W. W., Carmignato, S., Zanini, F., & Vaneker, T. H. J. (2016). Porosity testing methods for the quality assessment of selective laser melted parts. *CIRP Annals - Manufacturing Technology*, 65(1), 201–204. <https://doi.org/10.1016/j.cirp.2016.04.054>
- Yamaguchi, Y. (1994). Age-Dependent Effective Doses for External Photons. *Radiation Protection Dosimetry*, (June). Retrieved from <https://academic.oup.com/rpd/article-lookup/doi/10.1093/oxfordjournals.rpd.a082384>
- Yohannes, I., Kolditz, D., Langner, O., & Kalender, W. a. (2012). A formulation of tissue- and water-equivalent materials using the stoichiometric analysis method for CT-number calibration in radiotherapy treatment planning. *Physics in Medicine and Biology*, 57, 1173–1190. <https://doi.org/10.1088/0031-9155/57/5/1173>
- Zankl, M., Veit, R., Williams, G., Schneider, K., Fendel, H., Petoussi, N., & Drexler, G. (1988). The construction of computer tomographic phantoms and their application in radiology and radiation protection. *Radiation and Environmental Biophysics*, 27(2), 153–164. <https://doi.org/10.1007/BF01214605>
- Zarb, F., Rainford, L., & McEntee, M. F. (2010). Image quality assessment tools for optimization of CT images. *Radiography*, 16(2), 147–153. <https://doi.org/10.1016/j.radi.2009.10.002>
- Zhang, M., Liu, K., Niu, X., & Liu, X. (2013). A method to derive appropriate exposure parameters from target exposure index and patient thickness in pediatric digital radiography. *Pediatric Radiology*, 43(5), 568–574. <https://doi.org/10.1007/s00247-012-2555-3>
- Zur, O. P. (1937). Rontgenstrahlenbehandlung oberblachlich gelagerter Tumoren. *Strahlentherapie*, 59(189).

Appendices

Appendix (I)

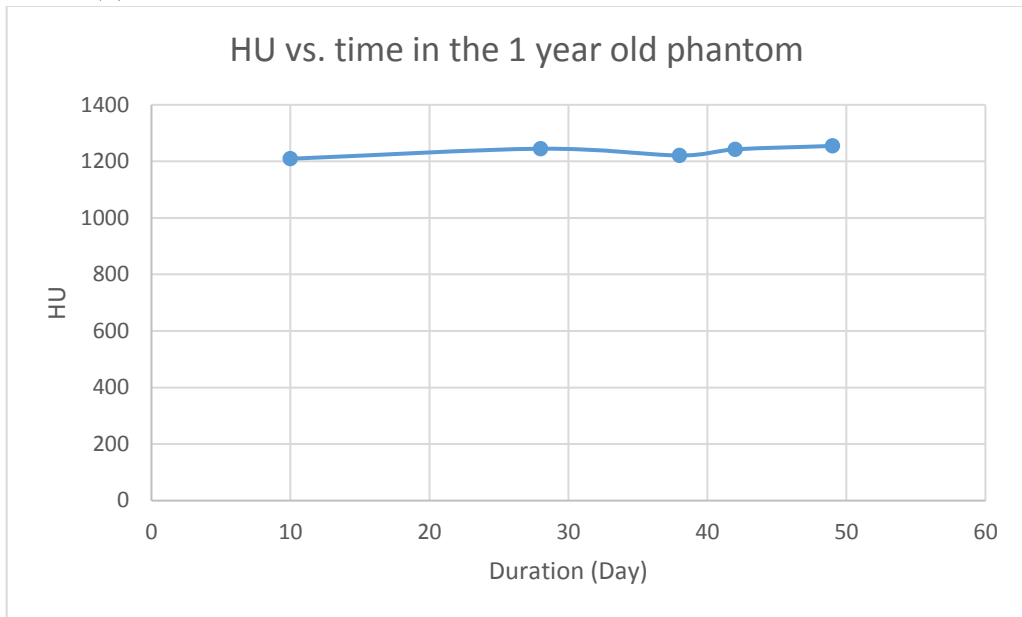


Figure (I-1): the stability of PoP in the 1 year old phantom.

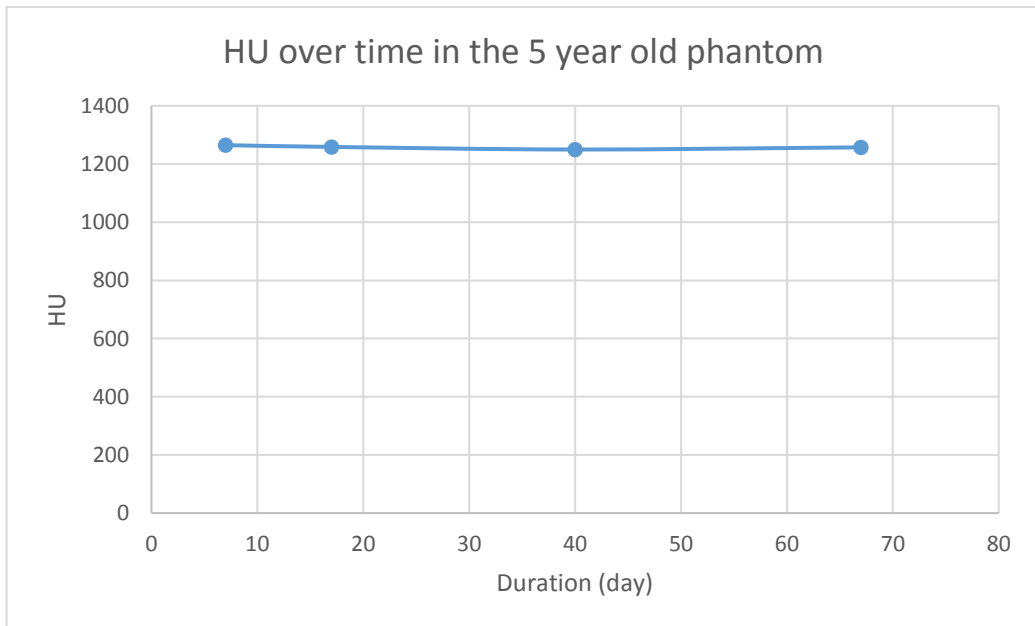


Figure (I-2): the stability of PoP in the 5 year old phantom.

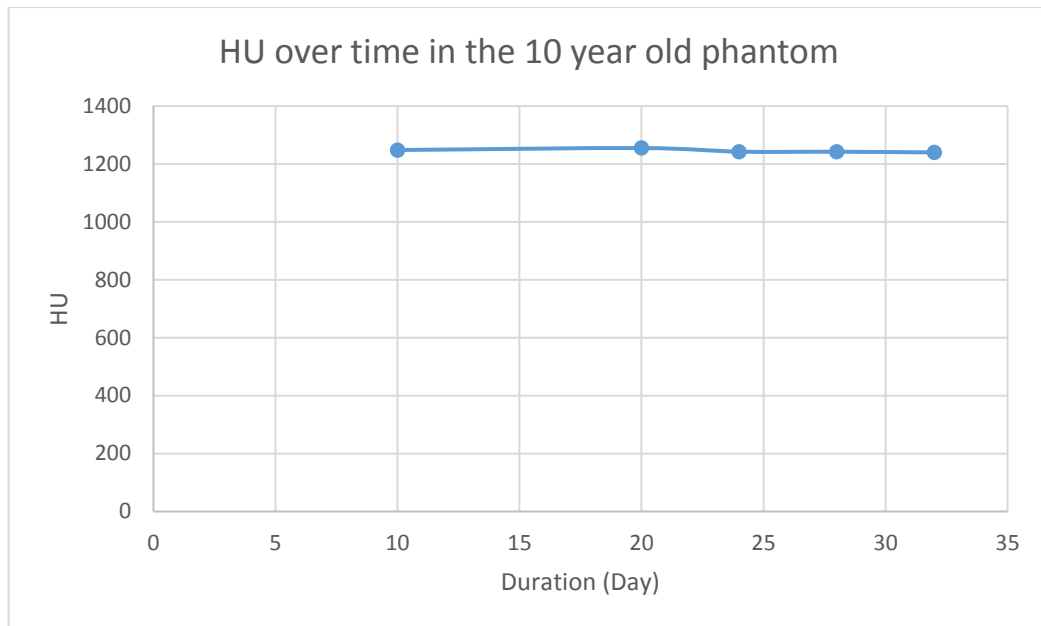


Figure (I-3): the stability of PoP in the 10 year old phantom.

Table (I-1): The HU measurements of cortical bone and soft tissue with their substitutes for 1 year old patient and phantom.

1 year old phantom							
	<u>Average HU (PoP)</u>						
Scan date	Femur	Pubis	AC	SIJ	IC	L5	Average
07-Jul-17	1222.4	1271.6	1233.1	1134.1	1175.0	1219.5	1209.32
	5	7	6	0	4	3	
21-Jul-17	1218.8	1448.4	1267.5	1114.6	1131.2	1287.0	1244.65
	9	8	1	9	3	8	
31-Jul-18	1224.2	1448.4	1261.7	1028.0	1083.1	1280.3	1221.01
	7	4	5	3	9	8	
04-Aug-17	1229.5	1429.2	1204.9	1138.4	1158.6	1293.8	1242.45
	9	5	0	5	6	7	
11-Aug-17	1229.7	1459.3	1199.9	1165.0	1157.4	1315.8	1254.58
	9	5	7	1	8	8	
	<u>HU (PMMA)</u>						Average
	101.5	71.28	66.08	90.3	74.92	82.11	90.53
	54.32	76.37	128.66	66.37	63.52	106.21	
	95.73	106.52	99.13	96.54	97.22	100.05	
	120.73	115.99	62.78	121.43	107.6	67.42	

1 year old real patient							
<u>Average HU (cortical bone)</u>							
	Femur	Pubis	AC	SIJ	IC		Average
	815.97	810.32	1222.8	810.51	957.15		923.36
			4				
<u>HU (soft tissues of 1 year old patient)</u>							Average
	70.67	63.91	69.96	34.92	56.98	60.76	66.53
	67.53	66.24	57.24	82.49	82.72	56.27	
	61.77	80.47	73.03	56.34	88.71		
	71.97	69.19	69.19	59.75	63.58		
SIJ: Sacrum-Ilium Joint, IC: Iliac crest, AC: Acetabulum							

Table (I-2): The HU measurements of cortical bone and soft tissue with their substitutes for 5 year old patient and phantom.

5 year old phantom							
<u>Average HU (PoP)</u>							
Scan date	Femur	Pubis	AC	SIJ	IC	L5	Average
11-Nov-16	1359.77	1309.83	1237.65	1213.34	1242.28	1225.75	1264.77
21-Nov-16	1319.37	1289.11	1237.76	1217.88	1268.89	1219.48	1258.75
14-Dec-16	1291.55	1267.06	1236.80	1211.26	1273.43	1218.98	1249.85
10-Jan-17	1306.01	1294.97	1254.03	1212.91	1246.79	1228.61	1257.22
<u>HU (PMMA)</u>							Average
	83.33	87.18	92.82	97.82			
	103.46	95.96	94.64				
5 year real patient							
<u>Average HU (cortical bone)</u>							
	Femur	Pubis	AC	SIJ	IC		Average
	1268.02	1300.85	1274.2	1142.4	1015.38		1200.16
<u>HU (soft tissues of 5 year old patient)</u>							Average
	68.5	83.38	73.12				74.01

	68.21	77.66	73.21				
SIJ: Sacrum-Ilium Joint, IC: Iliac crest, AC: Acetabulum							

Table (I-3): The HU measurements of cortical bone and soft tissue with their substitutes for 10 year-old patient and phantom.

10 year old phantom							
	<u>Average HU (PoP)</u>						
Scan date	Femur	Pubis	AC	SIJ	IC	L5	Average
21-Jul-17	1271.27	1229.83	1229.02	1232.10	1279.98	1246.47	1248.11
31-Jul-17	1318.00	1252.10	1239.44	1203.50	1287.76	1228.28	1254.85
04-Aug-17	1264.23	1267.74	1228.85	1233.53	1249.32	1210.54	1242.37
07-Aug-17	1281.09	1212.49	1219.30	1224.87	1293.46	1221.86	1242.18
11-Aug-17	1276.66	1215.19	1225.39	1191.62	1304.80	1224.93	1239.76
	<u>HU (PMMA)</u>						Average
	75.85	92.98	91.14	77.22	114.23		90.56
	100.96	122.81	80.99	84.85	78.66		
	64.98	77.17	90.96	88.12	99.92		
	104.19	102.18	109.14	93.2	85.16		
	85.64	115.44	65.24	79.16	71.87		
	62.07	105.86	74.63	99.02	74.54		
	87.33	110.66	95.54	103.12	109.67		
	88.56	81.64	94.94	108.39	79.55		
	106.84	97.67	83.29	69.05			
10 year old real patient							
	<u>Average HU (cortical bone)</u>						
	Femur	Pubis	AC	SIJ	IC		Average
	1341.51	1326.67	1356.33	1295.90	1015.87		1267.26
	<u>HU (soft tissues of 5 year old patient)</u>						Average
	69.67	67.15	75.94	81.18	65.26		73.61
	71.24	72.69	77.1	76.23	71.56		

	65.65	76.73	77.83	70.14	72.63		
	65.68	75.26	78.93	73.23	75.07		
	86.68	73.57					
SIJ: Sacrum-Ilium Joint, IC: Iliac crest, AC: Acetabulum							

Table (I-4): Correlation between the adult and 5 year-old with 12 cm thickness phantoms.

<u>Correlation coefficient (Spearman's Rho) (5 year with adult)</u>									
Changing mAs					Changing kVp				
<u>kVp</u>	<u>PMM</u>	<u>P-</u>	<u>P-</u>	<u>P-</u>	<u>mAs</u>	<u>PMMA</u>	<u>P-</u>	<u>P-</u>	<u>P-value</u>
	<u>A</u>	<u>value</u>	<u>bone</u>	<u>value</u>			<u>value</u>	<u>bone</u>	
50	1.00	0.00	1.00	0.00	1	0.79	0.00	0.98	0.00
53	0.99	0.00	0.99	0.00	2	0.74	0.00	0.23	<u>0.37</u>
56	0.98	0.00	0.98	0.00	2.8	0.47	<u>0.05</u>	-0.13	<u>0.60</u>
59	0.99	0.00	0.99	0.00	4	0.23	<u>0.35</u>	-0.46	<u>0.06</u>
62	0.93	0.00	0.94	0.00	5	-0.04	<u>0.87</u>	-0.59	0.01
65	0.95	0.00	0.95	0.00	6.3	-0.15	<u>0.55</u>	-0.83	0.00
68	0.95	0.00	0.97	0.00	7.1	-0.26	<u>0.30</u>	-0.87	0.00
71	0.87	0.00	0.87	0.00	8	-0.28	<u>0.27</u>	-0.90	0.00
74	0.69	0.00	0.68	0.00	9	-0.28	<u>0.25</u>	-0.92	0.00
77	0.55	0.00	0.55	0.00	10	-0.33	<u>0.18</u>	-0.94	0.00
80	0.97	0.00	0.97	0.00	11	-0.50	0.03	-0.96	0.00
83	0.94	0.00	0.94	0.00	12.5	-0.52	0.03	-0.98	0.00
86	0.87	0.00	0.86	0.00	14	-0.52	0.03	-0.98	0.00
89	0.83	0.00	0.82	0.00	16	-0.74	0.00	-0.98	0.00
92	0.93	0.00	0.93	0.00	18	-0.71	0.00	-0.99	0.00
95	0.90	0.00	0.90	0.00	20	-0.80	0.00	-0.97	0.00
98	0.79	0.00	0.81	0.00					
101	0.90	0.00	0.87	0.00					
	<u>averag</u>		<u>averag</u>			<u>Average</u>		<u>Average</u>	
	<u>e</u>		<u>e</u>						
	0.89		0.89			-0.28		-0.76	
Only correlation coefficients with P<0.05 were included									

Table (I-5): Correlation between the adult and 5 year-old calibrated thickness (21 cm) phantoms.

<u>Correlation coefficient (Pearson) (5 year with adult)</u>									
<u>Correlation coefficient (Adult&5year)</u>									
Changing mAs					Changing kVp				
<u>kVp</u>	<u>PMM</u>	<u>P-</u>		<u>P-value</u>	<u>mA</u>		<u>P-</u>		<u>P-</u>
	<u>A</u>	<u>value</u>	<u>bone</u>		<u>s</u>	<u>PMMA</u>	<u>value</u>	<u>bone</u>	<u>value</u>
50	1.00	0.00	0.99	0.00	1	0.98	0.00	0.97	0.00
53	0.98	0.00	0.98	0.00	2	0.95	0.00	0.92	0.00
56	0.99	0.00	0.99	0.00	2.8	0.93	0.00	0.89	0.00
59	1.00	0.00	1.00	0.00	4	0.90	0.00	0.82	0.00
62	0.99	0.00	0.99	0.00	5	0.89	0.00	0.79	0.00
65	0.99	0.00	0.99	0.00	6.3	0.86	0.00	0.72	0.00
68	1.00	0.00	1.00	0.00	7.1	0.84	0.00	0.65	0.00
71	0.99	0.00	0.99	0.00	8	0.82	0.00	0.58	0.01
74	1.00	0.00	1.00	0.00	9	0.80	0.00	0.49	0.04
77	0.99	0.00	0.99	0.00	10	0.76	0.00	0.35	<u>0.15</u>
80	0.99	0.00	0.99	0.00	11	0.74	0.00	0.30	<u>0.23</u>
83	0.99	0.00	0.99	0.00	12.5	0.72	0.00	0.14	<u>0.59</u>
86	0.98	0.00	0.98	0.00	14	0.68	0.00	-0.41	<u>0.87</u>
89	0.96	0.00	0.95	0.00	16	0.65	0.00	-0.18	<u>0.48</u>
92	0.98	0.00	0.98	0.00	18	0.58	0.01	-0.45	<u>0.06</u>
95	0.97	0.00	0.97	0.00	20	0.39	<u>0.13</u>	-0.81	0.00
98	0.98	0.00	0.98	0.00		<u>average</u>		<u>average</u>	
101	0.98	0.00	0.98	0.00		0.81		0.60	
	<u>averag</u>		<u>averag</u>			<u>Average (1-8</u>	<u>Average (1-8</u>		
	<u>e</u>		<u>e</u>			<u>mAs)</u>	<u>mAs)</u>		
	0.99		0.99			0.90	0.79		
						Average (1-8 mAs): 0.85			
Only correlation coefficients with P<0.05 were included									

Table (I-6): Correlation between the adult and 1 year-old calibrated thickness (21 cm) phantoms.

<u>Correlation coefficient (1 year with adult)</u>									
<u>Changing mAs</u>					<u>Changing KVP</u>				
<u>KVp</u>	<u>PMMA</u>	<u>P-value</u>	<u>bone</u>	<u>P-value</u>	<u>mAs</u>	<u>PMMA</u>	<u>P-value</u>	<u>bone</u>	<u>P-value</u>
50	0.33	<u>0.32</u>	0.41	<u>0.21</u>	1	0.97	0.00	0.98	0.00
53	0.85	0.00	0.85	0.00	2	0.99	0.00	0.98	0.00
56	0.76	0.00	0.78	0.00	2.8	0.99	0.00	0.98	0.00
59	0.88	0.00	0.88	0.00	4	0.98	0.00	0.96	0.00
62	0.65	0.02	0.76	0.00	5	0.90	0.00	0.74	0.00
65	0.17	<u>0.57</u>	0.23	<u>0.43</u>	6.3	0.97	0.00	0.98	0.00
68	0.93	0.00	0.94	0.00	7.1	0.54	0.03	0.57	0.02
71	0.85	0.00	0.88	0.00	8	0.92	0.00	0.82	0.00
74	0.87	0.00	0.87	0.00	9	0.92	0.00	0.94	0.00
77	0.66	0.01	0.65	0.01	10	0.88	0.00	0.89	0.00
80	0.64	0.01	0.69	0.01	11	0.73	0.00	0.82	0.00
83	0.86	0.00	0.88	0.00	12.5	0.84	0.00	0.85	0.00
86	0.45	<u>0.11</u>	0.43	<u>0.12</u>	14	0.58	0.02	0.53	0.03
89	0.46	<u>0.10</u>	0.45	<u>0.11</u>	16	0.49	0.05	0.53	0.03
92	0.90	0.00	0.90	0.00					
95	0.51	0.06	0.53	0.05					
98	0.88	0.00	0.83	0.01					
	<u>Average (P<0.5)</u>		<u>Average (P<0.5)</u>			<u>Average (P<0.5)</u>		<u>Average (P<0.5)</u>	
	0.81		0.83			0.86		0.83	
Only correlation coefficients with P<0.05 were included									

Table (I-7): Correlation between the adult and 10 year old calibrated thickness (21 cm) phantoms.

<u>Correlation coefficient (10 year with adult)</u>									
<u>Changing mAs</u>					<u>Changing KVp</u>				
<u>KVp</u>	<u>PMMA</u>	<u>P-value</u>	<u>bone</u>	<u>P-value</u>	<u>mAs</u>	<u>PMMA</u>	<u>P-value</u>	<u>bone</u>	<u>P-value</u>
50	0.61	0.03	0.66	0.02	1	0.98	0.00	0.98	0.00
53	0.57	0.04	0.56	0.04	2	0.98	0.00	0.98	0.00
56	0.96	0.00	0.96	0.00	2.8	1.00	0.00	0.94	0.00
59	0.92	0.00	0.91	0.00	4	0.98	0.00	0.84	0.00
62	0.78	0.00	0.83	0.00	5	0.93	0.00	0.74	0.00
65	0.41	<u>0.11</u>	0.44	<u>0.09</u>	6.3	0.96	0.00	0.82	0.00
68	0.95	0.00	0.95	0.00	7.1	0.58	0.01	0.10	<u>0.70</u>
71	0.88	0.00	0.90	0.00	8	0.94	0.00	0.63	0.01
74	0.89	0.00	0.90	0.00	9	0.97	0.00	0.70	0.00
77	0.69	0.00	0.72	0.00	10	0.82	0.00	0.54	0.02
80	0.78	0.00	0.95	0.00	11	0.68	0.00	0.01	<u>0.97</u>
83	0.85	0.00	0.97	0.00	12.5	0.70	0.00	0.40	<u>0.10</u>
86	0.47	<u>0.06</u>	0.46	<u>0.07</u>	14	0.73	0.00	-0.07	<u>0.79</u>
89	0.67	0.01	0.67	0.00	16	0.47	<u>0.05</u>	-0.30	<u>0.22</u>
92	0.74	0.00	0.79	0.00	18	0.74	0.00	0.13	<u>0.62</u>
95	0.47	<u>0.06</u>	0.51	0.04	20	0.69	0.00	-0.24	<u>0.33</u>
98	0.70	0.00	0.73	0.00					
100	0.67	0.01	0.72	0.00					
	<u>Average (P<0.5)</u>		<u>Average (P<0.5)</u>			<u>Average (P<0.5)</u>		<u>Average (P<0.5)</u>	
	<u>0.78</u>		<u>0.80</u>			0.85		0.80	
Only correlation coefficients with P<0.05 were included									

Table (I-8): Face validity questions.

Development of a Paediatric (5 Years) AP Pelvis Phantom

Name _____

Year of Study _____

With reference to the X-ray image displayed on the monitor in front (5 year old child) of you please answer the following questions.

1. The appearances of the Hip Joints reflect those typically visualised on a paediatric AP pelvis image.				
Strongly agree	Agree	Neither agree / disagree	Disagree	Strongly disagree
2. The appearances of the Greater Trochanters <i>do not</i> reflect those typically visualised on a paediatric AP pelvis image.				
Strongly agree	Agree	Neither agree / disagree	Disagree	Strongly disagree
3. The appearances of the Lesser Trochanters reflect those typically visualised on a paediatric AP pelvis image.				
Strongly agree	Agree	Neither agree / disagree	Disagree	Strongly disagree
4. The appearances of the Iliac Crests <i>do not</i> reflect those typically visualised on a paediatric AP pelvis image.				
Strongly agree	Agree	Neither agree / disagree	Disagree	Strongly disagree
5. The appearances of the Pubic & Ischial Rami reflect those typically visualised on a paediatric AP pelvis image.				
Strongly agree	Agree	Neither agree / disagree	Disagree	Strongly disagree
6. The appearances of the Proximal Femora <i>do not</i> reflect those typically visualised on a paediatric AP pelvis image.				
Strongly agree	Agree	Neither agree / disagree	Disagree	Strongly disagree
7. The appearances of the Sacro-iliac Joints reflect those typically visualised on a paediatric AP pelvis image.				
Strongly agree	Agree	Neither agree / disagree	Disagree	Strongly disagree
8. The appearances of the Femoral Necks <i>do not</i> reflect those typically visualised on a paediatric AP pelvis image.				
Strongly agree	Agree	Neither agree / disagree	Disagree	Strongly disagree
9. The appearances of the Sacrum and its inter-vertebral foramina reflect those typically visualised on a paediatric AP pelvis image.				
Strongly agree	Agree	Neither agree / disagree	Disagree	Strongly disagree
10. The appearances of the bone / soft tissue interface <i>do not</i> reflect those typically visualised on a paediatric AP pelvis image.				
Strongly agree	Agree	Neither agree / disagree	Disagree	Strongly disagree
11. The appearances of the body of L5 reflect those typically visualised on a paediatric AP pelvis image.				

Strongly agree	Agree	Neither agree / disagree	Disagree	Strongly disagree
12. The appearances of the Obturator Foramina <i>do not</i> reflect those typically visualised on a paediatric AP pelvis image.				
Strongly agree	Agree	Neither agree / disagree	Disagree	Strongly disagree
13. The appearances of the Acetabula reflect those typically visualised on a paediatric AP pelvis image.				
Strongly agree	Agree	Neither agree / disagree	Disagree	Strongly disagree
14. The levels of rotation and tilting <i>do not</i> reflect those typically visualised on a paediatric AP pelvis image.				
Strongly agree	Agree	Neither agree / disagree	Disagree	Strongly disagree
15. This image will allow an assessment of image quality versus the selection of exposure factors (optimisation) .				
Strongly agree	Agree	Neither agree / disagree	Disagree	Strongly disagree

Table (I-9): modified image quality scale of 1 year old phantom.

1. The appearances of the Hip Joints are.....				
Much better	better	same	worse	Much worse
2. The appearances of the Lesser Trochanters are.....				
Much better	better	same	worse	Much worse
3. The appearances of the Iliac Crests are.....				
Much better	better	same	worse	Much worse
4. The appearances of the Proximal Femora are.....				
Much better	better	same	worse	Much worse
5. The appearances of the Sacrum and its inter-vertebral foramina are.....				

Much better	better	same	worse	Much worse
6. The appearances of the body of L5 are.....				
Much better	better	same	worse	Much worse
7. The appearances of the Acetabula are.....				
Much better	better	same	worse	Much worse
8. The levels of rotation and tilting are.....				
Much better	better	same	worse	Much worse

Table (I-10): modified image quality scale of 5 year old phantom.

1. The appearances of the Hip Joints are.....				
Much better	better	same	worse	Much worse
2. The appearances of the Pubic & Ischial Rami are.....				
Much better	better	same	worse	Much worse
3. The appearances of the Sacro-iliac Joints are.....				
Much better	better	same	worse	Much worse
4. The appearances of the Femoral Necks are.....				
Much better	better	same	worse	Much worse
5. The appearances of the Sacrum and its inter-vertebral foramina are.....				
Much better	better	same	worse	Much worse

6. The appearances of the body of L5 are.....				
Much better	better	same	worse	Much worse
7. The appearances of the Acetabula are.....				
Much better	better	same	worse	Much worse

Table (I-11): modified image quality scale of 10 year old phantom.

1. The appearances of the Hip Joints are.....				
Much better	better	same	worse	Much worse
2. The appearances of the Pubic & Ischial Rami are.....				
Much better	better	same	worse	Much worse
3. The appearances of the Proximal Femora are.....				
Much better	better	same	worse	Much worse
4. The appearances of the Sacro-iliac Joints are.....				
Much better	better	same	worse	Much worse
5. The appearances of the Sacrum and its inter-vertebral foramina are.....				
Much better	better	same	worse	Much worse
6. The appearances of the Obturator Foramina are.....				

Much better	better	same	worse	Much worse
7. The appearances of the Acetabula are.....				
Much better	better	same	worse	Much worse
8. The levels of rotation and tilting are.....				
Much better	better	same	worse	Much worse

Table (I-12): the answers of 1 year old questionnaire.

ID	Q1	Q2	Q3	Q4	Q5	Q6	Q7	Q8	Q9	Q10	Q11	Q12	Q13	Q14	Q15
1	1	-1	1	-2		0	1	2	0	-2	2	-1	0	-2	1
2	0	-1	-1	-1	0	1	-1	0	-1	1	0	1	0	-1	-1
3	1	-1	1	-1	1	-1	1	-1	1	-1	1	-1	1	-1	1
4	1	0	0	-1	-1	1	-1	1	-1	0	-1	-1	0	-1	-1
5	1	-1	1	1	1	1	-1	-1	-1	1	-1	0	0	1	-2
6	0	0	0	-1	0	-1	1	0	1	0	1	0	0	0	0
7	1	1	1	1	1	1	1	-1	0	2	-1	1	1	1	2
8	1	1	-1	-1	1	1	-1	-1	0	1	0	0	1	1	2
9	1	2	-1	1	0	-1	1	1	2	-1	0	-1	-1	0	1
10	1	2	-1	1	0	-1	1	1	1	2	-1	0	-1	-1	1
11	1	2	-1	1	0	-1	1	1	1	2	-1	0	-1	-1	1
12	1	-1	1	0	0	-1	0	-1	0	1	0	0	0	0	0
13	2	-1	-1	-2	-1	0	-1	0	0	-1	0	0	1	0	0
14	2	-1	-1	-2	-1	0	-1	0	0	-1	0	1	1	1	0
15	1	1	1	-1	2	-1	-1	1	1	1	-1	2	-1	1	-1
16	1	-1	1	-1	1	-1	1	1	1	1	1	1	-1	-1	1
17	1	0	1	-1	-1	1	-1	1	-1	1	1	-1	-1	-1	1
18	1	0	1	-1	-1	-1	-1	1	1	1	1	0	-1	-1	1
19	1	0	1	-1	-1	-1	-1	1	1	1	1	0	-1	-1	1
20	0	-1	1	-1	0	-1	1	-1	1	0	1	-1	1	0	1

21	1	0	1	-1	-1	-1	1	-1	0	1	1	1	1	0	-1
22	2	1	1	1	1	2	1	1	1	0	1	1	1	1	1
23	1	0	1	-1	1	0	1	1	1	0	0	0	1	-1	1
24	1	1	-2	-1	1	1	0	-1	1	-2	0	-1	1	0	1
25	1	-1	1	-1	1	-1	1	0	1	-1	1	-1	1	1	1
26	1	-1	1	-1	-1	-1	1	-1	1	-1	1	1	1	-1	1
27	1	-1	-1	1	1	-1	-1	-1	1	1	1	-1	1	-1	1
28	1	1	1	-1	1	-1	1	1	1	1	1	-1	-1	-1	1
29	1	1	0	1	1	0	0	1	1	1	1	1	1	1	1
30	-1	0	0	1	-1	0	-2	0	-1	2	-2	1	0	0	0
31	-2	-2	1	1	-2	0	1	2	1	0	-2	-1	-2	-1	2
32	1	1	1	-1	-1	0	-1	-1	1	2	1	1	1	1	-1
33	1	1	1	1	0	2	2	1	0	1	2	-1	1	1	1
34	1	0	1	-1	0	1	1	-1	-1	0	-1	0	0	-1	1
mean	0.8		0.3	0.4	0.0	0.1	0.1		0.4						
	5	-0.03	2	1	6	2	5	-0.18	4	-0.41	0.24	0.00	0.15	0.21	0.56
SD	0.7		0.9	1.0	0.9	0.9	1.0		0.8						
	4	1.06	4	5	7	8	5	1.00	2	1.13	1.05	0.89	0.93	0.91	0.96
Average Q1-Q15	0.19														
2=strong positive, 1=Positive, 0=not decided, (-1)= Negative and (-2)= Strong Negative															

Table (I-13): the answers of 5 year old questionnaire.

ID	Q1	Q2	Q3	Q4	Q5	Q6	Q7	Q8	Q9	Q10	Q11	Q12	Q13	Q14	Q15
1	1	1	1	1	0	0	0	1	0	0	0	1	1	0	1
2	1	1	1	-1	-1	0	1	-1	1		1	0	2	1	2
3	1	0	0	-1	-1	1	0	0		0	1	0	-1	0	-1
4	1	1	0	1	1	1	0	0	0	-1	0	0	1	-1	1
5	1	1	2	-1	1	-1	1	-1	0	-1	1	0	1	0	1
6	1	1	1	-1	-1	1	1	-1	-2	1	1	0	1	1	2
7	-1	-1	0	-1	-1	-1	-1	-1	-1	1	1	1	-1	1	-1

8	-1	0	1	-1	-1	-1	-2	-1	-1	1	1	1	-1	1	-1
9	0	-1	0	0	1	-1	1	-1	-1	2	-1	1	-1	0	-1
10	1	-1	1	-1	0	-1	2	-1	1	-2	1	-1	0	-1	2
11	1	-1	1	1	1	-1	1	-1	1	-1	0	0	1	-1	1
12	2	2	1	1	2	1		2	1	1	1	2	1	1	2
13	2	-1	1	-2	1	-1	0	-1	1	-1	-1	0	2	-1	2
14	1	-1	1	-1	1	-1	1	-1	1	1	1	-1	1	-1	1
15	1	-1	1	-1	1	1	0	-1	1	-1	-1	-1	1	0	1
16	1	-1	2	-1	1	-1	2	-2	1	-2	1	-1	1	-1	1
17	1	1	0	0	1	-1	1	-1	0	1	1	-1	1	-1	0
18	1	-1	1	-1	1	-1	0	0	1		1	-1	0	0	0
19	1	0	1	0	1	-1	0	-1	1	1	1	1	1	1	1
20	1	1	1	-1	0	0	0	0	1	-1	1	-1	1	0	1
21	1	0	1	1	0	0		1	0	0	1	-1	1	-1	1
22	0	0	-1		-1	1	0	0	1	0	-1	0	0		1
23	1	-1	1	-1	1	-1	2	-2	1	-1	2	-2	1	-2	2
24	1	0	1	2	2	2	1	1	0	1	2	1	1	-1	1
25	1	1	1	-1	1	-1	1	0	1	0	1	-1		-1	1
26	1	-2	0	-1	1	-1	1	-1	2	-1	1	-1	1	-1	0
27	1	0	1	0	1	0	1	0	1	0	1	0	1	0	1
28	1	1	1	0	1	0	-1	1	1	1	1	1	0	-1	1
29	1	-1	1	-1	1	-1	1	-1	1	-1	1	-1	1	-1	1
30	1	1	2	-1	1	-1	2	-2		1	2	0	1	-2	2
31	1	1	1	1		-1	-1		1	1	1	1	1	1	1
32	1	-1	1	-1	1	-1	1	-1	1	-1	1	-1	1	-1	0
Mean	0.8	0.0		0.3	0.5	0.3			0.5	0.0			0.6		0.8
	8	3	0.84	9	5	4	0.53	0.52	3	3	0.75	0.13	8	0.35	4
SD	0.6	1.0		0.9	0.8	0.9			0.8	1.0			0.7		0.9
	1	0	0.63	5	9	0	0.97	0.96	6	7	0.80	0.94	9	0.91	2
Average Q1-Q15	0.50														

2=strong positive, 1=Positive, 0=not decided, (-1)= Negative and (-2)= Strong Negative

Table (I-14): the answers of 10 year old questionnaire.

ID	Q1	Q2	Q3	Q4	Q5	Q6	Q7	Q8	Q9	Q10	Q11	Q12	Q13	Q14	Q15
1	1	0	1	2	1	0	1	1	0	2	2	0	1	1	1
2	-1	1	1	1	2	-1	-1	-1	1	2	1	1	1	1	-1
3	-1	1	-1	1	-1	1	-1	1	1	1	-1	-1	-1	-1	-1
4	2	1	1	-1	0	1	1	-1	0	-1	0	-1	1	1	1
5	1	1	-1	2	-1	0	1	1	1	0	-1	0	0	-1	-1
6	1	-1		0	1	-1	1	-1	1	2	1	-1	1	0	1
7	1	1	1	-1	1	0	0	0	0	1	0	-1	-1	-1	-1
8	-1	1	-1	1	1	0	0	-1	1	1	-1	-1	-1	0	-1
9	1	1	-1	-1	1	-1	-1	-1	1	1	1	0	-1	0	0
10	1	-1	-2	-2	2	-2	1	-2	2	-1	2	-2	2	-2	2
11	-1	-1	-1	1	1	0	-1	-1	1	1	-2	1	1	-2	2
12	0	1	-1	1	0	-1	-1	-1	-1	0	-1	-1	-1	0	-1
13	-1	0	0	1	1	-1	1	1	-2	1	0	2	-1	0	1
14	-1	0	0	2	2	-1	1	1	-1	1	0	2	-1	0	1
15	1	0	1	1	1	0	1	0	-1	0	-1	0	-1	0	1
35	1	1	0	0	1	0	1	1	1	1	0	-1	-1	0	1
36	1	0	1	-1	1	0	-1	-1	0	1	1	1	0	-1	0
37	1	1	0	1	0	0	1	1	0	0	1	-1	0	0	1
38	1	1	0	-1	1	-1	0	-1	1	-1	0	0	1	0	-1
39	1	0	-1	-2	1	1	1	0	1	1	-1	-1	1	-1	1
40	1	-1	-1	1	1	0	-1	-1	1	1	-1	1	1	1	1
41	1	-1	-1	1	1	0	-1	-1	1	1	-1	1	1	1	1
42	1	-1	0	1	2	0	1	-1	1	2	-1	0	2	-1	1
43	1	2	1	-1	-1	1	1	1	1	2	1	-1	1	2	2
44	0	0	0	-1	1	-1	1	1	-1	1	-1	-1	1	0	0
45	1	1	0	1	-1	1	0	1	1	2	1	0	1	1	2
46	0	1	0	0	1	1	0	1	1	1	1	0	1	1	2

Mean	0.39	-0.24	-0.16	-0.02	0.78	0.13	0.15	0.04	0.46	-0.46	0.02	0.18	0.22	0.22	0.57
SD	0.95	0.96	0.85	1.18	0.79	0.86	0.97	0.97	0.94	1.13	1.01	0.98	1.07	1.01	0.96
Average Q1-Q15	0.15														
2=strong positive, 1=Positive, 0=not decided, (-1)= Negative and (-2)= Strong Negative															

Appendix (II)

Table (II-1): the visual image quality questions.

Question no	Sharpness
Q1	FEMORAL HEADS - SHARPNESS. The sharpness of the superior edge of the LEFT femur head is
Q3	FEMORAL EPIPHYSIS-SHARPNESS. The sharpness of the bony edges of the LEFT femoral epiphysis is
Q4	PUBIC BONES - SHARPNESS. The sharpness of the LEFT medial/superior edge of the pubis is
Q6	ISCHIUM - SHARPNESS. The sharpness of the LEFT medial/inferior edge of the ischium is
Q8	SACRO-ILIAC JOINTS - SHARPNESS. The sharpness of the LEFT edge of the sacro-iliac joint is
Q10	FEMORAL NECKS - SHARPNESS. The sharpness of the LEFT bony edge of the femoral neck is
Q12	SACRUM - SHARPNESS. The sharpness of the LEFT bony edge of the sacrum and its foramen is
Q14	L5 BODY - SHARPNESS. The sharpness of the bony edges of the L5 vertebral body is
Q16	ILIAC CRESTS - SHARPNESS. The sharpness of the LEFT superior bony edges of the iliac crests is
Q18	CHICKEN BONE - CORTEX. The sharpness of the inferior cortex of the chicken bone is
Q19	CHICKEN BONE - TRABECULAE. The sharpness of the internal trabecular pattern of the chicken bone is
	Visual Clarity (opposite meaning of noise)

Q2	FEMORAL HEADS - NOISE. The noise levels (graininess) over the LEFT femur head is
Q5	PUBIC BONES - NOISE. The noise levels (graininess) over the LEFT pubic bone is
Q7	ISCHIUM - NOISE. The noise levels (graininess) over the LEFT ischium is
Q9	SACRO-ILIAC JOINTS - NOISE. The noise levels (graininess) over the LEFT sacro-iliac joint is
Q11	FEMORAL NECKS - NOISE. The noise levels (graininess) over the LEFT femoral neck is
Q13	SACRUM - NOISE. The noise levels (graininess) over the sacrum is
Q15	L5 BODY - NOISE. The noise levels (graininess) over the L5 vertebral body is
Q17	ILIAC CRESTS - NOISE. The noise levels (graininess) over the LEFT superior component of the iliac crest is

Table (II-2): ICC between the researcher and the observers.

ICC (Sharpness)				ICC (Noise)			
<u>Observer no</u>	<u>Sharpness</u>	<u>Upper bound</u>	<u>Lower bound</u>	<u>Observer no</u>	<u>Noise</u>	<u>Upper bound</u>	<u>Lower bound</u>
1	0.911	0.823	0.95	1	0.965	0.928	0.981
2	0.827	0.731	0.889	2	0.93	0.874	0.959
3	0.937	0.886	0.963	3	0.971	0.947	0.983
4	0.919	0.871	0.949	4	0.948	0.919	0.967
5	0.924	0.882	0.951	5	0.951	0.924	0.969
Repeated random sample	0.757	0.477	0.87	Repeated random sample	0.847	0.69	0.915

Table (II-3): Normality test of all the parameters and the variables for 1, 5 and 10 year old.

Tests of Normality (1 year old)						
	Kolmogorov-Smirnov			Shapiro-Wilk		
	Statistic	df	Sig.	Statistic	df	Sig.
KVp	0.10	1318	0.00	0.94	1318	0.00
mAs	0.13	1318	0.00	0.93	1318	0.00
SID	0.17	1318	0.00	0.86	1318	0.00
Filteration	0.22	1318	0.00	0.79	1318	0.00
Dose	0.14	1318	0.00	0.84	1318	0.00
SNR	0.05	1318	0.00	0.98	1318	0.00
CNR	0.04	1318	0.00	0.99	1318	0.00
IQ (sharpness)	0.31	1318	0.00	0.70	1318	0.00
IQ (clarity)	0.25	1318	0.00	0.80	1318	0.00
IQ (sharpness & clarity)	0.21	1318	0.00	0.88	1318	0.00
Tests of Normality (5 year old)						
	Kolmogorov-Smirnov			Shapiro-Wilk		
	Statistic	df	Sig.	Statistic	df	Sig.
KVp	0.10	2007	0.00	0.94	2007	0.00
mAs	0.09	2007	0.00	0.95	2007	0.00
Filter	0.22	2007	0.00	0.79	2007	0.00
SID	0.17	2007	0.00	0.86	2007	0.00
Dose	0.14	2007	0.00	0.83	2007	0.00
SNR	0.09	2007	0.00	0.96	2007	0.00
CNR	0.03	2007	0.00	1.00	2007	0.00
IQ (sharpness)	0.36	2007	0.00	0.60	2007	0.00
IQ (clarity)	0.25	2007	0.00	0.77	2007	0.00
IQ (sharpness & clarity)	0.23	2007	0.00	0.86	2007	0.00
Tests of Normality (1 year old)						
	Kolmogorov-Smirnov			Shapiro-Wilk		

	Statistic	df	Sig.	Statistic	df	Sig.
				c		
KVp	0.10	132	0.00	0.94	132	0.00
SID	0.22	132	0.00	0.84	132	0.00
Filter	0.22	132	0.00	0.79	132	0.00
Dose	0.12	132	0.00	0.91	132	0.00
DAP	0.11	132	0.00	0.92	132	0.00
SNR	0.10	132	0.00	0.95	132	0.00
CNR	0.11	132	0.00	0.94	132	0.00
IQ (sharpness)	0.20	132	0.00	0.84	132	0.00
IQ (clarity)	0.31	132	0.00	0.78	132	0.00
IQ (sharpness & clarity)	0.11	132	0.00	0.95	132	0.00

Table (II-4): The correlation coefficients for 1 year old between all the parameters.

Spearman's rho correlation coefficient (r)						
	Dose	SNR	CNR	IQ (sharpness)	IQ (clarity)	IQ (sharpness and clarity)
KVp	0.48	0.57	0.28	-0.25	0.48	0.09
Sig. (2-tailed)	0.00	0.00	0.00	0.00	0.00	0.00
mAs	0.67	0.68	0.76	0.55	0.63	0.69
Sig. (2-tailed)	0.00	0.00	0.00	0.00	0.00	0.00
SID	-0.32	-0.24	-0.27	-0.22	-0.23	-0.26
Sig. (2-tailed)	0.00	0.00	0.00	0.00	0.00	0.00
Filtration	-0.36	-0.24	-0.38	-0.23	-0.22	-0.29
Sig. (2-tailed)	0.00	0.00	0.00	0.00	0.00	0.00
Dose	1.00	0.96	0.94	0.47	0.90	0.79
Sig. (2-tailed)		0.00	0.00	0.00	0.00	0.00
SNR	0.96	1.00	0.93	0.40	0.90	0.73
Sig. (2-tailed)	0.00		0.00	0.00	0.00	0.00
CNR	0.94	0.93	1.00	0.62	0.85	0.85
Sig. (2-tailed)	0.00	0.00		0.00	0.00	0.00
IQ (sharpness)	0.47	0.40	0.62	1.00	0.45	0.83

Sig. (2-tailed)	0.00	0.00	0.00		0.00	0.00
IQ (clarity)	0.90	0.90	0.85	0.45	1.00	0.83
Sig. (2-tailed)	0.00	0.00	0.00	0.00		0.00
IQ (sharpness and clarity)	0.79	0.73	0.85	0.83	0.83	1.00
Sig. (2-tailed)	0.00	0.00	0.00	0.00	0.00	

Table (II-5): The correlation coefficients for 5 year old between all the parameters.

Spearman's rho correlation coefficient (r)						
	Dose	SNR	CNR	IQ (sharpness)	IQ (clarity)	IQ (sharpness & clarity)
KVp	0.43	0.39	-0.19	0.05	0.41	0.23
Sig. (2-tailed)	0.00	0.00	0.00	0.04	0.00	0.00
mAs	0.73	0.73	0.75	0.63	0.70	0.72
Sig. (2-tailed)	0.00	0.00	0.00	0.00	0.00	0.00
SID	-0.33	-0.21	-0.17	-0.25	-0.19	-0.23
Sig. (2-tailed)	0.00	0.00	0.00	0.00	0.00	0.00
Filtration	-0.33	-0.25	-0.36	-0.15	-0.17	-0.18
Sig. (2-tailed)	0.00	0.00	0.00	0.00	0.00	0.00
Dose	1.00	0.92	0.68	0.67	0.88	0.83
Sig. (2-tailed)		0.00	0.00	0.00	0.00	0.00
SNR	0.92	1.00	0.77	0.69	0.86	0.84
Sig. (2-tailed)	0.00		0.00	0.00	0.00	0.00
CNR	0.68	0.77	1.00	0.68	0.60	0.69
Sig. (2-tailed)	0.00	0.00		0.00	0.00	0.00
IQ (sharpness)	0.67	0.69	0.68	1.00	0.71	0.89
Sig. (2-tailed)	0.00	0.00	0.00		0.00	0.00
IQ (clarity)	0.88	0.86	0.60	0.71	1.00	0.92
Sig. (2-tailed)	0.00	0.00	0.00	0.00		0.00
IQ (sharpness & clarity)	0.83	0.84	0.69	0.89	0.92	1.00
Sig. (2-tailed)	0.00	0.00	0.00	0.00	0.00	

Table (II-6): The correlation coefficient for 10 year old (at orientation HA and two outer ionisation chambers).

Spearman's rho correlation coefficient (r)							
	Dose	DAP	SNR	CNR	IQ (sharpness)	IQ (clarity)	IQ (sharpness & clarity)
KVp	-0.90	-0.93	-0.68	-0.83	-0.86	-0.71	-0.89
Sig. (2-tailed)	0.00	0.00	0.00	0.00	0.00	0.00	0.00
SID	0.07	-0.09	0.68	0.49	0.15	-0.14	0.09
Sig. (2-tailed)	0.41	0.30	0.00	0.00	0.09	0.12	0.33
Filtration	0.41	-0.35	0.04	0.05	-0.06	0.06	-0.03
Sig. (2-tailed)	0.00	0.00	0.62	0.53	0.53	0.53	0.72
Dose	1.00	0.99	0.53	0.71	0.80	0.62	0.81
Sig. (2-tailed)		0.00	0.00	0.00	0.00	0.00	0.00
DAP	0.99	1.00	0.55	0.74	0.81	0.65	0.83
Sig. (2-tailed)	0.00		0.00	0.00	0.00	0.00	0.00
SNR	0.53	0.55	1.00	0.95	0.67	0.41	0.65
Sig. (2-tailed)	0.00	0.00		0.00	0.00	0.00	0.00
CNR	0.71	0.74	0.95	1.00	0.78	0.53	0.77
Sig. (2-tailed)	0.00	0.00	0.00		0.00	0.00	0.00
IQ (sharpness)	0.80	0.81	0.67	0.78	1.00	0.65	0.95
Sig. (2-tailed)	0.00	0.00	0.00	0.00		0.00	0.00
IQ (clarity)	0.62	0.65	0.41	0.53	0.65	1.00	0.81
Sig. (2-tailed)	0.00	0.00	0.00	0.00	0.00		0.00
IQ (sharpness & clarity)	0.81	0.83	0.65	0.77	0.95	0.81	1.00
Sig. (2-tailed)	0.00	0.00	0.00	0.00	0.00	0.00	

Table (II-7): 1 year old regression analysis for all the parameters.

Regression (1 year old)													
		Dose		SNR		CNR		IQ (sharpness)		IQ (clarity)		IQ (sharpness & clarity)	
	R²	0.91		0.99		0.98		0.92		0.98		0.97	
	P (F-test)	0.00		0.00		0.00		0.00		0.00		0.00	
	Constant	0.00		0.00		0.00		0.00		0.00		0.00	
kVp	B P-value	2.80	0.00	2.16	0.00	0.43	0.00	0.001	0.22	0.05	0.00	0.02	0.00
	95%CI	2.69		2.11		0.41		0.00		0.05		0.02	
		2.92		2.21		0.44		0.01		0.05		0.03	
mAs	B P-value	11.70	0.00	9.10	0.00	2.86	0.00	0.15	0.00	0.19	0.00	0.17	0.00
	95%CI	11.21		8.88		2.78		0.14		0.18		0.16	
		12.19		9.31		2.93		0.17		0.19		0.18	
SID	B P-value	-1.25	0.00	-0.71	0.00	-0.11	0.00	0.01	0.00	-0.01	0.00	0.003	0.00
	95%CI	-1.31		-0.74		-0.11		0.01		-0.01		0.00	
		-1.19		-0.69		-0.10		0.02		-0.01		0.00	
Filtration	B P-value	-26.76	0.00	-12.46	0.00	-4.61	0.00	-0.17	0.00	-0.21	0.00	-0.19	0.00
	95%CI	-28.51		-13.22		-4.87		-0.21		-0.24		-0.22	
		-25.01		-11.69		-4.36		-0.12		-0.18		-0.15	

Table (II-8): 5 year old regression analysis for all the parameters.

Regression (5 year old)													
		Dose		SNR		CNR		IQ (sharpness)		IQ (clarity)		IQ (sharpness & clarity)	
	R²	0.91		0.98		0.95		0.93		0.98		0.97	
	P (F-test)	0.00		0.00		0.00		0.00		0.00		0.00	
	Constant	0.00		0.00		0.00		0.00		0.00		0.00	
kVp	B P-value	4.99	0.00	1.04	0.00	0.09	0.00	0.01	0.00	0.04	0.00	0.03	0.00
	95%CI	4.82		1.00		0.08		0.01		0.04		0.02	
		5.16		1.07		0.11		0.01		0.04		0.03	
mAs	B P-value	17.27	0.00	3.92	0.00	1.32	0.00	0.07	0.00	0.14	0.00	0.11	0.00
	95%CI	16.75		3.81		1.27		0.07		0.14		0.10	
		17.80		4.03		1.37		0.08		0.15		0.11	
SID	B P-value	-2.54	0.00	-0.23	0.00	0.05	0.00	0.01	0.00	-0.01	0.00	0.001	0.00
	95%CI	-2.64		-0.25		0.04		0.01		-0.01		0.00	
		-2.44		-0.21		0.06		0.01		-0.01		0.00	

Filtration	B P-value	-49.62	0.00	-6.50	0.00	-2.69	0.00	-0.06	0.00	-0.18	0.00	-0.12	0.00
	95%CI	-52.50		-7.10		-2.95		-0.09		-0.20		-0.14	
		-46.74		-5.90		-2.43		-0.03		-0.15		-0.09	

Table (II-9): 10 year old regression analysis for all the parameters.

Regression (10 year old)														
		Dose		DAP		SNR		CNR		IQ (sharpness)		IQ (clarity)		IQ (sharpness & clarity)
	R²	0.89		0.92		0.89		0.91		0.78		0.47		0.78
	P (F-test)	0.00		0.00		0.00		0.00		0.00		0.00		0.00
	Constant	1569.41		695.84		57.42		48.62		7.63		5.66		6.65
kVp	B P-value	-13.44	0.00	-6.08	0.00	-0.51	0.00	-0.76	0.00	-0.07	0.00	-0.03	0.00	-0.05
	95%CI	-14.34		-6.42		-0.56		-0.80		-0.08		-0.04		-0.06
		-12.53		-5.74		-0.47		-0.71		-0.06		-0.03		-0.05
SID	B P-value	-0.96	0.00	-0.46	0.00	0.28	0.00	0.28	0.00	0.006	0.00	-0.002	0.00	0.002
	95%CI	-1.53		-0.67		0.26		0.25		0.002		-0.006		-0.001
		-0.40		-0.25		0.31		0.31		0.010		0.002		0.005
Filtration	B P-value	-76.24	0.00	-28.31	0.00	0.16	0.00	-0.71	0.00	-0.06	0.00	0.006	0.00	-0.03
	95%CI	-86.76		-32.26		-0.32		-1.27		-0.13		-0.06		-0.08
		-65.72		-24.36		0.65		-0.16		0.02		0.08		0.03

Appendix (III): Brochures of Commercial Phantoms

1. The data sheet for ATOM dosimetry phantoms:



FEATURES

- Phantom models cover a wide range of patient ages
- Organ specific dosimetry with minimal detectors
- Superior tissue simulation and lifelike imaging properties
- Homogeneous bone
- Accommodates wide variety of detectors
- Age appropriate references

CIRS

CIRS ATOM® phantoms are a full line of anthropomorphic, cross sectional dosimetry phantoms designed to investigate organ dose, whole body effective dose as well as verification of delivery of therapeutic radiation doses.

ATOM is the only line of dosimetry phantoms to range in sizes from newborn to adult. Six models are available: newborn, 1-year, 5-year and 10-year old pediatric phantoms as well as adult male and female phantoms.

Each phantom is sectional in design with traditional 25 mm thick sections. The sectional surfaces are extremely flat and smooth and do not require any special coatings or treatment. This results in minimal interfaces between the slabs when viewed in a scout or projection X-ray. The ATOM line also differs from other dosimetry phantoms by providing optimized TLD locations specific to 22 inner organs.

Tissue-equivalent epoxy resins are used in all aspects of the phantom. CIRS technology offers superior tissue simulation by covering a wider range of energy levels from diagnostic to therapeutic. In addition, all bones are homogeneous and are formulated to represent age appropriate, average bone composition. CIRS bone formulations offer distinct advantages over natural skeletons and other types of simulated bone.

Computerized Imaging Reference Systems, Inc is recognized world wide for tissue simulation technology and is the leader in the manufacture of phantoms and simulators for medical imaging and radiotherapy.

www.cirsinc.com

Anthropomorphic Phantoms From Adults to Infants

DOSE CALCULATIONS RELATED TO SIZE

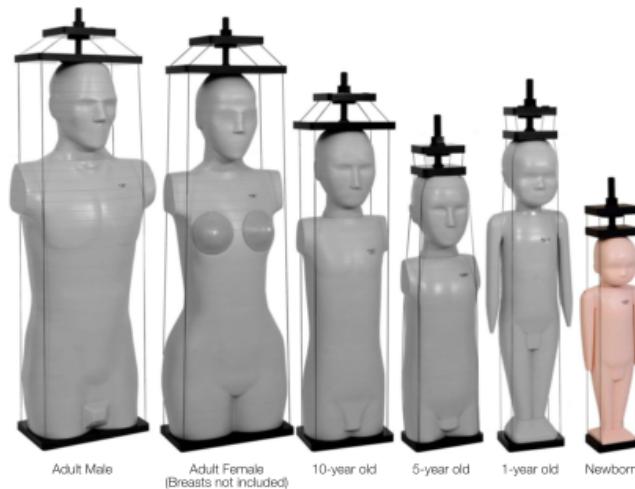
The size of each model is based on ICRP 23, ICRU 48 and available anatomical references (See Table 1). Only CIRS ATOM phantoms represent both pediatric and adult patient groups.

- Newborn
- 1-year old
- 5-year old
- 10-year old
- Adult Male
- Adult Female

This age range allows more accurate calculations of dose. The pediatric products support practitioners efforts to "child size" diagnostic scanning protocols in CT and more precisely determine effective doses in diagnostic radiology. Because scattering radiation can give a significant dose contribution to the surrounding tissue, the ATOM newborn and 1-year old are provided with arms and legs as a standard configuration. NOTE: Arms and legs on most ATOM models can be ordered as a separate option.

BONE SIMULATION APPROPRIATE TO AGE

Bone density varies significantly with age. This is especially significant in the pediatric models because the red bone marrow is distributed throughout the skeletal systems compared with adults. Proper bone simulation is also important for a pediatric patient because they have a higher sensitivity to the effects of radiation. Therefore, for more precise dosimetry measurements, ATOM phantoms are formulated with bone equivalent materials based on the appropriate bone composition typical of each age.



ATOM ANATOMICAL REFERENCES

(Based on ICRP 23, ICRU 48 and available anatomical reference data)

DESCRIPTION	HEIGHT, CM	WEIGHT, KG	THORAX DIMENSIONS, CM
ADULT MALE	173	73	23 cm x 32
ADULT FEMALE	160	55	20 x 25*
PEDIATRIC NEWBORN	51	3.5	9 x 10.5
PEDIATRIC 1 YEAR	75	10	12 x 14
PEDIATRIC 5 YEARS	110	19	14 x 17
PEDIATRIC 10 YEARS	140	32	17 x 20

*Measurement does not include breasts

Table 1

PHANTOM BONE MATERIAL SPECIFICATIONS

DESCRIPTION	PHYSICAL DENSITY, G/CC	ELECTRON DENSITY, 1/CC
ADULT MALE	1.60	$5.030 \cdot 10^{23}$
ADULT FEMALE	1.60	$5.030 \cdot 10^{23}$
PEDIATRIC NEWBORN	1.41	$4.498 \cdot 10^{23}$
PEDIATRIC 1 YEAR	1.45	$4.606 \cdot 10^{23}$
PEDIATRIC 5 YEARS	1.52	$4.801 \cdot 10^{23}$
PEDIATRIC 10 YEARS	1.56	$4.878 \cdot 10^{23}$

Table 2

2. The data sheet for 5 year Pediatric Anthropomorphic Training Phantoms Model Series 715:



Pediatric Anthropomorphic Training Phantoms

Model 715 Series



SPoRT™ The World's First Sectional Pediatric Radiography Trainer

An ideal addition to any imaging department or Radiologic Technology training program, the CIRS Model 715 Series can assist in the monitoring, training and improvement of parameters and protocols common to most pediatric imaging procedures.

SPoRT™ is designed to aid teaching and improvement of patient positioning, collimation and anatomical comprehension and it's wide range of features facilitate effective instruction of safe, high quality, pediatric imaging.

The phantom represents a typical 5-year old in both size and structure, making it portable and easy to position. The full body with head, arms and legs measures 110 cm (43 in) tall and weighs 20 kg (44 lb).

Components are made from propriety urethane and epoxy materials that mimic X-ray attenuation properties of human tissues for both diagnostic and therapy energy ranges (50keV-25MeV). The materials are durable, impact resistant and suitable for continuous handling.

SPoRT™ can be used in film radiography, CR, DR and Computed Tomography.

The Model 715 series consists of six sectional phantoms available separately or as a complete set. Complete set includes head, trunk, right and left arms with natural and oblique hand positions and right and left legs with natural and plantar flexion foot positions.

2428 Alameda Avenue Suite 316 • Norfolk, Virginia 23513 • USA
Tel: 800.617.1177 • 757.855.2765 • Fax: 757.857.0523

www.cirsinc.com

CIRS

Tissue Simulation & Phantom Technology

3. The data sheet for ALDERSON phantoms:

4/29/2017



ALDERSON PHANTOMS

THE ALDERSON RADIATION THERAPY PHANTOM (ART)



The Worldwide Standard for Quality Assurance for Radiation Therapy

The Alderson Radiation Therapy phantom (ART) and its earlier version, the Alderson RANDO phantom, have been in use for over 30 years. The ART has been refined and improved in both design and materials. These phantoms are indispensable quality-assurance tools; about 2,000 are in use all over the world. They provide integrated tests of the entire chain of treatment planning and delivery.

ART phantoms are molded of tissue-equivalent material, they are designed within highly sophisticated technological constraints and follow ICRU-44 standards. They are also designed for accuracy and ease of use.

ANATOMY

The male ART represents a 175 cm (5 ft. 9 in.) tall, 73.5 kg (162 lb.) male, and the female ART represents a 155 cm (5 ft. 1 in.) tall, 50 kg (110 lb.) female.

The ART phantom is transected-horizontally into 2.5 cm thick slices. Each slice has holes which are plugged with bone-equivalent, soft-tissue-equivalent or lung tissue-equivalent pins which can be replaced by TLD holder pins. The holder pins are ordered separately.

Soft-tissue-equivalent coatings produce slices with glass-smooth interfaces. These coatings are cut away over the air spaces of the oronasal pharynxes, trachea and stem bronchi.

Male ART and Female ART

Appendix (IV): Ethical Approvals



University of
Salford
MANCHESTER

Research, Innovation and Academic
Engagement Ethical Approval Panel

Research Centres Support Team
G0.3 Joule House
University of Salford
M5 4WT

T +44(0)161 295 2280

www.salford.ac.uk/

21 February 2017

Dear Ali,

RE: ETHICS APPLICATION–HSR1617-78–‘Investigating the impact of changing patient size on image quality and radiation dose for paediatric pelvic radiography using digital radiography.’

Based on the information you provided I am pleased to inform you that application HSR1617-78 has been approved.

If there are any changes to the project and/or its methodology, then please inform the Panel as soon as possible by contacting Health-ResearchEthics@salford.ac.uk

Yours sincerely,

A handwritten signature in black ink, appearing to read 'Sue McAndrew'.

Sue McAndrew
Chair of the Research Ethics Panel

(A)



University of
Salford
MANCHESTER

Research, Innovation and Academic
Engagement Ethical Approval Panel

Research Centres Support Team
G0.3 Joule House
University of Salford
M5 4WT

T +44(0)161 295 2280

www.salford.ac.uk/

10 March 2017

Dear Ali,

RE: ETHICS APPLICATION–HSR1617-77–‘Impact of changing patient size on image quality and radiation dose for paediatric pelvic radiography – Observer assessment of image quality variability study.’

Based on the information you provided I am pleased to inform you that application HSR1617-77 has been approved.

If there are any changes to the project and/or its methodology, then please inform the Panel as soon as possible by contacting Health-ResearchEthics@salford.ac.uk

Yours sincerely,

Sue McAndrew
Chair of the Research Ethics Panel

(B)

Appendix (V): Quality Control Tests

Table (V-1): Radiation output repeatability and reproducibility.

Set-up:					
	FFD (cm)	kV	Focus	mAs	Other
A	100	60	Fine	4	
B	100	80	Broad	10	
C	100	100	Broad	20	

Baseline:		
Output A	Output B	Output C
71.0	353.8	1.2

Measurements:												
Date	Initial	A1	A2	A3	Result	Average A	Result	B	Result	C	Result	Action taken
31/03/2016	CB/AKT	71.0	71.8	71.9	Pass	71.5	Pass	353.8	Pass	1.2	Pass	kV OK
12/07/2016	CB/AKT	69.8	70.5	70.8	Pass	70.4	Pass	353.4	Pass	1.2	Pass	
09/02/2017	CB/AKT	71.4	70.9	71.0	Pass	71.1	Pass	354.1	Pass	1.2	Pass	
27/03/2017	CB/AKT	66.8	67.9	68.0	Pass	67.6	Pass	338.4	Pass	1.2	Pass	Following Service
05/05/2017	CB/AKT	67.1	67.4	66.9	Pass	67.1	Pass	338.1	Pass	1.2	Pass	
05/06/2017	CB/AKT	66.4	66.9	66.8	Pass	66.7	Pass	338.5	Pass	1.2	Pass	
14/09/2017	CB	60.6	59.7	60.6	Pass	60.3	Pass	335.4	Pass	1.2	Pass	
23/03/2018	CB	70.7	70.5	70.8	Pass	70.7	Pass	337.2	Pass	1.1	Pass	
28/06/2018	CB	63.0	63.4	63.4	Pass	63.3	Pass	329.9	Pass	1.1	Pass	Service

Table (V-2): X-ray / light beam alignment and centring.

Set-up			
FFD (cm)	kV	mAs	Focus
100	45	5	Fine

Measurements:						
Date	Initial	Misalignment (cm)	Result	Miscentering (cm)	Result	Action taken
31/03/2016	CB/AKT	0.0	Pass	0.0	Pass	
12/07/2016	CB/AKT	0.0	Pass	0.0	Pass	
09/02/2017	CB/AKT	0.0	Pass	0.0	Pass	
27/03/2017	CB/AKT	0.0	Pass	0.0	Pass	
05/05/2017	CB/AKT	0.0	Pass	0.0	Pass	
05/06/2017	CB/AKT	0.0	Pass	0.0	Pass	
14/09/2017	CB/AKT	0.0	Pass	0.0	Pass	
23/03/2018	CB/AKT	0.0	Pass	0.0	Pass	
28/06/2018	CB/AKT	0.0	Pass	0.0	Pass	

Table (V-3): AEC sensitivity.

AEC sensitivity (CR14) - Table bucky											
Set-up:	FFD (cm)	kV	Filtration	Chamber	Grid	Density	Other				
A	110	80	none	centre	y	0					
B	110	80	none	lateral x2	y	0					
C	110	80	none	all	y	0					
Baseline:											
mAs (A)	DDI (A)	mAs (B)	DDI (B)	mAs (C)	DDI (C)						
2.2	295.0	2.2	279.9	2.2	281.0						
Measurements:											
Date	Initial	mAs (A)	DDI (A)	Result	mAs (B)	DDI (B)	Result	mAs (C)	DDI (C)	Result	Action taken
31/03/2016	CB/AKT	2.2	295.3	Pass	2.2	279.8	Pass	2.2	281.1	Pass	
12/07/2016	CB/AKT	2.2	295.1	Pass	2.2	279.7	Pass	2.2	281.1	Pass	
09/02/2017	CB/AKT	2.2	294.6	Pass	2.2	280.2	Pass	2.2	280.7	Pass	
27/03/2017	CB/AKT	2.3	295.2	Pass	2.2	279.4	Pass	2.4	281.5	Pass	Following Service
05/05/2017	CB/AKT	2.3	294.8	Pass	2.2	278.9	Pass	2.4	280.9	Pass	
05/06/2017	CB/AKT	2.3	295.3	Pass	2.2	279.4	Pass	2.4	281.2	Pass	
14/09/2017	CB/AKT	2.2	294.2	Pass	2.2	279.1	Pass	2.3	280.6	Pass	
23/03/2018	CB/AKT	2.6	297.3	Pass	2.5	281.3	Pass	2.5	281.7	Pass	
28/06/2018	CB	2.6	248.9	Pass	2.6	226.0	Pass	2.6	231.1	Pass	Service

Table (V-4): Quality control for the Raysafe X2.



The Christie
NHS Foundation Trust

Christie Medical Physics & Engineering
The Christie NHS Foundation Trust
Withington, Manchester
M20 4BX, UK

Diagnostic X-Ray QC Equipment Performance Evaluation

Report No: 0035/SUSFU/18	Report Date: 6 February, 2018
--------------------------	-------------------------------

Customer:	Salford University
Equipment:	Raysafe X2 (our ref. Q2) [Unit s/n 212896, R/F detector s/n 214341]
Date of test:	12/1/18
Previous relevant reports:	051/SUSFU/17
Sent to:	Andrew Tootell, Radiation Protection Supervisor Chris Beaumont Radiation Protection Supervisor Christie Theodorakou, CMPE
Contact:	Andy Shaw on (0161) 446 3550 or e-mail andy.shaw@christie.nhs.uk

Diagnostic Radiology and Radiation Protection Group
BSI registered - certificate number: FS 37543

Measurement	Tolerance	Outcome	
		Pass	Fail
kV accuracy	±3%	Pass	
Dose accuracy	±5%	Pass	
Timer accuracy	±1% or ±0.33 ms	Pass	

Conclusions

This unit is acceptable for:

- Checking radiographic outputs over the range 40 to 130 kV and 1 to 100 mAs
- Checking kVp accuracy over the range 50 to 130 kV
- Checking exposure times over the range 10 to 500 ms

Our next scheduled checks on this equipment will be due in Jan 2019.

Note

This check does not constitute a full calibration of the equipment but is intended to give a guide to its accuracy compared to instruments whose calibration is traceable back to national standards and to act as a baseline for future checks on the consistency of the equipment.